



Manufacture, characterisation and *in vivo*
assessment of nerve guidance conduits containing
physical guidance cues.

Jonathan Field

A thesis submitted to The University of Sheffield, Faculty of Medicine, Dentistry
and Health for the degree of Doctor of Philosophy.

School of Clinical Dentistry
Department of Materials Science and Engineering

October 2019

Abstract/Summary

Current methods for peripheral nerve repair have a number of drawbacks and limited success rates. Nerve guidance conduits (NGCs) can be used as an alternative to the gold standard autograft treatment, but current products with simple designs are only effective in short distance nerve gaps. With the aim of improving regeneration in NGCs, this study explored the production of NGCs containing physical guidance cues which have been shown to provide guidance to regenerating cells. Conduits containing aligned grooves and aligned microfibres were produced by microstereolithography (μ SL) and electrospinning and assessed *in vivo* for their nerve regeneration potential.

A photocurable resin, with tuneable degradation and mechanical properties, was developed for use in μ SL by controlled methacrylation of poly(caprolactone) (PCL). The resin was used in μ SL to produce NGCs and photoabsorbers were added to enable the production of complex 3D structures.

Conduits with aligned luminal grooves were fabricated directly by μ SL. Separately, fibre-filled conduits were produced by filling μ SL tubes with highly aligned, electrospun PCL fibres. Fibres were produced to precisely controllable diameters and fibre-filled conduits were analysed with gas pycnometry and micro-computed tomography which allowed control over fibre packing density.

Preliminary *in vitro* testing confirmed the biocompatibility of the poly(caprolactone)-methacrylate (PCLMA) material, which supported the growth of Schwann and RN22 cells. In collaboration with another project, fibre-filled conduits were tested in an *ex vivo* nerve injury model to determine optimal parameters. Here, plasma treatment of conduits improved dorsal root ganglion outgrowth and conduits containing 10 μ m fibres at 10% packing density were selected as the primary candidate for initial *in vivo* testing.

Grooved and fibre-filled conduits were used to repair nerve injuries in thy-1-YFP mice. Their performance was compared to autografts and plain conduit controls in terms of axon number, axon disruption and success rates. Grooved and plasma-treated fibre-filled conduits supported nerve regeneration comparable to autografts and outperformed controls in certain parameters. This demonstrated the beneficial effect of the intraluminal guidance cues, however future work is necessary to test these conduits in longer distance nerve gaps.

Acknowledgements

Firstly, I would like to give thanks to my supervisors, Fiona Boissonade, Frederik Claeysens and John Haycock for their expert advice and guidance throughout the project. Without such a strong supervisory team, I would not have achieved all that I have. To Fiona for her support, motivation and keen interest and for giving me the freedom to explore areas of my own interest. To Fred for his endless enthusiasm and for always encouraging me to try out new and interesting ideas. To both for securing the funding to allow me to undertake this work and to the EPSRC and the University of Sheffield, Faculty of Medicine, Dentistry and Health for providing the funding.

I would like to thank all the PhD students, post-docs and staff at the Kroto Research Institute for all their help and contributions and for making my PhD a hugely enjoyable experience. Thank you to George and Sarina for being there from the beginning and the rest of the office: Mehrie, Marcella, Kat, Darren and Ahssad. Also to Tom and Sarah for their support and PhD-related advice.

Thanks to Colin for always wanting to discuss problems, find solutions and pushing me to think critically. To Caroline for training me up in the lab in the early days of my SURE scheme project, for passing on her electrospinning expertise and for providing the primary Schwann cells. Thanks to Sabi for his help with the mechanical testing of the polymer samples and for being an all-round helpful guy. Huge thanks go to Adam Harding for training me up with the *in vivo* model and spending many long days in the lab, showing a great deal of patience. Thank you to Sam for giving me a job during my writing up period and encouraging me to apply my skills to new applications.

Thank you to my family, especially my parents who supported me through my years of education and always pushed me to be the best I could be. Without your help, I wouldn't be where I am today (despite the phase of "When will you be finished?" coming almost weekly from my dad's mouth). To my grandparents, whose positive outlook and attitude towards life has always been an inspiration. Finally, to Rach – your constant, never ending encouragement and support has been more than I could ever ask for. Thank you for believing in me when I did not, and putting up with the stressful times, the late nights and the boring weekends of work. I couldn't have done it without you.

Conference presentations and awards

Oral presentations

Nerve guidance conduits fabricated by microstereolithography and electrospinning - characterisation and in vivo assessment.

European Society for Biomaterials Annual Meeting, Athens, 4th-8th September 2017.

Composite nerve guidance conduits containing aligned fibres for enhanced guidance properties.

White Rose Biomaterials and Tissue Engineering Group Meeting, Leeds, 18th December 2017

- **Awarded 1st place oral presentation prize**

Characterisation and in vivo assessment of physical guidance cues in nerve guidance conduits.

Tissue and Cell Engineering Society Annual Meeting, Keele, 2nd-4th July 2018

(Flash oral presentation and Poster presentation)

- **Awarded 2nd place poster prize**

Intraluminal guidance cues for nerve guide conduits.

European Society for Biomaterials Annual Meeting, Maastricht, 9-13th September 2018

Poster presentations

Conduits for peripheral nerve repair fabricated using by microstereolithography and electrospinning.

Tissue Engineering and Regenerative Medicine International Society EU Meeting, Uppsala, 28th June-1st July 2016

- **Awarded 3rd place poster prize**

Conduits for peripheral nerve repair fabricated using microstereolithography and electrospinning.

White Rose Biomaterials and Tissue Engineering Group Meeting, Durham, 14th December 2016

Composite nerve guidance conduits fabricated using microstereolithography and electrospinning.

Tissue and Cell Engineering Society Annual Meeting, Manchester, 5th-7th July 2017

Intraluminal Guidance Cues for Promoting Regeneration in Nerve Guidance Conduits.

International Association for Dental Research General Session, London, 25th-28th July 2018

- **Awarded a commendation in the Unilever poster competition**

Publications in preparation

1. J. Field, F. M. Boissonade, F. Claeysens. A tuneable, photocurable poly(caprolactone)-based resin for use in microstereolithography – synthesis, characterisation and 3D structuring.
2. J. Field, A. Harding, J. W. Haycock, F. Claeysens, F. M. Boissonade. Microstereolithography and in vivo assessment of poly(caprolactone)-based conduits containing aligned grooves for peripheral nerve repair.
3. J. Field, A. Harding, M. Behbehani, J. W. Haycock, F. Claeysens, F. M. Boissonade. The effect of aligned electrospun fibres and air-plasma treatment on peripheral nerve regeneration through nerve guidance conduits in vivo.

Table of contents

Abstract/Summary	iii
Acknowledgements	iv
Conference presentations and awards	v
Oral presentations	v
Poster presentations	v
Publications in preparation	vi
Table of contents	vii
List of figures	xiii
List of tables	xvi
List of equations	xvi
Abbreviations	xvii
1. Chapter 1: Introduction and General Literature review	19
1.1 The anatomy of the peripheral nervous system	19
1.2 Peripheral nerve injury and repair	21
1.2.1 Peripheral nerve injury.....	21
1.2.2 Nerve Injury in dentistry	22
1.2.3 Peripheral nerve regeneration.....	24
1.2.4 Impact of scarring on nerve regeneration	26
1.2.5 Surgical repair & current treatments	26
1.2.6 Conclusions	29
1.3 Nerve guidance conduits	29
1.3.1 The Ideal NGC.....	30
1.3.2 Mechanism of regeneration through a NGC.....	31
1.3.3 Commercially available NGCs.....	33
1.3.4 Conclusions	36
1.4 Manufacture methods for NGCs	36
1.4.1 Current NGC manufacture methods	36
1.4.2 Alternative manufacture methods.....	37
1.4.3 Stereolithography	37

1.4.4	NGCs produced by stereolithography	39
1.4.5	Conclusions	40
1.5	Methods to improve NGC designs.....	41
1.5.1	Contact guidance, a history.....	41
1.6	Modern strategies to include contact guidance in NGCs.....	42
1.6.1	Electrospinning	43
1.6.2	Influence of aligned fibres on Schwann and neuronal cell growth	44
1.6.3	Conduits manufactured with electrospun fibres	47
1.6.4	Conduits containing fibres produced by alternative methods.....	52
1.6.5	Microgrooves for guidance in NGCs.....	53
1.6.6	Conclusions	56
1.7	Project Aims and Objectives	57
1.7.1	Main project Aim:	57
1.7.2	Objectives	57
2.	<i>Chapter 2: PCLMA production, characterisation and use in microstereolithography..</i>	58
2.1	Chapter Introduction	58
2.2	Background	59
2.2.1	Materials for NGCs.....	59
2.2.2	Photocurable materials for stereolithography.....	59
2.2.3	Varying the Degree of Polymer Methacrylation and the effects	64
2.2.4	Photoabsorbers for stereolithography.....	67
2.2.5	Conclusions from literature	69
2.3	Aims for this chapter	70
2.4	Materials and Methods	71
2.4.1	PCL methacrylation and characterisation	71
2.4.2	Prepolymer resin preparation.....	72
2.4.3	Mechanical testing of cured PCLMA	73
2.4.4	Soluble fraction calculation of cured PCLMA	75
2.4.5	Degradation study.....	75
2.4.6	Microstereolithography for scaffold production	76
2.4.7	Investigation of photoabsorber use in μ SL	79
2.4.8	Statistical analysis	81
2.5	Results.....	82
2.5.1	PCL methacrylation and characterisation	82

2.5.2	Microstereolithography – Parameter optimisation for tube production.....	90
2.5.3	General appearance of PCLMA tubes produced by μ SL using optimum parameters	92
2.5.4	Photoabsorber suitability and the effect of their use in μ SL	94
2.6	Discussion	101
2.6.1	PCL Methacrylation	101
2.6.2	PCLMA resin formulation	106
2.6.3	The microstereolithography process	108
2.6.4	Presence of microgrooves on constructs produced by microstereolithography	111
2.6.5	The addition of photoabsorbers to μ SL resins	112
2.7	Conclusions	114
3.	Chapter 3: Conduit design, production & analysis	115
3.1	Chapter Introduction	115
3.2	Background	116
3.2.1	3D printing of conduits with guidance cues.....	116
3.2.2	Combining microstereolithography and electrospinning for NGCs	117
3.2.3	Incorporating Electrospun fibres into NGCs.....	118
3.2.4	Conclusions	119
3.3	Aims for this chapter	119
3.4	Materials and Methods	120
3.4.1	Production of plain conduits	120
3.4.2	Production of conduits with aligned grooves	120
3.4.3	Electrospinning for the production of aligned PCL fibres	121
3.4.4	Incorporating electrospun fibres into tubes produced by microstereolithography	123
3.4.5	Analysis of the packing density of the fibre-filled conduits by gas displacement pycnometry....	124
3.4.6	Analysis of fibre-filled conduits via micro-computed tomography	125
3.4.7	Production of fibre-filled tubes for <i>in vivo</i> use.....	125
3.4.8	Production of smooth tubes via injection moulding.....	128
3.4.9	Laser-cutting of conduits.....	129
3.4.10	Imaging of conduits via scanning electron microscopy	129
3.4.11	Optical microscopy for measurement of tube dimensions	129
3.4.12	Cryosectioning of conduits	130
3.4.13	Statistical analysis.....	131
3.5	Results.....	132
3.5.1	Plain conduits produced by microstereolithography	132

3.5.2	Grooved conduits produced by microstereolithography.....	132
3.5.3	SEM analysis of PCL fibres produced by electrospinning.....	136
3.5.4	Fibre-filled conduits – general observations via SEM and micro-CT imaging	139
3.5.5	Analysis of fibre packing density with gas displacement pycnometry.....	142
3.5.6	Analysis of fibre packing density with micro-computed tomography	144
3.5.7	Fibre-filled conduits for <i>in vivo</i> use: modular conduit design.....	145
3.5.8	Smooth conduits produced by injection moulding.....	147
3.5.9	Handling properties of PCLMA tubes.....	148
3.5.10	Autoclavability of PCLMA conduits.....	149
3.6	Discussion	150
3.6.1	Grooved conduits.....	150
3.6.2	Fibre-filled conduits	151
3.6.3	Autoclavability of PCLMA conduits	153
3.7	Conclusions	154
4.	Chapter 4: <i>In Vitro</i> analysis of conduit performance.....	155
4.1	Chapter Introduction	155
4.2	Background	156
4.2.1	Plasma Treatment.....	156
4.2.2	Assessment of nerve regeneration <i>in vitro</i> – the effect of different fibre diameter and the importance of 3D culture	157
4.2.3	Effect of fibre packing density.....	158
4.2.4	Conclusions from literature	159
4.3	Aims for this chapter	160
4.4	Materials and Methods	161
4.4.1	General cell culture.....	161
4.4.2	Biocompatibility testing of NGC materials.....	162
4.4.3	Schwann cell migration study in fibre-filled conduits.....	164
4.4.4	Effect of plasma treatment.....	166
4.4.5	<i>Ex vivo</i> DRG culture in fibre-filled conduits.....	168
4.4.6	Statistical analysis	169
4.5	Results.....	170
4.5.1	PCLMA Biocompatibility.....	170
4.5.2	Beta-carotene biocompatibility	172
4.5.3	Cell migration through fibre-filled conduits <i>in vitro</i>	173

4.5.4	Effect of plasma treatment on water contact angle	175
4.5.5	DRG outgrowth in fibre-filled conduits	176
4.6	Discussion	179
4.6.1	Biocompatibility testing of NGC materials	179
4.6.2	Schwann cell migration study	180
4.6.3	Plasma treatment.....	181
4.6.4	The effect of fibre parameters/properties on DRG outgrowth.....	182
4.7	Conclusions	184
5.	Chapter 5: In Vivo analysis of conduit performance	185
5.1	Chapter Introduction	185
5.2	Background	186
5.2.1	Methods of assessing nerve regeneration <i>in vivo</i>	186
5.2.2	The thy-1-YFP mouse model	187
5.2.3	Methods of assessing regeneration with the thy-1-YFP mouse model.....	188
5.2.4	Method of nerve repair.....	189
5.3	Aims for this chapter	191
5.4	Materials and Methods	192
5.4.1	Conduit preparation.....	192
5.4.2	In vivo surgery methods.....	194
5.4.3	Imaging of YFP nerve harvests	200
5.4.4	Analysis of YFP nerve harvest images	200
5.4.5	Sample size calculations.....	205
5.4.6	Statistical analysis	206
5.5	Results.....	207
5.5.1	Preliminary <i>in vivo</i> studies	207
5.5.2	General observations regarding failed regeneration	215
5.5.3	Study 1: The effect of aligned grooves on nerve regeneration.....	217
	(Plain conduits vs Grooved conduits).....	217
5.5.4	Study 2: The effect of aligned fibres and plasma treatment on nerve regeneration.....	224
	(Fibre-filled vs plain conduits, with and without plasma treatment).....	224
5.5.5	The effect of beta-carotene: Plain conduit vs Plain conduit containing beta-carotene	229
5.5.6	Study 3: The effect of μ SL microfeatures on nerve regeneration	230
	(Plain vs Smooth conduits).....	230
5.5.7	Overall success/failure: Comparison between all repair types.....	233

5.6	Discussion	235
5.6.1	Preliminary experiments.....	235
5.6.2	The advantages of confocal over fluorescence microscopy: allowing an improved axon tracing method.....	236
5.6.3	Study 1: The effect of aligned grooves on nerve regeneration.....	238
5.6.4	Study 2: The effect of aligned fibres and plasma treatment on nerve regeneration.....	245
5.6.5	Study 3: The effect of μ SL microfeatures on nerve regeneration.....	252
5.7	Conclusions	253
6.	<i>General Discussion and Future work</i>.....	254
6.1	Materials.....	254
6.1.1	Suitability of PCLMA as a NGC material	254
6.1.2	Porous materials	256
6.2	The <i>in vivo</i> model	257
6.2.1	Use of thy-1-YFP mice – Analysis methods	257
6.2.2	The importance of nerve gap length and recovery time.....	258
6.2.3	Ideas for conduit improvements.....	259
6.2.4	More complex nerve injury models and other applications	260
7.	<i>Final Conclusions</i>	261
8.	<i>Appendix</i>.....	262
9.	<i>References</i>.....	264

List of figures

Figure 1. A simplified view of the anatomy of the peripheral nerve.	20
Figure 2. Flowchart, describing the branching of the trigeminal nerve into the lingual and inferior alveolar nerves.....	23
Figure 3. Diagram outlining the anatomical positions of the lingual and inferior alveolar nerves.	23
Figure 4. The stages of axonal regeneration following a nerve transection injury.	25
Figure 5. A nerve guidance conduit (NGC) positioned between the proximal and distal ends of a severed peripheral nerve.....	29
Figure 6. The stages of regeneration through a hollow guidance tube.	32
Figure 7. SEM images of commercially available NGCs.	34
Figure 8. The cyclic process of stereolithography.	38
Figure 9. The principle behind the DMD function	39
Figure 10. Diagram of an electrospinning set-up.....	44
Figure 11. Conduits produced by Chew et al.	47
Figure 12. Multi-lumen silk conduit produced by Dinis et al.	48
Figure 13. Electrospun fibre yarn-containing conduits fabricated by Koh et al.	50
Figure 14. Shapes of microgrooves investigated by Mobasserri et al.	56
Figure 15. Gyroid structures produced via μ SL by Barker et al.	69
Figure 16. PCL methacrylation reaction scheme.	72
Figure 17. Specifications of the 'dog bone' tensile test piece adapted from the ASTM D638 - 14.....	73
Figure 18. PCLMA tensile testing.	74
Figure 19. The microstereolithography (μ SL) set-up.	77
Figure 20. Production of 3D structures via microstereolithography.	78
Figure 21. Intermittent grooved channels.....	80
Figure 22. Proton NMR spectra of unmethacrylated and methacrylated PCL triol.....	83
Figure 23. PCLMA produced with varying degree of methacrylation (DM).	85
Figure 24. Mechanical testing of cured PCLMA.	86
Figure 25. The effect of the degree of methacrylation on the Young's Modulus of cured PCLMA.....	87
Figure 26. The effect of degree of methacrylation on the soluble fraction of cured PCLMA.....	88
Figure 27. Accelerated degradation of PCLMA and PCL discs.....	89
Figure 28. A: SEM image of PCLMA tubes produced by μ SL.....	92
Figure 29. The absorbance spectra of the three photoabsorbers	94
Figure 30. Photoabsorbers mixed with PEGDA.	95
Figure 31. Photoabsorbers mixed with PCLMA.	95
Figure 32. Grooved channels produced by μ SL	96
Figure 33. Strut length:gap length (S:G) ratios.	97
Figure 34. Scanning electron micrographs of PEGDA grooved channels	98

Figure 35. Bifurcated tubes produced by μ SL.....	99
Figure 36. 3D constructs produced from PCLMA	100
Figure 37. Graphs showing the DM of PCLMA calculated via two separate methods.....	102
Figure 38. Conventional stereolithography methods which cure sequential layers.....	108
Figure 39. A bottom-up stereolithography system with the laser directed at the base of the resin vat.....	109
Figure 40. DMD image used to produce tubes by microstereolithography and a magnified section of the DMD image showing the pixellation which represents the individual micromirrors.....	111
Figure 41. The effect of light absorbers in μ SL.....	112
Figure 42. DMD Images used to produce plain tubes (A) and grooved tubes (B).	121
Figure 43. The electrospinning set-up	122
Figure 44. Threading electrospun PCL fibres into PCLMA tubes.....	124
Figure 45. The design and assembly process for the fibre-filled tubes with empty cuffs.	127
Figure 46. The mould construction used for production of smooth PCLMA tubes via injection moulding.....	128
Figure 47. Optical microscopy images of plain and grooved tubes showing the measurements made in red. .	130
Figure 48. Sections of grooved tubes (obtained using a cryostat)	133
Figure 49. SEM of PCLMA tubes fabricated by μ SL using PCLMA resin containing 0.075% beta-carotene.....	134
Figure 50. Annotated image of a grooved tube	136
Figure 51. The effect of flow rate and polymer concentration on the diameter of electrospun PCL fibres.....	137
Figure 52. SEM images of aligned PCL microfibres fabricating using different parameters.	138
Figure 53. Longitudinal cross-sectional image of a fibre-filled tube	139
Figure 54. SEM images of PCL tubes containing aligned PCL microfibres.....	140
Figure 55. Fibre-filled conduits cut with a scalpel.	141
Figure 56. Graphs showing the packing density (percentage fill of the lumen) of PCLMA conduits filled with electrospun PCL fibres.....	143
Figure 57. Method of calculating fibre packing density from micro-CT images.....	144
Figure 58. Modular design for the fibre-filled conduits.....	145
Figure 59. SEM images of assembled fibre-filled conduits.....	146
Figure 60. SEM images of smooth PCLMA conduits.....	147
Figure 61. Bending of a PCLMA tube produced by injection moulding.	148
Figure 62. SEM images of autoclaved PCLMA conduits.	149
Figure 63. Cell seeding protocol for migration experiment in fibre-filled conduits.	165
Figure 64. Biocompatibility testing of PCLMA, assessed by MTT assay.	171
Figure 65. Biocompatibility testing of beta-carotene-containing PCLMA, assessed by MTT assay.	172
Figure 66. Confocal microscopy images of RN22 cells growing on electrospun fibres.....	173
Figure 67. Water contact angle measurements for glass, PCLMA and PCL before and after air-plasma treatment.....	175
Figure 68. The effect of different fibre packing densities on the outgrowth of axons from DRGs cultured in fibre-filled conduits.....	178

<i>Figure 69. Photographs of common fibular repair surgery.</i>	198
<i>Figure 70. Photographs of the conduit harvest.</i>	199
<i>Figure 71. Unique axon tracing of YFP nerve repairs.</i>	202
<i>Figure 72. A magnified view of a sprouting axon.</i>	203
<i>Figure 73. Axon disruption measurements.</i>	204
<i>Figure 74. Fluorescence microscopy images of nerve harvests from preliminary experiment 1.</i>	208
<i>Figure 75. Fluorescence microscopy images of nerve harvests from preliminary experiment 2.</i>	210
<i>Figure 76. Confocal fluorescence microscopy images of nerve harvests from preliminary experiment 3.</i>	212
<i>Figure 77. Sprouting index measurements from preliminary experiment 3.</i>	213
<i>Figure 78. Increased image quality when imaging YFP harvests with confocal vs fluorescence microscopy.</i>	214
<i>Figure 79. Examples of two failed conduit repairs.</i>	216
<i>Figure 80. Typical images for common fibular nerve repairs with Graft (A), Plain conduit (B) and Grooved conduit (C), (Both conduits containing beta-carotene).</i>	218
<i>Figure 81. Sprouting index values at 0.5 mm intervals along the repair for Graft repairs (N=7), Plain and Grooved conduits (both containing beta-carotene (BC), N=6).</i>	220
<i>Figure 82. Unique axon tracing.</i>	221
<i>Figure 83. Axon disruption measurements.</i>	222
<i>Figure 84. Example axons traced for axon disruption measurements.</i>	223
<i>Figure 85. Typical images for common fibular nerve repairs with Plain conduits.</i>	225
<i>Figure 86. Typical images for common fibular nerve repairs with Fibre-filled conduits.</i>	226
<i>Figure 87. Sprouting index values at 0.5 mm intervals along the repair for Graft repairs (N=7), Plain conduits (plasma-treated and non-treated, N=7) and Fibre-filled conduits (plasma-treated and non-treated, N=5).</i>	228
<i>Figure 88. Sprouting index values at 0.5 mm intervals along the repair for Plain conduits (taken from Figure 87) and Plain conduits containing beta-carotene (BC).</i>	229
<i>Figure 89. Typical images for common fibular nerve repairs with Plain conduits (A) and Smooth conduits (B).</i>	231
<i>Figure 90. Sprouting index values at 0.5 mm intervals along the repair for Graft repairs, Plain conduits and Smooth conduits.</i>	232
<i>Figure 91. The overall success/failure of each conduit type, quantified using 2 criteria:</i>	234
<i>Figure 92. Image quality of YFP nerve harvests imaged by fluorescence vs confocal microscopy.</i>	237
<i>Figure 93. Sample size calculation results (from PiFace software) for Study 1 and Study 3,</i>	262
<i>Figure 94. Sample size calculation results (from PiFace software) for Study 2,</i>	263

List of tables

<i>Table 1. A number of FDA approved, commercially available NGCs.</i>	<i>34</i>
<i>Table 2. A summary of a number of clinical studies using commercial NGCs.</i>	<i>35</i>
<i>Table 3. A summary of research into controlling the degree of methacrylation (DM) of various polymers.</i>	<i>66</i>
<i>Table 4. Reaction parameters used to produce PCLMA and the resulting degree of methacrylation (DM).</i>	<i>85</i>
<i>Table 5. The effect of laser power and stage speed on PCLMA tube quality.</i>	<i>90</i>
<i>Table 6. The effect of raised prepolymer temperature on PCLMA tube quality with increasing stage speeds. ...</i>	<i>91</i>
<i>Table 7. Measurements of Grooved and Plain tube dimensions from optical microscopy images.</i>	<i>135</i>
<i>Table 8. The different parameter sets used in the electrospinning of PCL and the fibre diameters produced... </i>	<i>137</i>
<i>Table 9. Schwann cell migration in fibre-filled tubes.</i>	<i>174</i>
<i>Table 10. Animal numbers for the three main studies.....</i>	<i>195</i>
<i>Table 11. Summary data from sample size calculations</i>	<i>206</i>

List of equations

<i>Equation 1. The Beer-Lambert Law.....</i>	<i>67</i>
<i>Equation 2. Cure depth</i>	<i>67</i>
<i>Equation 3. Calculation of the soluble fraction of cured PCLMA.....</i>	<i>75</i>
<i>Equation 4. Calculation of the degree of methacrylation (DM) of PCLMA.....</i>	<i>82</i>
<i>Equation 5. An alternative method for calculation of the degree of methacrylation (DM) of PCLMA.....</i>	<i>102</i>
<i>Equation 6. Calculation of fibre packing density of fibre-filled conduits.....</i>	<i>125</i>

Abbreviations

μSL	microstereolithography
2PD	two-point discrimination
3DP	3D printing
AM	additive manufacturing
CAD	computer-aided design
CAP	compound action potential
CNS	central nervous system
DAPI	4'-6-Diamidino-2-phenylindole
DCM	dichloromethane
DM	degree of methacrylation
DMD	digital micromirror device
DMEM	Dulbecco's Modified Eagle's Medium
DRG	dorsal root ganglion
ECM	extracellular matrix
FDM	fused deposition modelling
FITC	fluorescein isothiocyanate
GDNF	glial cell line-derived neurotrophic factor
IAN	inferior alveolar nerve
IP	intraperitoneal
IPA	isopropanol (2-propanol)
LN	lingual nerve
M2PD	moving two-point discrimination
MAA	methacrylic anhydride
M _w	molecular weight
NGC	nerve guidance conduit
NGF	nerve growth factor
NMR	nuclear magnetic resonance
NTF	neurotrophic factor
NVP	N-vinyl-2-pyrrolidone (NVP)
PμSL	projection micro-stereolithography
PBS	phosphate-buffered saline
PC12	pheochromocytoma cells
PCL	poly(caprolactone)

PCLMA	poly(caprolactone)-methacrylate
PDMS	poly(dimethylsiloxane)
PEG	poly(ethylene glycol)
PEGDA	poly(ethylene glycol)-diacrylate
PGA	poly(glycolic acid)
PGS	poly(glycerol sebacate)
PGS-M	poly(glycerol sebacate)-methacrylate
PHB	poly(3-hydroxybutyrate)
PLA	poly (lactic acid)
PLGA	poly(lactic-co-glycolic acid)
PNI	peripheral nerve injury
PNS	peripheral nervous system
PPF	Poly(propylene fumarate)
S2PD	static two-point discrimination
SD	standard deviation
SEM	scanning electron microscope
SL	stereolithography
SLS	selective laser sintering
TCP	tissue culture plastic
TEA	triethylamine
WT	wild type
YFP	yellow fluorescent protein

1. Chapter 1: Introduction and General Literature review

1.1 The anatomy of the peripheral nervous system

The nervous system of the human body can be divided into two parts; the central nervous system (CNS) and the peripheral nervous system (PNS). The CNS consists of the brain, brain stem and spinal cord whereas the PNS consists of the nerves which extend outwards from the CNS to transmit nerve signals between the CNS and the peripheries. The PNS contains sensory neurons, which relay information from the external environment via sensory receptors towards the CNS, and motor neurons, which transmit motor signals from the CNS towards the peripheries to control organs and tissues [1], [2]. The cell bodies of motor neurons reside in the anterior horn of the spinal cord and those of sensory neurons reside in the dorsal root ganglia (DRGs) [3]. Neuronal processes extend from cell bodies to form axons which are grouped into bundles to constitute the nerves of the PNS. Nerves can be classified as containing primarily sensory neurons, motor neurons or a mixture of both [4].

Figure 1 shows the cross-section of a peripheral nerve where we can see the hierarchical structure. Axons are surrounded by myelin-containing Schwann cells which are the main support cell in the PNS. Larger diameter axons ($>1\ \mu\text{m}$) are wrapped by Schwann cells in a process called myelination, forming the myelin sheath, which provides protection to the axon as well as improving the conduction velocities of nerve signals [5]. The Schwann cells lie along the axon length separated by Nodes of Ranvier. Smaller diameter axons are bundled together in groups and ensheathed by a single Schwann cell, with axons being separated by cytoplasm, rather than myelin, deeming them 'unmyelinated' [5]. Schwann cells are important for neuronal survival and play an important role in the response to nerve injuries, discussed in section 1.2.3.

Myelinated and unmyelinated axons are structured into nerves within three connective tissue layers: the endoneurium, perineurium and epineurium (Figure 1). Individual axons are surrounded by the endoneurium and grouped into fascicles which are, in turn, surrounded by the perineurium. The structure of the perineurium acts to provide tensile strength to the nerve as well as maintaining the endoneurial fluid that surrounds the axons within [6], [7]. The epineurium surrounds the fascicles, grouping them together as well as forming the epineurial sheath around the entire the structure of the peripheral nerve, providing protection to the nerve tissue [6], [8]. Surrounding the epineurium, is the mesoneurium in which blood vessels are present to deliver a blood supply to the endoneurium via a network of capillaries [8].

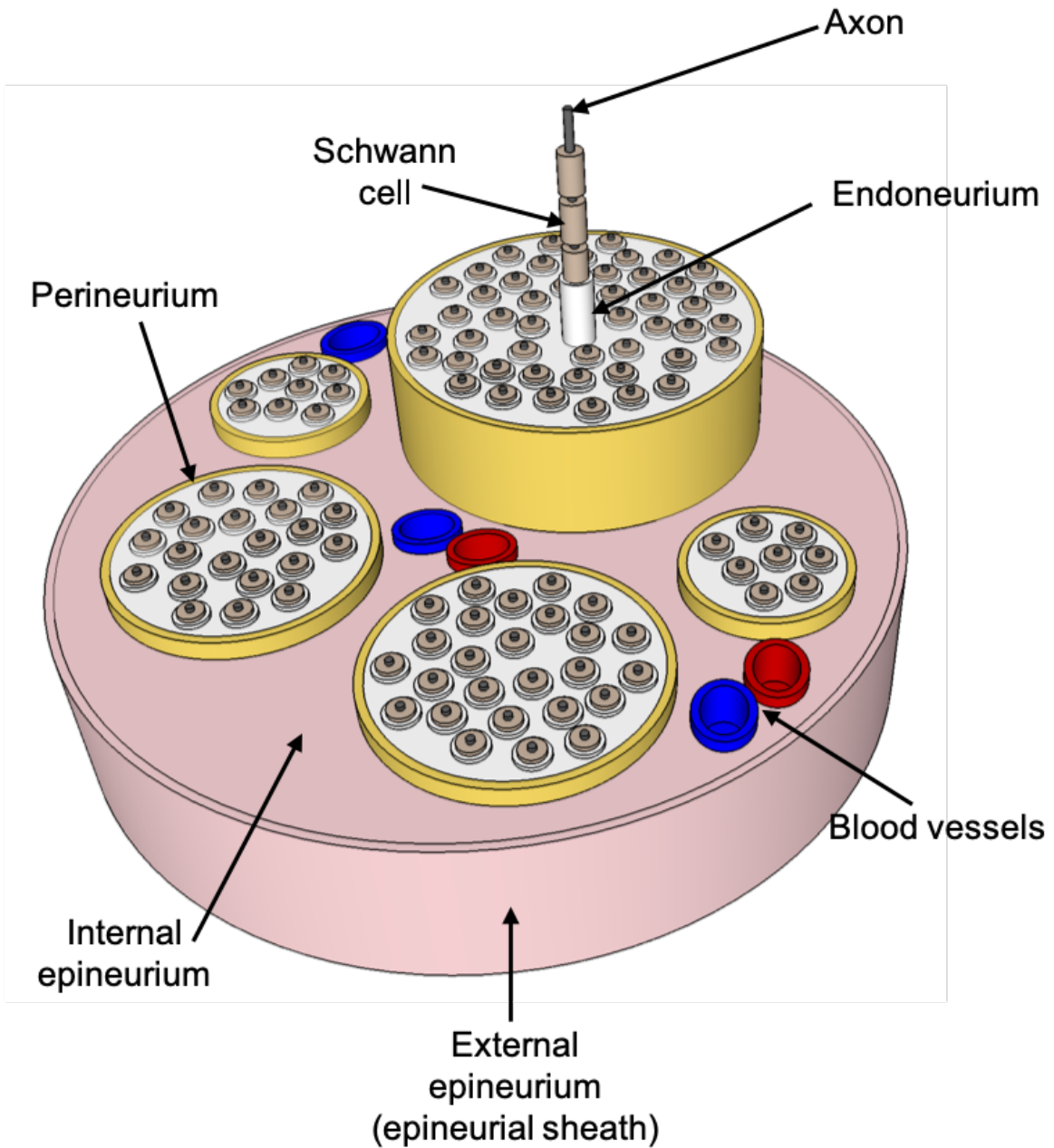


Figure 1. A simplified view of the anatomy of the peripheral nerve. Axons (grey) are ensheathed by Schwann cells and surrounded by the endoneurium (white). Axons are grouped into fascicles which are surrounded by the perineurium (orange). The Epineurium (pink) groups fascicles together to form the structure of the peripheral nerve.

1.2 Peripheral nerve injury and repair

1.2.1 Peripheral nerve injury

Injury to the peripheral nervous system is estimated to occur in around 14-23 people per 100,000 per year worldwide [9], [10], with 300,000 annual cases in Europe alone [11]. Peripheral nerve injury (PNI) most commonly occurs as a result of trauma from a variety of circumstances. Road traffic accidents, penetration/laceration injuries (i.e. from knife wounds or broken glass) and falls are attributed to 44%, 21% and 13% of PNI cases respectively. Injuries often affect the upper limbs with the ulnar, brachial plexus and radial nerves being the most frequently affected [12]. PNI may result from fractures such as humeral fractures causing damage to the radial nerve [13] or fractures to the mandible resulting in trauma to the inferior alveolar nerve [14]. The injury may be sustained during the fracture itself or during surgical procedures in the treatment and fixation of the fracture. In addition to traumatic injuries, PNI may result from surgical intervention which contributes to 12% of cases [15]. These iatrogenic injuries often involve procedures such as tumour resection (one third of cases [15]) and also include injection injuries either from direct needle trauma or from a neurotoxic effect of the injected substance such as anaesthetics [16]–[18].

Injuries to peripheral nerves usually result in a sensory or motor deficit. A wide range of symptoms are possible, corresponding to the type and severity of the injury and the resulting inflammatory response and axon degeneration (see: Wallerian degeneration, discussed further in section 1.2.3). The different types of injury include compression injury, which can result in oedema and changes in the connective tissue of the nerve; stretch injury, which can cause rupturing of the neural connective tissue (endo-/peri-/epi-neurium); chemical injury, causing neural sensitisation and inflammation; and finally transection, caused by laceration or complete rupture [19]. These injuries can result in differing degrees of damage which can be classified as follows using the Seddon classification of nerve injury [20]. ‘Neurapraxia’, the mildest form of injury, is defined as a transient conduction block which results in motor or sensory impairment but where no axonal degeneration is present. Such symptoms may stem from ischemia and present focal demyelination but are usually followed by full, rapid recovery [13], [20]. In ‘axonotmesis’, axonal damage leads to Wallerian degeneration of the distal nerve but the endoneurium remains intact, allowing easier regeneration. In ‘neurotmesis’ (the most severe cases of PNI) total severing of the nerve leads to complete loss of function and unlikely spontaneous recovery [13], [21]. For instances of sensory impairment, in less severe cases, a patient may experience mild paraesthesia (altered sensation such as numbness or tingling) whereas more severe cases can present dyesthesia (stronger, painful sensations that can be acute and constant

[22]), anaesthesia (complete loss of sensation) or even combinations of the above [23]. These symptoms can obviously have a large detrimental effect on a patient's quality of life so treatments are desirable to restore normal nerve function.

1.2.2 Nerve Injury in dentistry

The repair of peripheral nerve injuries has significant applications in dentistry due to complications associated with dental procedures. The most common procedure to result in PNI is third molar removal, contributing to around 50% of cases, with other procedures such as local anaesthetic injections, implant surgery, osteotomy and tumour excision being responsible for the remaining 50% [22], [24]. During third molar removal, the most common nerve injuries are to the inferior alveolar nerve (IAN) and the lingual nerve (LN). As detailed in Figure 2 and Figure 3, the IAN and LN both stem from the mandibular nerve, which is the third branch of the trigeminal nerve (the fifth cranial nerve). The IAN innervates the mandible, supplying sensation to the molar and premolar teeth as well as the surrounding gingiva. Branching into the mental nerve, it also supplies sensation to the chin and lower lip. The LN supplies sensation to the tongue. As a result, even a slight deficit of this sensory activity can impose difficulties in everyday activities such as speech, eating and drinking and lead to psychological problems and social insecurities in affected persons [25], [26].

A number of case studies report that IAN injuries occur in around 4% of third molar removal procedures [27]–[30] (though older case studies report incidence rates of up to 8.4% [31]) and LN injuries occur in around 2-6% of cases [28]–[30]. Increased risk of nerve injury is associated with certain necessary techniques such as bone removal [27] or raising of the lingual flap [28], [32]. With time, as some injuries are allowed to heal, the percentage of patients experiencing prolonged sensory deficit falls, however a significant number of patients experience long-term effects (1.7% of patients still experienced either IAN or LN problems 2 years postoperatively in an extensive study by Jeres et al. [29]). This may seem like a low occurrence but since third molar removal is such a common procedure there are many patients affected.

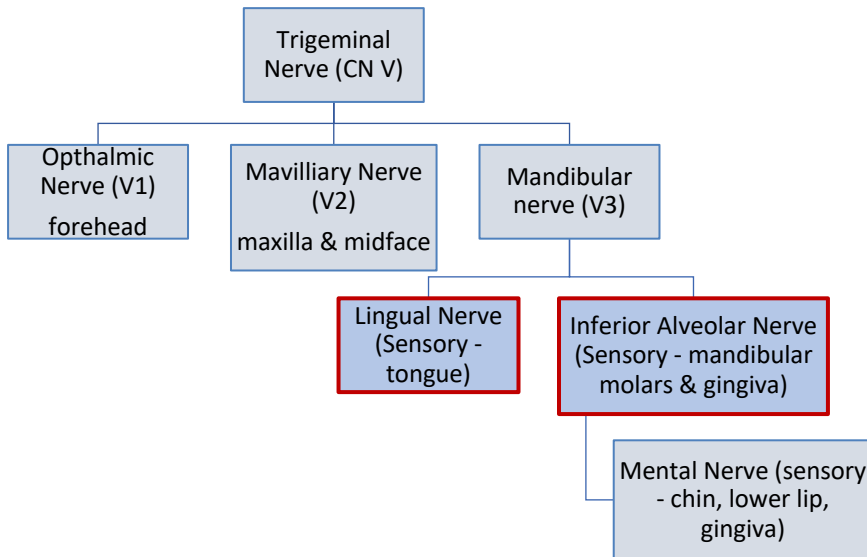


Figure 2. Flowchart, describing the branching of the trigeminal nerve into the lingual and inferior alveolar nerves.

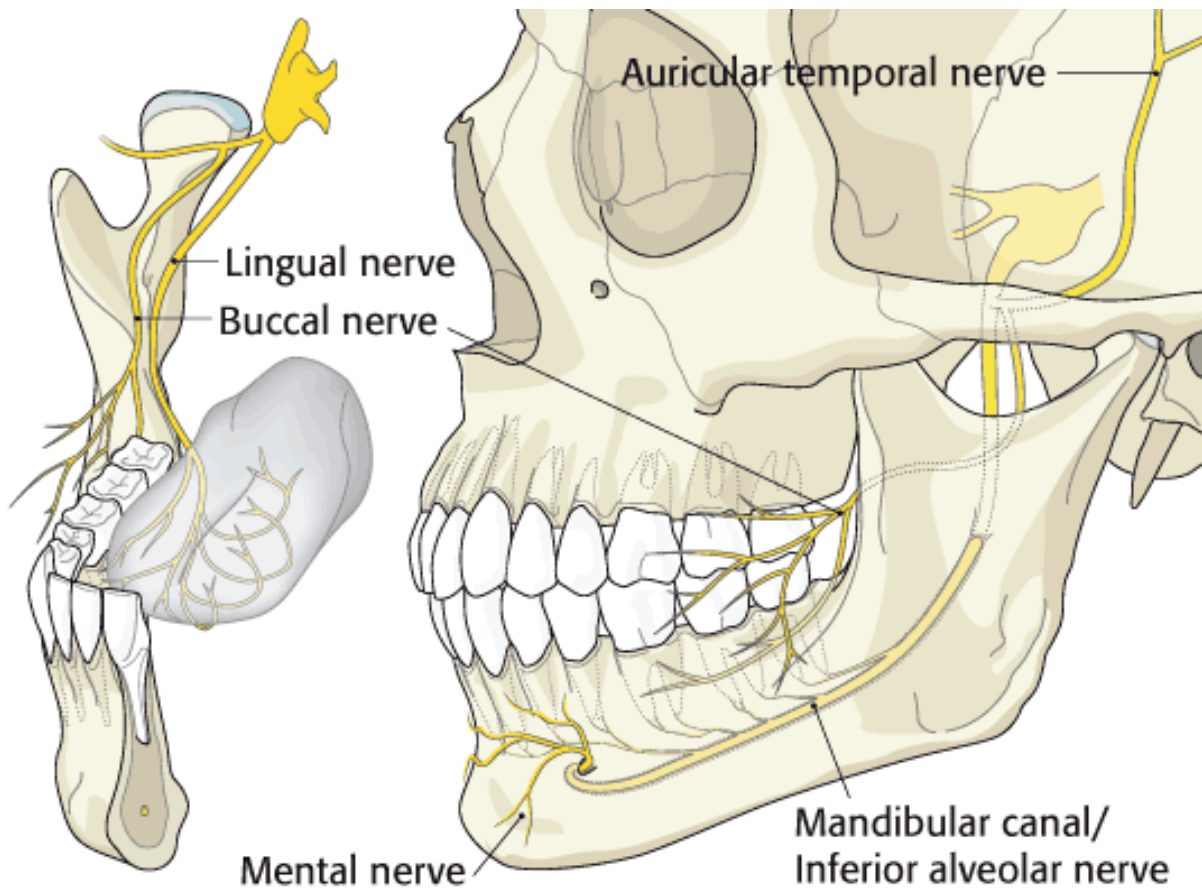


Figure 3. Diagram outlining the anatomical positions of the lingual and inferior alveolar nerves. The inferior alveolar nerve lies in the mandibular canal, in close proximity to the root of the 3rd molar. Copyright AO Foundation, Switzerland. Reprinted with permission from the AO foundation [33].

1.2.3 Peripheral nerve regeneration

Peripheral nerves have an innate capacity for regeneration and axons can regrow at rates of up to 1 mm per day [34]–[36]. Figure 4 describes the stages of axonal regeneration within nerve tissue. Following nerve injury, Wallerian degeneration occurs in the distal stump: the myelin sheaths and the axons within degenerate. Macrophages are recruited to the injury site following disruption to the blood-nerve barrier and phagocytose the remaining debris leaving only Schwann cells and the surrounding connective tissue, including the endoneurial tubes [37], [38]. The Schwann cells then enter a proliferative state, caused by loss of contact with proximal axons [39]. This allows them to proliferate and extend across the nerve gap as well as along the endoneurial tubes of the distal stump [40]. Schwann cells elongate and form Bands of Büngner, long cable-like tracks which act as guidance for regenerating axons [41], [42]. Regenerating axons form growth cones at their tip which send out filopodia to explore the surrounding area and direct the axon advancement towards favourable surfaces [34], [43]. By this way, axons are able to extend towards the distal stump, guided by the Bands of Büngner. Once the axons enter the distal portion of the transected nerve, pre-existing endoneurial tubes provide an excellent framework for regeneration, containing native extracellular matrix (ECM) proteins in the form of Schwann cell basal lamina [44]. Here, with the support of Schwann cells, axons are able to grow long distances to eventually reinnervate the original target area. When the growth cones reach the target organ, growth is halted and synapses form to restore the function lost due to nerve injury.

There are a number of growth factors play an important role, mediating many of the processes that occur during nerve regeneration. Nerve growth factor (NGF), brain-derived neurotrophic factor (BDNF) and glial cell line-derived neurotrophic factor (GDNF) are all upregulated following PNI with level of increase in line with the severity of the injury [45], [46]. Many studies have shown the ability of BDNF and GDNF to promote the survival of motor and sensory neurons and their importance in aiding the recovery and development of regenerating nerves [47]–[50]. Additionally, GDNF has also been shown to stimulate Schwann cell migration and promote enhanced myelination [51]. NGF is also known to promote the survival of certain classes of neurons and to control axonal outgrowth by increasing the motility of growth cones [34].

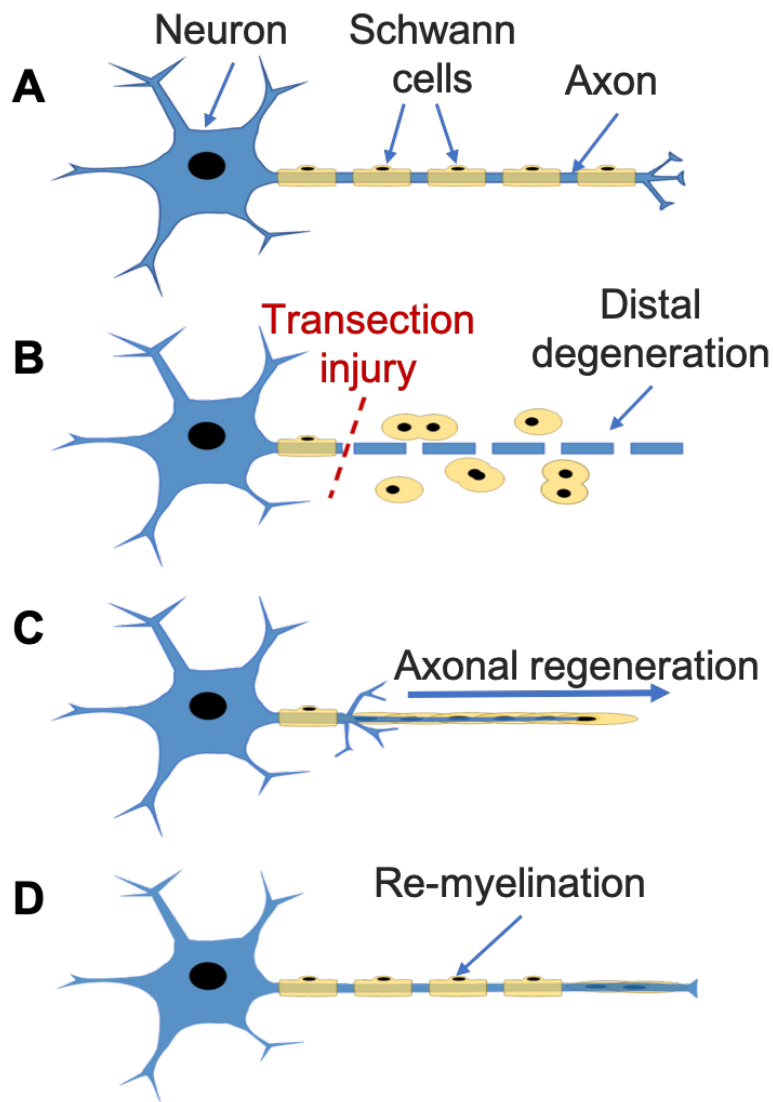


Figure 4. The stages of axonal regeneration following a nerve transection injury. A: Normal, undamaged nerve. B: Injury occurs, distal portion of axon degenerates and is phagocytosed by macrophages (not shown). Schwann cells proliferate. C: Axon regenerates, guided by the Bands of Büngner formed by migrating Schwann cells. D: Nerve maturation occurs where Schwann cells myelinate the newly-grown axon.

1.2.4 Impact of scarring on nerve regeneration

The repair mechanism described above indicates what may happen in the case of ideal recovery, however misdirected axon growth and invasion of unwanted cell types such as fibroblasts can cause the production of scar tissue. This can slow the growth of the axons across the nerve gap or prevent them from reaching their target, leading to neuroma formation [13], [44]. This scar tissue invasion can arise from the proliferation of cells in the damaged epineurium and form physical barriers to the regenerating axons [40]. Atkins et al. found that an increased amount of scarring at the site of the nerve injury resulted in a decreased success of regeneration [52]. A reduction in scarring was also related to improved functional recovery [53]. This reinforces the suggestion that scarring during nerve regeneration is hugely detrimental to the recovery process and limiting scar tissue formation is necessary for a successful recovery.

1.2.5 Surgical repair & current treatments

In many cases, surgical intervention is necessary to ensure that the nerve regeneration process occurs to its full potential and maximal functional recovery is achieved. Treatment choice is highly dependent on the extent and type of nerve injury and, over the centuries in which nerve repair has been carried out, a number of standard procedures have been established. End-to-end coaptation (or anastomosis) via suturing is always preferable where minimal nerve tissue is lost and tension between the proximal and distal stumps is sufficiently low [54]. The first detailed description of the suturing of a transected nerve was recorded in 1596 by Gabriele Ferrara. He describes his procedure, which is relatively close to modern techniques, including the need to identify and release the separate nerve stumps, carefully suture together after disinfecting and immobilise limb during recovery [55]. Microsurgical techniques have evolved over the years and the advent of high magnification systems for surgical aid and improved surgical tools have made it possible for more complex procedures to be performed while reducing the trauma invoked during repair [56]. For larger nerves, interfascicular dissection may be performed on the nerve stumps to allow proper alignment of individual fascicles and correct reinnervation, for example distinguishing between motor and sensory pathways [57].

In cases where a segment of nerve tissue is lost or damaged and a large gap exists between the proximal and distal nerve stumps, end-to-end coaptation would result in excessive tension across the join and other repair methods must be pursued. Reports in literature vary as to the maximum gap size possible to repair by coaptation but it is generally accepted to be between around 5 and

10 mm [58], [59]. In such cases the gold standard treatment is the use of an autologous nerve graft. This is where a donor nerve is taken from elsewhere on the patient and transplanted to the injury site to reconnect the severed nerve endings. The most commonly used donor nerve is the sural nerve due to its relatively low donor site morbidity, ease of harvest and availability of longer segments [54]. Similar to the function of the native distal nerve segment, the autograft does not provide axons to reconnect the proximal stump to the target (as these will undergo Wallerian degeneration) but provides a connective tissue framework of endoneurial tubes (composed of Schwann cell basal lamina) surrounded by connective tissue, to guide the regenerating axons towards their distal target. The regeneration is also aided by the presence of Schwann cells and beneficial neurotrophic factors in the autograft tissue [60]. There are, however significant drawbacks related to the use of autografts, including (i) donor site morbidity such as a sensory deficit; (ii) limited availability, especially for lesions requiring multiple grafts (e.g. the brachial plexus); (iii) the difficulty of size-matching between the native nerve and the graft; and (iv) the need for an extra operation site, with obvious problems associated with increased recovery time and infection risk as well as a risk of neuroma formation at the donor site [58], [61].

The success rate of autografts is dependent on a number of factors. Patient age is important with reports suggesting that successful recovery occurs more often in persons under 20 years of age [62]. Nerve gap length is another strong factor as successful recovery is uncommon in gap lengths of over 5-10 cm. Finally, the duration of time between injury and surgical intervention can influence success rates with some reports suggesting that the best results occur when the operation takes place within 3 months of the injury [62]. This is partly attributed to the decrease of viable Schwann cells within the distal nerve after a few months post-injury [63]. However studies have shown that a 3 month delay has little effect on recovery [64] and that late repair of lingual nerves (7-32 month after injury) can still show good success rates, with all patients over the age of 20 [65]. As we can see, there is conflicting literature on the issue and predictors of successful recovery are not so easily generalised. Success is also dependent on the nerve in question; Autograft repairs are most successful in upper extremity nerve repairs, with positive results reported for many nerves including the median, ulnar and radial nerves [62]. Autologous nerve grafts also can be used in dentistry if direct suturing is not possible but the typical presence of short nerve gaps means that this is usually not the case. Sural nerve autografts can improve IAN function with pain relief and partial sensory recovery [22] but full recovery is not widely reported.

Similar to autografts, allografts may be performed where a donor nerve (usually cadaveric) is used to bridge the defect. This eliminates donor site morbidity and the risks associated with the second operation site. This option can also be used when the nerve gap is too large for a suitable length of autogenous nerve to be obtained [66]. The main drawback is the need for the administration of immunosuppressive drugs for a period of time after the operation to prevent adverse reactions until the host cells dominate the donor tissue (at approximately 24 months [63]). However acceptance is not guaranteed and graft-rejection may still occur [67]. Alternatively, decellularised autografts (such as the commercial product Avance® Nerve Graft from AxoGen) can be used with reduced need for immunosuppression. These obviously contain no Schwann cells to aid with regeneration but retain the beneficial architecture of the native nerve. This native ECM provides an excellent scaffold for nerve regeneration and positive results are reported in a number of studies [68]. The main drawback of such treatments is the prohibitively high cost of decellularised allograft products [69].

Another, less widely used alternative are vein grafts; this is where an autologous vein (e.g. the saphenous vein) is harvested and used to connect the proximal and distal nerve stumps [70]. Pogrel et al. has reported the use of vein grafts helping partial recovery of sensation in IAN injuries however with LN injuries partial sensation was only recovered in nerve gaps of less than 5 mm, with no sensory recovery present in lesions greater than 5 mm [70]. One disadvantage in the use of vein grafts is their low strength leading to the possibility of collapse and kinking which damages the nerve and hinders regeneration. This is thought to be the reason that vein grafts are less successful in the repair of LN injuries compared to IAN injuries as the former experiences more movement and is less protected from disruption than the IAN which lies within the mandibular canal [71].

Despite the widespread practise of nerve repair, functional recovery after surgery is still limited, even with gold standard autografts. A review by Ruijs et al. performed a meta-analysis of 23 studies (between 1968-2000) containing 623 cases of median or ulnar nerve transection injuries. It was reported that only 52% of patients experienced satisfactory motor recovery while satisfactory sensory recovery was only present in 43% of cases. Of the patients receiving grafts (57%), a slightly lower percentage achieved satisfactory motor or sensory recovery than those who did not require grafts however this difference was not significant [72]. A more recent, large-scale study from 2013 reporting from 87 publications and 3000 nerve repairs, compares the sensory recovery resulting from the use of various repair techniques. Direct coaptation resulted in 78% 'good' to 'excellent' recovery, while autograft success rates were 67%, though the difference was not significant [73].

This may show that patient outcome is improving with improved surgical techniques but there is still much room for improvement.

1.2.6 Conclusions

- Peripheral nerve injury can occur in a wide variety of situations, such as trauma or iatrogenic cases, resulting in significant decrease in patients' quality of life.
- There is no current treatment which provides full recovery for injury to peripheral nerves.
- More effective treatments are required which offer improved return of nerve function without the disadvantages of autografting.

1.3 Nerve guidance conduits

Due to the disadvantages associated with autografting and the poor results of larger gap repairs, it is evident that a satisfactory alternative to the currently available treatments is necessary. One such alternative is the use of a nerve guidance conduit (NGC) (Figure 5). This is an entubulation device used to connect the severed nerve endings and provide protection and guidance for the regenerating nerve. They can also aid recovery by creating a semipermeable environment allowing the build-up of beneficial neurotrophic factors and the exclusion of unfavourable cells and inhibitory factors as well as limiting scar tissue invasion. The use of a NGC eliminates the inherent disadvantages of autografting, such as donor site morbidity and the need for a second operation site, as well as the use of immunosuppression and the immune rejection risk associated with allografts. In cases where end-to-end coaptation is performed, a NGC could even be used in addition to this procedure (adding additional protection during recovery and helping the retention of growth factors) or used instead of direct suturing (to reduce potentially damaging tension in the join).

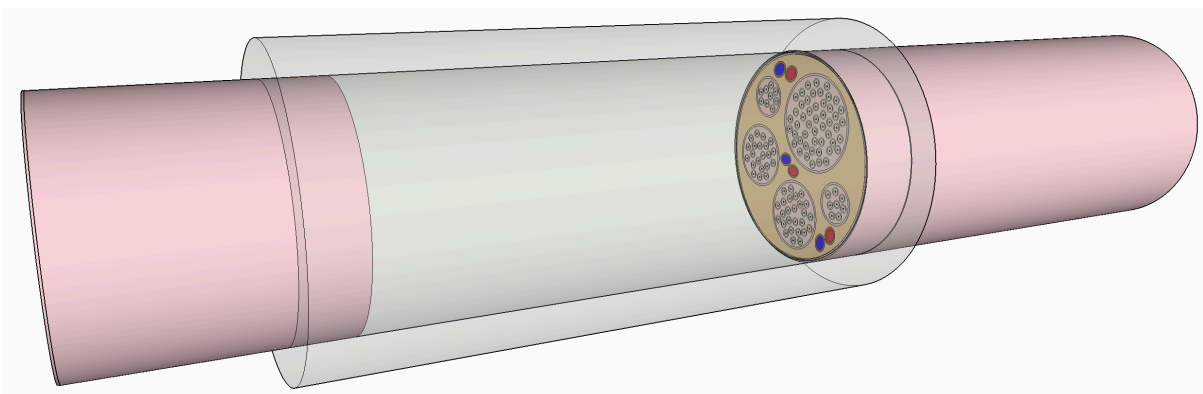


Figure 5. A nerve guidance conduit (NGC) positioned between the proximal and distal ends of a severed peripheral nerve.

1.3.1 The Ideal NGC

The properties and functions of the ideal NGC are widely believed to be as follows (each will be explored in more detail throughout the report):

- A NGC must be made from a **biocompatible**/non cytotoxic material that does not elicit a host response which would prove detrimental to the nerve regeneration process. Immunogenic, carcinogenic and thrombogenic responses are important to consider when determining a material's biocompatibility [74]. The biocompatibility of a biomaterial can also be influenced by the release of low M_w molecules (degradation products or leachable contents/impurities) and by the capacity of surrounding tissues to eliminate these by-products (dependant on vascularisation and metabolic activity).
- The material should be **biodegradable** and the conduit should degrade in a time which matches the regeneration period. The conduit should remain mechanically stable during this time to protect the nerve during regeneration and maturation before degrading once this function is complete. Long-term placement of materials within the body can cause a chronic foreign body reaction and scar tissue formation [58], [75] as the body tries to encapsulate and isolate the foreign material from interaction with host tissue. The products of degradation should also be biocompatible. Concern has been raised over the acidic degradation products of poly(glycolic acid) (PGA) and poly(lactic acid) (PLA) which have been seen to decrease local pH *in vitro* which could be detrimental to the healing process [76], [77]. However, the degradation rate of the polymer will have a direct effect on the concentration of the degradation products, including any effect on local pH. *In vivo*, if degradation products can be metabolised and eliminated at a rate which matches degradation, then detrimental effects can be limited.
- The conduit must have appropriate **mechanical properties** to allow bending without fracturing or kinking and to resist the pressure from surrounding tissues (both of which can lead to compression of the regenerating nerve). To prevent unnecessary inflammation, the conduit should also be soft enough not to damage surrounding tissues [61]. Materials with a wide range of mechanical properties have been used to produce NGCs. Examples include materials/conduits with tensile moduli of 0.022-15 MPa (collagen [78], [79]), 8-90 MPa (porous/electrospun PLGA [78], [80]) and 2-35 MPa (porous/electrospun PCL [81], [82]). It may be desirable to use materials with properties towards the lower end of this range, closer to that of the native nerve, for which tensile Young's modulus has been calculated to be around 0.6-8 MPa [83], [84]. The mechanical properties should also permit easy handling by the surgeon including the insertion of sutures and cutting the conduit to match the length of each specific injury.
- A **semipermeable** material is desirable to allow diffusion of nutrients and oxygen across the barrier, while retaining beneficial neurotrophic factors produced at the injury site and preventing the infiltration of myofibroblasts and scar tissue [85]. It has been found that a cut-off diffusion molecular weight of 50 kDa is beneficial for allowing nutrient diffusion while preventing cell migration leading to better regeneration with less scar tissue formation [86].

- The tubular nature of the conduit should provide **guidance** for axons and Schwann cells to direct their growth towards the distal stump. Additional guidance can be provided in the form of physical/topographical guidance cues in the lumen of the conduit such as aligned grooves or fibres which will be discussed in the following sections.
- As with any biomaterial implant, if a NGC is to be used clinically it must be **sterilisable** by an FDA approved technique such as autoclaving, gamma irradiation or ethylene oxide.

Additional components can be incorporated into the design to increase the potential benefit of implanted NGCs and allow longer/more complex injuries to be repaired.

- **Growth factors** may be incorporated into the design to supplement those produced *in vivo* in response to injury to further aid regeneration by promoting the growth and survival of regenerating axons. Growth factors can also be used to offer chemical guidance cues in the form of biochemical gradients [87].
- A **cellular component** may also be added to the NGC, usually in the form of Schwann cells, to augment those found proliferating at an injury site and amplify their therapeutic effect [88].

1.3.2 Mechanism of regeneration through a NGC

The regeneration of peripheral nerves through guidance tubes was characterised in 1983 by Williams et al. [35] who explained the sequential stages of such regeneration, outlined in Figure 6. First, the conduit fills with a fluid exudate from the proximal and distal stumps which contains neurotrophic factors produced by Schwann cells [89], [90]. These neurotrophic factors have been shown to promote the regeneration of neurons, with nerve growth factor (NGF) being particularly important for neuronal survival and differentiation [91]. Following this, a fibrin matrix forms within the conduit, connecting the proximal and distal nerve stumps. The fibrin filaments within this matrix have an oriented structure and form a cable which supports the migration of Schwann cells, fibroblasts and endothelial cells from both stumps into the gap [35]. Schwann cells subsequently form Bands of Büngner (discussed in section 1.2.3). The result is a cellular tissue cable which supports the following axonal regeneration. Axons extend from the proximal stump and traverse the injury site, guided by Schwann cells. Once the gap has been bridged, axons are able to continue growing down the distal stump towards the target organ as described in in section 1.2.3. It has been found that formation of this fibrin cable is critical if successful regeneration is to follow. If the fibrin matrix fails (i.e. in longer distance gaps), cellular migration is not supported and axonal regeneration cannot occur [92].

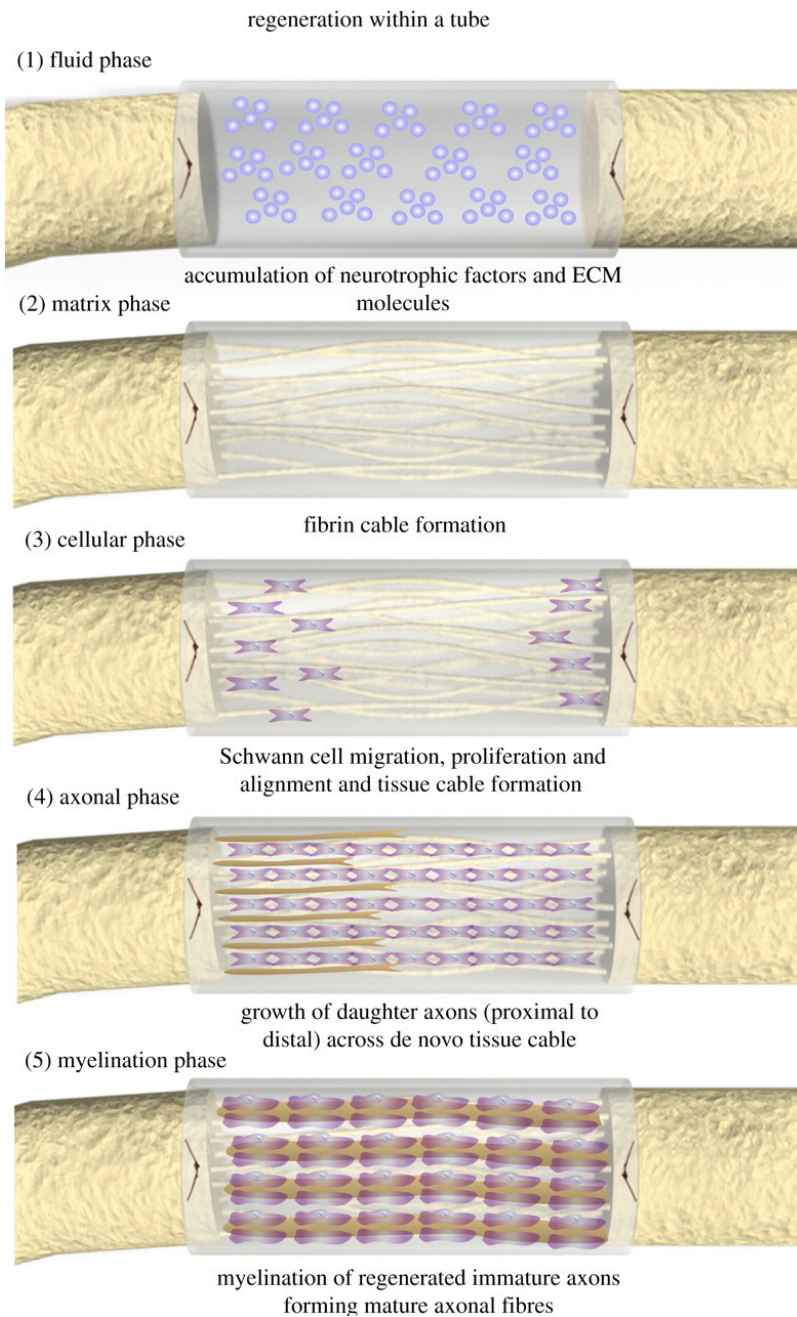


Figure 6. The stages of regeneration through a hollow guidance tube. Fluid fills the conduit (1) followed by the formation of a fibrin cable between the two nerve stumps (2). This matrix supports the migration of non-neuronal cells and the formation of a tissue cable (3). Axonal growth can then occur (4) followed by myelination in the later stages (5). Reprinted from Daly et al. with permission from The Royal Society [93].

1.3.3 Commercially available NGCs

There are a number of commercial, FDA-approved NGCs which are made from a variety of natural and synthetic materials (see Table 1 and Figure 7). Many groups report comparable results of nerve repairs with conduits to that of autografts or sutures, however these are mostly in the repair of short distance nerve gaps. These devices all have simple, plain tubular designs which generally only support effective regeneration over gaps of around 2-4 cm [42], [61], [94].

Table 2 outlines a number of clinical studies that have utilised the most common commercial NGCs, Neurotube[®], NeuraGen[®] and Neurolac[®] (displayed in Figure 7). They have largely been used in repairs of nerves upper extremities but other nerve types have been reported including the LN and IAN. As can be seen, the studies report some positive results following nerve repair with commercial NGCs, including improvements in sensory recovery [59], [95], [96], reduced neuropathic pain [97] and improved motor function [98]. However, the results are hugely variable and leave much room for improvement. The most successful studies report that excellent sensory recovery still only occurs in 44-60% of patients [59], [95] but this can be as low as 14% [99]. Poor sensory recovery is also commonly reported with a large number of patients presenting limited to no sensory recovery (100% [97], 55-65% [96] and 27% of patients [95]).

Most of these papers report case studies with no comparison to control procedures (i.e. autograft or direct suture repairs). It is therefore difficult to see how they might compare, though the success rates reported of NGCs seem lower than the 67-78% success rates of direct coaptation and autograft repairs, reported earlier [73] (section 1.2.5). The study by Weber et al. reported that conduits supported significantly better sensory recovery compared to direct coaptation (for small gaps, ≤ 4 mm) and significantly better sensory recovery compared to autografts (for larger gaps, > 8 mm) [59]. This suggests that there is still promise for NGCs however for more widespread success, conduit design may need to be improved.

Table 1. A number of FDA approved, commercially available NGCs.

<u>Product Name</u>	<u>Material</u>	<u>Biodegradable?</u>
	Synthetic	
Neurotube®	Woven mesh of poly-glycolic acid	3 months
Neurolac®	Poly(DL-lactide-co-ε-caprolactone)	16 months
Salutunnel™	Polyvinyl alcohol hydrogel	no
	Natural	
NeuroFlex™/ NeuroMatrix™	Type I, bovine collagen	4–8 months
NeuraGen®	Type I, bovine collagen	36–48 months
AxoGuard™	Porcine small intestinal submucosa	3 months
Avance®	Decelularised human allograft	

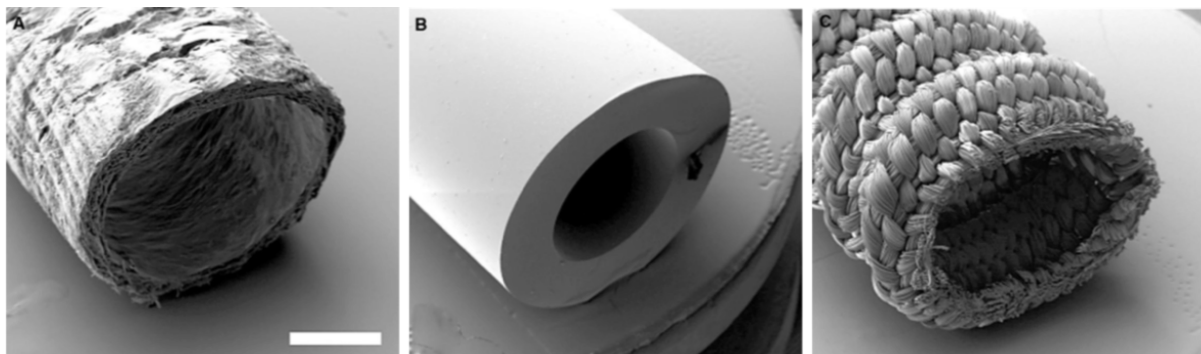


Figure 7. SEM images of commercially available NGCs. A: NeuraGen, B: Neurolac, C: Neurotube
Reprinted from Schloschauer et al. with permission from Oxford University Press [94].

Table 2. A summary of a number of clinical studies using commercial NGCs. S/M2PD: Static/motor two-point discrimination.

Product	Studies using the product	Study outcome/comments
Neurotube®	Weber et al. [59] - 98 patients, 136 nerve repairs (102 followed up) - Digital nerves - 3-12 month follow up	- Conduits compared to the 'standard' repair (direct suture for gaps of ≤ 4 mm and autograft for gaps of ≥ 8 mm) - Recovery in conduits was significantly better than direct suture (≤ 4 mm gap) and significantly better than the autograft (> 8 mm gap). Both results showing a lower mean M2PD and greater percentage of patients with 'excellent' recovery - No significant difference for $4 \text{ mm} < \text{gap} < 8 \text{ mm}$ (surgeon's choice of conduit/graft) - 'Excellent' sensory recovery only reported in up to 44% of patients
	Navissano et al. [99] - 7 patients - Facial nerve, 1-3 cm gap, 7-12 month follow up	- Five out of seven patients presented positive results in functional muscle recovery but only one was classed as 'very good' - Case studies, no control groups for comparison
	Munding et al. [97] - 5 patients, iatrogenic inferior alveolar nerve injuries - 14-108 month follow up	- All patients had reduced neuropathic pain but limited to no sensation recovery was achieved in all patients - Lack of comparison to control procedures
	Rosson et al. [100] - 6 patients - Medial/ulnar/spinal accessory nerves, 1.5-4 cm gap - 4-66 month follow up	- All patients recovered some useful motor function allowing some of them to return to work or activities such as violin playing - Case studies, no control groups for comparison
	Donoghoe et al. [98] - 2 patients - Medial nerves, 3 cm gaps	- Complex case using multiple NGCs: Nerve reconstructed with 4 conduits (one for each fascicle) - Grip strength improved from 50% to 89% and 37% to 76% in the two patients respectively - Improvements were also seen in sensory recovery (2PD)
NeuraGen®	Wangenstein et al. [96] (retrospective study) - 96 patients (126 nerve repairs) 64 followed up - Mainly nerves in upper extremities - Mean follow up, 9 months	- Quantitative sensory recovery testing in 26 repairs (electromyography/2PD/SW monofilament testing): 35% reported an improvement and 31% required revision surgery - Qualitative assessment in 60 repairs: 45% reported an improvement and 5% required revision surgery - Lack of comparison to control procedures
	Bushnell et al. [101] - 12 patients (9 followed up) - Digital nerves, 1-2 cm gaps, 12-22 month follow up	- 4/9 patients showed 'good' 4/9 showed 'excellent' sensory recovery (2PD, Semmes-Weinstein monofilament testing) - Lack of comparison to control procedures
	Taras et al. [95] - 19 patients with 22 repairs - Digital nerves, 5-17 mm gap, 12-59 month follow up	- 'Excellent' recovery in 13/22 (≤ 4 mm M2PD or ≤ 6 mm S2PD), 'good' recovery in 6/22 repairs ($5-7$ mm M2PD or $7-8$ mm S2PD) - M2PD was recovered in all patients (mean 5 mm), S2PD was not recovered in 6 patients - Lack of comparison to control procedures
Neurolac®	Bertleff et al. [76] - 30 patients, 34 repairs - Digital nerves, up to 20 mm gap, 12 month follow up	- Comparable sensory recovery to control procedures (direct suture) assessed by 1PD and 2PD (motor and sensory) - Comments that the conduit is Transparent for easy surgical positioning and that degradation products are less acidic compared to PGA

1.3.4 Conclusions

- NGCs can be used in the repair of peripheral nerve injury as an alternative to autografting.
- Current commercial products have simple designs with many reporting low success rates or limited recovery.
- There is limited clinical data of NGCs performance vs autograft controls.
- Improvement to the simple designs of commercial products is necessary to improve their performance and allow regeneration over longer distances.

1.4 Manufacture methods for NGCs

1.4.1 Current NGC manufacture methods

NGCs are mostly produced using simple manufacturing techniques such as extrusion, using a piston and a hydraulic press [80] or a screw extruder [102]. Such methods only allow for the production of simple, tube designs of constant cross-sections and fixed dimensions with the need to redesign the equipment to make tubes of different sizes. The process also involves heating of the polymer to ensure it has the correct properties for processing. Other techniques such as injection moulding [103] allow for slightly more complex designs such as inclusion of luminal channels by inserting wires into the moulds [104]. The design of the conduit is still however determined by the shape of the mould with fixed diameter & length with new moulds required to be designed to produce conduits of different dimensions. Other techniques involve the production of flat substrates – polymer films or electrospun fibre sheets – which are then rolled and sealed using solvent, glue or heat to produce tubes [105], [106]. This is a time-consuming process which doesn't lend itself to easy scale-up. Braiding or knitting methods are sometimes used to produce tubular scaffolds [36], [107], [108] such as the commercial product Neurotube® which is composed of a woven PGA mesh [109]. These manufacturing techniques have obvious drawbacks and are mostly constrained to producing simple geometries. The advent of additive manufacturing has allowed the relatively easy production of much more complex designs.

1.4.2 Alternative manufacture methods

Additive manufacturing (AM) is an umbrella term used to describe the collective of fabrication techniques which are based on 3D printing methods, such as stereolithography (SL), selective laser sintering (SLS) and fused deposition modelling (FDM) [110]. Additive manufacturing is a bottom-up fabrication technique which produces structures in a layer-by-layer process from cross-sectional data of 3D computer-aided design (CAD) models [111]. AM techniques can create complex geometries and intricate internal structures which are difficult or even impossible to produce with conventional, top-down/subtractive fabrication methods.

Since the advent of AM in 1987 with 3D Systems' first commercial stereolithography machine, the use of AM methods has expanded into medical fields and revolutionised the field of biomaterials and tissue engineering by allowing the production of complex scaffolds with almost limitless design possibilities. Other advantages include the possibility for patient-specific implants; by teaming AM methods with medical imaging data, one can produce CAD designs for scaffolds to fit a specific patient's defect allowing for seamless integration into the body. Examples include the production of patient-specific titanium prostheses for mandible reconstruction [112] or the production of customised elbow implants [113]. Additionally, medical imaging data can be used to manufacture anatomically accurate models for surgical investigation. One example of this is the use of stereolithography to create models of patients' skull defects to aid in the planning of oral & maxillofacial surgery [114].

1.4.3 Stereolithography

Stereolithography is a type of AM which uses UV or visible light to cure successive layers of a 3D CAD model. The light source (usually a laser) is directed at the surface of a photocurable prepolymer resin which solidifies under UV light. The laser selectively cures the resin to produce a crosslinked polymer in the shape of the desired cross-section. The stage upon which the object is being fabricated is then lowered to allow fresh liquid prepolymer to flow over the surface and for the next cross-section to be cured. This cyclic process is described in Figure 8.

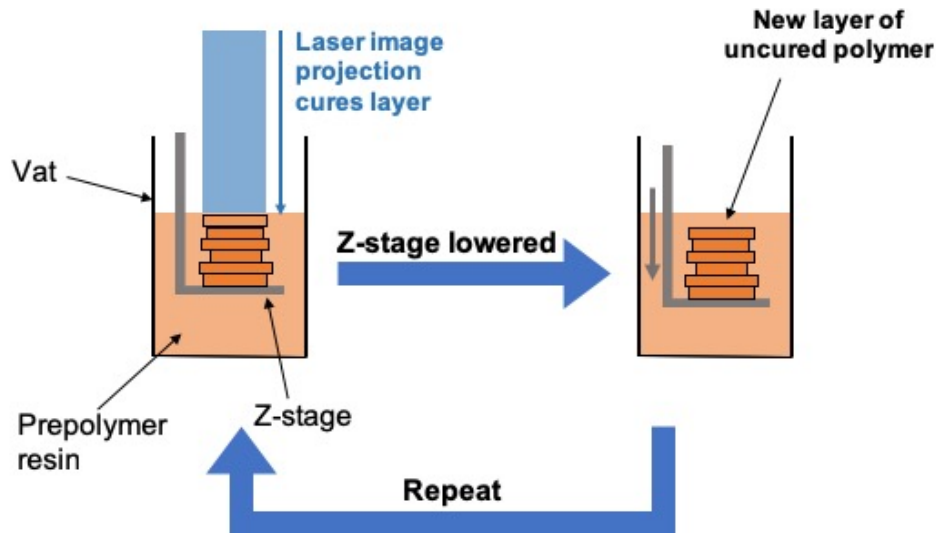


Figure 8. The cyclic process of stereolithography. Sequential cross-sections are cured by exposure to UV light.

The modern stereolithographic technique was patented by Hull in 1986 [115], (improved in subsequent years [116], [117]) which describes the process and apparatus involved in the layer-by-layer fabrication of an object via the selective solidification of a liquid medium using radiation.

Over the years there has been much research into the development of these stereolithographic techniques to produce structures with micrometer resolution and as a result, two main types of micro-stereolithography (μ SL) have emerged: scanning and projection. The earlier, scanning micro-stereolithography, introduced by Ikuta and Kirowatari in 1993 [118], works by focusing a laser beam to a small spot on the prepolymer surface. Via the use of a galvanometer mirror or movement of an x-y stage, the laser spot is scanned over an area in the shape of the desired cross-section, thus curing the polymer in the required shape [119]. The characteristics of this method impose inherent limitations on production times and object resolution due to laser scan speeds and focal spot size.

Projection micro-stereolithography (P μ SL) is a more modern approach which uses a dynamic mask to shape the laser light into the desired cross-sectional image. This is projected onto the surface of the prepolymer and the entire cross-section is cured at one time without x-y movement of the laser spot or stage, allowing faster fabrication times. First proposed by Bertsch et al. in 1997 was the use of a liquid crystal display (LCD) as the dynamic mask for P μ SL and this led to huge improvements in the possible resolution of μ SL systems [120]. Latterly, this technique was improved by substituting the LCD mask with a digital micromirror device (DMD), removing problems associated with limited contrast of the LCD [121].

The DMD, invented by Texas Instruments, is an electromechanical device which consists of an array of (originally) 1024 x 768 micromirrors (each $\sim 13.5 \mu\text{m}$ in size). The mirrors represent the pixels in an image and each mirror is oriented by a computer into an 'on' or 'off' state, $+12^\circ$ or -12° respectively from the central state. Consequently, the light from each mirror/pixel is either 'selected' and reflected in one direction towards the subsequent optical components or 'rejected' and reflected in another direction towards a light absorber [122][123] (see Figure 9). Via selecting the 'on' mirrors to display the shape of a specific image it is therefore possible to selectively reflect the light in the shape of the desired cross-section and project this laser image onto the prepolymer surface.

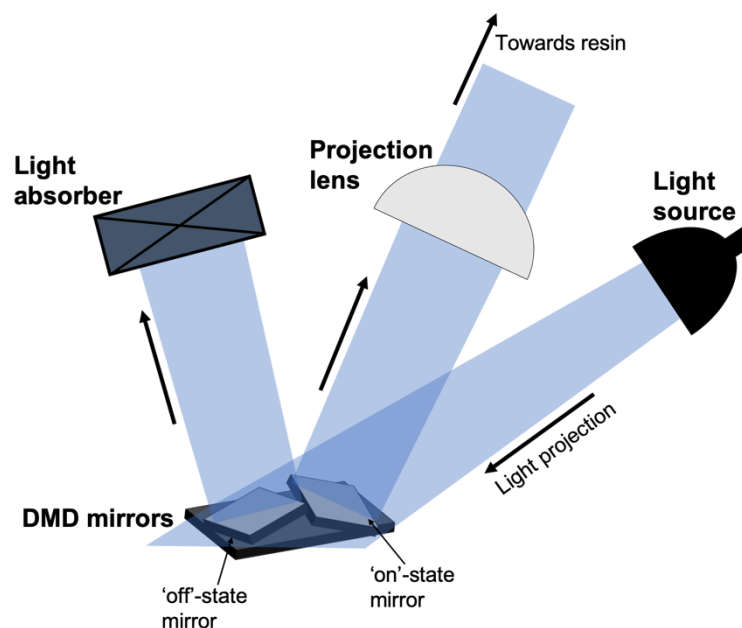


Figure 9. The principle behind the DMD function, showing example 'on' and 'off' state pixels/mirrors. The black arrows indicate the direction of the light projection and reflection off the mirrors in the two states.

1.4.4 NGCs produced by stereolithography

μSL offers many benefits over to the conventional techniques used to produce NGCs. As with all AM technologies, using CAD, μSL allows precise control over the design of the conduit such as diameter, wall thickness and the presence of internal channels without the need to redesign and produce separate moulds. This way we can easily produce customised NGCs specifically the right size for individual patients so there is no need to be limited by predetermined dimensions of off-the-shelf designs.

Despite the potential benefits of μSL for the production of NGCs, there has been little research into the topic. Arcaute et al. produced poly(ethylene glycol)-diacrylate (PEGDA) NGCs with intraluminal

channels [124] [125]. These were implanted in rats to investigate their *in vivo* potential for nerve regeneration and it was found that the single lumen conduits supported partial nerve regeneration however the regeneration in the multilumen conduits was drastically reduced [126]. This could be due to the large cross-sectional area blocked by the material and emphasises the importance of conduit design and appropriate material choice. The group used a 3D Systems Model 250/50SL, a commercial line-scan stereolithography machine and therefore subject to the limitations discussed in section 1.4.3. Due to the device's minimum spot size of 250 μm , the best possible resolution achieved was an internal channel diameter of 400 μm . This is far larger than the resolution possible to achieve from in-house built P μ SL systems such as that by Sun et al. which is reported to produce 3D features as small as 30 μm [127].

In previous work from The University of Sheffield, Pateman and Harding et al. used an in-house built P μ SL system to produce PEGDA NGCs. The conduits produced performed well in an *in vivo* mouse model, promoting successful regeneration over a 3 mm nerve injury [128]. No significant difference was found in axon proportion crossing the nerve gap in the NGCs vs the autograft control.

Additionally, the sprouting index in the NGC recoveries was significantly lower than the autografts which could suggest the NGCs were less disruptive to axon growth. These are surprisingly positive results considering the use of PEGDA, a non-biodegradable, stiff and brittle material, well known for its poor cell attachment properties. The properties of poly(ethylene glycol) will be discussed in more detail in the following chapter (section 2.2.2.1). These conduits, however, were only implanted for 21 days which is too short to notice any ill effects from a chronic inflammatory response resulting from the presence of a non-biodegradable material. In more recent work from the group, the biodegradable material poly(glycerol sebacate)-methacrylate (PGS-M) was produced and used in a similar study. PGS-M conduits were produced by μ SL and supported regeneration in the same 3 mm nerve injury model [129]. Regeneration was lower compared to autograft controls, but the use of a biodegradable material offers clear advantages over non-degradable alternatives.

1.4.5 Conclusions

- μ SL offers many advantages over current manufacture techniques for NGC production
- There is limited research into NGC production using μ SL
 - Preliminary research shows promise
 - More clinically relevant materials are needed

1.5 Methods to improve NGC designs

As we have seen there are a number of commercial NGCs in use however these designs, consisting of simple hollow tubes, have limited capacity for promoting *in vivo* nerve regeneration, preventing their widespread clinical use. It is therefore essential to integrate other features into the design of NGCs to promote improved regeneration. Many different avenues have been pursued by research groups looking to improve the performance of NGCs and produce devices that out-perform current designs. Examples include the incorporation of growth factors such as NGF to enhance nerve growth [130]–[132] and the pre-seeding of Schwann cells within conduits [88], [133] to accelerate the initial Schwann cell-mediated mechanisms of nerve regeneration and amplify their therapeutic effect. Other directions include the use of ECM proteins such as laminin [132], [134] and fibronectin [135] to provide attachment sites for advancing cells. The use of conductive materials to apply electrical stimulation to regenerating cells has also been explored [136], [137].

1.5.1 Contact guidance, a history

An alternative approach to improve nerve regeneration, and the one that will be the focus of this thesis, is the incorporation of physical guidance cues within the lumen of the conduit. The idea that cells could be guided by physical structures is not a new one, with early experiments dating back to the early 1900s. Much work of this early work was carried out by Ross G. Harrison (and then continued in later years by his student Paul Weiss) investigating the mechanisms of how cells respond to surfaces and structures, looking at responses such as cell elongation, orientation and migration. The research was directed at the growth of nerves with the aim of furthering understanding of nerve regeneration and repair [138].

In Harrison's early experiments in 1914, cells (from the central nervous system of frog and chick embryos) were observed migrating along the fibres of spider webs [139]. Harrison discusses the importance of the presence of solid structures for the locomotion and shape changes of cells, referencing experiments where cells were cultured in clotted lymph: cells were able to migrate through clotted lymph but in liquid medium they formed uncharacteristically round appearances and were unable to migrate.

Weiss lead on from this work by investigating the effect of ECM-derived structures on the outgrowth of axons and advancing cells from chick embryo brain explants. Blood plasma was clotted in an oriented manner and axons and cells were seen to grow and orientate in the direction of the clotted

plasma. He concluded from his experiments that the dominant factor in the guidance of the growing and migrating nerve cells was the mechanical guidance provided by the fibrin in the clot [140].

Paul Weiss later coined the term 'contact guidance' to describe the effects of physical structures on the growth and behaviour of cells. He went on to conduct a number of further experiments to investigate the effect of other solid structures in the migration and growth of nerve cells [138]. In culturing chick DRG explants on scratches in culture plates, he found that axons would grow out from the tissue and extend along these scratches. Secondly, rat nerves were cultured in a blood plasma clot with aligned glass fibres of 8-26 μm diameter. Schwann cells migrated along these fibres and oriented along the direction of the fibres. Comparing Schwann cell migration along the fibres to migration within the plasma clot, migration along the fibres was much more oriented and double the speed.

Weiss concludes his paper with the statement [138]:

“The fact that Schwann cells and axons can be oriented into straight parallel courses by strands of parallel fibers of glass or other materials, even if the latter are embedded in a blood plasma clot, raises hopes that it might become possible to develop artificial bridges for the spanning of nerve gaps by embedding suitable fibers, properly spaced, in a cylindrical clot, sheathed by a suitable membrane.”

This statement paves the way for much of the current research into physical guidance cues for NGCs. It is the idea that by providing the solid structures necessary for cells to migrate, it may be possible to enhance the migration of Schwann cells and the advancement of axons to allow faster or more effective regeneration.

1.6 Modern strategies to include contact guidance in NGCs

Since the time of Harrison and Weiss, there has been much research into the use of topographical guidance cues to guide regenerating and migrating cells, especially in the field of nerve regeneration. Conduits have been made with multi-lumen/microchannel structures [81], [133], [141], [142] or aligned pores from directional freezing methods [143]–[145]. Here we will focus on two main methods for guiding cells: the use of aligned microfibres and aligned grooves. Both types of structure can be fabricated from a variety of materials and used to provide topographical cues to cells in order to promote alignment and migration with the aim of encouraging more directed and efficient nerve regeneration.

1.6.1 Electrospinning

One type of guidance cue that is popular in literature is the use of aligned polymer fibres produced by electrospinning. Electrospinning (described in Figure 10) is a manufacturing technique that is able to produce polymer fibres of a highly controllable diameter in the nanometre to micrometre range. This is useful in tissue engineering as the nano/micro-fibre scaffolds produced, mimic the structure of the native ECM of tissues (e.g. collagen and elastin fibres, or fibrin in the case of nerve regeneration) [146]. The ECM provides an important base for cell attachment, organisation and migration so it is important to consider its structure and function when producing scaffolds for tissue engineering. The ability of cells to attach and migrate directly influences their viability and has obvious implications for nerve regeneration.

The technique, first invented in 1900 [147], re-emerged in the early 90s and the process was described in detail in by Reneker and Chun in 1996 [148]. Using a syringe pump, a polymer solution is ejected at a controlled rate through a hypodermic needle/spinneret into a high voltage gap (Figure 10). The polymer solution is charged, by applying a high voltage to the tip of the needle, and is attracted to a grounded collector. When the electrostatic forces acting on the ejected polymer droplet overcome the surface tension, a jet forms and the polymer solution is accelerated across the gap. Solvent evaporation from the polymer jet forms a fine fibre which is deposited on the collector [146].

Randomly oriented fibres can be produced using a flat collector (such as a sheet of copper or aluminium foil) and these form scaffolds with a highly porous, interconnected structure [149] and a large surface area for cell attachment. However, for the field of nerve regeneration it is of interest to produce aligned fibres to guide the regenerating and migrating cells from the proximal and distal stump. Highly aligned electrospun fibres can be produced using a rotating, cylindrical collector (Figure 10) where increasing the rotational speed produces fibres with a higher degree of alignment [150].

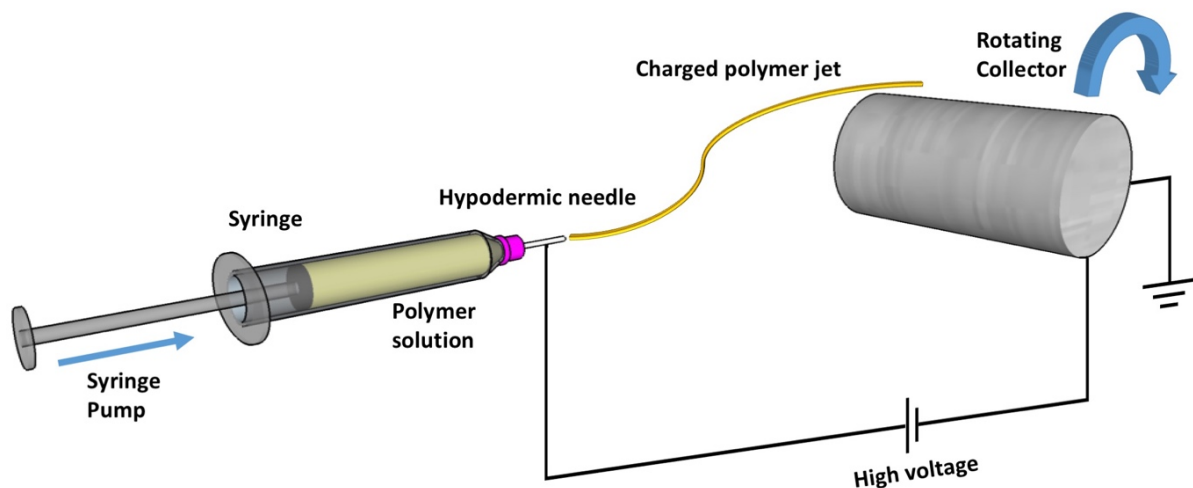


Figure 10. Diagram of an electrospinning set-up. Polymer solution is ejected from a charged needle and accelerated towards a grounded collector. Solvent evaporation results in the formation of a polymer fibre. Collected fibres can be oriented with the use of a rotating collector, as shown.

Electrospinning is a very versatile and controllable technique; as well as having the ability to produce aligned and random fibres, the parameters of the system can be changed to produce fibres of different diameters and morphologies. The controllable variables include the flow rate (at which the polymer is ejected from the syringe), the voltage across the gap, the needle-to-collector distance, and the needle diameter. Additionally, the solution parameters can be altered for an effect on fibre morphology, such as the polymer molecular weight, polymer concentration, viscosity and conductivity. However, for a given polymer, these solution properties are very closely dependable on each other and changing one will have an effect on the others. Thirdly, the ambient environment i.e. temperature, humidity and pressure, can also affect fibre morphology [149], [151], [152].

1.6.2 Influence of aligned fibres on Schwann and neuronal cell growth

It has been shown by many groups that electrospun fibres can provide physical guidance to both neuronal and glial cells. In previous work at the university of Sheffield, Daud et al. performed an in-depth study on the production of highly aligned electrospun fibres and their effect on the growth and alignment of neuronal cells and Schwann cells [153]. Highly aligned Polycaprolactone (PCL) fibres were produced at controlled diameters of 1 μm , 5 μm and 8 μm . Cell cultures were performed with the neuronal cell model, NG108-15, rat primary Schwann cells and rat dorsal root ganglion (DRG) explants. It was found that the 8 μm fibres promoted the longest neurite length however the 1 μm fibres promoted the best Schwann cell adherence and elongation. Co-cultures were also

performed, where NG108-15 cells were cultured on electrospun scaffolds pre-seeded with primary Schwann cells. It was seen that the presence of pre-seeded Schwann cells increased neurite length compared to neurite length of NG108-15 cells grown alone on electrospun scaffolds. This, emphasises the important role that Schwann cells play in the regeneration of peripheral nerves. In the DRG cultures, the outgrowth of the cells from the DRG explant was measured and the 1 μm fibres supported the furthest Schwann cell migration and neurite outgrowth. An interesting and possibly very important observation made was that axonal growth was always preceded by Schwann cell migration in that the limit of axonal growth always lagged behind the advancing Schwann cells [153]. This finding has been mirrored in other in vivo studies where axons were always found co-localised with Schwann cells and never found alone, whereas Schwann cells could be found in the absence of axons [154]. Complementary to the other results, these findings support the idea that leading Schwann cell migration is necessary to allow axonal regeneration, by providing guidance in the form of Bands of Büngner. These results suggest that instead of designing conduits to promote the best neurite growth, attention should be placed on designs that promote the best migration and alignment of Schwann cells which will, in turn, encourage improved neurite growth.

As expected, fibre alignment has a significant effect on the growth of Schwann and neuronal cells. Corey et al. produced 500 nm, highly aligned PLA fibres via electrospinning and found that Schwann cells from DRG explants assumed a narrower, elongated morphology on the fibres compared to those grown on glass coverslips. Additionally, increasing degrees of fibre alignment promoted increasingly longer neurites; a 20% increase in neurite length was seen on the highly aligned fibres compared to the random fibres [155]. Similarly, Xie et al. cultured DRG explants on electrospun PCL nanofibres [156]. As expected, neurites extended radially in all directions when cultured on a mat of randomly aligned fibres and extended bidirectionally along fibre direction when cultured on mats of aligned fibres. The maximum neurite length extended from the DRG was also found to be two times greater on the aligned fibres than on the random fibres. When cultured on the border between random and aligned fibres, neurites from the same DRG grew radially and directionally on each respective side, corresponding to the random or aligned fibres. DRGs were also found to adhere better to random electrospun fibres after laminin coating. However, DRGs adhered well to both laminin-coated and non-coated aligned fibres. On aligned fibres, neurites were observed to project from the DRG and then turn to grow in the direction along the fibres. This effect was more exaggerated on laminin-coated fibres suggesting the potential benefit of laminin coating for enhancing neurite guidance by fibres [156].

Aside from guiding cell alignment, electrospun fibres have shown some additional properties which could be useful for tissue engineering. It has also been found that aligned nanofibres have the ability to promote and enhance the differentiation of mouse embryonic stem cells into neural cells [157].

Though there is much evidence that neurites align parallel to oriented fibres some alternative growth patterns have been observed when the properties of the electrospun mats are altered. In another study by Xie et al. chick DRGs were cultured on aligned electrospun PCL fibres and some interesting behaviour was seen. DRGs grown on relatively low density aligned fibres (electrospinning collection time of 4 minutes) produced neurites growing parallel to the fibres. Laminin coating of the fibres was also seen to increase the elongation of neurites. However, when grown on high fibre density mats (collection time of 15 minutes), the neurites were observed to grow perpendicularly to the aligned fibres. However, with the addition of laminin-coating, neurites would grow parallel to even the high fibre density mats [158]. These results hint at more complex interactions than what might first appear most obvious and emphasise the importance of controlling parameters such as fibre density.

Electrospinning is not limited to the use of synthetic polymers but can be carried out with natural, biological polymers also. Schnell et al. produced nanofibers (~550 nm diameter) using a 70:20 blend of PCL:collagen (PCL/C). These aligned fibres caused directed Schwann cell migration from DRG explants and the collagen content of the PCL/C fibres enhanced the migration speed compared to the PCL fibres, as well as promoting improved neurite orientation [159]. Beneficial results have also been seen with blends of PCL/laminin [134] and these studies suggest that the inclusion of natural ECM proteins may help the fibres better mimic the ECM of the native tissue, increasing their therapeutic effect.

1.6.3 Conduits manufactured with electrospun fibres

As we can see, there is much evidence showing the beneficial effects of aligned fibres on the growth of neural cells suggesting that the incorporation of such fibres into NGCs would improve their ability to promote nerve regeneration. There are a few different methods reported in literature of integrating fibres into NGCs such as the direct fabrication of electrospun tubes or rolling of electrospun mats into tubular constructs. The former approach was taken by Yao et al. who fabricated bilayered PCL tubes directly from electrospinning. In a two-step process, aligned fibres were spun along a wire (diameter = 1.4 mm) followed by random fibres being spun on top. The result was a conduit (1.4 mm internal diameter) with aligned fibres running along the lumen and random fibres forming the outer layer [160]. Using the latter rolling method, Chew et al. fabricated conduits using a poly(caprolactone-ethyl ethylene phosphate) co-polymer. Fibres were electrospun on top of the polymer film which was rolled and sealed to produce a conduit with aligned fibres along the internal luminal surface (Figure 11a) [105].

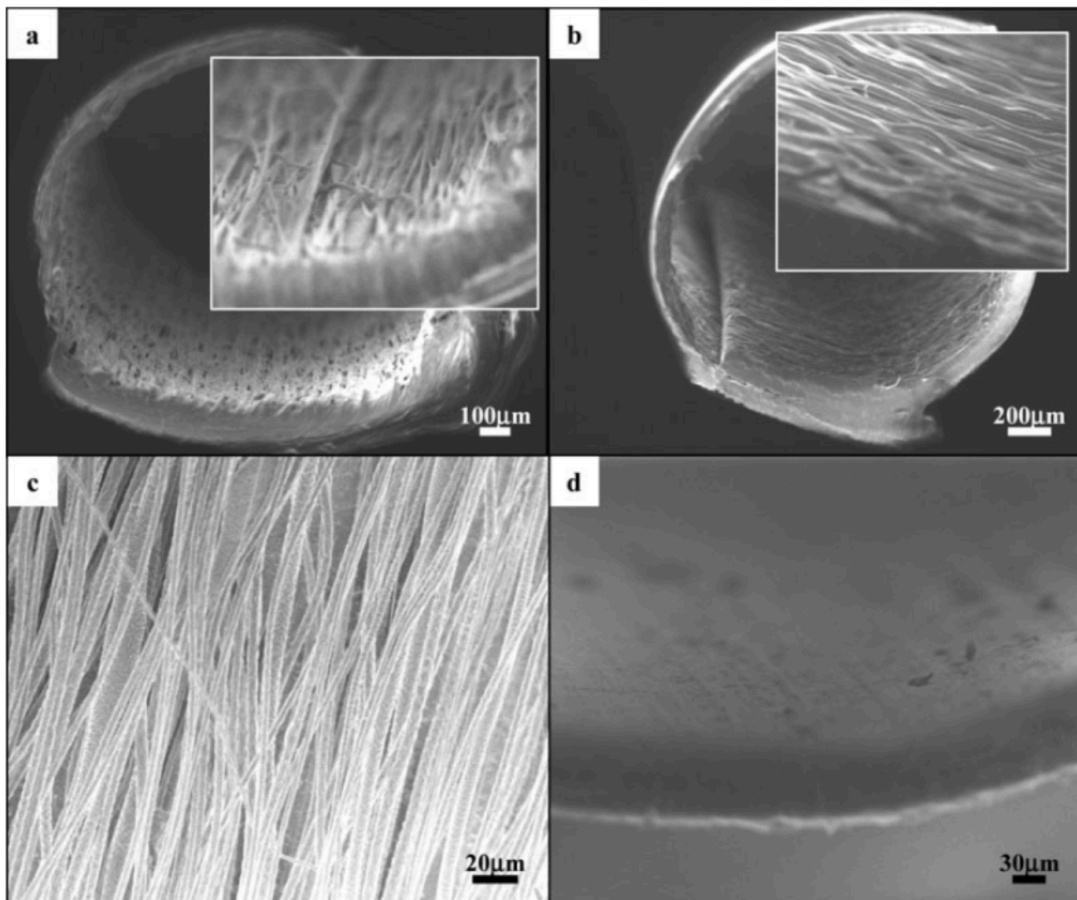


Figure 11. Conduits produced by Chew et al. a/b: bilayered conduits with an inner lumen of longitudinally/circumferentially aligned fibres (insets: higher magnification views), c: electrospun fibres, d: empty polymer film which forms the outer tube in a/b. Reprinted from Chew et al. with permission from John Wiley and Sons [105].

While fabricating the NGC tube from aligned electrospun fibres may provide some guidance to the regenerating nerve cells, this method leaves the lumen of the conduit empty which may not be conducive to effective regeneration. It is thought that increasing the surface area within the conduit will provide a greater area for cell adhesion and aid in more effective regeneration. One way of doing this is to include multiple channels in the lumen of the conduit.

The technique of rolling electrospun mats into conduits has been used to produce such conduits with multiple channels within the lumen. These multi-lumen conduits were produced by Jeffires et al. by placing aligned sutures on top of a mat of random electrospun PCL fibres. Another layer of random PCL fibres was electrospun on top of the sutures, sandwiching them between two layers of fibres. The resulting mat was then rolled into a spiral and the sutures removed to leave parallel channels. Channels of varying diameters ($\sim 30\text{-}180\ \mu\text{m}$) could be produced by using different diameters of suture [161]. The group demonstrated the ability to culture Schwannoma cells within the conduits but the conduit design was far from optimised. One notable feature was their use of random PCL fibres which, considering the results from previously mentioned studies, would likely provide poor guidance to regenerating nerve cells. Dinis et al. fabricated conduits in a similar manner but using aligned fibres [162]. Electrospun sheets of aligned silk fibres were rolled around Teflon sticks resulting in a conduit with a number of parallel channels of around $180\ \mu\text{m}$ in diameter (Figure 12). Multi-lumen conduits have also been fabricated by rolling electrospun matts into multiple, small-diameter tubes and arranging inside a larger tube made from the same fibre mat [163].

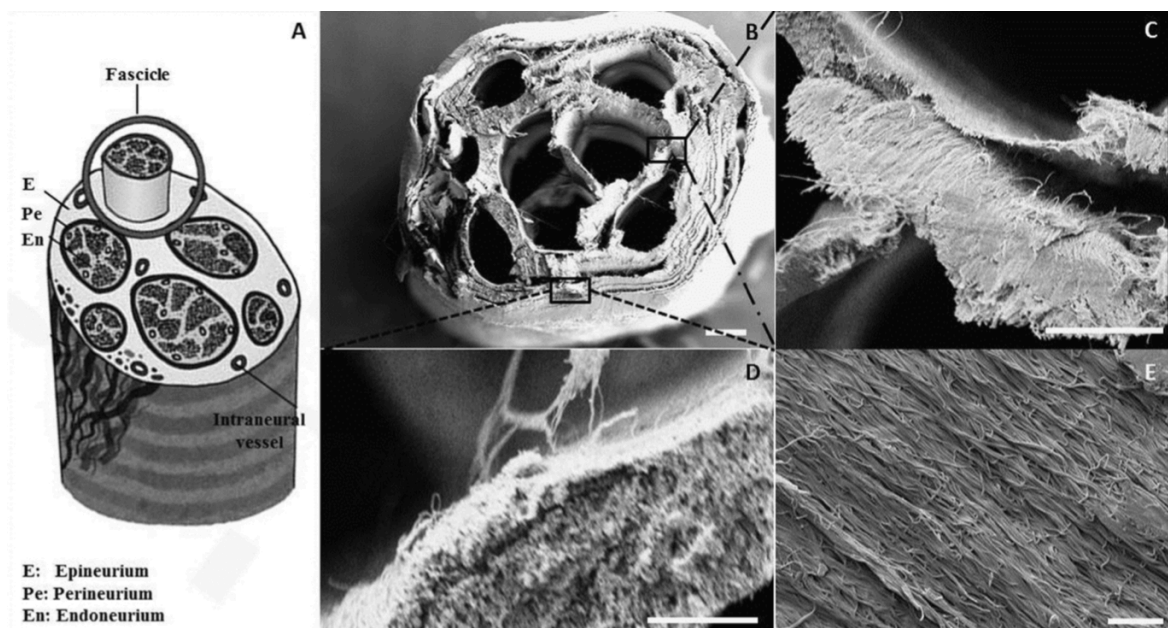


Figure 12. Multi-lumen silk conduit produced by Dinis et al. (B-E) in comparison to the fascicular structure of the native nerve (A). Reprinted from Dinis et al. with permission from Elsevier [162].

While these multi-lumen NGCs may provide a large surface area for nerve regeneration, the walls between the lumens occupy a large percentage of the conduit cross-sectional area. Analysis of the conduits by Dinis et al. showed the total lumen area to be only 25% with the remaining 75% being occupied by the electrospun fibre walls. The large amount of material occluding the conduit lumen may in fact act as a barrier to regenerating cells/tissue. This barrier effect has been seen in studies using dense electrospun fibres [164], gels [165] or collagen sponges [166] within the lumen which impeded regeneration.

Spiral conduits have also been produced with an intraluminal structure extending into the centre of the lumen but still leaving a large amount of the luminal space unoccupied. Chang et al. fabricated spiral conduits by electrospinning PCL nanofibres onto a PCL film and wrapping the sheet into a spiral shape [167]. Conduits of different designs (containing aligned or random fibres) were tested in a 10 mm rat sciatic gap. The functional recovery was assessed by walking track analysis and electrophysiology but no significant differences were found between the different conduit groups. Some conduits did perform comparably to the autograft positive controls. A greater number of myelinated axons were also found in the centre of the spiral conduits compared to the tubular conduits in which axons were mainly found around the circumference. This highlights the benefit of intraluminal guidance structures being able to support axonal regeneration across the whole conduit lumen.

An alternative idea may be to incorporate the electrospun fibres into the lumen of the conduit so that the aligned fibres run through the lumen and homogeneously fill the space while still leaving a large percentage of the area free from material. The aim would be to provide intraluminal guidance cues to support cell migration throughout the whole luminal cross-section, without impeding overall growth. There is however limited literature on the use of NGCs with electrospun fibres inserted directly into the lumen and the groups that have fabricated conduits of this sort have used a variety of assembly techniques such as the formation of fibre yarns or the stacking of fibre films and inserting onto split conduits. An optimal design and construction method is far from being established with much research being needed on the topic.

Koh et al. fabricated bilayered PLA conduits by first producing a sheet of aligned nanofibres (250-1000 nm diameter) spun onto a rotating collector. This sheet was then wrapped around a 1.5 mm rod and randomly oriented fibres were spun on top of this to form the outer layer [168]. The result was a bilayered conduit, similar to that by Yao et al. however this group took the design a step

further by including intraluminal guidance structures. Electrospun poly(lactic-co-glycolic acid) (PLGA) fibres (200-600 nm diameter) were gathered together into bundles to produce 25 μm diameter ‘yarns’ composed of the aligned fibres. These yarns were then inserted into the conduit to act as ‘intraluminal guidance channels’ (Figure 13). Implantation of these NGCs into 10 mm rat sciatic nerve gaps was performed, and beneficial effects were seen in terms of improved sensory recovery and muscle reinnervation. After 12 weeks, 100% of all groups treated with nanofiber yarns responded to thermal stimuli, compared to 50% and 43% treated with empty conduits and grafts, respectively. Electrophysiological analysis of the regenerated nerves was performed to give an additional measure of functional recovery. Both the amplitude and conduction velocities of the nerve action potential were measured but significant differences were not found between any groups [168].

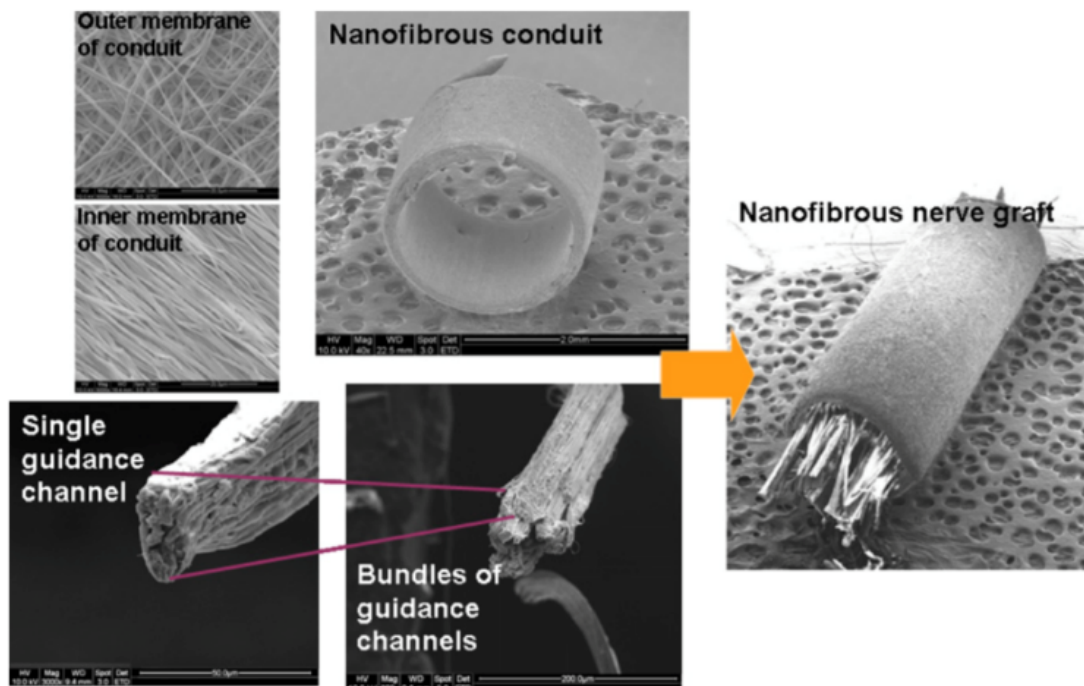


Figure 13. Electrospun fibre yarn-containing conduits fabricated by Koh et al. Reprinted from Koh et al. with permission from Elsevier [168].

In 2015, Li et al. fabricated similar conduits to Koh et al. with a slightly different technique. 600 nm electrospun PLA fibres were gathered into 50 μm diameter yarns and fixed together along a metal rod. P(LA-CL) fibres were then electrospun on top of this as it slowly rotated to produce a random mesh of fibres forming the conduit wall and the metal rod was subsequently removed. Schwann cells were cultured on these nanofibre yarns and seen to align along the direction of the fibres as well as having increased proliferation rates in comparison to Schwann cells cultured on nanofibre film.

Schwann cells were also seen to migrate through the tubes *in vitro* and increase in viability over 7 days [169].

Aligned electrospun fibre-containing conduits have also been fabricated by the insertion of stacked electrospun films into a solid-walled conduit. Kim et al. produced 20 µm thick films of aligned, 400-600 nm diameter poly(acrylonitrile-co-methylacrylate) fibres [154]. Ten to twelve of these sheets were stacked and inserted into the lumen of longitudinally split polysulphone conduits, which were then resealed with adhesive. The tubes were inserted into 17 mm rat tibial nerve gap and histological analysis revealed Schwann cell migration and axonal growth across the gap, similar to the autograft controls. In contrast, saline-filled conduits with no internal fibres, exhibited no Schwann cell migration or axonal regeneration, demonstrating the beneficial effect of the aligned fibres. Conduits containing randomly oriented fibres were also tested and these showed both significantly lower Schwann cell migration and number of axons traversing the gap compared to the aligned constructs.

Another study to investigate the effect of fibre orientation on nerve regeneration was that of Neal et al. [134]. Outer conduits of randomly oriented PCL microfibrils were filled with sheets of PCL or PCL-laminin nanofiber sheets with either aligned or random orientations. These were used to repair 10 mm rat tibial nerve injuries. When PCL-laminin fibres were used, sensory recovery was significantly improved in the aligned fibre conduits compared to ones with randomly oriented fibres. Electrophysiological analysis revealed the conduction velocity of the regenerated nerve was significantly increased with the use of aligned fibres compared to random fibres. In conduits containing no fibres, there was very little sensory recovery and no conduction velocity was detected. Histological data backed up these findings showing much higher axonal ingrowth and a greater degree of longitudinal organisation into the aligned fibre constructs. The result of improved regeneration with aligned fibres vs random fibres (from Neal et al. [134] and Kim et al. [154]) mirrors the *in vitro* observations discussed in section 1.6.2, demonstrating that similar contact guidance effects can be seen *in vivo*. The results highlight the importance of appropriate guidance cues for the promotion of successful nerve regeneration and the significant impact of directional cues.

Previous work at the University of Sheffield includes a pilot study carried out by Pateman and Harding, involving the implantation of aligned fibre-filled NGCs into a PNI model using thy-1-YFP transgenic mice. The mouse neurons express the fluorescent protein, YFP, which allows each individual axon to be visualised and traced across the injury gap for a novel and in-depth assessment

of nerve regeneration. PCL fibres were inserted into PEGDA conduits at two arbitrary packing densities: 'high' and 'low'. No regeneration was seen in the high packing density conduits and it was hypothesised that this was due to an inhibition of Schwann cell migration and signalling factor diffusion by the densely packed fibres. On the other hand, the conduits with low fibre packing density performed better, albeit with much variability in the results. Two out of four of these conduits promoted a high degree of axonal regeneration across the nerve gap with a large number of axons reaching the distal stump [170]. These results emphasise the importance of the optimisation of new conduit designs and the consideration of all factors (such as fibre packing density) that may influence the physiological processes occurring during recovery.

1.6.4 Conduits containing fibres produced by alternative methods

It is worth noting that a number of *in vivo* studies have been carried out with conduits containing guidance cues in the form of larger diameter fibres made by methods other than electrospinning. Examples include studies by Cai et al. [171] and Ngo et al. [172] who fabricated PLA fibres using an extrusion-based wet spinning process. Fibres in the range of 40-100 μm were produced and inserted into conduits to repair rat sciatic nerve injuries. In both studies, a greater number of axons were seen traversing across an 18 mm nerve gap in the conduits containing fibres, compared to the empty controls. The fibres were also seen to improve Schwann cell migration [171]. Ngo et al. also investigated the effect of different packing densities of fibres by inserting different numbers of fibres. As with the study by Pateman and Harding, lower packing densities (3.75% vs 30%) were found to promote better regeneration, with a greater degree of axonal regeneration [172]. The results of these studies and how the findings relate to the current work will be discussed in more detail in the following chapters.

Larger diameter fibres have also been produced from ECM proteins such as collagen. Daly et al. repaired a 10 mm rat sciatic nerve gap with conduits containing 50 μm collagen fibres (produced by extrusion). Retrograde tracing revealed that a larger number of axons reached the distal end compared to the empty conduits. Interestingly, the fibres lead to decreased axon misdirection with fewer axons growing down both the tibial and common fibular branches of the sciatic nerve [173]. Impressive results have also been seen with collagen fibres promoting regeneration over much longer distances. Matsumoto et al. repaired 80 mm common fibular nerve in beagle dogs with conduits containing 50 μm laminin-coated collagen filaments. The conduits supported axonal regeneration across the whole nerve gap (12 month recovery) with conduction velocities reaching

normal levels however no empty controls were included in the study so the specific benefit of the fibres could not be investigated [36].

1.6.5 Microgrooves for guidance in NGCs

Another area of interest in the guidance of Schwann cells and neuronal cells within a NGC is the use of parallel microgrooves to encourage alignment and directional migration. These types of structures can be fabricated in a variety of ways and have been tested by a number of groups both *in vitro* and *in vivo* to assess their potential in nerve guidance.

1.6.5.1 *In vitro* studies

Cai et al. fabricated 5-90 μm microgrooved substrates from PCL triacrylate and investigated the growth of a Schwann cell precursor line (SpL201) and a neuronal cell model, pheochromocytoma cells (PC12). Both cell types were shown to have increasing alignment with decreasing groove spacing with 95% of SpL201 cells aligned (within $\pm 15^\circ$ from the groove direction) on the 5 μm grooves substrates. Additionally there was a 400% increase in expression of S100 by SpL201 cells on 5 and 15 μm grooves vs the flat controls, indicating the ability of the grooves not only to promote alignment but also Schwann cell differentiation [174]. Despite this data that narrower (5 μm) grooves may promote improved alignment, there is also evidence to suggest that primary Schwann cells are more influenced by larger grooves. Hsu et al. cultured primary Schwann cells on microgrooved silicone substrates and found a 58% increase in alignment on grooves with a width/spacing of 20/20 μm vs 10/10 μm [175].

In similar work by Miller et al. primary rat Schwann cells were cultured on 10-20 μm grooved, laminin-coated PLA substrates and found that these effectively promoted alignment of the cells [176]. The same group then continued the use of these substrates with co-cultures of primary Schwann cells and neurons from dissociated rat DRGs. Results showed that in the absence of Schwann cells, neurite alignment was increased on deeper grooves (4 μm vs 3 μm) however the presence of pre-seeded Schwann cells decreased this dependence on groove depth and neurites were also seen to align on shallower grooves. Secondly, for neurons seeded with Schwann cells, neurite alignment was maintained even after the degradation of the scaffold whereas this was not the case for neurons seeded alone [177]. This finding is concurrent with others that have found that neurite growth can be effectively guided by aligned Schwann cells. Neurites from neurons cultured on aligned Schwann cell monolayers are seen to align in the direction of the Schwann cells in contrast to randomly oriented neurites produced by neurons cultured on non-aligned Schwann cells

[178]. These examples yet again emphasise the important role of Schwann cells during nerve regeneration due to their ability to influence neurite growth.

For this reason, it is important to study the behaviour of Schwann cells on the grooved substrates such as work by Mitchel and Hoffmam-Kim on Schwann cell migration. The group cultured primary rat Schwann cells on laminin-coated, microgrooved PDMS substrates, investigating groove spacings of 30 μm and 60 μm . Schwann cells were seen to align and migrate parallel to the groove direction on both substrates, with a more directed motion than those cultured on flat controls on which the cells migrated in all directions. Using time-lapse microscopy, it was found that on the 30 μm grooves Schwann cells exhibited a higher degree of directionality in their migration, indicated by a greater percentage of aligned steps between the image time-points. It was also noted that Schwann cells within the grooves migrated faster than those on plateaus between the grooves [179].

While most groups are researching the effect of grooves smaller than 100 μm , research into larger grooves has also been carried out. Suo et al. fabricated grooved polyacrylonitrile conduits with grooves along the luminal wall ranging from 183 to 349 μm (ridge size 73 to 113 μm) [180]. After 72-120 hours the neurites expressed by the PC12 cells were seen to align to the direction of the grooves. As neurite length increased over the 5-day culture period, alignment increased as neurites were long enough to be able to sense the edge of the grooves. As groove size decreased, this effect was amplified and a larger percentage of neurites aligned in the direction of the grooves. On the smallest grooves (183 μm grooves and 73 μm ridges) 70% of neurites were aligned within 30° of the groove direction. Both cells in the grooves and on the ridges were aligned with more pronounced alignment seen in the cells on the ridges. Since the ridges were narrower than the grooves, the neurites seemed constrained to this smaller width and experienced a greater alignment. It was hypothesised that the walls of grooves present barrier to cells both in grooves and on ridges due to the inflexibility of microtubules which control the growth of the neurites. These results show promise for the use of microgrooves in the order of 100 μm even though these are much larger than most studied by other groups.

1.6.5.2 *In vivo* studies

Microgrooved conduits with varying groove size have been tested *in vivo* by a number of groups and these are usually produced by the rolling of grooved films like those described in the previous section. Hsu et al. fabricated 20 μm grooved PLA sheets which were rolled around a 1.5 mm mandrel and sealed with a solvent. These were implanted into a 10 mm rat sciatic gap and successful bridging of the nerve gap was seen in 3/3 of cases with the grooved conduits, compared to 2/3 of the smooth controls. It was also observed that the regenerated nerves within the grooved conduits exhibited a larger area of axons, a larger number of myelinated axons and a greater degree of vascularisation [106]. In a later study, conduits with the same grooved features and different degrees of porosity were implanted in a larger study and similar findings were found. In some groups, grooved conduits resulted in a larger number of regenerating axons, a greater degree of myelination and greater functional recovery [181]. Conduits with smaller grooves (5 μm) were tested *in vivo* by Kim et al. who rolled grooved PLGA films into tubes in a similar way to Hsu et al. Testing in a 10 mm rat sciatic nerve gap, significantly more regenerating axons and migrating Schwann cells were seen in the grooved vs non-grooved conduits [182]. These successful results suggest that guidance effects seen from grooves *in vitro* may also play a role *in vivo*, demonstrating the potential clinical benefit of grooved conduits.

Interestingly, not all studies have shown such a clear benefit of grooved conduits. Rutkowski et al. fabricated similar conduits from grooved PLA films (10 μm grooves) which were rolled and inserted into tubes [183]. In the repair of a 10 mm rat sciatic nerve gap, no difference in axon number or functional recovery was seen between the grooved and non-grooved conduits. However, when conduits were pre-seeded with Schwann cells 24 hours prior to implantation, the grooved conduits promoted increased functional recovery. Non-grooved conduits, pre-seeded with Schwann cells, did not have a similar effect. This suggests that though the grooves themselves did not have an effect on nerve regeneration, they were able to facilitate the beneficial effect of the Schwann cells.

As well as the size of the grooved structures, groove shape has also been investigated. Mobasseri compared the effect of sloped grooves (SL), V grooves (V) and square grooves (SQ) (Figure 14). *In vitro* testing showed the SL and V grooved films to promote improved cell attachment and proliferation compared to SQ grooves so these were selected for *in vivo* testing in a 10 mm rat sciatic nerve gap. The cross-sectional area of regenerating axons was significantly greater for SL grooves vs V grooves which in turn was significantly greater than for non-grooved conduits. Comparing the regeneration within a SL conduit vs an autograft control, there were no significant differences in

axon number/density or the extent of myelination. Additionally, functional muscle recovery, assessed by electrophysiology testing showed no significant differences between the two groups [184]. These results show that shape may be an important factor to take into account when considering groove design and that if the right morphology is chosen, these grooved conduits could offer a promising alternative to autografts.

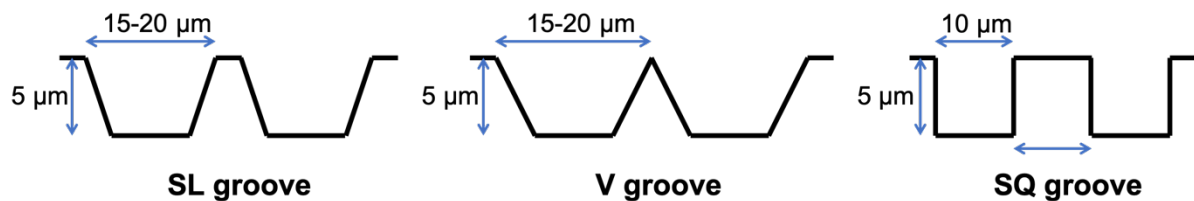


Figure 14. Shapes of microgrooves investigated by Mobasseri et al. [184]

As we can see from these studies, microgrooved structures can provide guidance to cells *in vitro* and have shown the ability to enhance nerve regeneration *in vivo*. However common manufacturing methods for these types of structures involve complex, multi-step procedures involving lithographic techniques using photoresist masks often followed by plasma etching to create grooves and casting or stamping from a mould [106], [177], [179]. Additionally, these films then have to be rolled and sealed with heat or a solvent which could damage the structures or be detrimental to the tube's mechanical properties. As discussed previously, micro-stereolithography could offer a much easier and more adaptable, one-step production of microgrooved conduits without the need for the complex production of moulds or rolling of films.

1.6.6 Conclusions

- Aligned electrospun fibres show potential for enhancing nerve regeneration but there is little *in vivo* data on their performance.
- There are few groups directly inserting fibres into the lumen of tubes without intermediary steps such as the formation of fibre yarns or sheets.
- No groups have performed analysis of the density of electrospun fibres within the scaffolds.
- Microgrooves can effectively promote cell alignment, encourage directional migration and improve *in vivo* nerve regeneration.
 - Beneficial effects have been seen from grooves ranging from 5 μm to 100+ μm
- μSL may offer easier and more adaptable manufacturing of microgrooved structures.

1.7 Project Aims and Objectives

1.7.1 Main project Aim:

Produce NGCs containing physical guidance cues, which are more successful in the repair of peripheral nerve injuries compared to simple designs. Aligned grooves and aligned microfibres will be investigated for their ability to facilitate cell guidance and support improved regeneration.

1.7.2 Objectives

- 1) Produce a photocurable prepolymer resin which cures to form a biocompatible, biodegradable material
- 2) Use this material in microstereolithography to produce NGCs and other 3D structures
- 3) Produce and characterise NGCs containing intraluminal physical guidance cues
 - a) Produce conduits with aligned grooves in the luminal wall, directly by microstereolithography
 - b) Combine microstereolithography constructs with electrospun fibres to produce conduits with aligned microfibres within the lumen
- 4) Demonstrate the biocompatibility of the materials and suitability of the conduit designs via *in vitro* testing
- 5) Investigate the performance of these NGCs in comparison to plain designs and graft controls using an *in vivo* nerve injury model and determine the effect of the physical guidance cues

Chapter 2 will focus on the synthesis and characterisation of a photocurable prepolymer resin. This resin will then be used in μ SL and the process optimised to produce NGCs and other 3D structures to a high quality. Chapter 3 will explore the design and production of NGCs containing physical guidance cues (aligned grooves and aligned microfibres) with the focus of creating implantable conduits for use *in vivo*. The production of aligned fibres via electrospinning will be discussed as well as characterisation techniques for determining parameters such as fibre packing density. In chapter 4, *in vitro* work will be discussed, testing the biocompatibility of the materials used in μ SL as well as determining the optimal conduit designs to take forward to the initial stages of *in vivo* testing. In chapter 5 the different conduit designs will be tested *in vivo* to determine their ability to support nerve regeneration and the effect of the intraluminal guidance cues. Conduits containing aligned grooves and aligned fibres will be tested in a 3 mm mouse nerve injury model.

2. Chapter 2: PCLMA production, characterisation and use in microstereolithography

2.1 Chapter Introduction

This chapter focuses on the production and characterisation of a photocurable resin for use in microstereolithography. Since the mechanical properties and degradation rate are important for NGCs (or any biomaterial application) the aim was to produce a material with tuneable properties.

The polymer used to produce this resin was poly(caprolactone)-methacrylate (PCLMA), a photocurable form of the biodegradable and biocompatible polymer, poly(caprolactone). PCLMA prepolymer was synthesised and characterised and it was shown that the mechanical properties and degradation rate of the cured polymer could be tuned by varying the parameters used in the polymer synthesis reaction.

The PCLMA was used in microstereolithography to produce a variety of structures including simple tubes for NGCs. The curing parameters such as laser power, stage speed and resin temperature were optimised to produce tubes of an excellent quality. Additives to the photocurable PCLMA resin were also investigated to improve the quality of the structures produced. Namely, the addition of photoabsorbers was considered to improve the z-resolution of the printed constructs and allow the production of more complex 3D scaffolds.

Though the work in this thesis is directed towards the production of NGCs, the PCLMA resin developed in this chapter and its use in stereolithography could be applied to the production 3D scaffolds of any design for a variety of applications in tissue engineering.

2.2 Background

2.2.1 Materials for NGCs

In chapter 1, the ideal NGC is described as being biocompatible, biodegradable and having the appropriate mechanical properties. These are all directly influenced by the choice of material used to fabricate the NGC. Biocompatibility is important when considering any tissue engineering scaffold, as to encourage the effective growth of tissues it is important not to provoke an immune reaction or inflammatory response which could lead to tissue damage and scarring. Related to this is the biodegradability; unless the implant is removed via a 2nd operation (which has obvious disadvantages), a non-biodegradable material will remain in the injury site inducing a chronic foreign body reaction. This would lead to an adverse immune response including scar tissue formation and the hindrance or decline of recovery [58]. The mechanical properties of a NGC are also important to allow adequate flexion without kinking and for it to be able to resist compression without damaging the surrounding tissues.

There is a plethora of commonly used biomaterials for the production of NGCs, ranging from natural materials such as collagen [185], silk [162] and chitosan [103], [186] to synthetic polymers such as PGA [109], PLA [187] and polyurethane [11]. These materials are able to be processed in a variety of ways for the production of NGCs but for use in stereolithography, materials must possess a certain chemistry.

2.2.2 Photocurable materials for stereolithography

When considering materials for stereolithography, the requirement is that the material must be photocurable. That is that the prepolymer is in a liquid form until exposure to irradiation (either in the UV or visible spectra) which induces crosslinking to form a solid polymer structure. To render a polymer photocurable, it must be functionalised by the addition of certain functional groups which facilitate crosslinking between prepolymer molecules. Acrylate or methacrylate groups are often added for this purpose [188] usually replacing hydroxyl groups in the original molecules. A resin is then produced from the photocurable prepolymer and this must have a low enough viscosity for use in stereolithography. If the prepolymer is not already a liquid or of a low enough viscosity at room temperature, it can be heated or mixed with solvents to create a suitable resin. A photoinitiator (often a benzoin derivative) is added to the prepolymer resin which, upon absorption of UV or visible irradiation, generates free radicals which initiate chain polymerisation. This free radical

polymerisation occurs between the functional groups (i.e. acrylate/methacrylate groups) and results in a crosslinked, solid polymer [189], [190].

2.2.2.1 Poly(ethylene glycol)

Poly(ethylene glycol) (PEG) is commonly used in μ SL due to its commercial availability in dimethacrylated or diacrylated form. Various groups have used photocurable forms of PEG to fabricate scaffolds for tissue engineering applications [191], [192]. More common however, is the use of PEG dissolved in water and cured to form a hydrogel. This method has been used to fabricate hydrogel scaffolds [193]–[195] and cell-encapsulating hydrogels [195]–[197]. Hydrogels exhibit a large degree of swelling in water which can lead to deformation and dimensional changes [198] as well as poor mechanical properties, so are not ideal for NGC use.

PEG also has unfavourable biological properties. It is inherently a bioinert material and therefore demonstrates poor cell attachment properties [199], [200]. Moeller et al. demonstrated the poor protein and cell adhesion properties of PEG compared to glass and tissue culture plastic [200]. It has also been shown that the addition of PEG to hydrogels decreases their protein binding properties [201]. PEG is also non-biodegradable which could cause the problem of an evoked immune response during long term implantation and may require a second surgery to remove. Lastly, in its bulk form, PEG can be very brittle, especially low molecular weight PEG. For thin walled PEG structures (i.e. NGCs) this could lead to fracturing during handling. A related property is its low elasticity which does not adequately match the tissue at the site of a nerve injury and could lead to tissue damage *in vivo*. These properties all contradict the ideal properties of a NGC discussed in section 1.3.1. Despite PEG's poor cell adhesion properties, it has been shown that in a bulk form, PEG can support cell growth, especially after prolonged washing which can increase the supported cell viability [202]. This biocompatibility was demonstrated in the NGC implantation study by Pateman and Harding et al. discussed earlier [128].

The results in this chapter will include some discussion of the use of PEG-diacrylate (PEGDA, a photocurable form of PEG) in stereolithography. For obvious reasons the aim here is not to produce an optimal PEGDA resin for the production of NGCs but only to use it as a platform for testing the effect of different additives to the prepolymer resin. PEGDA will be used to test the effect of different photoabsorbers (discussed in more detail in section 2.2.4) on the structures produced by μ SL. This work with PEGDA forms a proof of concept study that can then be applied to materials with more desirable properties for tissue engineering applications i.e. poly(caprolactone).

2.2.2.2 Poly(caprolactone)

A more appropriate material to use for NGC fabrication would be a biodegradable, elastic polymer that is more favourable for cell growth. Poly(caprolactone) (PCL) satisfies these requirements. PCL is biodegradable via the hydrolysis of ester linkages in the polymer backbone [203], [204] as well as via enzymatic action by lipases [205], [206]. This would allow a PCL NGC to be degraded over time as the injured nerve regenerates and matures. Importantly, PCL-containing medical devices have been FDA approved for use in various applications, such as sutures (e.g. Monacryl by Ethicon, a copolymer of glycolide and ϵ -caprolactone [207]) and drug delivery systems (e.g. Capronor™, a subdermal contraceptive device [208]). This approval makes PCL a clinically relevant material meaning that a novel PCL nerve guide product would have a more favourable passage through the approval process of the FDA and other regulatory bodies.

Non-photocurable forms of PCL are widely used in the field of biomaterials. Examples include biodegradable particles for drug delivery [209], knitted scaffolds for aortic valve [210] and electrospun scaffolds for various applications in bone [211], cartilage [212] and nerve [213]. It is also the material of choice for many groups producing scaffolds for tissue engineering by additive manufacturing. PCL's low melting point of 60°C makes it suitable for use in FDM and is widely used to produce woodpile scaffolds such as those by Hutmacher et al. [214]. Porous PCL scaffolds are also produced by SLS for applications such as bone and cardiac tissue engineering [215]–[217]. PCL has had limited use in stereolithography due to its inherent non-photocurability, however it can be functionalised to allow it to be photocured. Various formulations of photocurable PCL resin have been reported, however some of these require a number of additives (e.g. crosslinkers or reactive diluents) or the use of heat to produce a usable resin.

Early reports of methacrylated PCL can be found in work by Storey et al. who methacrylated PCL triol by reacting with methacryloyl chloride. The work included homopolymerisation and copolymerisation of this PCL-methacrylate (PCLMA) with mixtures of other polymers (methyl methacrylate, styrene, and 2-methylene-1,3-dioxepane) to give cured materials of different mechanical properties [218]. All polymers were thermally cured into bulk structures and though this is a different system than that used in stereolithography, the work could be translated to inform work with UV-curable systems.

More recent work has been carried out by Elomaa et al. who produced a photocurable PCL resin and demonstrated biocompatibility and 3D structuring [219]. PCL triol was produced by ring opening polymerisation of ϵ -caprolactone monomers and methacrylated with methacrylic anhydride. The resulting three-armed PCLMA molecules were photocurable with the addition of a photoinitiator (Irgacure 2959) but required heating to produce a liquid resin. The resin was cured using UV light and by varying the molecular weight (M_n) of the PCLMA prepolymer from 800-6000 the Young's modulus of the resulting material was varied from 15.4-6.7 MPa. Thin PCLMA films were shown to be biocompatible, supporting fibroblast growth, without the need for treating or coating with other substances. The resin was also used to produce 3D, PCLMA scaffolds using a commercial stereolithography machine.

Other photocurable forms of PCL have also been produced by utilising different functional groups in place of methacrylate groups. Ronca et al. incorporated vinyl end groups in a PCL molecule to enable photocurability [220]. This required a two-step reaction for ring-opening and vinyl termination of ϵ -caprolactone, followed by reaction with fumaryl chloride to produce divinyl-fumarate poly- ϵ -caprolactone. The resulting polymer was UV crosslinkable but due to the lower reactivity of the vinyl groups compared to the methacrylate groups it was necessary to include a crosslinker (N-vinylpyrrolidone, NVP) at 30 to 50 wt% in the resin mixture. 2 mm thick discs were produced by photocuring under UV light for 30 mins. Two types of macro-porous scaffold were also created, using a commercial stereolithography machine, with gyroid and diamond shaped pores (710 μm and 400 μm average pore sizes). Photocured polymer films were shown to support the growth of human mesenchymal stem cells however metabolic activity was lower than the tissue culture plastic (TCP) controls.

PCL has also been copolymerised with trimethylene carbonate (TMC) to producing poly(CL/TMC) and made photocurable with coumarin [221] and acrylate [222] functionalisation. Coumarin-functionalised molecules cure slowly due to crosslinking occurring as a result of a photodimerization reaction between associated pairs of groups. This limited the UV curability of the resin to only thin films. Free radical polymerisation (that which occurs between acrylate and methacrylate groups) occurs much more rapidly and makes it possible to produce much thicker 3D structures. The acrylate-functionalised poly(CL/TMC), similarly to the other resins discussed, could be used to fabricate simple 3D structures by μSL , including simple tubes and microneedle arrays. However the resolution demonstrated was limited to around 500 μm [223].

2.2.2.3 Examples of other polymers

Poly(propylene fumarate) (PPF) is a widely used polymer in the formulation of resins for stereolithography and is biodegradable via hydrolysis of ester linkages [224]. PPF can be synthesised by reacting diethyl fumarate with 1,2-propylene glycol and polymerising the resulting dimer. Lee et al. produced such a resin and used a commercial 3D Systems stereolithography machine to produce scaffolds with controllable macro-porosity in the range of 450-900 μm [225]. PPF has also been used to create structures with micro-sized features such as that by Choi et al.; the group used a PPF-based resin in a custom μSL set-up to fabricate microstructures with a feature size of 30 μm [119].

Melchels et al. prepared a novel, photocurable poly(D,L-lactide) (PDLLA) resin which is crosslinkable without the need for a reactive diluent to act as a crosslinker. 2-, 3- and 6-arm PDLLA oligomers were synthesised and functionalised with methacryloyl chloride to produce methacrylated PDLLA [226]. A methacrylated poly(D,L-lactide-co- ϵ -caprolactone) (P(DLLA-co-CL)) co-polymer was also produced and used to fabricate structures with more flexible properties (the bulk elastic modulus of P(DLLA-co-CL) was 2 MPa compared to 2.5×10^3 MPa of PDLLA) [227]. The polymers were mixed with solvent (either 19% ethyl lactate or 40% N-methylpyrrolidone) to produce resins with appropriate viscosity for use in stereolithography. 2-6% photoinitiator (Lucirin TPO-L), 0.025% inhibitor (hydroquinone) and 0.2% Orasol Orange G dye were also added. Using a commercial stereolithography machine, both resins were used to fabricate macro-porous scaffolds with cuboidal, diamond and complex gyroid structures. Pore size was in the range of 200-550 μm for the different designs and pore architectures.

2.2.3 Varying the Degree of Polymer Methacrylation and the effects

As discussed, the work in this study will focus on the use of PCLMA. As far as can be seen from the literature, little work done to vary mechanical properties of photocurable PCL, aside from mixing with different materials or varying the molecular weight. An alternative method would be to vary the degree of functionalisation of the prepolymer which may allow a greater control over the Young's modulus of the material. As described in section 2.2.2, photocurable functionality can be added to a prepolymer via the addition of methacrylate groups which facilitate the crosslinking between molecules. It then follows that varying the number of methacrylate groups per prepolymer molecule leads to a change in crosslinking density in the cured polymer. This affects the mechanical properties (Young's modulus, tensile strength), degradation rate and swelling characteristics.

The extent of polymer methacrylation is measured by the degree of methacrylation (DM). This is defined as the percentage of available functional groups (e.g. hydroxyl groups) in the initial molecule that have reacted to form methacrylate groups in the end product. In other words:

$$\text{Degree of methacrylation (DM)} = \frac{\text{no. of methacrylate groups (per molecule)}}{\text{initial no. of functional groups available for methacrylation (per molecule)}} \times 100 (\%)$$

The variation of polymer DM is a well-known practice and can be achieved by controlling various parameters in the chemical reaction, such as the reagent concentration, reaction time and reaction temperature. Displayed in Table 3 is a summary of the work by a number of groups into the methacrylation of various polymers and the control of DM by varying such reaction parameters.

The most common method of controlling DM is by varying the molar quantities of the reagents used in the reaction. The required amount of 'methacrylating reagent' (e.g. methacrylic anhydride (MAA)) can be estimated by calculating the number of functional groups in the prepolymer molecule which are available for methacrylation. A 1:1 molar ratio reaction (or 1× molar excess) means that for every 1 mole of available functional groups, 1 mole of methacrylating reagent is provided in the reaction. Since most methacrylation reactions are not 100% efficient, an excess of reagents is often used to drive the methacrylation reaction further. When the molar excess of the reagents is increased, the effect is an increasing DM of the resulting polymer.

This effect has been demonstrated in the methacrylation of various polymers such as hyaluronic acid [228], gelatin [229], [230], chondroitin sulphate [231], alginate [232] and poly(glycerol sebacate) [233] (see Table 3). For example, Hoch et al. increased the amount of MAA from a 1.5× molar excess to a 20× molar excess, effectively increasing the DM of gelatin from 68% to 98% [2]. Similar effects were seen in studies by Abbadessa et al. [231] and Jeon et al. [232] where an increased molar excess resulted in increased DM of chondroitin sulphate and alginate, respectively. Pashneh-Tala et al. demonstrated the use of a molar insufficiency of reagents in the methacrylation of poly(glycerol sebacate). A molar insufficiency of 0.3×, 0.5× and 0.8× resulted in 30%, 50% and 80% DM, respectively, implying a 100% efficiency in the methacrylation reaction [233]. Another method of increasing DM is to increase the reaction time. Abbadessa et al. increased the reaction time of Chondroitin sulphate methacrylation from 1.5 hours to 7 days, resulting in a DM increase from 4% to 43% [231].

A combination of methods is often used to drive the reaction and increase DM. Bencherif et al. experimented with the methacrylation of hyaluronic acid. Reaction temperature was decreased from 40°C to 25°C and the amount of glycidal methacrylate was increased from 50× molar excess to 100× molar excess. The carrier solvent was also changed from 100% PBS to 50% PBS/50% dimethylformamide, improving the dissolution of the hyaluronic acid and increasing its availability for the reaction. These three changes resulted in an increase in DM from 14%-90% [228].

The increase in DM of a prepolymer results in an increased crosslinking density in the cured polymer and hence a stiffer material (see Table 3). Bencherif et al. demonstrated a 4-fold increase in shear modulus of methacrylated hyaluronic acid hydrogel as DM was increased from 14-90%. Increased storage modulus and Young's modulus with increasing DM were also demonstrated by Hoch et al. (methacrylated gelatin) and Pashneh-Tala et al. (methacrylated poly(glycerol sebacate)).

The increased crosslinking density (due to increasing DM) also acts to slow the degradation of the crosslinked polymer. Jeon et al. demonstrated this effect with the degradation of methacrylated alginate hydrogels. By increasing DM from 4% to 25% slower degradation was seen with complete mass loss occurring after 5 weeks in compared to 2 weeks [232].

Table 3. A summary of research into controlling the degree of methacrylation (DM) of various polymers. Displayed here are the reaction parameters which were varied, the effect on the DM and resulting properties of the crosslinked polymer. A molar excess of <1x denotes an insufficiency of reagents.

Group	Methacrylated polymer <i>Reaction</i>	Reaction parameters to control DM		Resulting DM	Resulting change in polymer properties
		Variable	Constant		
Hoch et al. [229], [230]	Gelatin methacrylamide <i>Gelatin (G) + methacrylic anhydride (MAA)</i>	Molar excess of MAA: 1.5x -> 20x excess	2-day reaction 40-50°C	68% -> 98%	Higher DM gelatin resulted in stiffer hydrogels, represented by an increased storage modulus e.g. 2x excess: ~31 kPa, 10x excess: ~57 kPa
Jeon et al. [232]	Methacrylated alginate <i>Alginate +2-aminoethyl methacrylate (AEMA)</i>	Amount of AMEA	24 hr reaction Room temperature	4 -> 25%	For DM increase of 4-25%: - Increase in elastic modulus: 43-175 kPa - Slower degradation: 2-5 weeks for complete mass loss (water, 37°C)
Abbadessa et al. [231]	Chondroitin sulphate methacrylate <i>Chondroitin sulphate + glycidal methacrylate (GM)</i>	Molar excess of GM: 0.1x -> 3.2x excess	2-day reaction	8% -> 49%	
		Reaction time: 1.5 hour -> 7 days	1x molar excess	4% -> 43%	
Bencherif et al. [228]	Hyaluronic acid - glycidal methacrylate conjugates <i>Hyaluronic acid (HA) + GM</i>	Reaction temperature: 40°C -> 25°C	50x molar excess 10-day reaction	14 -> 21%	For DM increase of 14-90%: - 4-fold increase in shear modulus from 16 kPa to 65 kPa (Uniaxial compression testing) - Decrease in swelling ratio from 93-27 ($\frac{\text{swollen gel mass}}{\text{dry gel mass}}$)
		Solvent ratio (PBS:DMF): 100:0 -> 75:25	50x molar excess 10-day reaction 25°C	21 -> 32%	
		Molar excess of GM: 50x -> 100x excess PBS:DMF ratio: 75:25 -> 50:50	10-day reaction 25°C	32 -> 90%	
Pashneh-Tala et al. [233]	poly(glycerol sebacate) (PGS) methacrylate <i>PGS + triethylamine (TEA) and MAA</i>	Molar excess of TEA, MAA: 0.3x -> 0.8x excess (insufficiency)	24 hr reaction Room temperature	30 -> 80%	For DM increase of 30-80%: - Increase in Young's modulus: 0.5-7.5 MPa - Increase in ultimate tensile strength: 1-4 MPa - Slower degradation with cholesterol esterase.

2.2.4 Photoabsorbers for stereolithography

Once the photocurable prepolymer is produced, a resin must be formulated for use in stereolithography. We have already discussed the need for photoinitiators and the requirements of some prepolymers to be mixed with a reactive/non-reactive diluent (section 2.2.2). Additionally, a photoabsorber is sometimes included in the resin formulation to absorb UV light and control the depth penetration of the laser. The z-resolution in constructs produced by stereolithography is limited by the laser depth penetration so this must be controlled to produce high quality 3D scaffolds; too high depth penetration results in poor z resolution, i.e. large layer thickness.

Laser depth penetration is determined by the Beer-Lambert law (Equation 1) which states that laser power (I) decreases with depth (l) travelled through the material, at rate determined by the material's absorbance.

$$\text{Beer-Lambert law: } A = \log_{10} \frac{I_0}{I} = \epsilon l c$$

$$\text{Rearranging we get: } I = I_0 \times \frac{1}{10^{\epsilon l c}}$$

Equation 1. The Beer-Lambert Law, describing the absorbance of radiation travelling through a material. Absorbance (A), initial intensity of radiation at surface (I_0), intensity through solution (I), length of solution light passes through (l), concentration of absorber within the solution (c), molar absorption coefficient of absorber (ϵ)

From this equation, if we assume that there is a threshold (critical energy, E_c) at which laser power is too low for polymer curing to be initiated, there will be a depth (l) which corresponds to the laser intensity (I) falling below this threshold. This depth is known as the cure depth (Cd) which was described by Jacobs et al. in 'Fundamentals of Stereolithography' [234] (Equation 2).

$$Cd = Dp \times \ln \left(\frac{E_{max}}{E_c} \right)$$

Equation 2. Cure depth (Cd) is determined by the penetration depth (Dp), critical energy (E_c) and laser power at resin surface (E_{max} , equivalent to I_0 in the Beer-Lambert Law). The Dp is determined by the depth of resin which will reduce the irradiance to $1/e$ (about 37%) of the surface irradiance [234].

From Equation 1 we can see that the absorbance properties of the material (c and ϵ) affect the attenuation rate of the laser light as it passes through the solution. This determines how far the laser can penetrate through the material (the depth penetration, Dp , Equation 2) which in turn influences

the apparent cure depth (Cd) of the system and, by extension, the achievable z-resolution. It then follows that to decrease cure depth in the μ SL system, the absorbance of the prepolymer resin must be increased (in the wavelength range of the light source). This can be done with the addition of photoabsorbers. Referring to Equation 1, increased absorbance can be achieved either by choosing a photoabsorber with an increased molar absorption coefficient (ϵ) or by increasing the concentration (c) of a particular photoabsorber in the prepolymer resin.

There are several photoabsorbers used in literature, however different light sources require photoabsorbers with absorbance peaks at different wavelengths, and resins of different properties require photoabsorbers with different properties to allow dissolution. There is also limited knowledge of the biocompatibility of most available photoabsorbers.

Choi et al. investigated the effect of a popular photoabsorber, Tinuvin 327™, on the cure depth of a monomer resin. As expected, increasing concentration of Tinuvin 327™ (from 0 to 0.15 wt%) in the resin resulted in a decreased depth penetration and a resultant decrease of cure depth (from 200-30 μ m) [235].

Other than well-known photoabsorbers such as Tinuvin™, some groups have used other substances including the food additive, paprika extract (Kalsec Durabrite®) used by Barker et al. in their μ SL system with a 465 nm light source. Without the light absorber, cure depth in the resin was >500 μ m and with the addition of 0.1 and 0.4 wt% paprika extract this was decreased to 254 μ m and 82 μ m, respectively. Higher concentrations of paprika extract resulted in films becoming too brittle to measure due to insufficient crosslinking. This decrease in cure depth allowed the production of complex 3D networks with a gyroid structure, seen in Figure 15. Biocompatibility testing of the paprika extract-containing resins was conducted using bovine intervertebral disc cells similar proliferation rates were seen over 5 days, comparing the crosslinked polymer constructs to a TCP control [236]. Elomaa et al., mentioned previously in section 2.2.2.2, produced similar gyroid structures using Orasol Orange G dye (Ciba Specialty Chemicals) as a photoabsorber in their PCLMA resin. This was chosen for its high absorbance in the wavelength range emitted by light source in the commercial EnvisionTEC stereolithography machine. The gyroid structures had interconnected pores with an average pore size of 465 μ m. Basic biocompatibility testing showed that the PCLMA networks supported fibroblast cell growth but biocompatibility studies were not carried out with dye-containing PCLMA [219].

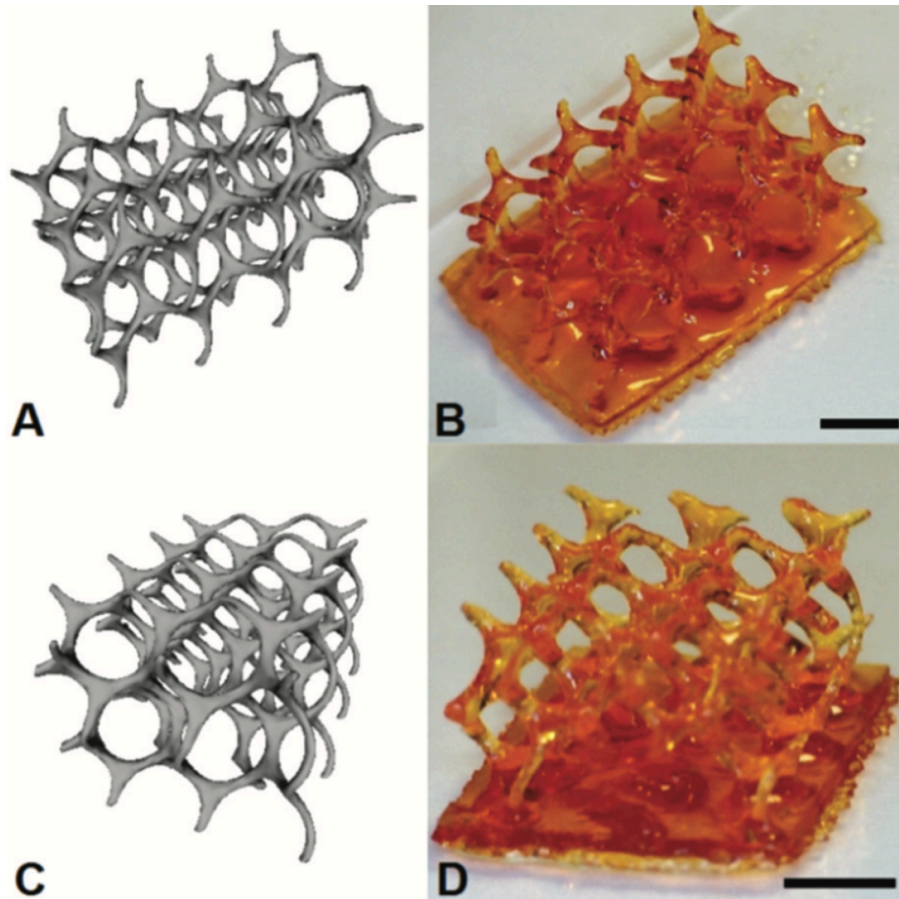


Figure 15. Gyroid structures produced via μ SL by Barker et al. with paprika extract as a photoabsorber A,C: CAD model, B,D: photograph. Scale Bars: 2.5mm. Reprinted from Barker et al. - Published by The Royal Society of Chemistry under a Creative Commons licence [236].

2.2.5 Conclusions from literature

- There is a need for photocurable prepolymer resins for use in stereolithography
- PCL is a biocompatible, biodegradable polymer which can be made photocurable by the addition of methacrylate or other functional groups
- It is possible to vary the degree of methacrylation of a prepolymer to have an effect on the mechanical properties and degradation rate of the cured polymer but no studies to date have altered the DM of PCLMA or assessed the effect of this on material properties
- There is a need for photoabsorbers for use in stereolithography and a variety have been used in previous studies
 - Different photoabsorbers are required for different wavelength light sources and prepolymer resins with different properties
 - Limited data can be found of biocompatibility testing of various photoabsorbers, especially in neural applications

2.3 Aims for this chapter

Develop a tuneable, photocurable prepolymer resin for use in stereolithography and use this to produce NGCs and other 3D structures. To achieve this, the following objectives were addressed:

- 1) Synthesise photocurable PCLMA with varying DM to produce a material with tuneable properties
 - a) Assess the effect of DM on mechanical properties and degradation rate
- 2) Optimise the production of PCLMA NGCs by μ SL
 - a) Find optimal production conditions by investigating the effect of laser power, stage speed and resin temperature
- 3) Identify and optimise the use of a suitable photoabsorber to improve the resolution of PCLMA constructs produced by μ SL
 - a) Assess the suitability of a number of photoabsorbers in terms of light absorption and solubility in prepolymer resins
 - b) Produce 3D structures with photoabsorber-containing resins

2.4 Materials and Methods

All chemicals and reagents used were purchased from Sigma-Aldrich unless otherwise stated.

2.4.1 PCL methacrylation and characterisation

PCL triol was methacrylated to add photocurable functionality and allow its use in μ SL. The following reaction resulted in the addition of methacrylate groups to the terminal hydroxyl groups of the 3-armed PCL molecule. Methacrylation was confirmed by nuclear magnetic resonance spectroscopy.

2.4.1.1 Synthesis of poly(caprolactone)-methacrylate prepolymer

PCL triol (M_n : 900 g/mol) was reacted with methacrylic anhydride (MAA) in the presence of triethylamine (TEA) to produce poly(caprolactone)-methacrylate (PCLMA) (see Figure 16 for reaction scheme). The molar ratio of the three reactants was varied along with the reaction time to control the degree of methacrylation in the resultant PCLMA. For example, for a 2 \times molar excess reaction: 1 molar equivalent PCL triol (e.g. 30 g) was dissolved in dichloromethane (DCM, Fisher Scientific) and added to a 3 necked flask along with 6 molar equivalent TEA (20.02 g). The reagents were continually stirred and the flask cooled over ice. The flask was fitted with a dropping funnel, a nitrogen inlet and a condenser and was purged with nitrogen prior to the reaction. 6 molar equivalent MAA (30.8 g) was added dropwise and the reaction was left stirring for 1-5 days (depending on the degree of methacrylation required) in dark conditions, under nitrogen. The resulting PCLMA solution was washed 3 times with 1 M hydrochloric acid (Fisher Scientific), separating in a separating funnel after each wash. This was followed by 2 washes with deionised water. The solvent was then removed from the PCLMA by rotary evaporation. The resulting prepolymer was purified by washing in methanol; PCLMA was shaken with methanol and separated overnight at -80°C . The methanol was removed and new methanol added to repeat this washing step 3-4 times. The final methanol was removed and any left-over solvent was removed by rotary evaporation until constant weight was reached.

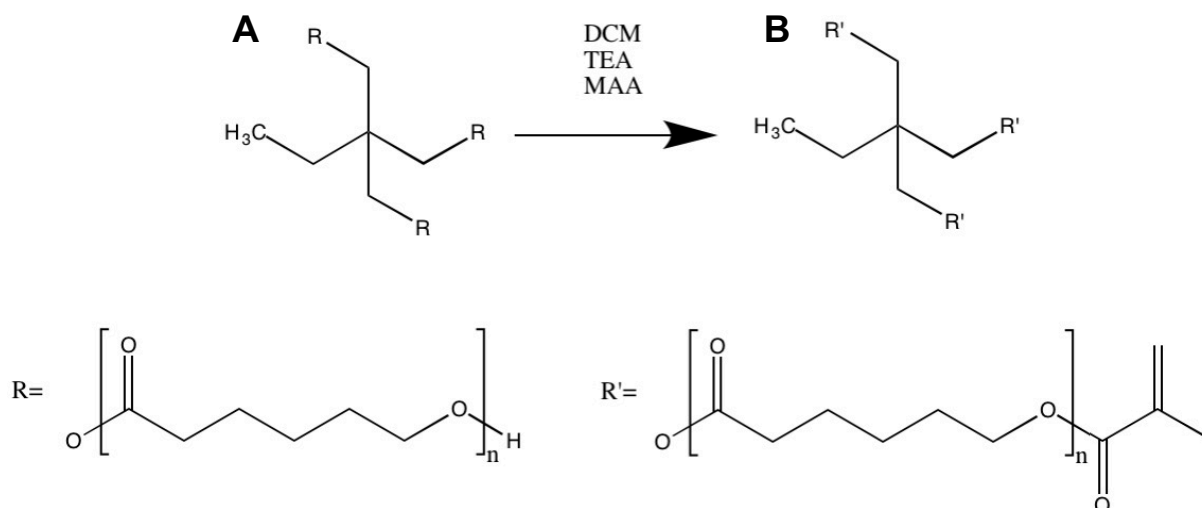


Figure 16. PCL methacrylation reaction scheme. PCL triol (A) dissolved in DCM, was reacted with MAA in the presence of TEA to produce three-armed PCLMA (B).

2.4.1.2 Nuclear magnetic resonance (NMR) spectroscopy

Proton NMR was performed to allow calculation of the DM of the PCLMA i.e. the percentage of end groups (OH) in the PCLMA molecules, substituted with methacrylate groups. This indicates the number of end groups that are able to be involved in cross linking reactions to form polymer networks on photocuring. 20 mg samples of PCLMA prepolymer were placed in 5 mm NMR tubes and solvated with 0.5 ml of deuterated chloroform. The samples were analysed in a Bruker AV3HD-400 NMR spectrometer at 400 Hz at room temperature.

2.4.2 Prepolymer resin preparation

Photocurable PCLMA resin for UV curing applications was produced by the addition of 2 wt% photoinitiator to the PCLMA prepolymer. The photoinitiator used was a 50:50 blend of diphenyl(2,4,6-trimethylbenzoyl)phosphine oxide and 2-hydroxy-2-methylpropiophenone. Mixing was achieved using a vortex mixer followed by sonication for 10 minutes.

For some of the following experiments, photocurable poly(ethylene glycol)-diacrylate (PEGDA) resins were used and these were prepared in the same way, using PEGDA (M_n : 700 g/mol) in place of the PCLMA.

2.4.3 Mechanical testing of cured PCLMA

Tensile mechanical testing was performed on photocured PCLMA specimens to determine the effect of DM on the mechanical properties of the material.

2.4.3.1 PCLMA dog bone production

PCLMA 'dog bones' were prepared to specifications adapted from ASTM D638 - 14 'Standard Test Method for Tensile Properties of Plastics' type V specimen (see Figure 17). Dog bone test pieces were printed to the defined specifications using a commercially available stereolithography printer (Form 1, Formlabs). The printed pieces were used to produce negative polydimethylsiloxane (PDMS) moulds for the production of PCLMA dog bones as follows. Silicone prepolymer (Sylgard 184, DOW Europe GmbH) was mixed thoroughly with curing agent at a ratio of 10:1 and centrifuged at 1000 rpm for 5 mins to remove air bubbles (centrifuge rotor radius (r_{\max})=155 mm). The printed dog bones were glued to the bottom of petri dishes and the silicone was poured into the dish to fully cover the printed part. The petri dishes were placed under vacuum to remove any remaining air bubbles before curing at 60°C for 2 hours. The cured PDMS was then removed from the petri dish to reveal the mould used to cure the PCLMA dog bones. PCLMA resins were prepared according to section 2.4.2 using PCLMA of varying DM. PCLMA resin was dispensed into the PDMS mould and excess resin scraped away to leave a flat surface. Resin-filled moulds were placed under a UV lamp (OmniCure S1000, Exfo) for 1 minute at 30% power before increasing to 100% power for a further 4 minutes. Samples were then flipped and cured for a further 5 minutes at full power to ensure even curing of both sides. Cured constructs were removed from the moulds, briefly washed in methanol and left to dry overnight before mechanical testing.

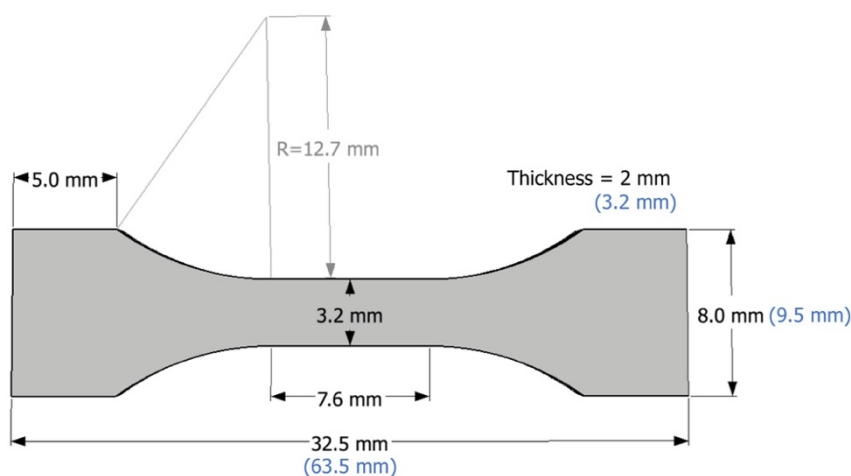


Figure 17. Specifications of the 'dog bone' tensile test piece adapted from the ASTM D638 - 14 'Standard Test Method for Tensile Properties of Plastics' Type V specimen. For those dimensions that were altered from the original specifications, the original specifications are displayed in blue.

2.4.3.2 Tensile testing of PCLMA dog bones

Tensile testing was performed using an EnduraTEC ELF 3200 load frame system (Bose Ltd) with a 450 N load cell. Dog bone test pieces were placed vertically, secured between grips with an initial separation of 22.5 mm (see Figure 18). A strain rate of 0.1 mms^{-1} was applied to the samples until either failure occurred, or the grips began to slip due to insufficient friction between the grips and the test piece. Force-displacement data was obtained and converted to stress-strain measurements using the individual test piece dimensions. The linear region of each individual stress-strain curve was selected (see Figure 24B) and linear regression analysis was carried out with Prism (GraphPad) to calculate the gradient, representing the Young's modulus of the material. 4-7 samples of each PCLMA resin were tested to obtain average values of the Young's modulus of each material ($n=4-7$).

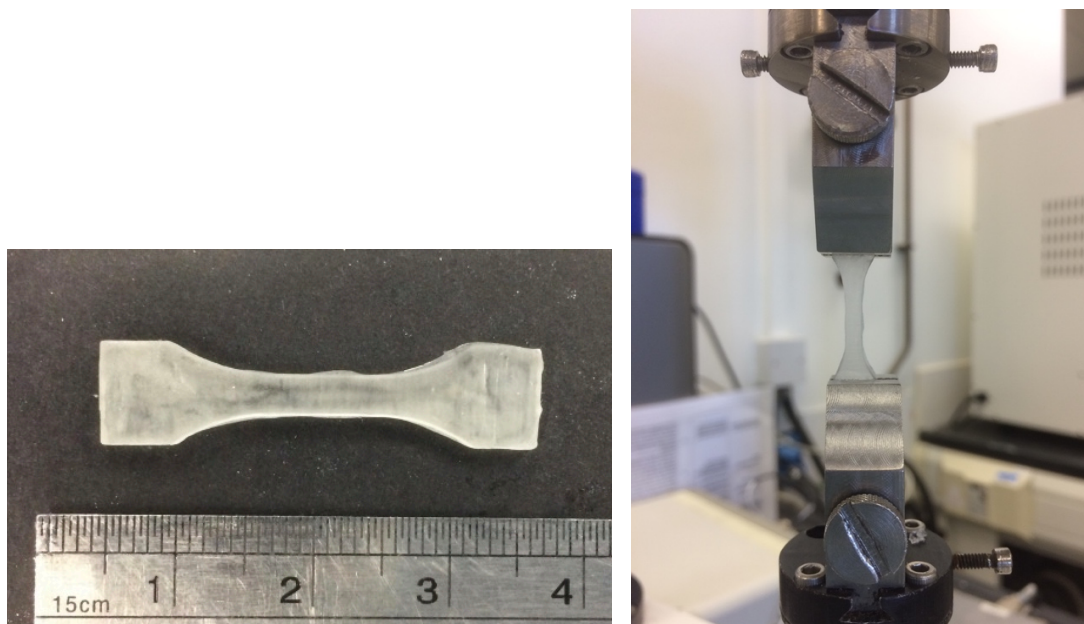


Figure 18. PCLMA tensile testing. A: Cured PCLMA dog bone. B: The dog bone held in place between the grips of the BOSE Electroforce 3200 prior to mechanical testing.

2.4.4 Soluble fraction calculation of cured PCLMA

Cured PCLMA was solvated in DCM to dissolve the uncured prepolymer resin, not incorporated into the polymer network on photocuring. The soluble fraction of the cured PCLMA could then be calculated. PCLMA resins were prepared as described in section 2.4.2. Polymer discs (4 mm diameter, 1.3 mm thickness) were cured in PDMS wells by dispensing resin into the mould, scraping away excess resin and curing under the UV lamp at 30% power for 1 minute followed by 4 minutes at 100% power. The samples were flipped and cured for a further 5 minutes at 100% power. Cured discs were placed under vacuum for 2 hours to remove any residual solvent and weighed ($m_{initial}$). The discs were then washed in DCM for 5 days to swell and remove any uncured prepolymer. The samples were then removed from the solvent, dried under vacuum and weighed again (m_{final}). The difference between the start and end weights was used to calculate the soluble fraction of the cured constructs (Equation 3). The experiment was performed in triplicate (n=3).

$$\text{Soluble fraction (\%)} = \frac{m_{initial} - m_{final}}{m_{initial}} \left(\frac{\text{polymer removed during solvation}}{\text{total polymer}} \right) \times 100$$

Equation 3. Calculation of the soluble fraction of cured PCLMA.

2.4.5 Degradation study

A degradation study was performed in sodium hydroxide (NaOH) to simulate accelerated hydrolysis and used to compare the degradation rates of the PCLMA with different degrees of methacrylation. Cured PCLMA discs were prepared as in section 2.4.4 using PCLMA resins of varying DM and washed in DCM for 5 days to remove the soluble fraction. Additional discs of commercially available PCL were produced for comparison. PCL pellets (M_n 80 000 g/mol, Sigma-Aldrich) were placed in silicone moulds and heated in an oven to 100°C for 1 hour to melt the PCL. Moulds were removed from the oven and excess molten PCL was scraped from the top of the mould using a hot scalpel knife. PCLMA and PCL discs were dried under vacuum and individually weighed before placing each disc in the well of 6-well plate with 7 ml of 5 M NaOH. The well plates were placed on a rocker for the duration of the study. Samples were removed from NaOH at timepoints of 5-21 days, washed three times in PBS and dried under vacuum. Discs were then weighed and each disc was compared to its individual start weight to calculate the percentage weight remaining. The experiment was performed in triplicate (three samples were used per timepoint, n=3) with separate samples for each time point.

2.4.6 Microstereolithography for scaffold production

PCLMA and PEGDA resins were prepared according to section 2.4.2 and used in μ SL to produce scaffolds of a variety of designs.

2.4.6.1 The microstereolithography set-up

An in-house built μ SL set up (modified from that described by Pateman et al. [128]), displayed in Figure 19 was used to fabricate polymer constructs from the PEGDA and PCLMA prepolymer resins. This consisted of a 405 nm violet laser (Vortran Stradus, Vortran Laser Technology Inc) which was passed through a series of beam-expanding optics to reflect off a DMD (DLP® 0.7" XGA, Texas Instruments Inc). The reflected image (scaffold cross-section) was passed through a set of focussing optics and focused on the platform of a one-axis motorised translation stage (Thorlabs Ltd). The stage was controlled by computer software (APT Software, Thorlabs Ltd) allowing precisely controllable, micrometre adjustment in the z direction. A vial of photocurable prepolymer resin was placed under the stage with the level of the resin matching the level of the stage at the focal point of the projected image.

2.4.6.2 DMD image production

DMD images for tube production consisted of simple circles (Figure 19, inset) and were created using MATLAB (MathWorks) to allow for precise control over dimensions such as internal diameter and wall thickness. DMD images for grooved channel production (e.g. section 2.4.7.3) were adapted from these using Preview (Apple Inc). All DMD images were raster format consisting of 1024×768 pixels to match the number of micromirrors on the DMD (see section 1.4.3).

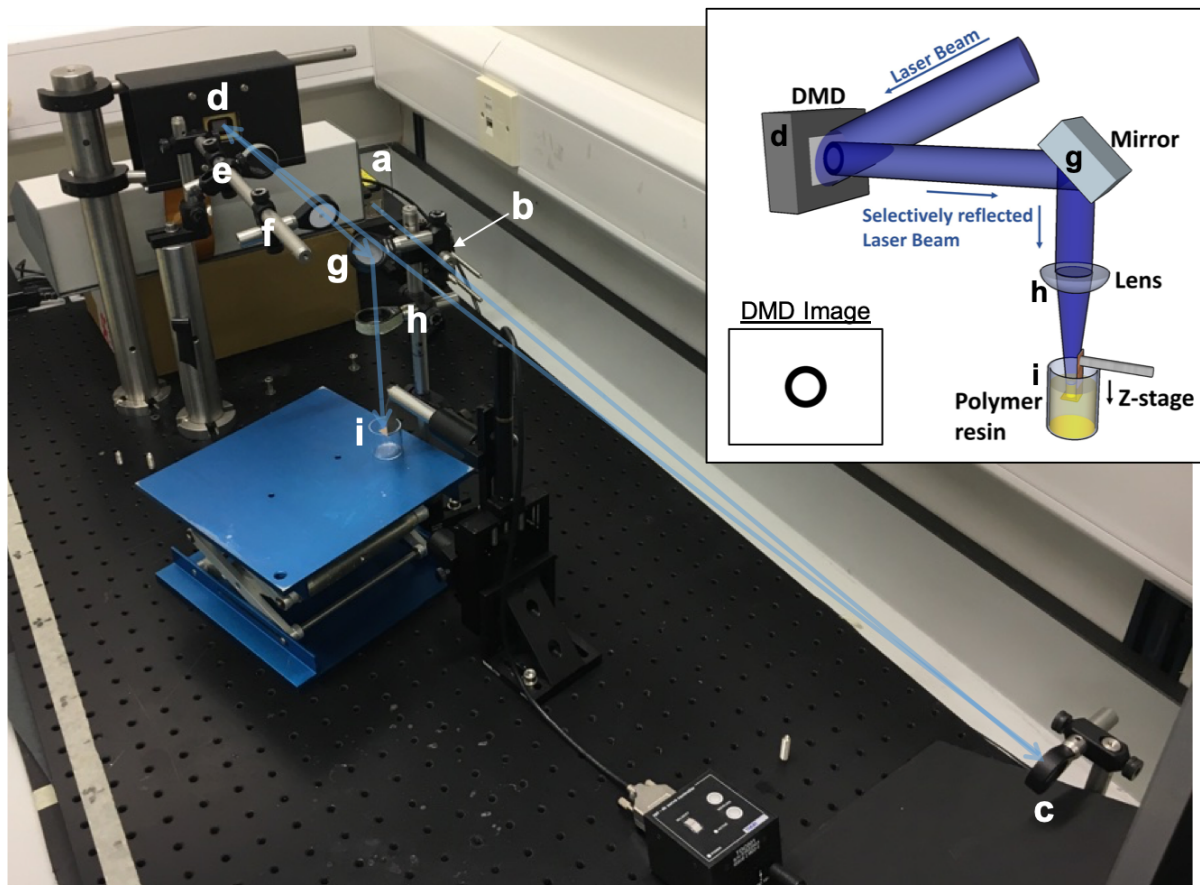


Figure 19. The microstereolithography (μ SL) set-up. **Inset:** Schematic of the set-up. An expanded laser beam hits the DMD which selectively reflects the laser beam in the shape of the desired image which is focused on the surface of a vial of prepolymer resin. Example DMD image shown for use in tube production. **Main image:** The experimental μ SL set-up. A laser beam from source (a) is passed through a spatial filter (b) and reflected off a mirror (c) towards a DMD (d). The selectively reflected image from the DMD is passed through a 25 cm focal length lens (e) followed by an iris (f) to remove multiple images caused by diffraction. The image is then reflected down by a second mirror (g) and focused by a 10 cm focal length lens (h) onto the stage in the vial of prepolymer resin (i). The blue arrow illustrates the laser beam path.

2.4.6.3 2.5D structure fabrication

The μ SL set up was used to produce structures (e.g. tubes) with a uniform cross-section along their length and these were described as 2.5-dimensional (2.5D) structures. A cross-sectional image of the tube was uploaded onto the DMD so that when the laser was turned on, the cross-sectional image was projected onto the stage at the surface of the prepolymer resin, curing the first part of the structure and attaching it to the stage. The stage was set to descend and the prepolymer continually cured at the surface while the surrounding resin flowed over the cured structure. This formed a tube with the cross-section of the uploaded image. Laser powers of 10-40 mW were used with stage

speeds of 0.03-0.005 mms^{-1} . These two parameters were balanced to produce tubes of a high quality.

2.4.6.4 3D structure fabrication

3-dimensional (3D) structures with non-uniform cross-sections (e.g. bifurcated tubes) were created by the same process as 2.5D tubes, however the image displayed on the DMD was changed as the stage descended. The 3D tube was designed in CAD software (SolidWorks) and 'sliced' to produce images of the tube cross-section at sequential positions through the structure (Figure 20A). These multiple images were uploaded onto the DMD and as the stage descended the images were displayed in sequence to correspond the shape of the current cross-section being cured. The layer thickness of the structure was determined by the time that each image was displayed for and the speed of the stage. This process is described in Figure 20.

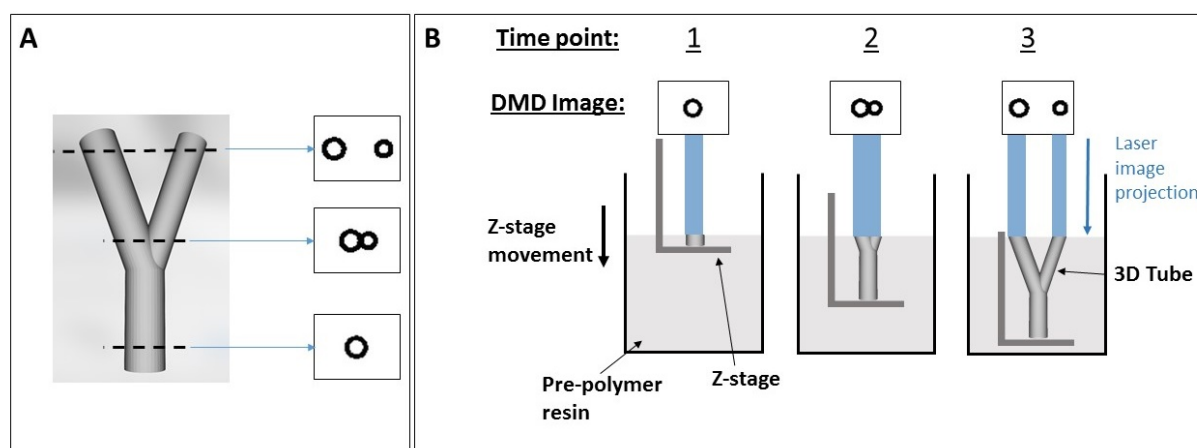


Figure 20. Production of 3D structures via microstereolithography. A: 3D bifurcated tube designed in SolidWorks and 3 example cross-sectional images obtained from the 'slicing' process. B: The process of curing a 3D tube by sequentially displaying the cross-sectional images on the DMD. (3 arbitrary time points shown.)

2.4.6.5 The effect of prepolymer resin temperature on the μ SL process and tube quality

It was thought that increasing the temperature of the prepolymer resin during the curing process may decrease its viscosity, allowing it to flow more easily over the descending stage and subsequently improve the quality of the cured structures. To investigate this, the same set-up as in Figure 19 was used to produce simple tubes, however, the vial of prepolymer resin was placed in a heated water bath, maintained at a constant temperature of 60°C.

2.4.6.6 Scaffold post-production

After production of by μ SL, the construct was removed from the stage and washed in isopropanol (IPA) to remove any uncured prepolymer resin and unreacted photoinitiator. If the scaffold was to be used *in vitro* (chapter 4) or *in vivo* (chapter 5) IPA washing was carried out for at least 1 week with regular changes. This is an important step as it has been previously found that long-term washing of photocured polymer structures increases cell viability [202].

2.4.6.7 Imaging of μ SL structures

To determine the quality of the structures produced by μ SL, samples were imaged by optical microscopy (Stemi 305, Zeiss, equipped with AxioCam 105 camera) or scanning electron microscopy (SEM) (Inspect F50, FEI). Prior to SEM imaging, tubes and other structures were sputter coated with gold (SC500, Emscope). All measurements from optical microscopy and SEM images were carried out in ImageJ (NIH).

2.4.7 Investigation of photoabsorber use in μ SL

2.4.7.1 Addition of photoabsorbers to PCLMA and PEGDA resins

Photoabsorbers were added to the prepolymer resins to reduce the laser depth penetration and consequently improve the z-resolution in the fabricated structures. The photoabsorbers investigated were beta-carotene, Alizarin Red S (Alizarin Red) and Riboflavin. The aim was to produce a PCLMA resin with decreased cure depth but the ready availability of PEGDA made it a useful material for testing the effect of these photoabsorbers before moving on to using PCLMA. Photoabsorbers were added to PEGDA and PCLMA prepolymers at varying concentrations (up to 1%) depending on their solubility and stirred until homogeneous. The photoabsorber was deemed soluble if it fully dissolved in the prepolymer to produce a coloured but translucent solution. Particulates left in solution due to non-solubility or saturation caused scattering of light to produce an opaque, cloudy solution.

PEGDA resins containing the three photoabsorbers were used in the μ SL set-up to produce 3D structures to assess the effect of the photoabsorbers on laser depth penetration and cure depth. Due to the hydrophobic nature of the PCLMA, it was only possible to produce a solution with beta-carotene so this was the only photoabsorber used. To fully dissolve the beta-carotene, it was stirred with the PCLMA for 1 hour at 60°C.

2.4.7.2 Evaluation of photoabsorber suitability by analysis of absorbance spectra

UV-VIS spectrometer (Perkin Elmer Lambda 900) was used to measure the absorbance spectra of the photoabsorbers to determine the absorbance at 405 nm. The 3 photoabsorbers were mixed into PEGDA at concentrations that were low enough for the absorbance values of the solutions to fall within the dynamic range of the spectrometer. The samples were measured in the range 300-600 nm against a reference vial of PEGDA to obtain the absorbance spectra of the photoabsorbers.

2.4.7.3 Evaluation of photoabsorber suitability by analysis of laser depth penetration

Intermittently-grooved channel constructs (Figure 21A) were produced from PEGDA and PCLMA by μ SL. The DMD image was altered between a smooth channel and a grooved channel (Figure 21B,C) with each image being displayed for the same duration. With minimal depth penetration of the laser light, the prepolymer would only be cured at the surface of the resin and a channel would be produced with equal strut length and gap length. However, with increased laser depth penetration, the light from the grooved image (Figure 21C) will penetrate too deep and cure grooved constructs where the channel should be smooth (Figure 21D). The structures were imaged with optical microscopy (section 2.4.6.7) and the lengths of the struts and gaps were measured to calculate a ratio, 'strut length:gap length'. The closer this ratio was to 1, the lower the laser depth penetration and therefore the better performance (higher absorbance) of the photoabsorber.

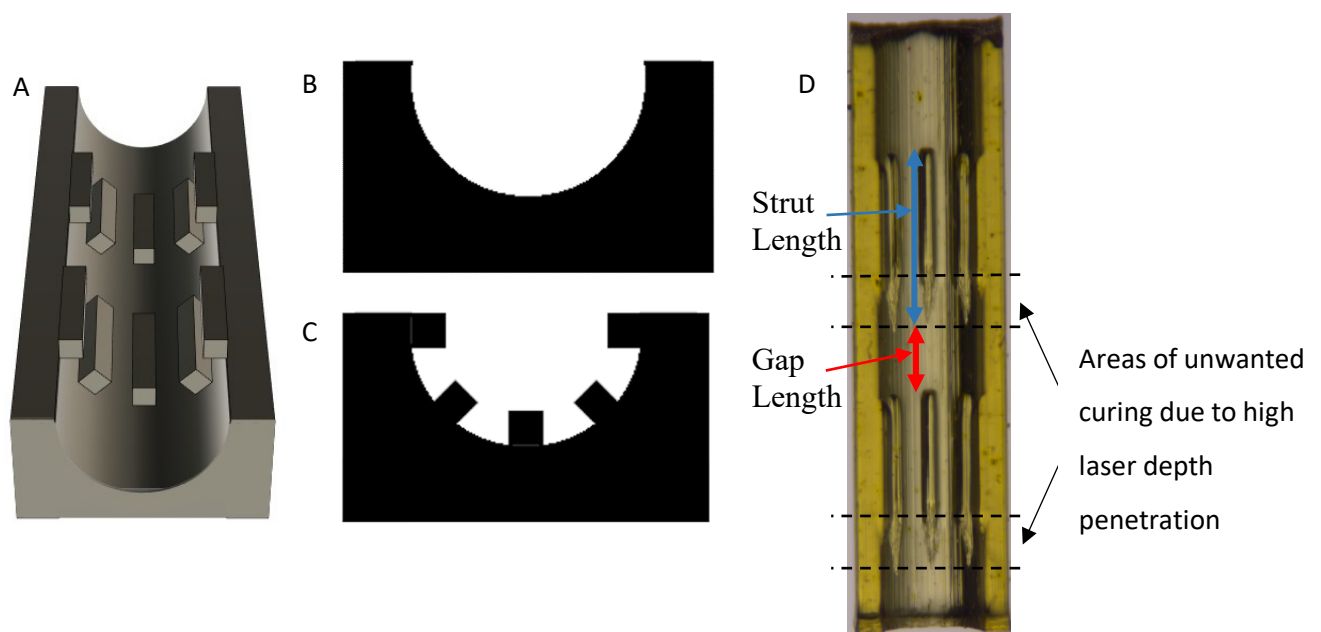


Figure 21. Intermittent grooved channels. A: model of a channel with intermittent grooves fabricated by alternating the DMD image between a smooth channel cross-section (B) and a grooved channel cross-section (C). D: an example construct produced with high depth penetration and example measurements of strut length and gap length (optical microscopy image).

2.4.8 Statistical analysis

Statistical analysis was performed with GraphPad Prism. Data was tested for normality using Shapiro-Wilk normality test and found to be normally distributed. To test for significant differences between groups, ANOVA was used, followed by Tukey's multiple comparison tests. For data affected by one factor, one-way ANOVA was used and for data affected by two factors, two-way ANOVA was used. $P < 0.05$ was used to determine a statistical difference. All data is presented as mean \pm standard deviation (SD). Sample sizes are presented as N=experimental repeats, n=replicates per experiment i.e. N=1, n=3 signifies an experiment performed once in triplicate.

2.5 Results

2.5.1 PCL methacrylation and characterisation

2.5.1.1 Determination of methacrylation with NMR spectroscopy

Unmethacrylated PCL triol and PCLMA prepolymer samples were analysed by proton NMR spectroscopy. Figure 22 shows example spectra of PCL triol and PCLMA with varying degrees of methacrylation. The spectra peaks were identified with the help of a previous publication by Elomaa et al. on PCL triol methacrylation [219]. These are displayed in Figure 22, with the corresponding hydrogen environments labelled on the molecule diagrams. The position of the peaks representing the methacrylate group was confirmed by other sources [228], [237]. The appearance of the peaks *i* (6.09 ppm), *j* (5.55 ppm), *k* (1.93 ppm) and *a''* (4.14 ppm) confirmed the presence of the methacrylate groups in the PCLMA. These peaks increased in size with increasing DM of the prepolymer sample. The decrease in size of the *a'* peak (3.64 ppm) indicates that the OH group from the original PCL triol molecule had become less prevalent in the reaction products, showing that these OH groups had been substituted for methacrylate groups.

For quantitative analysis, the *i*, *j* and *a''* peaks were integrated with the *h* peak (0.88 ppm) set as a reference, equal to 3 protons. This is a reliable reference peak as it represents the three protons in environment *h* which have no nearby electronegative bonds, so peak splitting is unlikely. As we tend towards 100% methacrylation we should see the complete disappearance of the *a'* peak and the growth of the *a''* peak integral, tending towards 6 protons. The summation of the *i* and *j* peak integrals should also tend towards 6 protons.

In short, for 100% methacrylation the following should be true:

$$\int i + \int j = \int a'' = 6, \quad \int a' = 0$$

For quantitative analysis of DM the following calculation was used:

$$DM = \frac{\frac{\int i}{\int i_{100\%DM}} + \frac{\int j}{\int j_{100\%DM}} + \frac{\int a''}{\int a''_{100\%DM}}}{3} = \frac{\frac{\int i}{3} + \frac{\int j}{3} + \frac{\int a''}{6}}{3}$$

Equation 4. Calculation of the degree of methacrylation (DM) of PCLMA from the integral of peaks *i* (6.09 ppm), *j* (5.55 ppm) and *a''* (4.14 ppm) in the NMR spectra (Figure 22).

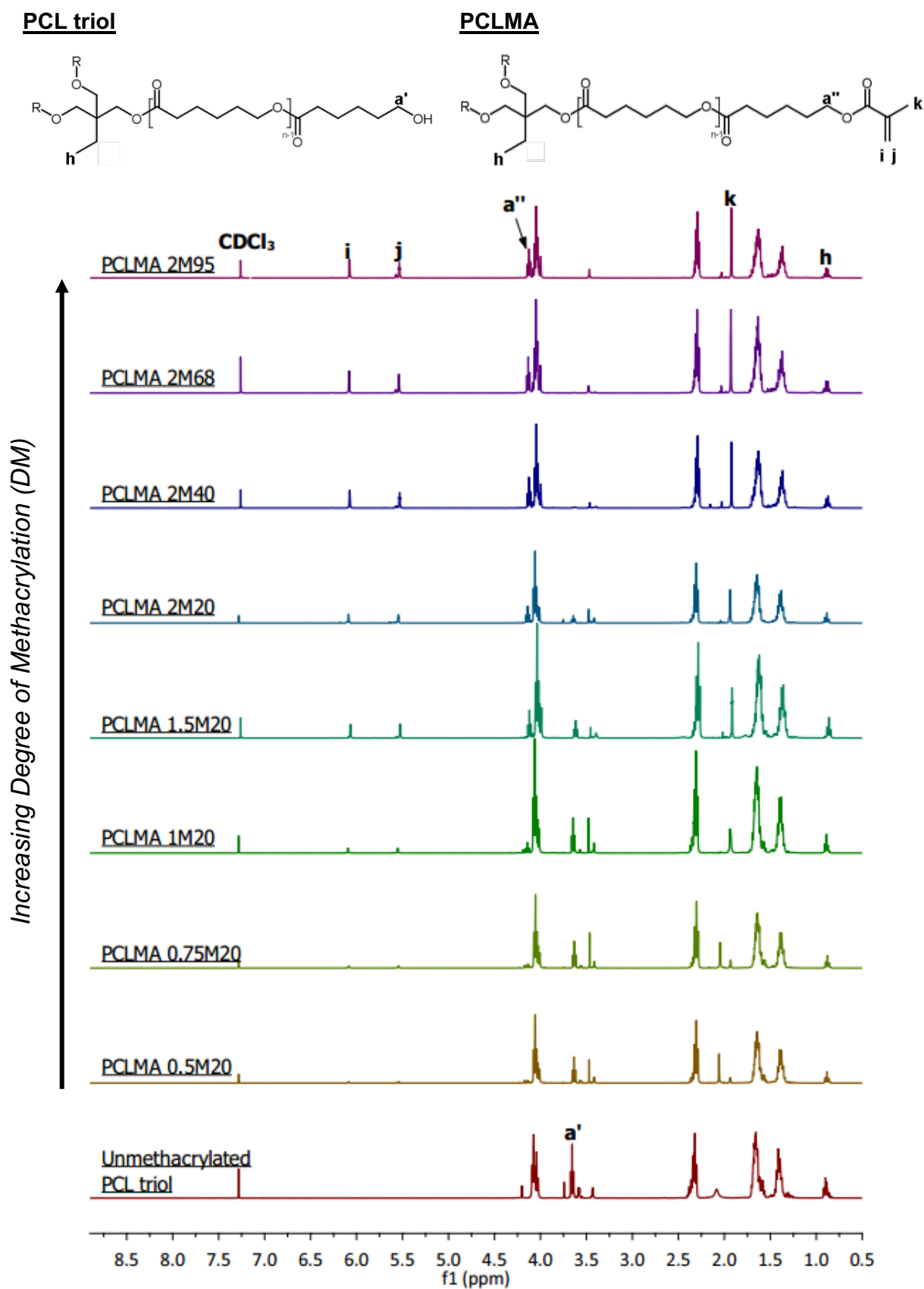


Figure 22. Proton NMR spectra of unmethacrylated and methacrylated PCL triol. The PCL triol and PCLMA molecule diagrams are displayed (top) with the hydrogen environments labelled (a' , a'' and $h-k$) corresponding to the relevant peaks in the NMR spectra used to determine degree of methacrylation. a'' , i , j and k are present only in methacrylated PCL and the size of these peaks increases with increasing DM.

2.5.1.2 The effect of reaction parameters of the degree of PCL methacrylation

Notation for reaction parameters

The following results describe a series of reactions which aimed to produce PCLMA prepolymer with a range of DM by varying the reaction time and the molar ratio of the reactants. Per 1 mole of PCL triol, 3 moles of TEA and MAA are required to provide enough reactants to produce a methacrylate group on each of the three arms of the PCL molecule. This will be described as a 1:1 reaction ratio (1M). The reaction was also carried out with either an insufficiency or an excess of MAA and TEA to reduce/increase the concentration of the reactants, altering the reaction rate and the resulting DM. For example, a 2× excess in the molar ratio would require 1 mole of PCL and 6 moles of MAA and TEA, defined as a 1:2 reaction ratio (2M). The reaction time was also varied from 20-95 hours. The reactions/products were named according to these two conditions (see Table 4) i.e. 2M20 refers to a 1:2 reaction with a 20 hour duration.

The effect of Molar concentration and reaction time on degree of methacrylation

As described in Table 4, methacrylation reactions were carried out where the reaction ratio was varied from 1:0.5 (providing half the reactants required for full methacrylation, 0.5M) to 1:2 (a 2× molar excess in the required reactants, 2M). The reaction time was kept constant at 20 hours. As we can see in Figure 23A, increasing the excess of TEA and MAA in the reaction resulted in a linear increase in the DM from 8% to 47% (0.5M and 2M reactions respectively). To increase the DM further, the reaction time was increased to give more time for the methacrylation to occur. 2M reactions were carried out for 20, 40, 68 and 95 hours. Figure 23B shows that the increasing the reaction time in this range resulted in an increased DM from 47% to 77%. However this was not a linear increase that we see in Figure 23A but increases with an exponential decay. This is to be expected – as time progresses the reagents are used up in the reaction so a smaller amount of the reagents remain and the reaction rate slows.

Table 4. Reaction parameters used to produce PCLMA and the resulting degree of methacrylation (DM). DM was altered by varying the molar ratio of reactants and the reaction time. $N=1$, $n=1$, except for 2M20 where $N=3$, $n=1$ so mean \pm SD shown only for 2M20.

	Notation	Reaction ratio (Mol of PCL: Molar excess of MAA/TEA)	Moles of MAA/TEA per 1 Mole of PCL	Reaction Time	Resulting Degree of Methacrylation
Varying reaction ratio	0.5M20	1:0.5	1.5	20 hours	8%
	0.75M20	1:0.75	2.25	20 hours	11%
	1M20	1:1	3	20 hours	17%
	1.5M20	1:1.5	4.5	20 hours	39%
	2M20	1:2	6	20 hours	47 \pm 2%
Varying reaction time	2M20	1:2	6	20 hours	47 \pm 2%
	2M40	1:2	6	40 hours	66%
	2M68	1:2	6	68 hours	73%
	2M95	1:2	6	95 hours	77%

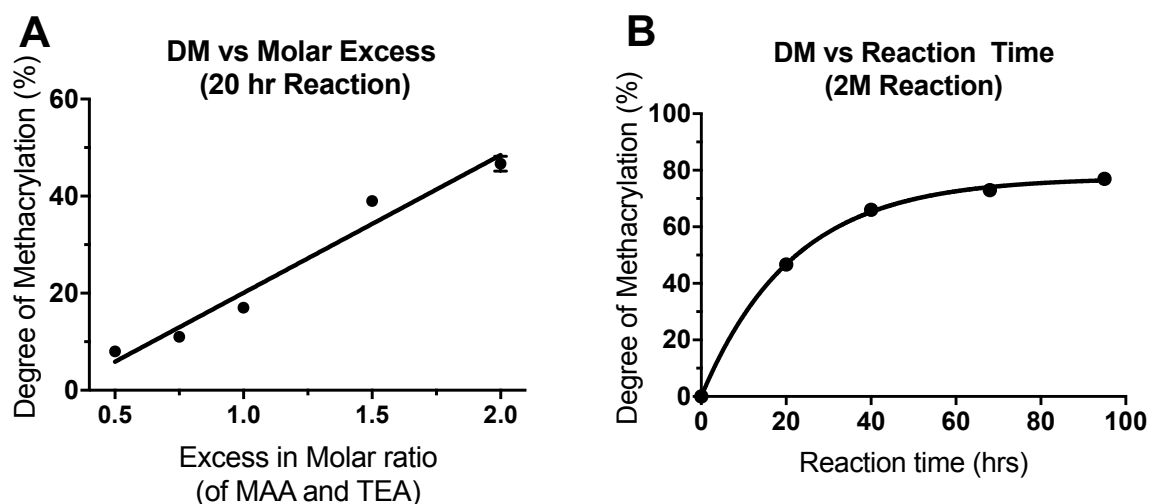


Figure 23. PCLMA produced with varying degree of methacrylation (DM). DM was altered by A: varying the molar ratio of reactants (linear regression curve fitted, $R^2=0.96$) and B: varying the reaction time (one phase decay curve fitted, $R^2=0.99$). $N=1$, $n=1$, except for 2M20 where $N=3$, $n=1$ so mean \pm SD shown only for 2M20 (error bars are too small to be seen in B).

2.5.1.3 Effect of the degree of methacrylation on the mechanical properties of cured PCLMA

PCLMA prepolymer of varying DM was photocured into dog bone test-pieces and tested under tensile conditions. Photocuring of PCLMA was only possible with prepolymer of a high enough DM. The two PCLMA batches below 17% DM (0.5M20 and 0.75M20) did not form bulk, solid structures when photocured but formed a more gel-like consistency. An example set of stress strain curves from the cured 2M20 PCLMA samples can be seen in Figure 24A. Young's modulus was calculated from the linear region of each sample's stress-strain curve (Figure 24B). There was low variation in the Young's Modulus calculated from the samples, evident from the similar slopes in Figure 24A and the small standard deviations in Figure 25A. On the other hand, the ultimate tensile strength varied quite considerably between each sample. It is thought that early failure occurred in some samples due to the concentration of stresses around imperfections such as small bubbles in the cured test pieces or microfractures created at the point where the grips were tightened to the sample ends. For PCLMA test-pieces of higher DM, slipping of the grips usually occurred before failure of the material. Slipping could be reduced by tightening the grips but overtightening caused cracking of the PCLMA constructs. Therefore, grips were tightened enough to allow an accurate calculation of Young's modulus with the sacrifice of not being able to calculate ultimate tensile strength.

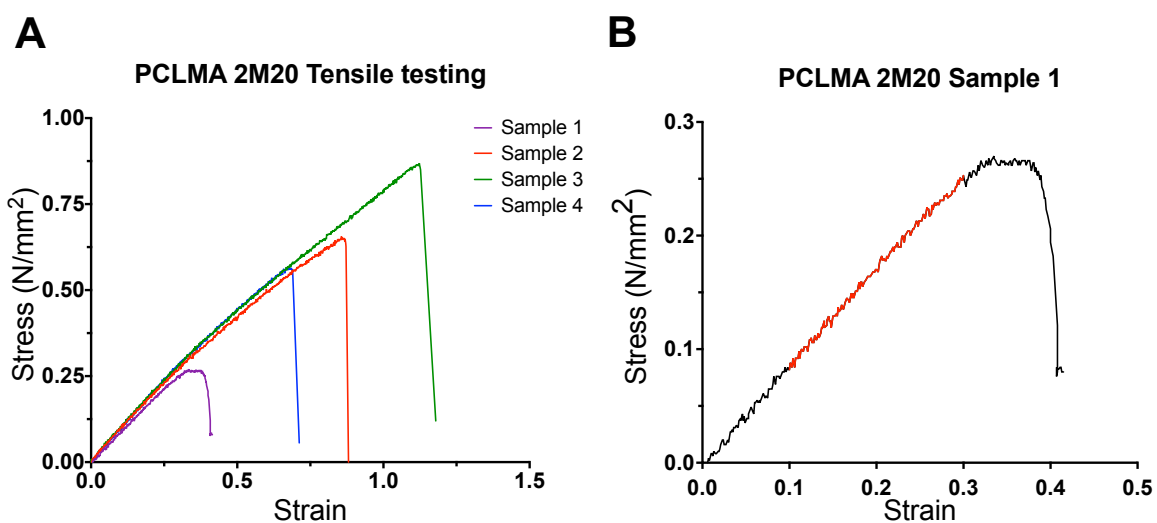


Figure 24. Mechanical testing of cured PCLMA. A: Stress-strain plots from 4 separate PCLMA samples (2M20). B: Stress-strain plot from sample 1. Highlighted in red: linear region used for calculation of Young's Modulus.

Comparing the Young's modulus of the different cured PCLMA samples, we see an increase of Young's Modulus with increasing DM (Figure 25A). A comparison of typical stress-strain plots of each PCLMA type is displayed in Figure 25B. This result is as we expect, as increasing the number of methacrylate groups in the PCLMA allows for a greater degree of crosslinking in the cured product and therefore results in a stiffer material. We can see an almost 30-fold increase in Young's modulus from 0.12 ± 0.20 MPa to 3.51 ± 0.25 MPa (in the 17% and 77% DM PCLMA, respectively). The difference in Young's modulus between each group of PCLMA was statistically significant ($P \leq 0.005$), except for 1.5M20 vs 2M20 (39% and 47% DM, respectively) (one-way ANOVA with Tukey's multiple comparisons).

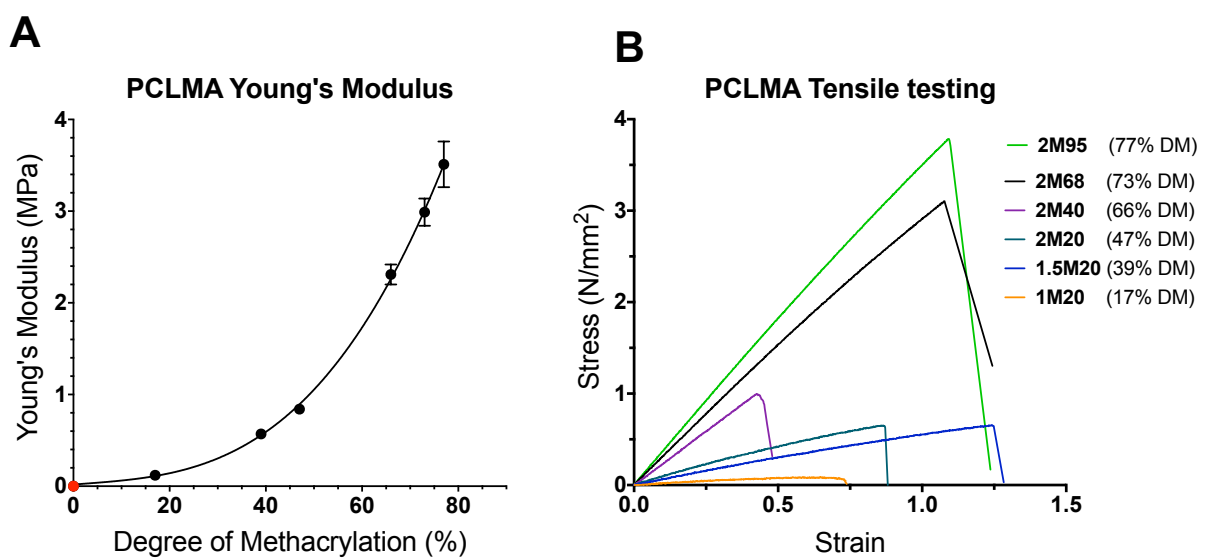


Figure 25. The effect of the degree of methacrylation on the Young's Modulus of cured PCLMA. A: The Young's modulus of cured PCLMA plotted against the degree of methacrylation of the prepolymer ($N=1$, $n=4-7$). Values displayed mean \pm SD. (N.B. The SD in the 17% 39% and 47% DM is too small for the error bars to be visible.) The point in red signifies a theoretical (0,0) representing a 0 MPa Young's Modulus for 0% DM PCLMA (since curing of solid structures to test under tensile loading is not possible). Cubic polynomial regression curve fitted ($R^2=0.99$). B: A comparison of the stress-strain plots of each variant of PCLMA. One stress-strain plot (representing a typical sample) was taken from each group for the sake of comparison.

2.5.1.4 Effect of degree of methacrylation on PCLMA soluble fraction

Cured PCLMA of varying DM was solvated in DCM to dissolve any uncured prepolymer. Samples were weighed before and after solvation to measure the soluble fraction of the cured material. Increasing the DM of the PCLMA prepolymer led to a decrease in the soluble fraction of the cured PCLMA (seen in Figure 26) as a greater percentage of molecules are incorporated into the network. The least methacrylated PCLMA (17% DM) had a soluble fraction of $53.1 \pm 2.1\%$ but this dropped to $0.6 \pm 0.8\%$ as DM increased to 77%.

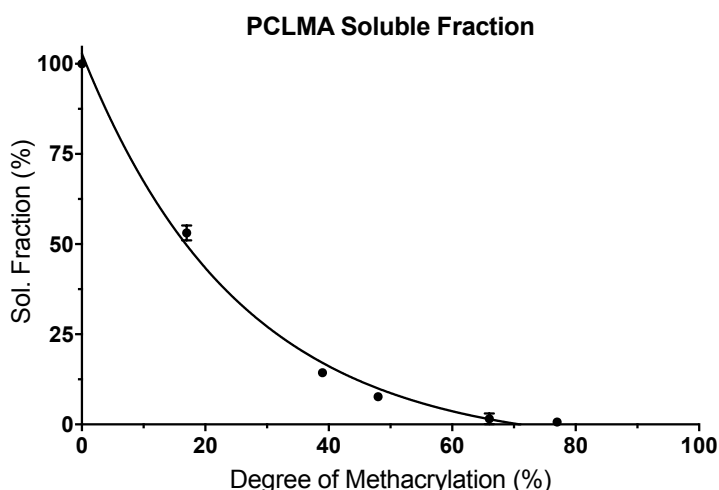


Figure 26. The effect of degree of methacrylation on the soluble fraction of cured PCLMA. Values displayed mean \pm SD (some SD values are too small for error bars to be visible). N=1, n=3.

2.5.1.5 Effect of degree of methacrylation on PCLMA degradation

Cured PCLMA with different DM was degraded using NaOH and compared to commercial, non-photocurable PCL. The results are displayed in Figure 27. Over the course of the study, there was no significant degradation of the commercial PCL with $99.0 \pm 1.1\%$ still remaining after 21 days. Degradation was also very low for the 2M95 and 2M40 PCLMA samples, with $92.9 \pm 1.4\%$ and $93.1 \pm 0.2\%$ remaining respectively. The degradation of the PCL, 2M95 PCLMA and 2M40 PCLMA were not significantly different from each other at any time point. The 2M20 and 1.5M20 PCLMA degraded faster than the previous 3 ($45.1 \pm 5.1\%$ and $43.1 \pm 1.6\%$ remaining respectively after 21 days) but were not significantly different to each other at any time point. The 1M20 PCLMA degraded still faster with complete degradation occurring in 17 days. By day 9 the mass remaining of the PCL, 2M95 PCLMA and 2M40 PCLMA were significantly different to the 2M20 and 1.5M20 PCLMA ($P < 0.05$). Additionally, the mass remaining of the 1M20 PCLMA was significantly different to both the 2M20 and 1.5M20 PCLMA ($P < 0.0001$) (two-way ANOVA with Tukey's multiple comparisons). These significant differences continued for all remaining time points ($P < 0.0001$ in both cases, at days 13, 17 and 21).

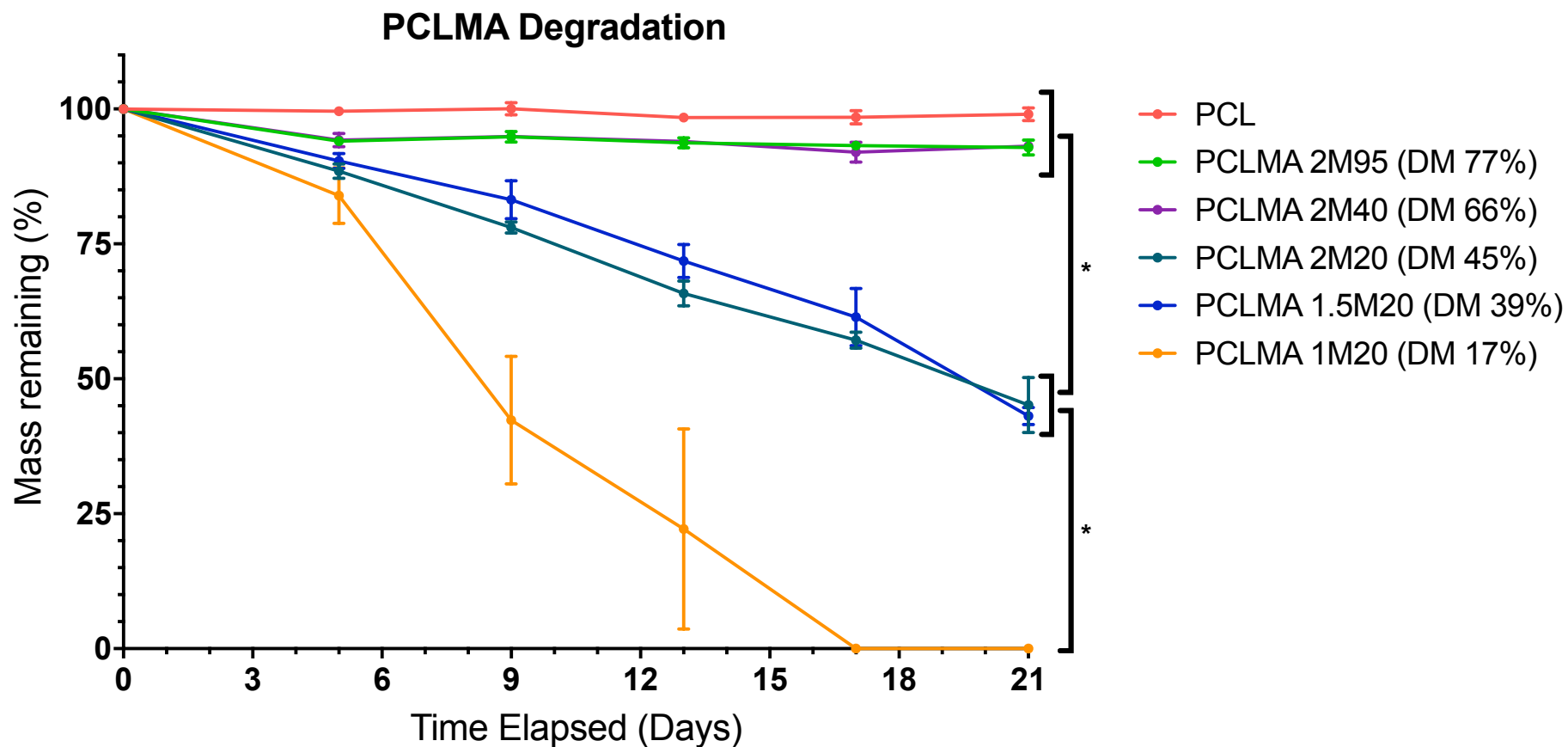


Figure 27. Accelerated degradation of PCLMA and PCL discs in 5M NaOH and the effect of degree of methacrylation. Value displayed mean \pm SD (N=1, n=3).

* denotes significant differences between groups at days 9, 13, 17 and 21 (two-way ANOVA with Tukey's multiple comparisons).







2.5.2 Microstereolithography – Parameter optimisation for tube production

The μ SL set-up (Figure 19) was used to produce plain PCLMA tubes and various parameters were investigated to determine their effect on tube quality. All PCLMA tubes and other structures produced by μ SL were made using resin containing 2M20 PCLMA (47% DM) and 2% photoinitiator.

2.5.2.1 Effect of laser power and stage speed on tube quality

It was found that when curing tubes via μ SL from PCLMA resins, it was important to find the right balance between laser power and stage speed. If the laser power was too low for a certain stage speed, the tubes were under-cured and had thin walls, often with a hole or thin section down the side of the tube. Conversely, if the laser power was too high in relation to the stage speed, over-curing would result in lateral lines/ridges caused by rapid curing and viscous flow of the prepolymer as the stage descended. These observations can be seen in the PCLMA tubes displayed in Table 5.







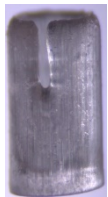




Table 5. The effect of laser power and stage speed on PCLMA tube quality.

<u>Stage Speed</u>	<u>0.015 mms⁻¹</u>			
<u>Laser Power</u>	20 mW  Thin/under-cured strip down side of tube.	21 mW  Thin strip and also over-curing present.	22 mW  Lateral ridges from over-curing.	Comments No laser power that produces good quality tubes at this stage speed.
<u>Stage Speed</u>	<u>0.01 mms⁻¹</u>			
<u>Laser Power</u>	10 mW  As above - power too low.	12 mW  Suitable power/speed combination.	15 mW  As above - power too high.	Comments At a slower stage speed (0.01mms ⁻¹), a suitable balance can be found between power and speed.

2.5.2.2 Effect of prepolymer resin temperature on tube quality

Heating the prepolymer resin decreased its viscosity and allowed faster speeds to be used without the appearance of lateral lines/ridges caused by viscous flow of the resin. These effects can be seen in Table 6, with good quality tubes being produced at 60°C.

Table 6. The effect of raised prepolymer temperature on PCLMA tube quality with increasing stage speeds.

Stage Speed	0.01 mms⁻¹			
Resin Temp.	Room temperature			
Laser Power	14 mW 	18 mW 	20 mW 	Comments No laser power that produces good quality tubes at this temperature.
Stage Speed	0.01 mms⁻¹			
Resin Temp.	60°C			
Laser Power	14 mW  Slight under-curing but most of tube length is of good quality. Top end can be trimmed.	18 mW 	30 mW  Over-curing.	Comments Tubes are of higher quality than any produced at room temp.
Stage Speed	0.02 mms⁻¹			
Resin Temp.	60°C			
Laser Power	14 mW  Under-curing causing hole down side.	25 mW  Slight imperfection present	34 mW  Over-curing.	Comments 25 mW: tube looks of ok quality.
Stage Speed	0.03 mms⁻¹			
Resin Temp.	60°C			
Laser Power	30 mW  Under-curing causing hole down side.	32 mW  Slight under-curing.	34 mW  Over-curing.	Comments 32 mW: tube looks of ok quality and usable if ends are trimmed.

2.5.3 General appearance of PCLMA tubes produced by μ SL using optimum parameters

For the observations described in Table 5 and Table 6, it is important to note that when using different batches of PCLMA resin or when curing tubes of different diameters and wall thicknesses it was necessary to re-optimize the curing parameters. The SEM images in Figure 28 show that when the curing parameters are optimized (i.e. in this case: 60°C resin temperature, 10 mW laser power and 0.02 mms⁻¹ stage speed) the tubes are produced to a very high quality. The tubes have straight sides with no lateral lines/ridges, a circular internal diameter and an even wall thickness.

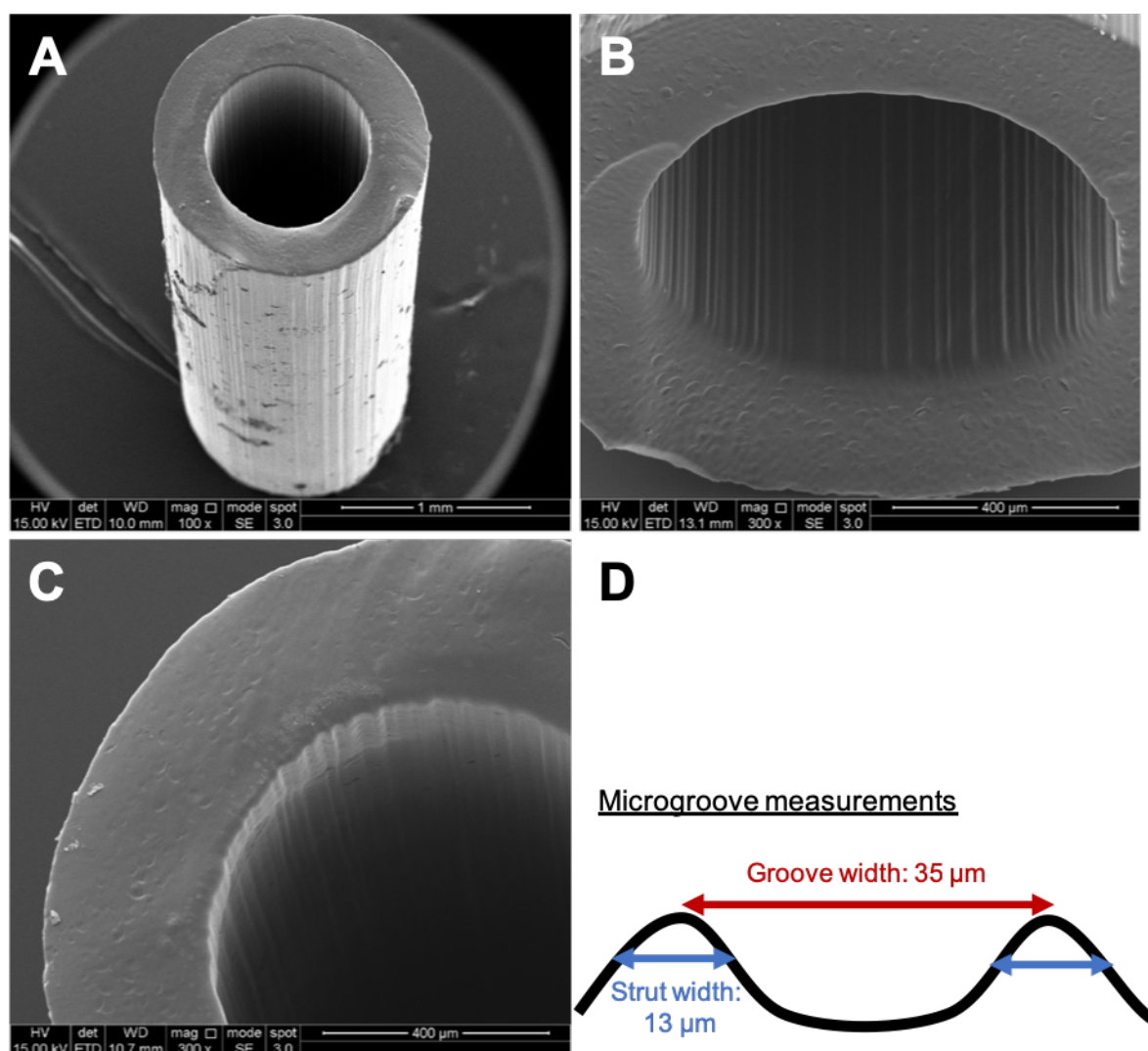


Figure 28. A: SEM image of PCLMA tubes produced by μ SL. B,C: higher magnification images showing the presence of microgrooves on the tube's inner surface. D: The two distances measured to characterise the microgrooves. The red arrow indicates the microgroove width (peak to peak distance) and the blue arrows indicate the strut width (distance across peak).

2.5.3.1 The presence of microgrooves

An interesting feature to note are the microgrooves seen on internal and external surface of tubes produced by μ SL. These run longitudinally along the surface of the cured tubes and are present due to presence of individual micromirrors forming the pixels of the DMD.

These features were measured from SEM images to determine two measurements: microgroove width and strut width (detailed in Figure 28D). Average microgroove width (peak to peak distance) was $35\pm 10\ \mu\text{m}$ and average strut width (distance across peak) was $13\pm 4\ \mu\text{m}$.

2.5.4 Photoabsorber suitability and the effect of their use in μ SL

Various photoabsorbers were tested in the prepolymer resins to improve the quality of structures produced via μ SL. The photoabsorber compounds were first tested in PEGDA resins as a proof-of-concept before using the results obtained and translating this to their use in PCLMA resins. All resins (PEGDA and PCLMA) used in μ SL contained 2% photoinitiator.

2.5.4.1 Absorbance spectra of the photoabsorbers

The absorbance spectra of the 3 photoabsorbers were measured (Figure 29A) to see which was most suitable for absorbance of the 405 nm laser light used in the μ SL setup. Alizarin Red had an absorption peak nearest 405 nm (at around 430 nm) and beta-carotene's absorbance peaked around 465 nm. The absorbance spectrum of riboflavin did not vary much over the 300-600 nm range. It should be noted that for the absorption level of each to fall within the dynamic range of the spectrometer, they were all dissolved in PEGDA at different concentrations. To get an idea of their relative absorbances at 405 nm, the spectra were linearly scaled to extrapolate their absorbance at a 1% concentration (Figure 29B). This showed that beta-carotene had the highest absorbance at 405 nm. However, since each compound has different solubilities in in PEGDA and PCLMA and therefore will be usable at different concentration, this does not make it directly obvious which is the most suitable for use as a photoabsorber in μ SL.

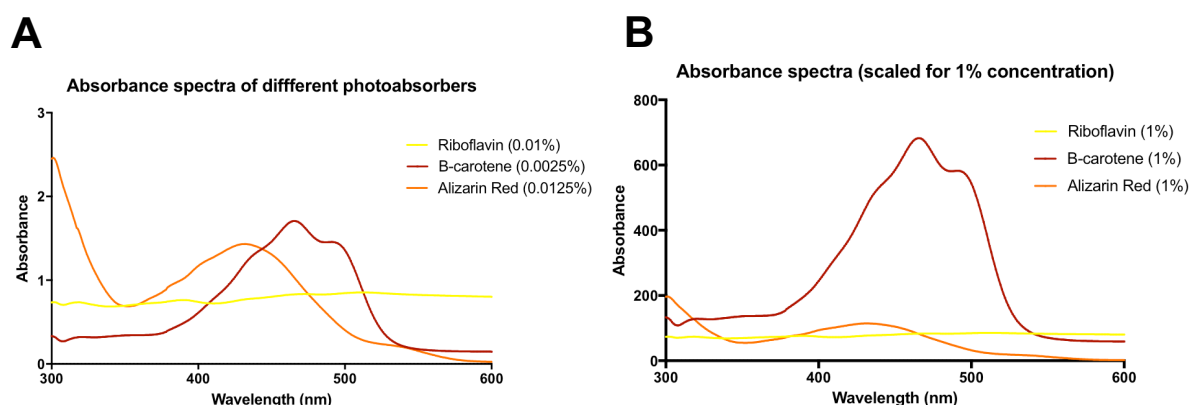


Figure 29. The absorbance spectra of the three photoabsorbers (A). B: The absorbance spectra scaled to visualise their theoretical absorbance when dissolved at the same concentration.

2.5.4.2 Addition of photoabsorbers to PEGDA resins

Photoabsorbers were mixed into PEGDA resin. Beta-carotene did not dissolve well in PEGDA due to its hydrophobic nature. It formed a cloudy solution indicating the presence of particulates and separated if left overnight (Figure 30A). Riboflavin mixed with PEGDA in a similar way to produce a cloudy yellow solution which separated over time. Alizarin Red dissolved well in PEGDA due to its hydrophilicity. At a concentration of 0.5% it produced a dark orange/amber colour solution and did not separate over time (Figure 30B).

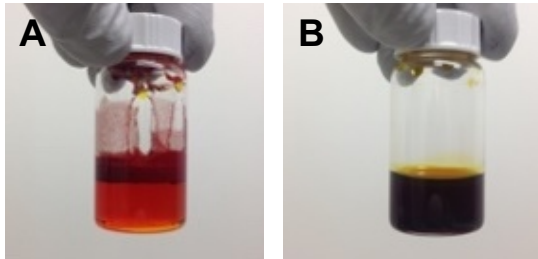


Figure 30. Photoabsorbers mixed with PEGDA. A: PEGDA with 1% beta-carotene, 2% photoinitiator. Mixed until homogeneous and left to settle over time. B: PEGDA with 0.5% Alizarin Red, 2% photoinitiator.

2.5.4.3 Addition of photoabsorbers to PCLMA resins

Photoabsorbers were mixed into PCLMA resin. Due to the hydrophobic nature of PCLMA, Alizarin Red did not dissolve well, with many particulates visible after stirring overnight (Figure 31A). However, beta-carotene dissolved well up to a concentration of 0.05-0.075% to produce a clear orange solution (Figure 31B). Riboflavin was not investigated due to its low absorbance at 405 nm.

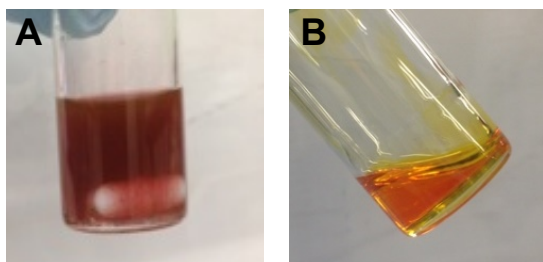


Figure 31. Photoabsorbers mixed with PCLMA. A: PCLMA with 0.5% Alizarin Red, stirred overnight at 60°C. B: PCLMA with 0.05% beta-carotene

2.5.4.4 Analysis of laser depth penetration in the manufacture of 3D PEGDA Tubes

The effect of laser power on cure depth was investigated by varying laser power in the fabrication of constructs with beta-carotene-containing PEGDA resins. A grooved, channel was designed with non-grooved ends/cuffs (Figure 32A) so that if the laser penetration was too high when fabricating, the result would be grooves that continue further into the empty end than in the designed construct. As expected, an increased laser power resulted in longer continuation of grooves (Figure 32C), indicating an increased cure depth.

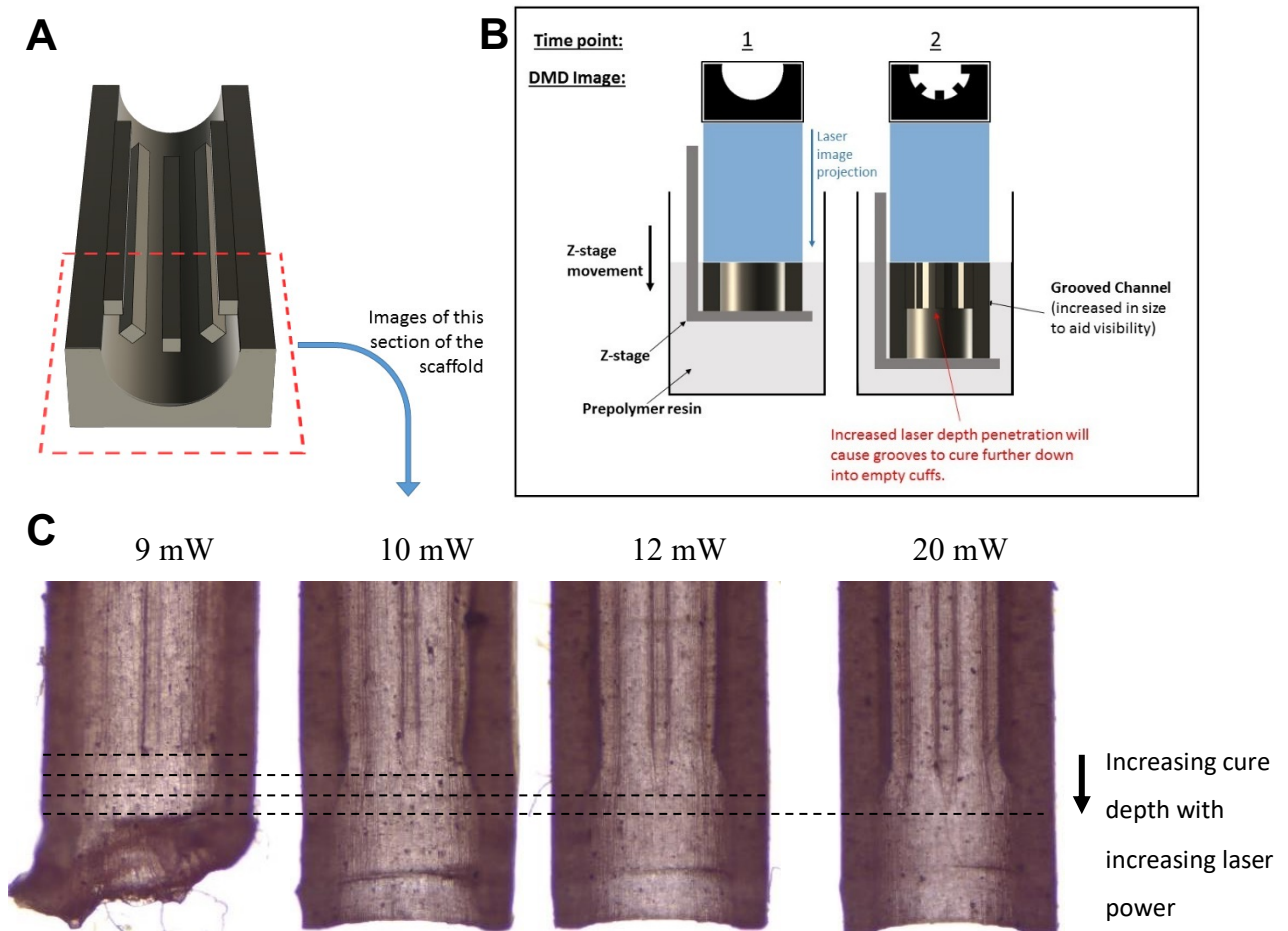


Figure 32. Grooved channels produced by μ SL (PEGDA with 0.5% beta-carotene, 2% photoinitiator). A: Designed construct. B: μ SL curing process for this construct. C: Light microscopy images of the bottom end of the grooved channel constructs showing longer continuation of the grooves (larger cure depth) with increased laser power.

Next, to assess the cure depth resulting from the use of the various photoabsorbers, intermittently grooved channels were produced as described in Figure 21 and the strut and gap length of each was measured to produce the strut length:gap length (S:G) ratio (Figure 33). Photoabsorbers were added to the base PEGDA resin: Alizarin Red (0.1% and 0.5%), beta-carotene (1%) and riboflavin (0.5%). 0.5% Alizarin Red and 1% beta-carotene produced channels with the smallest S:G ratios (1.16 ± 0.03 and 1.31 ± 0.07 respectively – not statistically different). 0.1% Alizarin Red and 0.5% riboflavin produced channels with significantly larger S:G ratios of 1.96 ± 0.24 and 2.31 ± 0.65 , respectively. The opaque appearance of the PEGDA constructs containing beta-carotene and riboflavin show the presence of undissolved particulates of the photoabsorbers left in the cured constructs. This contributed to poorer mechanical properties of the constructs compared to the Alizarin Red channels and they were more easily fractured during handling.

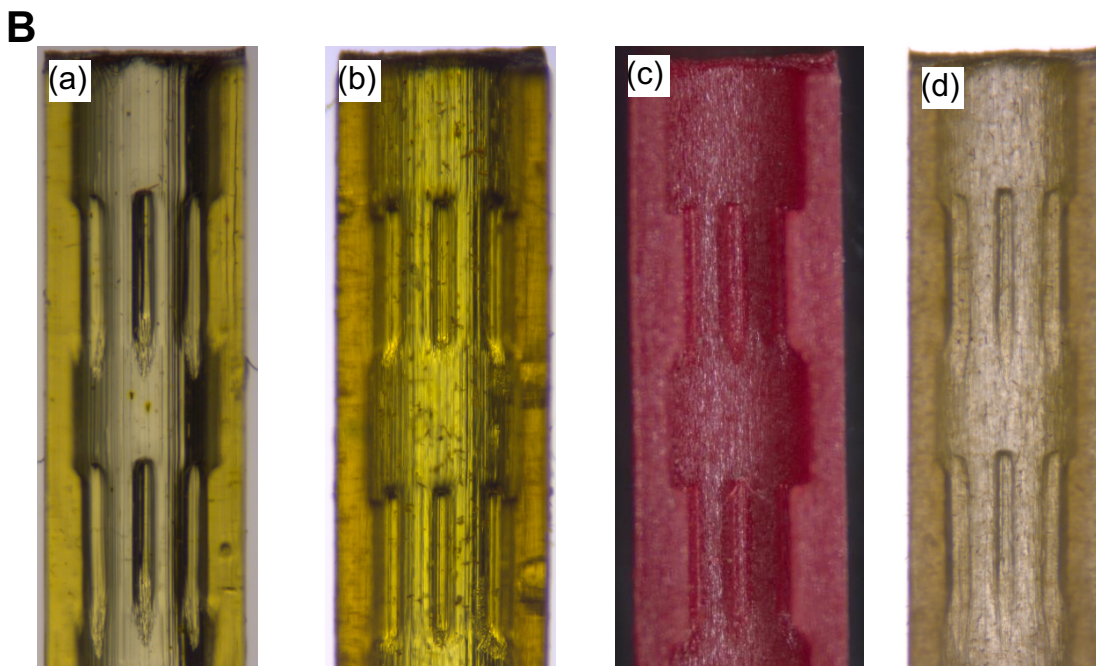
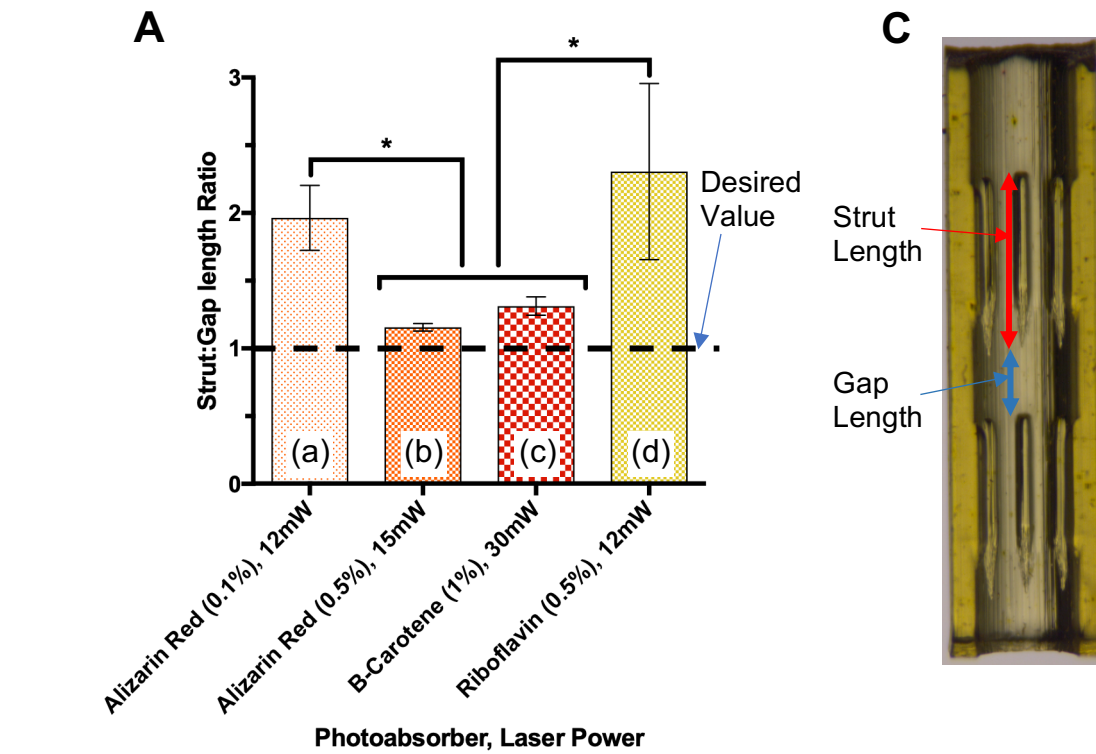


Figure 33. Strut length:gap length (S:G) ratios. A: Graph showing the S:G ratio of PEGDA constructs with different photoabsorbers (Alizarin Red, at 0.1% (a) and 0.5% (b), beta-carotene at 1% (c) and riboflavin at 0.5% (d)). Values displayed mean±SD (N=1, n=5). * denotes significant differences between groups. B: Example images of the corresponding constructs. C: Strut and gap length measurements.

2.5.4.5 Production and imaging of 3D PEGDA constructs

Grooved PEGDA channels containing 0.5% Alizarin red and 1% beta-carotene were imaged via SEM to determine their quality. The PEG/Alizarin Red structures (Figure 34A) had a smooth appearance, indicating the Alizarin red was well dissolved in the PEGDA resin. However, the strut features were thin and under-cured, implying that the concentration of Alizarin red was slightly too high. The PEG/beta-carotene structures (Figure 34B) had a rough, textured surface, indicating the presence of particulates/granules of undissolved beta-carotene. The groove features, however were well defined and not under-cured.

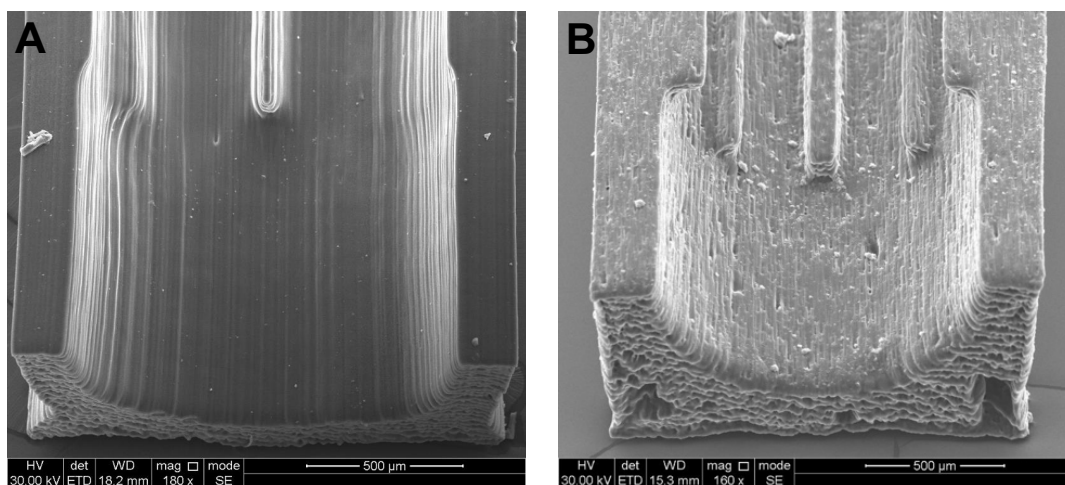


Figure 34. Scanning electron micrographs of PEGDA grooved channels with 0.5% Alizarin Red (A) and 1% beta-carotene (B).

Using these two photoabsorbers, more complex 3D constructs (bifurcated tubes, Figure 35A) were fabricated as described in Figure 20. Figure 35B shows the tubes produced using PEGDA (i), PEGDA + 1% beta-carotene (ii) and PEGDA + 0.5% Alizarin Red (iii). With the use of the photoabsorbers, the tubes produced (Bii and Biii) were a good representation of the designed construct, with clearly defined edges and open lumen throughout (demonstrated in Figure 35D). This was in contrast to the increased cure depth and over-curing seen in the PEGDA construct (Bi, Ci) marked by the cured material outside of the blue line in Figure 35Ci.

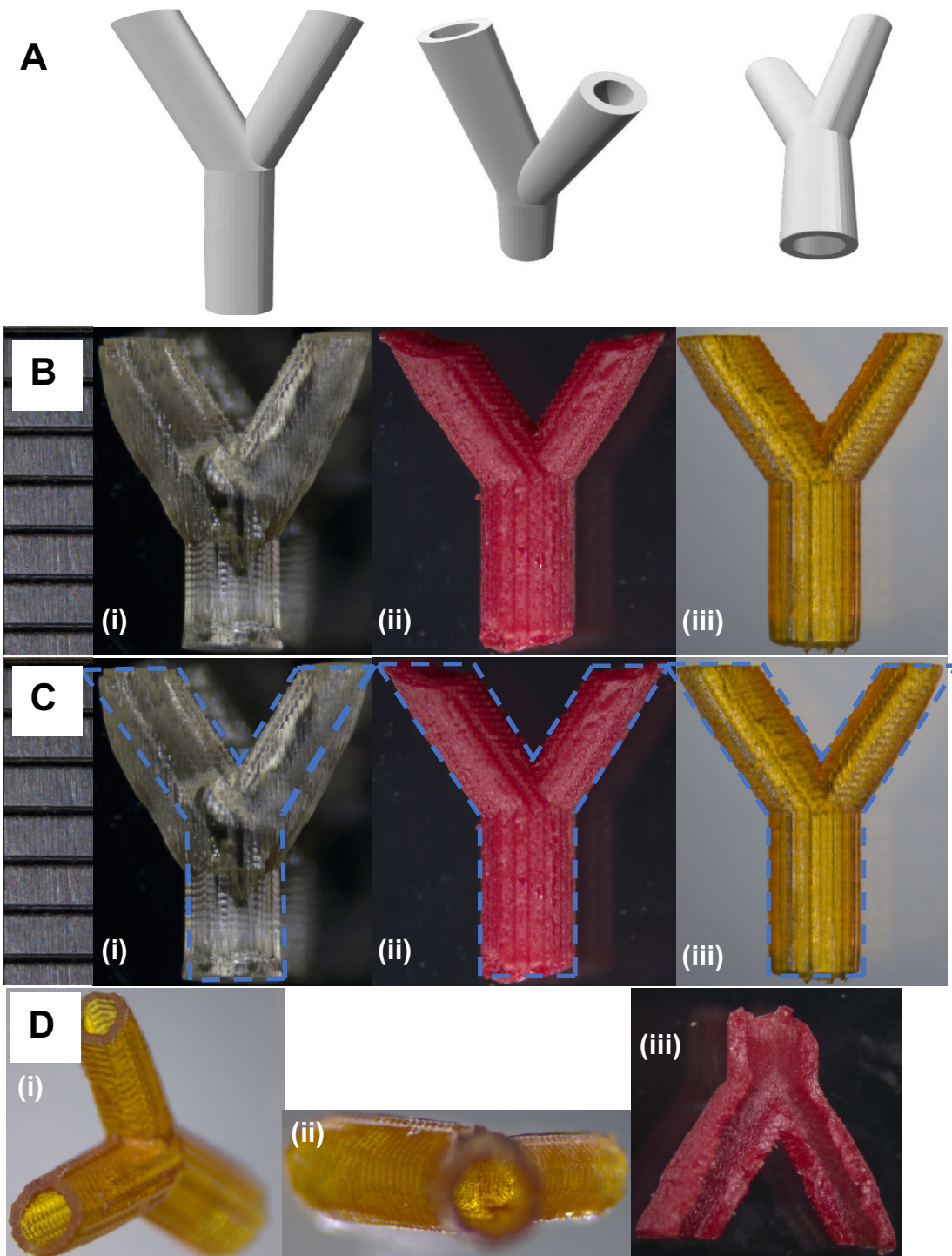


Figure 35. Bifurcated tubes produced by μ SL. **A:** STL file of designed construct (3 differently oriented views). **B-D:** Optical micrographs. **B:** Tubes fabricated from (i): PEGDA, (ii): PEGDA + 1% beta-carotene, (iii): PEGDA + 0.5% Alizarin Red (all with 2% photoinitiator). **C:** The same tubes as in B with a blue line marking the designed shape of the constructs. Material outside the line in (i) represents over-curing due to increased depth penetration in PEGDA without photoabsorbers. Scale bar divisions = 1mm. **D:** Different views of the tubes, showing the open lumen throughout. (i) and (ii): tube fabricated from PEGDA + 0.5% Alizarin Red, (iii): PEGDA + 1% beta-carotene (cut open to visualise lumen).

2.5.4.6 Manufacture of 3D PCLMA constructs

3D constructs (intermittently grooved channels and bifurcated tubes) were fabricated from PCLMA resin containing 0.05% beta-carotene as a photoabsorber. Figure 36A shows an intermittently grooved channel with small cure depth (S:G ratio=1.11±0.07), similar to that achieved by PEGDA resin with 0.5% Alizarin Red. A bifurcated tube Figure 36B was also produced with good resolution and similar quality to those in Figure 35. The low amount of beta-carotene (0.05%) meant that the transparent nature of PCLMA was maintained. This makes it possible to visualise an open lumen throughout the tube, indicating a good control over cure depth.

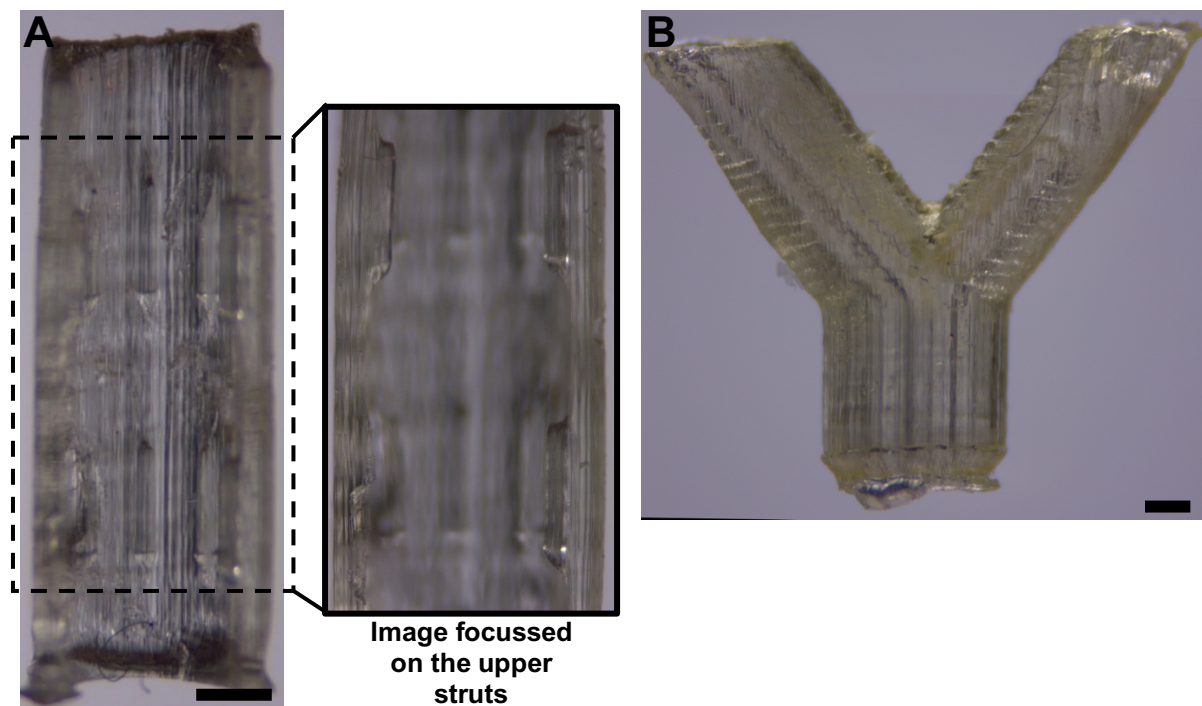


Figure 36. 3D constructs produced from PCLMA with 0.05% beta-carotene, 2% photoinitiator. A: Intermittently grooved channel with magnified image focussed on the upper struts. B: Bifurcated tube with open lumen visible. Scale Bars: 500 μ m.

2.6 Discussion

2.6.1 PCL Methacrylation

2.6.1.1 Controlling the degree of methacrylation

In the methacrylation of PCL triol, it was shown that the DM of the resultant PCLMA can be increased by either increasing the molar ratio of MAA/TEA:PCLMA (increasing the amount of methacrylation reagents) or by increasing the reaction time. For a 20 hour reaction, the methacrylation was not 100% efficient (a 2× molar excess reaction achieved only 47% DM) but increased reaction time lead to a further increase in DM. The increase of DM with time was not linear and when increasing the time of a 2M reaction to 95 hours, the rate of increase of DM dramatically slowed and levelled off at around 77%. A similar effect was seen by Abbadessa et al. in the methacrylation of chondroitin sulfate where the DM increased over the first 7 days before settling at around 43% for the remaining 2 weeks. They speculated that this was due to an equilibrium state being reached between the reacting molecules [231]. This could offer some insight into the reason behind the plateau of reactivity in our PCLMA reaction. When the molar excess of reagents was increased in the PCL methacrylation, no such plateau in the DM was reached. It seems logical then, that if a DM higher than 77% was required, the molar excess could be increased beyond 2x to drive the reaction further. It is not uncommon to use large molar excesses, with examples in the literature presented in section 2.2.3. Hoch et al. [229], [230] and Bencherif [228] et al. used up to 20x and 100x molar excess, in the respective methacrylations of gelatin and hyaluronic acid.

2.6.1.2 Determining degree of methacrylation via NMR spectroscopy

DM of the PCLMA prepolymer was assessed via NMR spectroscopy, based on the integral of the spectra peaks which correspond to the methacrylate group (*i*: 6.09 ppm, *j*: 5.55 ppm and *a''*: 4.14 ppm, Figure 22). This is a well-known method performed by other groups (i.e. in the methacrylations of hyaluronic acid [228] and chondroitin sulfate [231]). Alternatively, some groups have assessed DM based on the integral of the NMR peak representing the two hydrogens next to the hydroxyl group (*a'*, Figure 22). Elomaa et al. determined full methacrylation by disappearance of this hydroxyl peak [219]. In theory, this is a valid way of assessing methacrylation as disappearance of this peak signifies disappearance of the hydroxyl groups and therefore full methacrylate functionalisation. This method was considered in our work but it was noted that this peak is split by the strongly electronegative hydroxyl group and is reduced in height compared to its theoretical value; in the unmethacrylated PCL triol (Figure 22) *a'* should represent 6 hydrogens however it's integral is only 3.67. Using this integral to calculate DM would give a false impression that only 61% of the original hydroxyl groups

remain and that the unmethacrylated PCL triol is actually 39% methacrylated. This is obviously an erroneous result so this method of DM calculation could not be relied upon.

Alternatively, DM could be determined based on the integral of a' as a percentage of its integral in the unmethacrylated PCL triol, i.e:

$$DM (\%) = \left(1 - \frac{\int a'_{\text{methacrylated sample}}}{\int a'_{\text{unmethacrylated sample}}}\right) \times 100.$$

Equation 5. An alternative method for calculation of the degree of methacrylation (DM) of PCLMA, using the integral of the a' peak in the NMR spectra (Figure 22).

This is similar to Hoch et al.'s method for determining the DM of gelatin methacrylamide [229], [230]. Using this method, we get a much higher estimation of DM but the same trends are seen. (See Figure 37 for a comparison of the two methods.) In the NMR spectra of our 2M95 PCLMA, the a' peak is almost completely absent and so using this method calculates the sample to be almost 100% methacrylated (Figure 37A). However, the unreliability of this method can be demonstrated by looking at Figure 37B. Here, this alternative method calculates that the DM of the 0.5M20 PCLMA is less than 1 (due to the fact that $\int a'_{PCLMA\ 0.5M20} > \int a'_{unmethacrylated\ PCL\ triol}$). A negative DM is obviously not possible, so this highlights that in our case, the a' peak cannot be used for a reliable calculation of the DM of PCLMA.

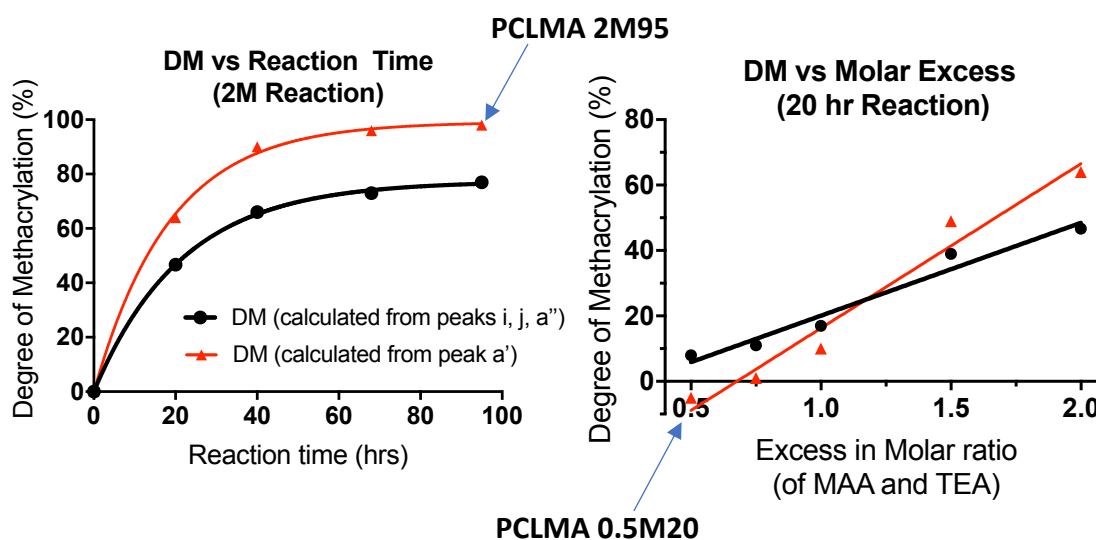


Figure 37. Graphs showing the DM of PCLMA calculated via two separate methods.

Black: (The method reported in this thesis, see Equation 4): DM calculated using the integral of peaks i , j and a'' (which represent the hydrogen environments associated with methacrylated functional groups).

Red: (Alternative method, see Equation 5): DM calculated using the integral of peak a' (which represents the hydrogen environment associated with the OH group in unmethacrylated functional groups).

2.6.1.3 Effect of DM on mechanical properties and other ways of varying mechanical properties

It was found that varying the DM of the PCLMA prepolymer had an effect on the mechanical properties of the crosslinked polymer. Increasing the DM means that more functional groups are present in the prepolymer molecules, resulting in a greater degree of crosslinking between molecules during photocuring and an increased Young's modulus. However, this is not the only way to change the stiffness of a photocured polymer. Other ways to do so involve varying the contents and additives of the prepolymer resin such as the amount of solvent, photoinitiator and reactive diluent.

Lee et al. experimented with different formulations of PPF resin to vary the mechanical properties of the cured polymer. Changing the prepolymer:solvent ratio and photoinitiator content resulted in cured polymer samples with varying compressive moduli, ranging from 19 MPa to 140 MPa. Both increasing prepolymer:solvent ratio and increasing photoinitiator content caused an increase in modulus [225]. The amount of a reactive diluent (crosslinker) can also be varied as shown by Jansen et al. who produced a photocurable resin comprised of PDLLA functionalised with fumaric acid monoethyl ester. By varying the content of NVP from 20-50 wt%, The Young's modulus of the crosslinked polymers increased from 1.5-2.1 GPa when tested in the dry state. However, the addition of NVP caused a dramatic increase in the water uptake of the polymer networks. Therefore, when testing in the wet state, increasing NVP content caused a significant decrease in Young's modulus [238].

To avoid changes in resultant material properties, be it swelling characteristics and resultant mechanical properties or biocompatibility from unwanted residual diluents, it would be more desirable to use resins without additional additives. To vary the mechanical properties of a crosslinked polymer without adding any extra components to the prepolymer resin, changes to the molecular structure of the prepolymer molecules could be investigated. Two ways of achieving this would be to either changing molecular weight of the prepolymer or varying the number of methacrylate-terminated arms in the molecule.

Green et al. performed tensile testing on cured samples of acrylated PCL triol (3-arm, PCLTA) and PCL diol (2-arm, PCLDA) of different molecular weights. The lower molecular weight prepolymers (e.g. PCLTA 300 g/mol vs 900 g/mol) cured to produce a material with higher Young's modulus and greater tensile strength (75% and 22% increase respectively). Prepolymers with a greater number of functionalised arms (e.g. PCLTA vs PCLDA) also resulted in a higher Young's modulus material [239].

Both of these results can be explained with a change of crosslink density. With the higher molecular weight molecules, there are longer polymer chains between the crosslinks, so a looser network is formed with lower mechanical properties. A fewer number of methacrylated arms in the diol molecule vs the triol also produces a network with a lower crosslinking density and therefore a lower stiffness material.

Polymer blends can also be used to vary mechanical properties. Chung et al. found that by mixing PCL triol methacrylate with di(propylene fumarate)–dimethacrylate compressive strength in the cured material could be reduced compared to networks comprised to PCL triol methacrylate alone [240]. This is likely due to the two-armed di(propylene fumarate)–dimethacrylate reducing the crosslinking density of the three-armed PCLMA.

In the present study, the DM of PCLMA was varied, altering the number of functional groups available for crosslinking and the subsequent crosslink density. The result is similar to changing the number of arms in a methacrylated molecule but gives more adaptability as we can produce PCLMA of any DM in the range of 17% to 77%. This essentially produces blends of 1-, 2- and 3- arm PCLMA with the average number of arms increasing with increasing DM. This allows us to fine-tune the mechanical properties and produce cured PCLMA with Young's modulus anywhere in the range of 0.12-3.51 MPa (a 30-fold change). This range of Young's modulus is lower and wider than that by Green et al. (4.0-6.9 MPa) [239] and Elomaa et al. (6.7-15.4 MPa) [219] achieved by varying the molecular weight of their PCL-based prepolymers. This highlights the advantage of our method, being able to produce a more elastic material with a wider range of properties.

This relationship of DM and Young's Modulus is similar to that seen by Pashneh-Tala et al. in their PGS-M. They calculated Young's modulus via tensile testing of dog bone structures and found a significant increase with increasing DM. Young's modulus ranged from around 0.5 MPa for 30% DM to around 7.5 MPa for 80% DM. The ultimate tensile strength was also seen to increase from around 1 MPa to 4 MPa with increasing DM [233].

2.6.1.4 Effect of DM on Soluble Fraction

It was seen that increased prepolymer DM resulted in a lower soluble fraction in the cured PCLMA. With increasing DM, the increased number of functional groups per PCLMA molecule means that on crosslinking, a higher proportion of the molecules will be incorporated into polymer network and less material is left free to dissolve in the solvent. In the 17% DM PCLMA (soluble fraction = 53%), an average of 0.5 arms per 3-arm molecule have been methacrylated i.e. ~50% of the molecules will have 1 methacrylate group and the remaining 50% will be completely unmethacrylated. Upon curing, the methacrylated molecules are able to form a crosslinked network however the unmethacrylated molecules will remain free. This explains why 50% of the prepolymer resin (in the 17% DM PCLMA) is not incorporated into network and comprises the soluble fraction.

2.6.1.5 Effect of DM on Degradation

Like many synthetic polymers, PCL degrades by hydrolysis of the ester linkages in the polymer backbone [241], [242]. Degradation of cured PCLMA and PCL was performed in NaOH, which simulates accelerated hydrolysis due to the presence of OH⁻ ions which catalyse the hydrolysis of ester bonds [243]. The linear decrease in mass seen in the results is suggestive of surface degradation which is usually preferable for tissue engineering scaffolds as mechanical properties are maintained throughout the degradation process, unlike with bulk degradation [244].

An increased DM of the PCLMA resulted in slower degradation rates for the same reason that we see a higher Young's modulus. This is due to the increased crosslink density, meaning more bonds need to be broken for material to degrade. These results are consistent with other studies in literature. Pashneh-Tala et al. found that increasing the DM of PGS-M lead to a decreased degradation rate in enzymatic degradation with cholesterol esterase [233]. Linear degradation was also seen, characteristic of surface degradation. This inverse relationship of polymer degradation rate and crosslink density has been shown in other studies with degradable poly(vinyl alcohol) scaffolds and PEG-co-PLA hydrogels [245], [246]. In a study with PCL, Green et al. compared the degradation of crosslinked PCL-triol acrylate and PCL-diol acrylate in 1M NaOH, 37°C. It was found that the diol acrylate (with a lower crosslink density) degraded much faster than triol acrylate (full degradation in 8-9 days vs 22 days respectively) [239].

The commercial PCL in our study was seen to degrade very slowly with minimal (non-significant) mass loss after 21 days. PCL is known to have a slow degradation rate with reports of ~2% degradation after 6 months *in vivo* [247], however our result was still surprising, considering the

strong (5 M) NaOH. Other studies degrading PCL scaffolds in the same concentration of NaOH report 80% degradation in 18 days [248] and complete degradation after 35 days [249]. These studies however, were both performed with porous, woodpile scaffolds which have a much larger surface area than the bulk discs in our study, allowing for much greater hydrolytic action. These studies were also performed at 37°C which would increase the rate of degradation.

2.6.2 PCLMA resin formulation

One advantage of PCLMA resin described in this work is its simple formulation compared to resins used by other groups, consisting of only the liquid PCLMA prepolymer and a photoinitiator. Since the mechanical properties and degradation rate of the material can be tuned by varying the DM of the prepolymer, there is no need for the additives discussed above (such as crosslinkers or solvents) which may cause problems or influence the properties of the fabricated part.

The necessity for solvent addition is also removed due to low viscosity of the PCLMA prepolymer. Since it is liquid at room temperature, it can be used in stereolithography without additional diluents. The low viscosity of the PCLMA could be explained by the loss of -OH groups (present in the unmethacrylated molecules) which contribute to hydrogen bonding [218]. For more viscous prepolymers or ones which are solid at room temperature, non-reactive diluents/solvents are often necessary to solubilise polymers or reduce their viscosity for printing. Melchels et al. used 19% ethyl lactate [226] and later 40% N-methylpyrrolidone [227] as diluents to make PDLLA and P(DLLA-co-CL) liquid at room temperature and allow scaffold production using a commercial stereolithography system. As with all methods which use solvent-containing resins, this resulted in shrinkage of the printed parts upon extraction of the solvents (10% and 22% shrinkage for the respective studies). Diethyl fumarate is commonly used as a solvent in PPF resins such as that used by Lee et al. who used 25-50% diethyl fumarate and saw up to a 12% shrinkage in the printed scaffolds [225]. Shrinking due to solvent use can present obvious problems when designing and producing a scaffold as it could result in significant distortions or dimensional changes [119] which need to be factored into the scaffold design. Even in the case of isotropic shrinkage, this can cause problems in design optimisation [227].

The necessity for crosslinkers in our PCLMA resin is also removed due to the high reactivity of the methacrylate groups compared to many alternatives [218]. When lower reactivity groups are used, a reactive diluent/crosslinker is usually required to produce a curable resin. This acts to increase the reactivity of the prepolymer by acting as a crosslinker or copolymer which becomes incorporated

into the network during photocuring. Both Jansen et al. [238] and Ronca et al. [220] required the use of NVP in their resins due to low reactivity of fumarate- and vinyl- terminated prepolymers, respectively. Without NVP, the vinyl-terminated PCL by Ronca et al. polymerised very slowly under UV light, forming a putty-like structure after 20 mins irradiation but with the addition of 30-50% NVP, sufficient crosslinking could occur to form complex structures by stereolithography. However, due to its hydrophilicity, the addition of NVP significantly increased the water absorption of the polymer networks [220]. This water uptake may be undesirable for some applications as it could result in swelling of the part or a reduction of mechanical properties [238] (as discussed in section 2.6.1.3). Additionally, unreacted NVP may cause toxicity [224].

Due to the low viscosity of the PCLMA, the high reactivity of the methacrylate groups and the ability to tune the DM, there is no need for the addition of either solvents or crosslinkers. This means that problems associated with their effect on the structural, chemical and biological properties of the material can be avoided. The simple resin formulation is also beneficial as for future medical device production it would be desirable to limit the resin components to materials already present in FDA approved products (such as PCL) with minimal additives, making the approval process more straightforward.

2.6.3 The microstereolithography process

The method of μ SL described in this thesis uses a continuous motion of the z-stage. This means that with the correct power/speed combination we can prevent transverse ridges forming within the construct which is obviously preferable when producing structures for nerve guidance. Most groups use a stop-start technique in which the stage is repeatedly lowered and raised between curing of cross-sections as described by Choi et al. [119] and shown in Figure 38. This technique cures distinct layers, one at a time, causing lateral lines to form between the layers. Using this process, it has been said that a layer thickness of 5 μm or less is generally needed for the production of smooth parts with no obvious layers [250].

As well as preventing the formation of distinct layers, the continual motion of the stage also removes the waiting time for resin to settle after lowering and raising of the stage (Figure 38, timepoint 2-3), which can take up to 10-15 seconds each time. This drastically limits fabrication time with fabrication speed reported of around 1-1.5 mm per hour [250]. Conversely, our continuous technique can fabricate structures at hugely accelerated speeds of up to 0.005-0.03 mms^{-1} (18-108 mm per hour).

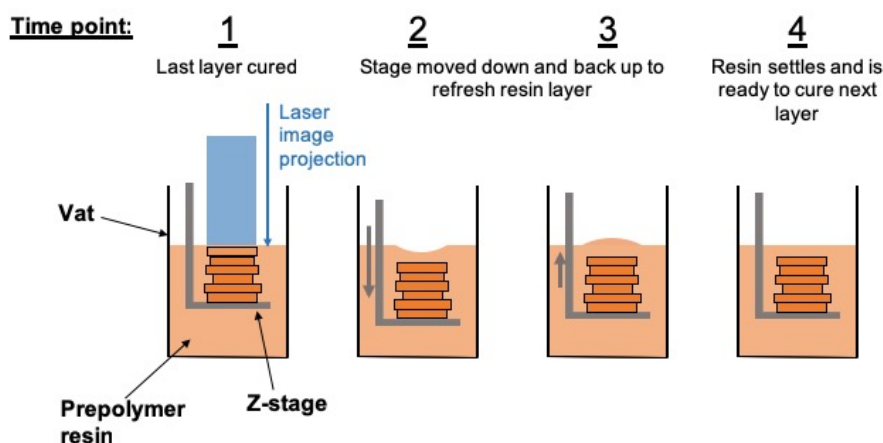


Figure 38. Conventional stereolithography methods which cure sequential layers, one at a time, with a stop-start motion of the stage. This results in the formation of lateral ridges within the construct.

The other main technique of stereolithography is to use a 'bottom-up' set-up where the laser image is projected, from below, at the base of a vat of prepolymer resin (Figure 39). The z-stage is then moved upwards so that the structure is seen to 'rise' from the resin. This is also a step-wise process that produces a layered structure; between the polymerisation of subsequent layers the structure needs to be detached from the bottom surface of the vat before the stage can be raised. In addition

to the formation of layers, another drawback of this technique is that the detachment produces a force which can be damaging to the construct and this has been studied by Zhou et al. [251].

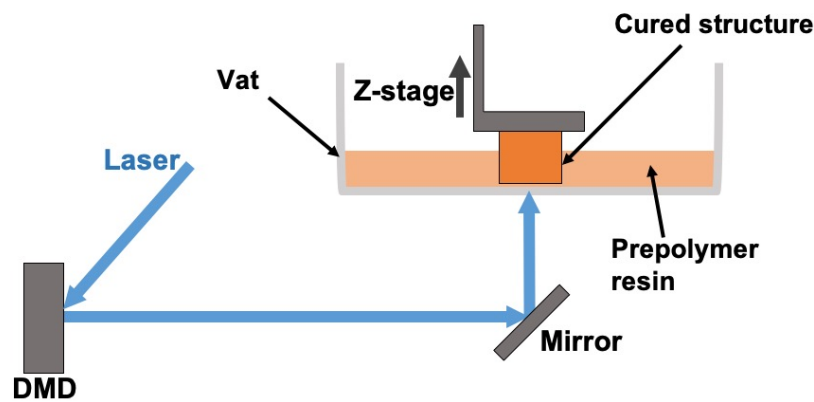


Figure 39. A bottom-up stereolithography system with the laser directed at the base of the resin vat.

There is however one group that uses a continuous bottom-up μ SL approach, coined 'CLIP' (continuous liquid interface production). This technique utilises an oxygen-permeable membrane in the bottom of the resin vat enabling there to be a thin layer where oxygen is present. This presence of oxygen facilitates oxygen inhibition of the free radical polymerisation producing a 'dead zone' between the construct and the vat floor where the prepolymer is prevented from curing. The polymer therefore does not adhere to the vat surface and a continuous production is permitted, similar to our top-down approach. The group can produce structures with micro-sized features at a speed of 25 mm per hour which is comparable to what we can achieve [252].

2.6.3.1 The effect of laser power, stage speed and resin temperature

During μ SL fabrication, we found that a careful balance of laser power and stage speed was necessary to achieve high quality parts. Too low laser power or too high stage speeds resulted in under-curing characterised by thin-walled, partially cured structures. Conversely, when the laser power was too high or the stage speed too slow, over-cured structures were produced, characterised by lateral ridges in the cured construct.

It was found that heating the PCLMA resin increased the quality of the printed parts, allowing constructs to be cured with faster z-stage speeds. This effect is seen due to the decrease of the resin viscosity as the temperature is raised. Low viscosity solutions are important in conventional stereolithography methods so that flow of the resin can allow the recoating process in Figure 38 to occur effectively, with the new resin layer settling in an appropriate time [235]. The same is true for

our method which uses continuous z-stage movement. If resin viscosity is too high compared to the stage speed, the continual curing process is disrupted as the resin cannot flow fast enough to keep a level surface as the stage descends. The effect was demonstrated in Table 5 and Table 6, where the PCLMA resin was too viscous (at low temperatures) or the laser power was too high compared to the stage speed. In such cases, it seems the available resin at the surface cures rapidly and the stage descends until the viscous prepolymer is able to flow over the construct and refresh the surface resin. This then repeats in a cyclical process, causing lateral ridges to form in the cured construct. This result is similar to what is seen in constructs produced with stop-start motion of the z-stage (Figure 38). By heating the resin, its viscosity was decreased and it was able to continually flow over the descending construct even at higher stage speeds. The laser power could then be selected to achieve a curing rate suitable for the stage speed, eliminating the formation of the lateral ridges.

Steyrer et al. demonstrated the same benefit of increased resin temperature in the printing of a dimethacrylate resin, reducing resin viscosity from 1.73 Pa s at 23°C to 0.036 Pa s at 70°C [253]. This resulted in reduced printing times at the higher temperature as the hold time for the resin to settle between printed layers was significantly reduced. This effect was also seen by Choi et al. who heated PPF resin while printing [119]. Steyrer et al. also found that the increased resin temperature resulted in a lower critical energy required for the polymer to cure and so the exposure time for each layer could be reduced. Generally, the parts printed at 70°C also exhibited higher tensile strength, Young's modulus and double bond conversion, however this difference was eliminated after post-curing of the parts. One downside was that the distinction between the layers of the 70°C-cured parts was more pronounced. This is likely due to the shorter exposure time resulting in reduced over-curing between layers and a reduction in inter-layer bonding. The result was that the parts printed at 70°C exhibited lower tensile strength (in the direction perpendicular to the layer formation) compared to the parts printed at 23°C (only in the post-cured specimens) [253].

These findings highlight another potential advantage of our continuous curing process which likely produces parts with better mechanical properties and better bonding between 'layers'. In the simple 2.5D tubes (Figure 28) there are no distinct layers present. This is because one DMD image is displayed, continually projecting the laser image at the resin surface as the z-stage continually descends. Even during the production of 3D constructs when the DMD image changes as the z-stage descends, in areas where sequential cross-sections overlap, there is no break in the light exposure so the resin keeps curing as if it were a continuous part. This is in contrast to other systems, where the light stops and starts over the whole cross-section, introducing weak points between layers that may

not be properly bonded together. In our continuous process, the outside of the part may show a stepped appearance (see Figure 35) where cross-sectional images have changed on the DMD, but in the bulk of the part there are no distinct layers present as the resin is cured continuously.

2.6.4 Presence of microgrooves on constructs produced by microstereolithography

It was noted that the tubes produced by μ SL have microgrooves present on the surface that run longitudinally along their length. These features were also observed by Pateman and Harding et al. and are an inherent feature caused by the pixellation of the DMD [128] (shown in Figure 40). The DMD image consists of pixels (representing the individual $14\ \mu\text{m}$ micromirrors in the DMD) and laser light reflecting of these individual mirrors/pixels results in the microgroove features in the cured product. It is possible that these microgrooves may offer physical guidance cues to migrating Schwann cells and regenerating axons as discussed in section 1.6.5. This idea will be explored further in chapter 5.

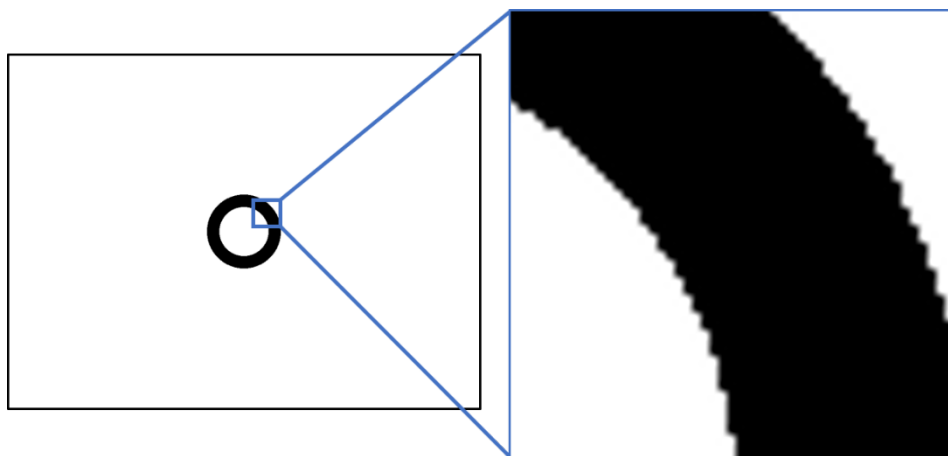


Figure 40. DMD image used to produce tubes by microstereolithography and a magnified section of the DMD image showing the pixellation which represents the individual micromirrors.

2.6.5 The addition of photoabsorbers to μ SL resins

The observation of cure depth increasing with laser power (section 2.5.4.4) is consistent with what is described by Jacobs in 'Fundamentals of Stereolithography' (see Equation 2) [234] and observed by Choi et al. in their investigation into the use of Tinuvin as a light absorber [235]. They demonstrated that cure depth increased linearly with the log of the exposure energy and increasing concentrations of Tinuvin resulted in a decrease in the cure depth. Additionally, they found that the higher the concentration of Tinuvin, the lower the rate at which cure depth increased with incident radiation power. This means that using a high concentration of light absorber may allow more flexibility over the laser power, making it possible to use higher laser powers without sacrificing z-resolution.

It is however, important to find the optimum concentration of light absorber to add to the resin. Even though larger concentrations lead to lower cure depths, when too much light absorber is present, features become thin and fragile due to under-curing. This effect was observed when using high concentrations of beta-carotene in PCLMA resins, resulting in under-cured PCLMA tubes (Figure 41A). To achieve adequate curing with a certain exposure energy, there therefore exists an optimum concentration of light absorber, where the light absorption is high enough to limit cure depth but not too high as to prevent the proper curing of features (see Figure 41B, where this was demonstrated by Choi et al. [235]). This balance was achieved in the present study with beta-carotene concentration of 0.05% in PCLMA resin.

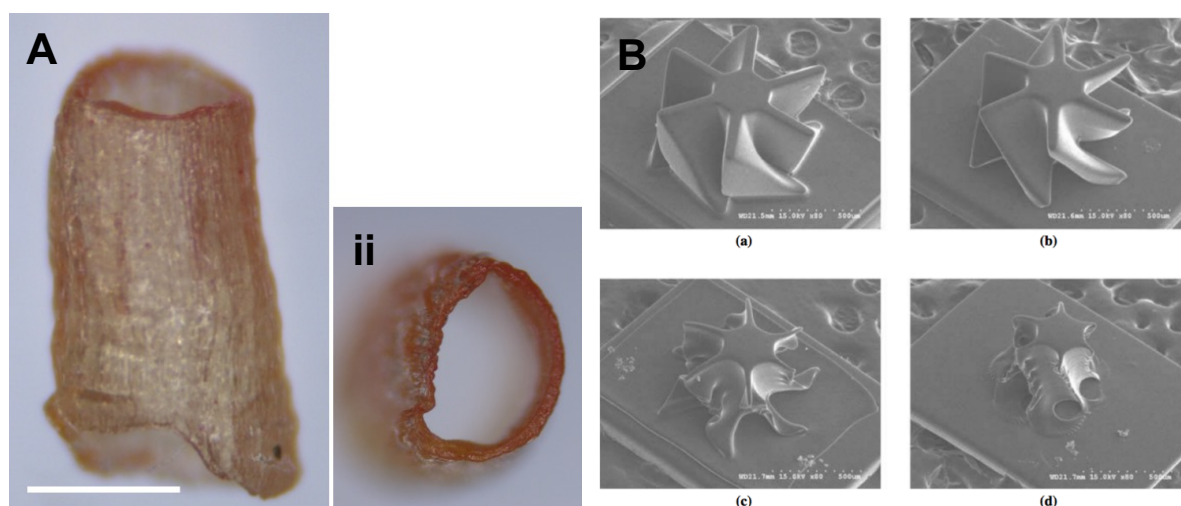


Figure 41. The effect of light absorbers in μ SL. A: Side view (i) and top view (ii) of an under-cured tube produced by μ SL with PCLMA containing too high a concentration of beta-carotene (0.2%). Scale bar: 1 mm. B: The effect of too much and too little light absorber. a: No light absorber leads to increased depth penetration and over-curing in the z-direction. b: optimum light absorber concentration leads to perfectly cured structure. c/d: too high concentration of light absorber leads to under-cured features. Reprinted from Choi et al. with permission from Emerald Publishing Limited [235].

It is evident that photoabsorbers are necessary to produce complex 3D structures via μ SL, however one main problem with most current photoabsorbers used in literature is the limited evidence of their biocompatibility. There is little data supporting the biocompatibility of Tinuvin with some studies showing possible cardiotoxic effects [254], [255]. Additionally, Barker et al. [236] used a paprika extract which may contain capsaicin, the active component in chili peppers which is well known for its sensory nerve activation and inflammatory properties [256], [257]. For these reasons it would be difficult for any products containing these substances to gain FDA approval for clinical use. It is obvious that biocompatible photoabsorbers would be necessary.

Beta-carotene may be a suitable alternative. While there is some evidence that beta-carotene may increase the incidence lung cancer in heavy smokers [258], the doses administered in these studies is upwards of 20 mg per day. This is orders of magnitude higher than the level of beta-carotene that the patient would be exposed to from an implanted conduit. Moreover, beta-carotene is a common substance in foods and multivitamin supplements and some studies have shown its potential benefits in neural applications. The anti-oxidant activity of beta-carotene has been shown to prevent the decrease in nutritive blood flow to sciatic nerve seen in diabetic rats [259] and it has also demonstrated potential in reducing neurogenic inflammation in response to certain substances [260].

In terms of assessing the effect of the addition of light absorbers into μ SL resins, PEGDA has been very useful due to its easy availability and low cost. It is however unlikely to be used in *in vivo* implantations due to its poor biocompatibility so we do not need to be concerned about the biocompatibility of the other photoabsorbers used (i.e. Alizarin Red). Conduits to be used *in vivo* will be fabricated from PCLMA containing beta-carotene and the biocompatibility of this material will be assessed in chapter 4.

The use of beta-carotene in PCLMA resins was shown to improve the resolution of structures fabricated by μ SL and this work seems to be the first report of beta-carotene's use as a photoabsorber. Before this research, our μ SL system had only been used to produce 2.5D structures such as simple tubes [128], for which basic manufacture methods such as extrusion could be used to produce these scaffolds at much faster rates. The addition of photoabsorbers into the prepolymer resins has given us control over the cure depth of the system and has allowed us to produce constructs with real 3D geometry (a non-uniform cross-section), much more difficult to produce with

alternative manufacturing techniques. We have been able to produce grooved channels with non-grooved cuffs, a feature which may be beneficial for conduits to allow easier implantation. Such structures would not be producible by extrusion or by the rolling of grooved films, performed by many groups [106], [183], [184] (see section 1.6.5.2). This highlights advantage of μ SL over conventional fabrication techniques. We have also shown the ability to produce much more complex 3D structures, such as bifurcated tubes. These are similar to the bifurcated nerve guides produced by Johnson et al. [87] who demonstrated that by including two types growth factors within the separate branches, it was possible to guide the growth of motor and sensory nerve branches along the different paths. This demonstrates the potential applications of the tubes produced in this work.

2.7 Conclusions

A tuneable, photocurable PCLMA resin was produced for use in stereolithography and successfully used to produce tubes and other 3D structures. PCL triol was successfully methacrylated to produce a photocurable PCLMA prepolymer. The DM was varied to alter crosslinking density in cured polymer, allowing the production of PCLMA with tuneable mechanical properties and degradation rate. An order of magnitude change in the Young's modulus was seen between the PCLMA with the lowest and highest DM. Relative degradation rate was also varied from no significant degradation in 21 days to complete degradation in 17 days, in an accelerated study. The photocurable PCLMA was used in microstereolithography to produce PCLMA tubes of an excellent quality which was dependent on curing parameters such as laser power, stage speed and resin temperature. Additionally, beta-carotene was found to be a suitable photoabsorber to improve z-resolution in printed constructs and allow the production of complex 3D scaffolds.

3. Chapter 3: Conduit design, production & analysis

3.1 Chapter Introduction

Using the photocurable PCLMA resin and the microstereolithography techniques described in chapter 2, this chapter explores the design and production of different types of NGCs. The conduit designs presented here will incorporate the two different types of physical guidance cue discussed in chapter 1: aligned grooves and aligned microfibres. The conduits described in this chapter will be used in the *in vitro* and *in vivo* models discussed in the following chapters, to assess the effect of the physical guidance cues on peripheral nerve regeneration.

Firstly, conduits containing aligned grooves along the luminal surface were produced via microstereolithography. The use of beta-carotene as a photoabsorber within the PCLMA resin was investigated to improve the resolution of the groove features.

Secondly, conduits containing aligned polymer microfibres were produced. Highly aligned PCL fibres were produced by electrospinning and incorporated into tubes produced by microstereolithography. These conduits were characterised by analysing parameters such as fibre diameter and fibre packing density. The manufacture and assembly methods used to produce these conduits was of importance as there was emphasis on producing a design that would allow for easy implantation *in vivo* within a nerve defect.

Thirdly, an injection moulding technique was used to produce conduits with a smooth luminal surface, absent of the inherent microgroove features present on tubes produced by microstereolithography. These could then be tested in the *in vivo* model to help determine the effect of the inherent microgrooves on nerve regeneration.

3.2 Background

3.2.1 3D printing of conduits with guidance cues

As discussed in chapter 1, physical guidance cues are of interest for NGCs due to their potential ability to guide migrating Schwann cells and advancing axons in regenerating peripheral nerves. Different types of guidance cues have been incorporated directly into the design of conduits, such as aligned grooves in the luminal wall, or channels running through the conduit, forming a multi-lumen structure. These conduits are usually made by conventional manufacturing techniques – for example multi-lumen conduits fabricated by using an injection moulding technique with stainless steel wires forming the channels [104]. Conduits with aligned grooves are often fabricated using multi-step methods involving rolling and sealing grooved sheets [106], [183], [184] (see section 1.6.5.2). These grooved sheets are often patterned using grooved silicone substrates produced by a combination of photolithography and etching techniques. Conduits with aligned grooves have also been fabricated with a dry-jet wet spinning process using a micro structured spinneret [180], [261].

Microstereolithography may be a useful alternative method for the production of NGCs with aligned physical guidance cues. As a type of 3D printing, μ SL is a versatile technique that could allow the for the design and production of complex NGCs. The use of 3D printing in NGC production is not a novel idea but most groups have used these methods to produce simple NGCs. Examples include filament extrusion (FDM) for PCL conduits [262], inkjet printing of poly (lactide-co-caprolactone) conduits [263] and work at the university of Sheffield producing PEGDA [128] and PGS-M [129] conduits by μ SL (see section 1.4.4). 3D printing has also been used to produce more complex conduits with physical guidance cues, with most groups focussing on conduits with intraluminal channels. Demonstrating an indirect use of 3D printing, Hu et al. used a commercial system to 3D print moulds which were filled with gelatin methacrylate to produce conduits with multi-lumen structures [264]. For direct 3D printing of NGCs with physical guidance cues, micro-extrusion methods have been utilised by a number of groups. Jakus et al. demonstrated the use of a graphene/poly(lactide-co-glycolide) ink in an extrusion-based setup to produce conduits, including those with a multi-channel lumen [265]. Cellular, multi-lumen conduits have also been produced by extrusion-based 3D printing, as demonstrated by Owens et al.; using a bioprinter, cylindrical cellular units were deposited into a tubular structure, with sacrificial agarose rods forming three luminal channels. After fusion of the cellular units and a 7-day maturation period, the result was a fully cellular construct containing bone marrow stem cells and Schwann cells which was implanted into a rat sciatic nerve gap. Extrusion methods have also been used to produce complex conduits with a grooved structure.

Johnson et al. used a custom microextrusion-based 3D printing system to produce bifurcated silicone conduits with aligned grooves (groove spacing $\sim 160 \mu\text{m}$, groove depth $\sim 15 \mu\text{m}$) in which gradients of NGF and GDNF were also incorporated [87]. The effect of these grooves however was not tested with no conduits being produced without a grooved structure.

Though these extrusion-based methods may allow for the production of NGCs containing physical guidance cues, extrusion techniques can often be slow and offer limited resolution.

Microstereolithography could offer advantages to these techniques in terms of fast print times and high resolution. Despite these potential benefits, studies from only two groups have been found which use μSL to produce conduits with guidance cues. Previously discussed in section 1.4.4 is the work by Arcaute et al. [124] and Evangelista et al. [126] producing PEG-based conduits by μSL , using a commercial 3D systems, scanning stereolithography machine. The group fabricated multi-lumen conduits with seven 0.5 mm luminal channels. These were tested in the repair of a 10 mm sciatic nerve gap but demonstrated very poor regeneration potential compared to the single-lumen alternatives. Suri et al. fabricated similar conduits from methacrylated hyaluronic acid using a custom stereolithography set-up consisting of a UV lamp and a DMD. These seven-lumen conduits were cultured *in vitro* with Schwann cells to show biocompatibility but no *in vivo* testing was performed to show the effect of the multi-lumen structure [266].

As far as can be seen from the literature, there have been no studies using stereolithography to produce conduits with aligned grooves. This is probably due to limitations in resolution present with most systems, preventing the production of grooves of a relevant size. In this chapter, we will explore the direct printing of grooved NGCs using μSL .

3.2.2 Combining microstereolithography and electrospinning for NGCs

The production of fibre-filled conduits will combine products from microstereolithography and electrospinning, two techniques which have not often been combined in research. One instance of this is research at the University of Sheffield for the application of corneal repair where electrospun fibres were deposited directly onto PEGDA rings produced by microstereolithography. These were used as scaffolds to culture cells from rabbit cornea [267]. Microstereolithography and electrospinning have been combined for neural applications but only in simple forms. Lee et al. used μSL to print PEGDA on top of aligned PCL and PCL/gelatin fibres. The result was PEGDA scaffolds consisting of an array of rectangular wells and a base of electrospun fibres. The scaffolds supported the growth of rat embryonic primary cortical neurons with longer neurites and greater alignment

being expressed on the PCL/gelatin fibres compared to the PCL fibres [268]. This model may prove a useful platform for testing different materials or fibre types but it has been developed for *in vitro* testing. If the aim was to use the model for *in vivo* device testing, the system would need to be redesigned, using more complex methods to incorporate the electrospun fibres into a NGC.

3.2.3 Incorporating Electrospun fibres into NGCs

Electrospun fibres have been incorporated into NGCs in a variety of ways, a review of which was presented in section 1.6.3. Examples include rolling electrospun sheets into single-lumen tubes/tubes with multiple channels [105], [161]–[163], stacking or folding sheets within tubes [134], [154] and the formation of electrospun fibre bundles/‘yarns’ which are inserted into tubes [168], [169]. In the present study, electrospun fibres will be directly threaded into the lumen of tubes produced by μ SL. This is done without the formation of ‘yarns’ or sheets so that the fibres are evenly spread throughout the tube lumen and offer maximum surface area throughout the lumen for the guidance of regenerating cells.

The work in this thesis follows on from early stage work done in a pilot study by Pateman et al. (also discussed in section 1.6.3). Here electrospun PCL fibres were incorporated into PEG conduits produced by μ SL and used to repair a 3 mm mouse nerve injury [170]. Importantly, the packing density of the fibres were not quantified but merely described as ‘high’ and ‘low’. The axonal regeneration within the ‘low’ packing density tubes was improved compared to the ‘high’ packing density, implying that fibre packing density is an important parameter to quantify to understand the performance of these conduits *in vivo*. The results were however hugely variable, possibly owing to the poor conduit design and variation between the conduits within each group. This emphasises the importance of properly characterising the fibres within the conduit and optimising parameters such as packing density. With regards to conduit design, the fibres continued all the way to end of the conduits, leaving no space for insertion of the nerve stumps. This makes surgery more difficult and means that axons may not be guided into conduit. A design incorporating an empty cuff at each end of the conduit would result in easier surgery and greater chance of the axons being directed into the fibrous lumen of the conduit. The conduits also were fabricated from PEGDA which is not a clinically relevant material. Improvements on the design used in this early study are obviously necessary along with the use of proper characterisation techniques, both of which will be addressed in this chapter.

3.2.4 Conclusions

- Research in 3D printed conduits with physical guidance cues has focussed on multichannel conduits which have often not been tested *in vivo* or have demonstrated poor results.
- Examples of 3D printing of conduits with aligned grooves is limited, especially the use of μ SL.
- Analysis of fibre-filled conduits prior to *in vivo* use is essential to understand the effect of various design parameters such as fibre packing density.
- The design of such fibre-filled conduits should be improved to allow easier implantation and more reliable use.

3.3 Aims for this chapter

Produce and characterise nerve guidance conduits containing physical guidance cues.

To achieve this, the following objectives were addressed:

- 1) Produce and characterise grooved PCLMA conduits via μ SL
 - a) Investigate the effect of the inclusion of a light absorber (beta-carotene) on the quality of the grooved features produced
 - b) Assess groove size in the NGCs produced
- 2) Produce and characterise fibre-filled conduits by combining products from μ SL and electrospinning
 - a) Produce highly aligned electrospun PCL microfibres to a range of diameters
 - b) Incorporate electrospun fibres into plain conduits produced by microstereolithography and quantitatively assess the packing density of the fibres within the conduit
 - c) Develop an easily implantable conduit design by incorporating empty cuffs at either end of the conduit
- 3) Produce smooth conduits with no luminal features

3.4 Materials and Methods

In all the following experiments, PCLMA tubes were fabricated using the μ SL apparatus described in chapter 2. The standard resin used was 2M20 PCLMA prepolymer with 2% photoinitiator. Any other supplements are described as necessary.

3.4.1 Production of plain conduits

Plain conduits were produced to act as a control during the *in vivo* testing of the grooved, fibre-filled and smooth conduits. These were fabricated using μ SL as described in section 2.4.6.3. The DMD image used is displayed in Figure 42A. The conduits were designed to have an internal diameter of 850-950 μ m and a wall thickness of 250-300 μ m and these dimensions would be replicated by the different types of conduits produced hereafter.

During μ SL fabrication, the PCLMA resin was heated to 70°C and the image was uploaded onto the DMD. The laser power was set to 23-24 mW and the stage set to descend 6 mm at a speed of 0.015 mms^{-1} . This produced 6 mm tubes that could be laser-cut to shorter lengths (see section 3.4.9). This was to remove the end of the tubes that were often of a lower quality or had different dimensions to the rest of the tube. After fabrication, structures were washed and stored in IPA until use.

3.4.2 Production of conduits with aligned grooves

Conduits containing aligned grooves running longitudinally along the lumen were produced by μ SL to study of the effect of aligned grooves on peripheral nerve regeneration *in vivo*.

Grooved conduits were produced using μ SL as described for the plain conduits, using the same fabrication parameters and the DMD image in Figure 42B. Tubes were produced using the standard PCLMA resin with no additives and also PCLMA resin containing 0.075% beta-carotene as a photoabsorber. This was to demonstrate the effect of beta-carotene on the x-y resolution of the grooves. Plain tubes were also produced (using the DMD image in Figure 42A) with beta-carotene-containing PCLMA resin.

When using standard PCLMA resin the stage speed was set to 0.015 mms^{-1} , but for resin containing beta-carotene the stage speed was reduced to 0.010 mms^{-1} . This was due to the light absorbing

effects of the beta-carotene causing in the resin to cure more slowly so a slower stage speed was necessary to increase the curing time. After fabrication, structures were washed and stored in IPA until use. 6 mm tubes were produced and cut to a shorter length before use (section 3.4.9).

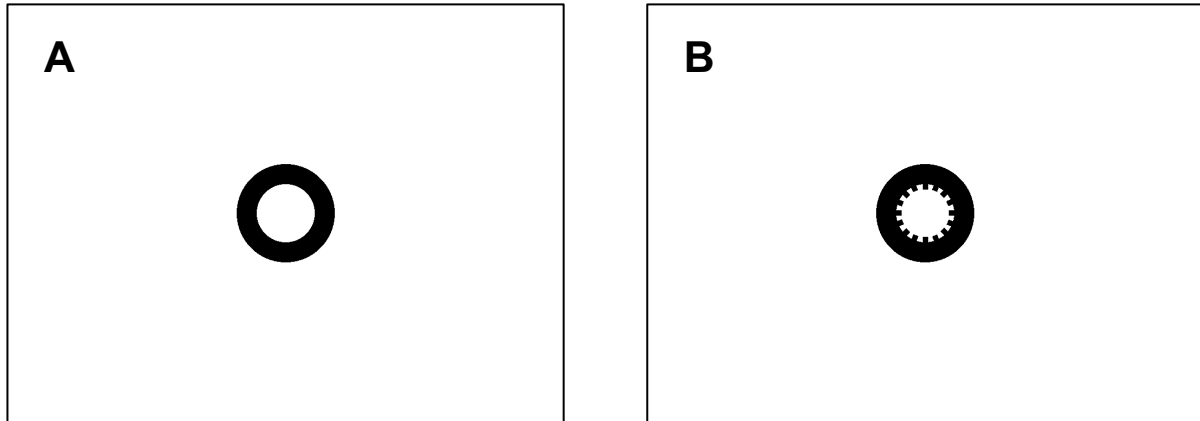


Figure 42. DMD Images used to produce plain tubes (A) and grooved tubes (B). The images were designed for the tubes to have an internal diameter of 850-950 μm and a wall thickness of 250-300 μm . The grooved tubes were designed to have an equal strut and groove size of around 80 μm .

3.4.3 Electrospinning for the production of aligned PCL fibres

Aligned PCL microfibres were produced by electrospinning. These would be combined with tubes produced by μSL to produce fibre-filled conduits to investigate the influence of aligned microfibres on peripheral nerve regeneration.

3.4.3.1 Preparation of PCL solutions for electrospinning

PCL, M_n 80 000 Da (Sigma-Aldrich) was dissolved in DCM to produce polymer solutions for electrospinning. 10-20 wt% solutions of PCL in DCM were produced by adding the polymer and solvent to a glass vial and placing in a 37°C water bath overnight to insure dissolution of the PCL.

3.4.3.2 Electrospinning of aligned fibres

The PCL solutions were electrospun as described previously by Daud et al. [153] and shown in Figure 43. A syringe was filled with polymer solution, capped with a blunt 20 G hypodermic needle, and placed in the syringe pump (WPI EU). A high voltage supply (Genvolt) was connected to the needle and used to ground the collector. The collector was a rotating mandrel powered by a motor (IKA Works) (mandrel diameter: 60 mm, rotation speed: 2200 rpm). The polymer solution was dispensed at a controlled rate (1-15 ml/hr) from the syringe, across the high voltage gap and fibres were deposited on aluminium foil wrapped around the rotating mandrel. For each combination of

parameters (polymer concentration and flow rate) the voltage was chosen so that a stable polymer jet was visible from the needle to collector (typical voltage 5-20 kV). The duration of electrospinning was varied (9-1440 seconds), depending on the fibre density required in the fibre sheet. The foil was then removed from the collector with the fibres attached. For all conditions, the needle-to-collector distance was 20 cm.

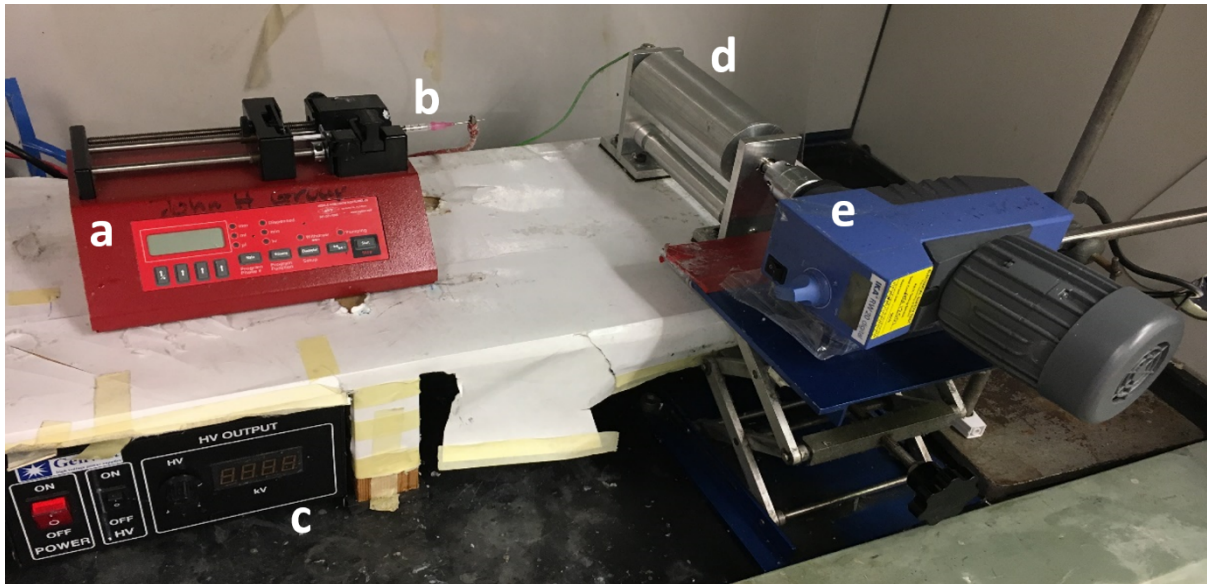


Figure 43. The electrospinning set-up consisting of a syringe pump (a) holding a syringe (b) capped with a blunt 20G needle which is connected to a high voltage supply (c). The rotating mandrel (d) is powered by a motor (e) and connected to the ground of the power supply (green wire).

3.4.3.3 Imaging of fibres via scanning electron microscopy

Electrospun PCL fibres were imaged by SEM (Inspect F50, FEI). Squares of aluminium foil, with the fibres attached, were cut from the electrospun sheets and placed on SEM stubs. Samples were sputter coated with gold (SC500, Emscope) prior to imaging.

3.4.3.4 Analysis of electrospun fibres

SEM images of electrospun fibres were analysed in ImageJ to determine the fibre diameter produced from each combination of electrospinning parameters. For each set of parameters, 3 fibre sheets were independently electrospun and a 1 cm x 1 cm square section was taken from each, for analysis. 4-5 SEM images (with around 10 individual fibres visible) were taken from different areas on each square sample. The diameter of every fibre in each image was measured so that an average of 151 fibres per parameter set were analysed - 3 samples per parameter set (N=3) and 50 fibres measured per sample (n=50).

3.4.4 Incorporating electrospun fibres into tubes produced by microstereolithography

Electrospun PCL fibres were incorporated into plain tubes to act as intraluminal guidance cues for regenerating cells. The tubes and fibres were produced separately by μ SL and electrospinning respectively before being combined into a composite device.

3.4.4.1 Plain tube production

Plain conduits were produced by microstereolithography as in section 3.4.1 and the plain DMD image shown in Figure 42A or a similar image with a different wall thickness. The standard PCLMA resin was used, with no photoabsorbers.

3.4.4.2 Inserting electrospun fibres into tubes

The electrospun fibres (section 3.4.3) were incorporated into the lumen of plain tubes using a careful threading technique. A 1-4 cm width of fibre sheet (still attached to the foil) was cut into a strip. The fibres at the end of the strip were lifted from the foil and rolled into a fine thread which was threaded through a plain PCLMA tube. The tube was then slid along the fibres so that the fibres lifted off the foil and entered the tube. Up to 13 tubes could be threaded onto the same bundle of fibres (Figure 44A), producing conduits containing the same density of fibres. The fibres were then cut with a scalpel between each tube to produce conduits with around 3 mm of fibres sticking out of each end (Figure 44B).

3.4.4.3 Cutting the ends of the fibre-filled tubes

To achieve a clean cut of fibres at the end of the tubes, the fibre-filled tubes were cut using a cryostat. The tubes were embedded upright in optical cutting temperature (OCT) gel and frozen with liquid nitrogen. The sample was mounted on the cryostat and 100 μ m slices were taken until the end of the tube was clearly visible. The sample was flipped and the second end cut in the same fashion. The number of 100 μ m sections taken from each end of the tube determined the final length of tube. The OCT gel was subsequently removed by washing the tubes overnight in distilled water. The cut, fibre-filled tubes were then stored in IPA until use.

Other methods of achieving a clean cut of the fibre ends were trialled for comparison to cutting on the cryostat. The ends of fibre-filled tubes were cut using a scalpel under different conditions: at room temperature and after freezing in liquid nitrogen. These methods proved less successful than

cutting using the cryostat (see section 3.5.4.2) so the cryostat method was selected and used from this point onwards.

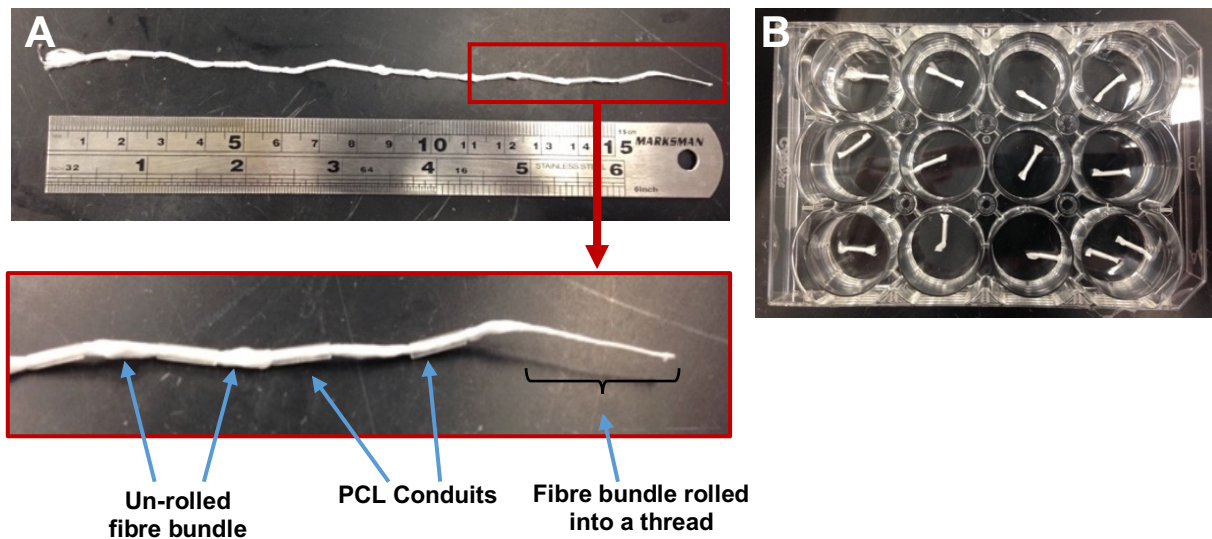


Figure 44. Threading electrospun PCL fibres into PCLMA tubes. A: 13 conduits threaded onto a single bundle of electrospun fibres and a magnified portion of A showing the conduits on the fibre bundle. B: individual fibre-filled conduits cut from the single thread.

3.4.5 Analysis of the packing density of the fibre-filled conduits by gas displacement pycnometry

To allow the production of fibre-filled conduits with specific and controllable fibre packing density, gas displacement pycnometry was used to measure the volume of the electrospun fibre bundles used to thread the tubes. Using the volume of the fibre bundle and the volume of the tube lumen it was possible to calculate the percentage volume of the conduit lumen occupied by fibres.

Electrospinning was carried out using a determined parameter set for the production specific diameter PCL fibres. Electrospinning duration was varied to produce electrospun sheets of varying densities. Fibres were removed from the aluminium foil and formed into bundles as if threading into tubes. 1 cm lengths of the fibre bundle were cut and measured using a gas pycnometer (AccuPyc II 1340, Micrometrics) (fill pressure:19.5 psi, equilibrium rate: 0.005 psi/min, number of cycles: 20). For each group, 3 fibre bundles were measured (1 sample each from 3 independently produced electrospun sheets) to calculate the average volume of the fibre bundles (N=3, n=1).

Optical micrographs were used to measure the internal diameter of the μ SL tubes (see section 3.4.11) and calculate the luminal area. This was multiplied by a 1 cm tube length (matching the 1 cm fibre bundle) to calculate the luminal volume. 5 independently fabricated tubes were measured to obtain the average luminal volume. The fibre packing density (percentage fill of conduit lumen) could be calculated using the measured volume of the fibre bundle and the measured luminal volume (Equation 6).

$$\text{Packing density} = \frac{\text{Average volume of 1 cm fibre bundle}}{\text{Average volume of 1 cm tube lumen}} \frac{\text{(Measured from He Pycnometry)}}{\text{(Measured from microscopy images)}} \times 100 (\%)$$

Equation 6. Calculation of fibre packing density of fibre-filled conduits. The result is the percentage fill of the conduit lumen, occupied by electrospun fibres.

3.4.6 Analysis of fibre-filled conduits via micro-computed tomography

Fibre-filled conduits were imaged using micro-computed tomography (micro-CT) using a SkyScan 1272 (Bruker) to visualise the fibres within the conduits. Scanning parameters were as follows. Source voltage: 40-50 kV, source current 200-250 μ A, rotational step: 0.7°, sample rotation: 180, filter: none, pixel size: 3-4 μ m. Scans were reconstructed using Nrecon (Bruker) to obtain either transverse or longitudinal slices of the sample. Images from the micro-CT reconstructions were used to demonstrate the possibility of measuring packing density using micro-CT and to compare with the pycnometry data. Reconstructed transverse images were processed into binary images via thresholding in ImageJ. The threshold value was chosen so that the fibres in the image were converted to black pixels and the empty luminal space was represented by white pixels. The area occupied by the fibres could then be easily calculated from these images by calculating the percentage of black pixels.

3.4.7 Production of fibre-filled tubes for *in vivo* use

3.4.7.1 Modular conduit design: thin-wall tube with cuffs

When designing the fibre-filled conduits, to allow for easier implantation *in vivo* it was desired to produce fibre-filled tubes with empty cuffs at either end. This was to allow the insertion and fixation of the proximal and distal nerve stumps during the nerve repair.

When threading electrospun fibres into tubes and cutting with the cryostat (described in section 3.4.4) it was only possible to create fibre-filled tubes in which the fibres were continuous to each end of the tube. To produce the empty cuff, the fibre-filled conduits were produced in three-part

modular design described in Figure 45. Thin-wall tubes were produced to house the fibres produced by electrospinning and the ends were cut on the cryostat. 3D cuffs were then produced to fit over the ends of the fibre-filled tubes.

3.4.7.2 Microstereolithography of thin-wall tubes and 3D cuffs

Thin-wall tubes were produced using μ SL as described for the plain conduits (section 3.4.1), using the DMD image in Figure 45(i). These tubes were designed to have an internal diameter to match the plain conduits in section 3.4.1 but half the wall thickness. Tubes 5 mm in length were produced which were later cut to 3 mm after filling with fibres.

The 3D cuffs were produced by μ SL, using the technique for production of 3D structures (section 2.4.6.4) by changing the DMD image displayed as the z-stage descended into the polymer. 2 separate DMD images were necessary (Figure 45 (ii) and (iii)). The DMD image (ii) was designed to produce the 1.5 mm long sleeve to fit over the thin-wall tube. The DMD image (iii) was designed to produce the 1 mm long empty cuff with a wall thickness equal to that of the inner tube plus the sleeve. This design meant that the assembled conduit was to have the same internal diameter and wall thickness as the plain tubes used as a control (internal diameter: 850-950 μ m and wall thickness: 250-300 μ m).

Both the thin-wall tubes and the 3D cuffs were produced using standard PCLMA resin with no photoabsorber. Microstereolithography parameters were as follows. Laser power: 25 mW, stage speed: 0.015 mms^{-1} , resin temperature: 70°C. After fabrication, structures were washed and stored in IPA until use.

3.4.7.3 Assembly of tube and cuffs

Thin-wall tubes were filled with fibres and cut to 3 mm length on the cryostat (as described in section 3.4.4) leaving a clean cut with fibres extending to the end of the tube. These were then assembled with the 3D cuffs as follows. The fibre-filled tubes and the 3D cuffs were removed from the IPA and left to dry. The outside of each tube was individually painted with a small amount of PCLMA resin and a 3D cuff was slotted over each end (Figure 45). The assembled construct was exposed to UV irradiation using a high power UV lamp (OmniCure S1000, Exfo) for 1 minute at full power. The construct was flipped over and exposed for a further 1 minute at full power. This UV exposure cured the PCLMA resin which acted as a 'glue' to secure the cuffs in place.

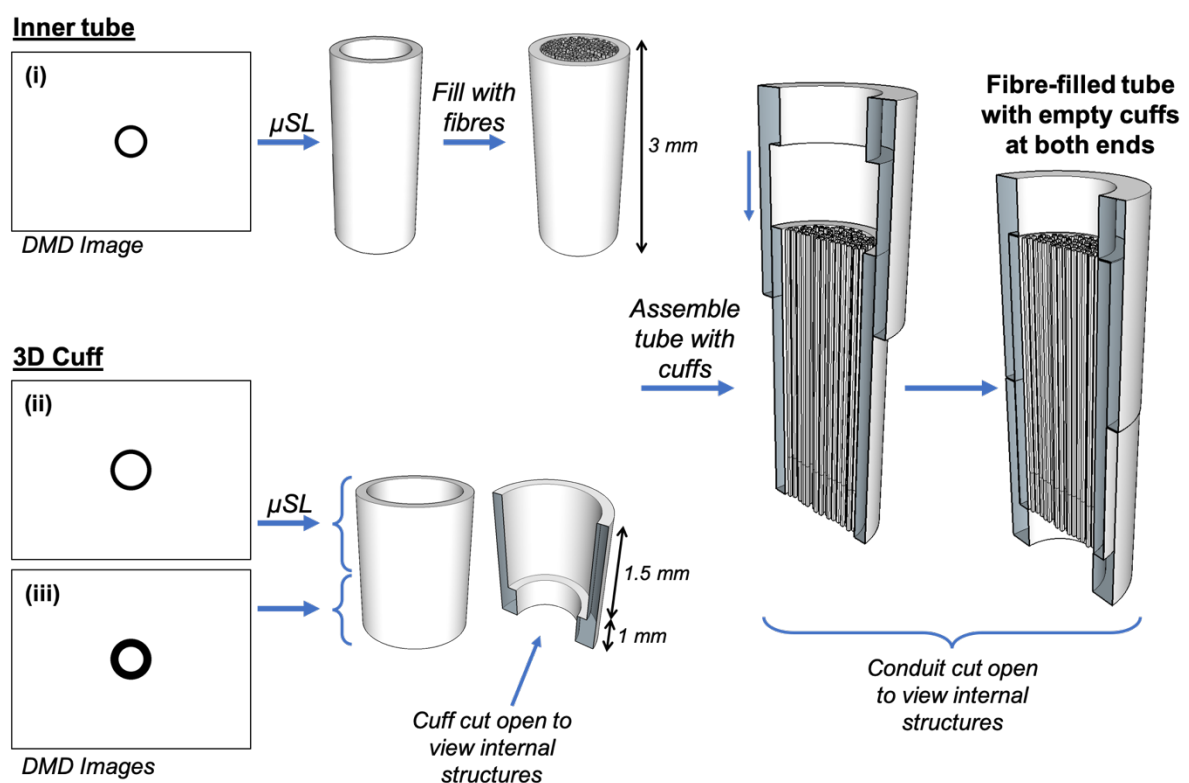


Figure 45. The design and assembly process for the fibre-filled tubes with empty cuffs. The inner tube was filled with fibres and the 3D cuffs were slotted over each end. On the left are the DMD images used to produce the thin-wall inner tube (i) and the 2 sections of the 3D cuff (ii: the sleeve to slot over the inner tube; iii: the empty cuff of the assembled tube).

3.4.8 Production of smooth tubes via injection moulding

PCLMA NGCs were produced with completely smooth luminal and outer surfaces, without the inherent microgrooves present from the use of the DMD in μ SL. This was to assess whether the inherent microgrooves present on the μ SL tubes had an effect on peripheral nerve regeneration.

The smooth conduits were produced by injection moulding with the mould described in Figure 46. PCLMA resin was pipetted into a void between a silicone tube (forming the outer diameter of the conduit) and a hypodermic needle (forming the lumen of the conduit). The shaft of the hypodermic needle was then held in place in the centre of the silicone tube with two P1000 pipette tips as shown. The filled mould was placed under a UV lamp (OmniCure S1000, Exfo) for 1 minute at 30% power followed by 3 minutes at full power. The construct was flipped and exposed for a further 4 minutes at full power to ensure even curing of both sides.

A 20 G needle was used (outer diameter: 0.9 mm) and the silicone tube had an internal diameter of 1.5 mm. This was to result in a PCLMA tube with internal diameter of around 900 μ m and a wall thickness of around 300 μ m. Long tubes (~25 mm) were produced which were laser cut into multiple shorter tubes prior to use (section 3.4.9).

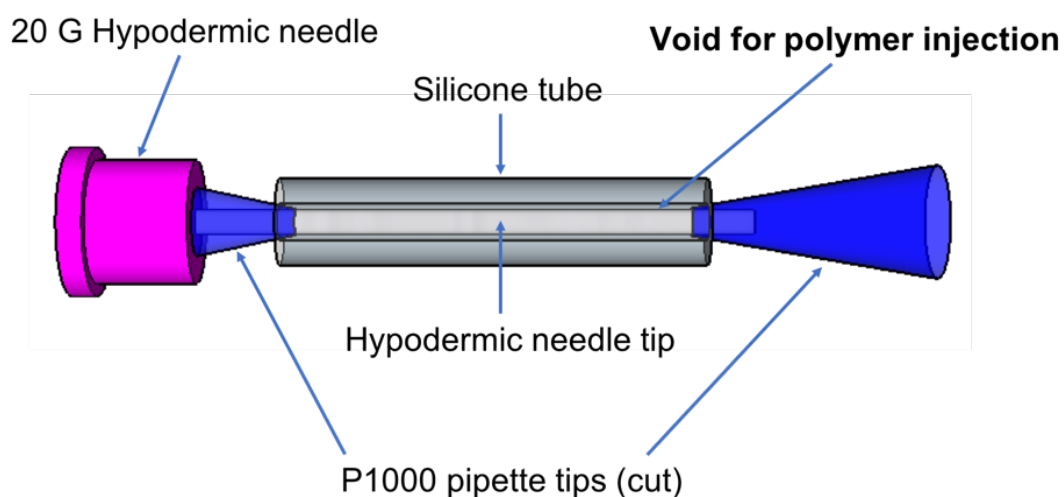


Figure 46. The mould construction used for production of smooth PCLMA tubes via injection moulding. A 20 G hypodermic needle was held in place inside a silicone tube by two P1000 pipette tips. The void between was filled with PCLMA resin which was cured using a high power UV lamp.

3.4.9 Laser-cutting of conduits

All conduits types (plain, grooved, fibre-filled with cuffs and smooth) were laser-cut to 4.5 mm in length before using *in vivo*. This was to ensure that all conduits were the same length before using in experiments and to remove the ends of the conduits which were often of a lower quality than the middle portion of the tube. Conduits were removed from IPA and left to dry before cutting. The laser cutter (Mini 18 Laser, Epilog Laser) was used at 30% speed, 10% power and 2500 Hz frequency. 3 passes of the laser were required to cut through the tubes. After cutting, conduits were washed and stored in IPA until use.

3.4.10 Imaging of conduits via scanning electron microscopy

To observe the overall quality of the 3D printed constructs and the fibre-filled conduits, samples were sputter coated with gold and imaged via SEM as in section 3.4.3.3 for the electrospun fibre samples.

3.4.11 Optical microscopy for measurement of tube dimensions

Optical microscopy images were used to obtain accurate measurements of the internal diameter and wall thickness of the conduits. Tubes were laser-cut to remove the ends that were often of a slightly different dimension to the middle portion of the tube. The conduits were then placed upright on a microscope calibration slide and imaged with a bottom-up microscope (Motic AE2000) equipped with a digital camera (Moticam 2, Motic). For each conduit type, at least 5 different conduits were imaged (1 image of each end obtained) (N=5). Analysis was performed with ImageJ. For each image, 4 internal diameter measurements were taken and 8 wall thickness measurements (Figure 47A) to obtain average values. For the grooved tubes, measurements were taken from the base of the grooves (Figure 47B).

From the same images of the grooved tubes, measurements were made to determine the size of the grooves. Three different distances were measured: strut width, groove width and peak-to-peak width (described in Figure 47C). 6-8 measurements for each groove parameter were taken from 5 grooved tube images and averaged to calculate mean values (N=5, n=6-8).

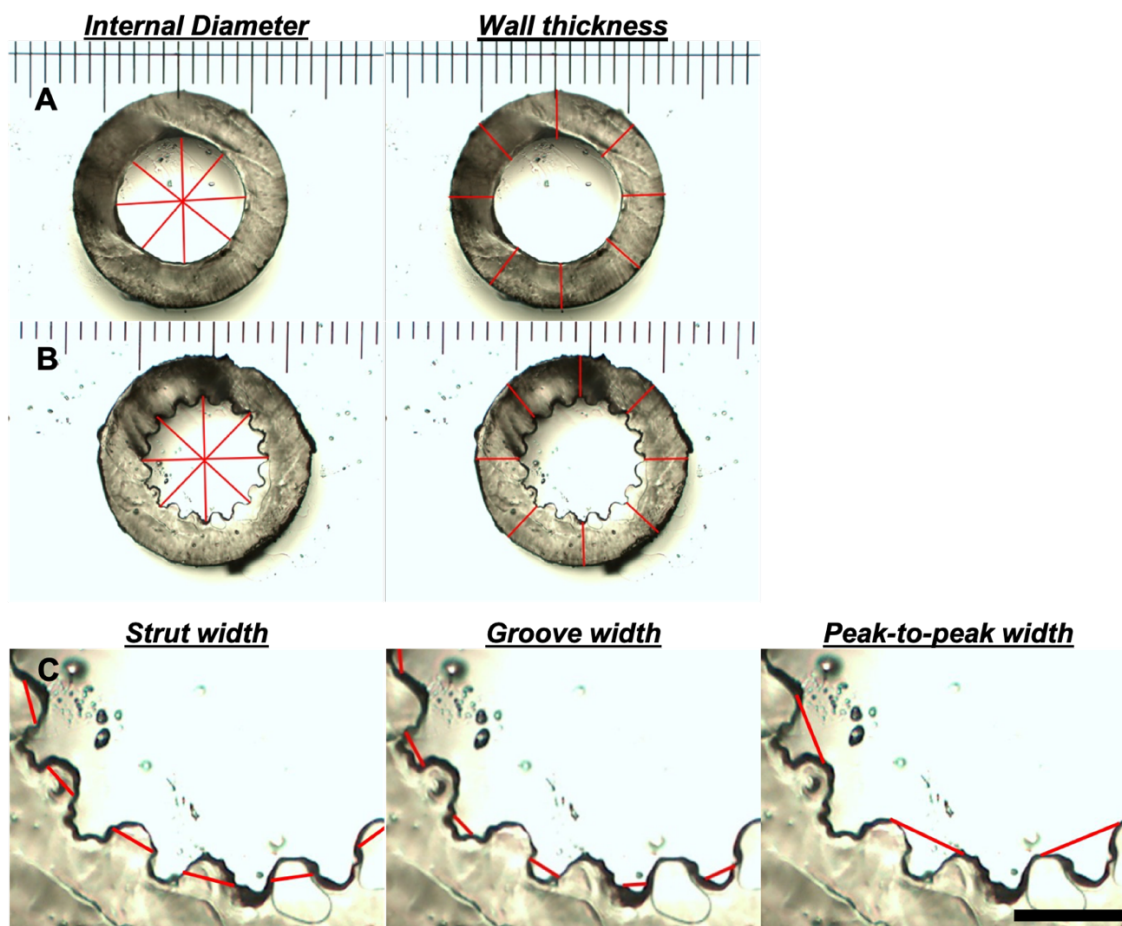


Figure 47. Optical microscopy images of plain and grooved tubes showing the measurements made in red. Internal diameter and wall thickness measurements from plain (A) and grooved (B) tubes (Scale divisions: 100 μm). C: The three different groove measurements made from the grooved tubes (Scale bar: 200 μm).

3.4.12 Cryosectioning of conduits

To further investigate the quality of the conduits, some were sectioned to visualise the internal features not visible from imaging whole conduits. Conduits were embedded in OCT gel and frozen using liquid nitrogen. Using a cryostat, 100 μm sections were obtained and mounted on a slide to image with optical microscopy. Grooved conduits were sectioned to analyse groove quality down the length of the tube to obtain further information than just visualising the grooves at the top opening. Thin-wall tubes assembled with cuffs were sectioned to determine the fit between the inner tube and the cuffs and ensure there was no empty space. The overall wall thickness of the tube and cuff was measured to ensure it was similar to the plain conduits.

3.4.13 Statistical analysis

Statistical analysis was performed with GraphPad Prism. Normality of the data was tested using Shapiro-Wilk normality test. To test for significant differences between groups, normally distributed data was tested with one-way ANOVA followed by Tukey's multiple comparison tests and for non-normally distributed data, Kruskal-Wallis test was performed followed by Dunn's multiple comparison tests. $P < 0.05$ was used to determine a significant difference. All data is presented as mean \pm SD.

3.5 Results

3.5.1 Plain conduits produced by microstereolithography

Plain PCLMA conduits were produced via μ SL and were representative of those in Figure 28. They possessed the characteristics described in section 2.5.3.1 i.e. the inherent microgrooves present from the use of the DMD. The tube dimensions were as follows. Internal diameter: $916\pm 44\ \mu\text{m}$; wall thickness: $284\pm 18\ \mu\text{m}$ (N=12).

3.5.2 Grooved conduits produced by microstereolithography

3.5.2.1 Effect of beta-carotene on groove quality

Grooved conduits were also fabricated via μ SL. For the tubes fabricated from PCLMA resin containing no beta-carotene, the grooves were well defined at the top of tube but became over-cured further down the tube. We can see from the cryostat sections in Figure 48 that further down the tube, the grooves lost definition and began merging together. The result was an undulating pattern around the tube lumen with little height difference between the top of the struts and the bottom of the grooves.

With the addition of beta-carotene, the structure of the grooves was maintained as we look further down the tube. There was still a slight decrease in groove quality as we move down the tube but the strut height/groove depth was maintained much more compared to the tube printed with resin containing no beta-carotene. The struts and grooves were more defined in the tube containing 0.075% beta-carotene compared to the tube with 0.05% beta-carotene.

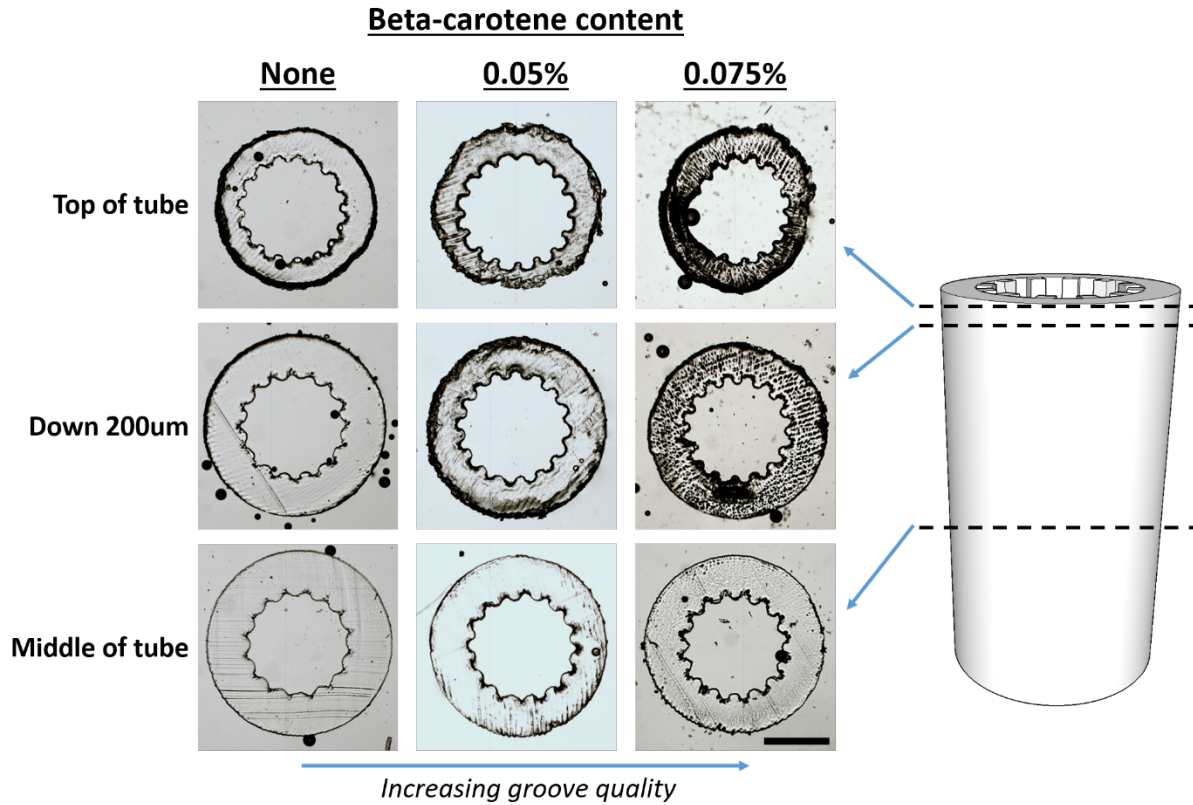


Figure 48. Sections of grooved tubes (obtained using a cryostat) showing the appearance of the grooves down the length of the tubes. Groove quality decreases towards the middle of the tube but improves with increasing amount of beta-carotene in PCLMA resin. Scale bar: 500 μm .

3.5.2.2 SEM imaging of grooved tubes and plain tubes (containing 0.075% beta-carotene)

Grooved and plain tubes were produced by μSL with PCLMA resin containing 0.075% beta-carotene. Tubes were laser-cut and imaged with SEM (Figure 49). The images provide us with greater detail and allow us to visualise the grooved structures. From Figure 49A-D we can see that the grooves in the grooved tubes were well defined and had a consistent structure around the perimeter of the lumen. The plain tubes (Figure 49E-F) were of a very similar appearance to the plain tubes produced using PCLMA resin without beta-carotene (Figure 28). The inherent microgroove features from the DMD were visible in both tube types but more evident in the plain tubes.

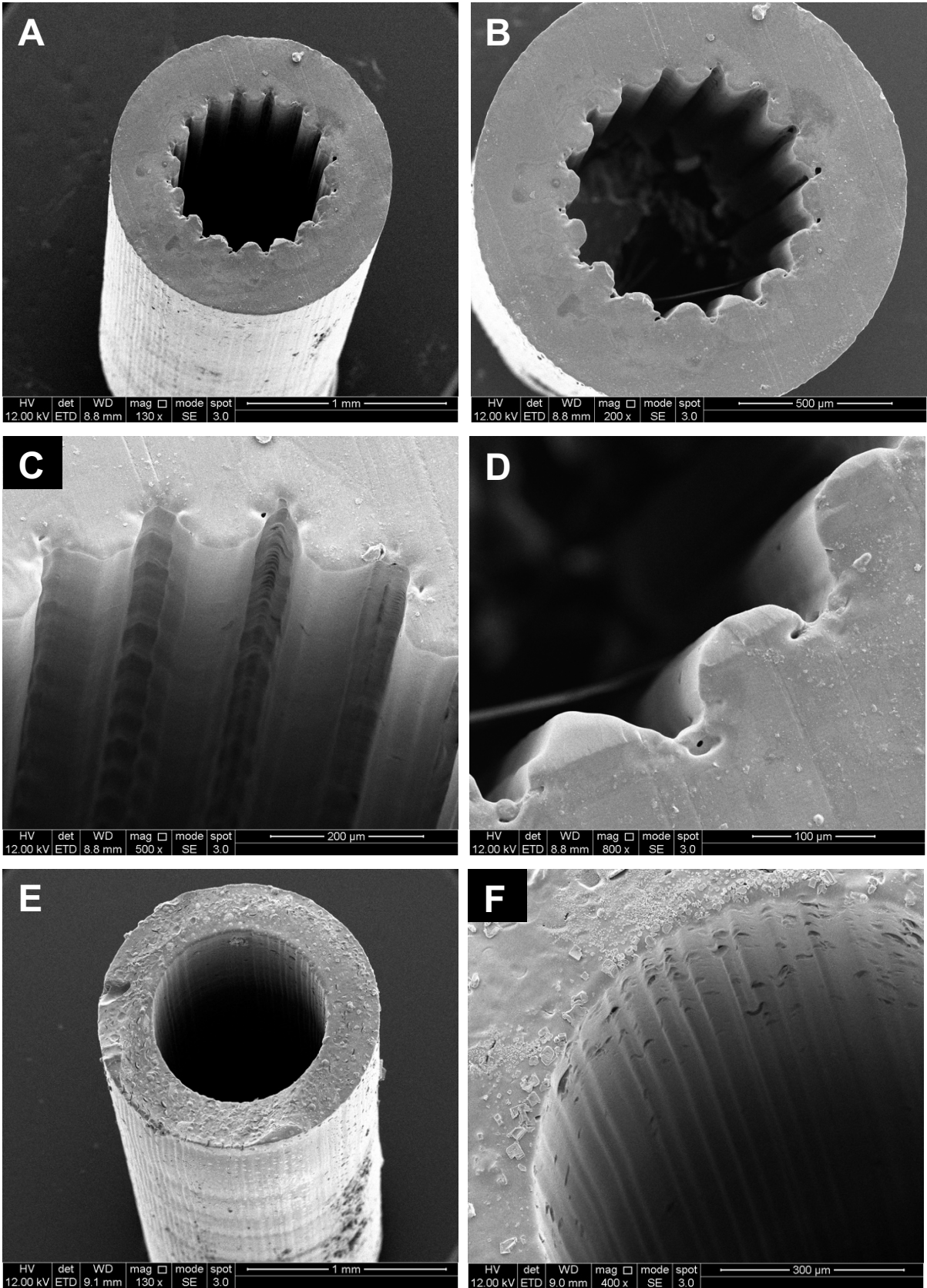


Figure 49. SEM of PCLMA tubes fabricated by μ SL using PCLMA resin containing 0.075% beta-carotene. A-D: Grooved tubes with well-defined grooves, consistent around the perimeter of the lumen. E, F: Plain tubes with circular lumen and visible microgroove features.

3.5.2.3 Measurements of grooved and plain tubes from optical microscopy and SEM

The dimensions of the plain and grooved conduits (containing 0.075% beta-carotene) were measured by optical microscopy. Measurements can be found in Table 7 and an annotated version of the image in Figure 49D showing the groove dimensions can be found in Figure 50. Internal diameter and wall thickness measurements were compared between the two conduit types and the plain conduits made without beta-carotene (section 3.5.1) (one-way ANOVA with Tukey’s multiple comparisons). The internal diameter ($897\pm 8\ \mu\text{m}$) and wall thickness ($283\pm 2\ \mu\text{m}$) of the plain conduits (containing beta-carotene) were not significantly different to those of the plain conduits made without beta-carotene. Comparing the two conduit types containing beta-carotene: the grooved conduits had a slightly reduced internal diameter ($833\pm 15\ \mu\text{m}$) compared to the plain conduits (significant difference, $P=0.02$). They also had a slightly increased wall thickness ($304\pm 11\ \mu\text{m}$) compared to the plain conduits (not significant). The decreased internal diameter and increased wall thickness was due to the merging of the groove features at the base of the struts. This also resulted in a rounded V-shape groove as opposed to the square groove designed in the DMD image.

The inherent microgrooves present on the surface of the conduits were also measured from SEM images of the plain tubes. The microgroove (peak-to-peak) width was $39\pm 6\ \mu\text{m}$ and strut width was $12\pm 1\ \mu\text{m}$. These measurements were not significantly different to the measurements of the microgrooves on the plain tubes (without beta-carotene) presented in section 2.5.3.1 (one-way ANOVA with Tukey’s multiple comparisons).

Table 7. Measurements of Grooved and Plain tube dimensions from optical microscopy images. N=5 for internal diameter and wall thickness measurements. N=5, n=6-8 for groove measurements.

Measurements (mean±SD)	Beta-carotene-containing conduits	
	Grooved Conduit	Plain Conduit
Internal Diameter	$833\pm 15\ \mu\text{m}$	$897\pm 8\ \mu\text{m}$
Wall thickness	$304\pm 11\ \mu\text{m}$	$283\pm 2\ \mu\text{m}$
Groove width	$48\pm 10\ \mu\text{m}$	-
Strut width	$83\pm 10\ \mu\text{m}$	-
Peak-to-peak width	$143\pm 14\ \mu\text{m}$	-

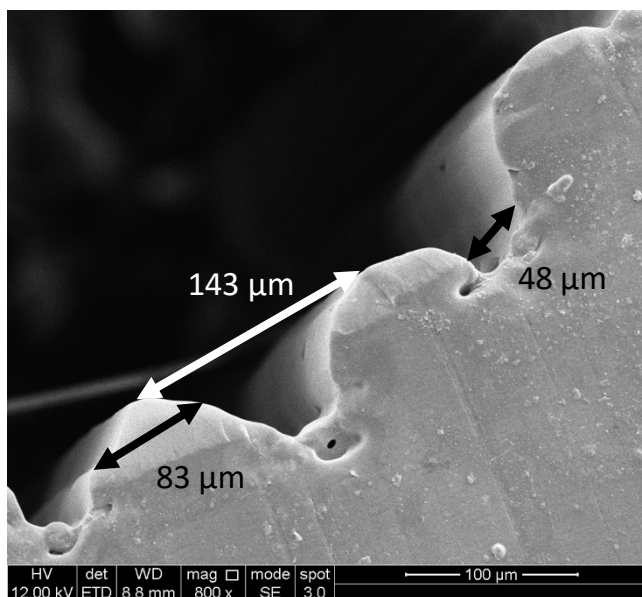


Figure 50. Annotated image of a grooved tube showing the average groove width (48 μm), strut width (83 μm) and peak-to-peak width (143 μm).

3.5.3 SEM analysis of PCL fibres produced by electrospinning

Electrospun PCL fibres were fabricated under a variety of different electrospinning conditions and imaged via SEM (Figure 52). All fibres displayed a high degree of alignment. Polymer concentration and flow rate were varied to determine the effect of these conditions on fibre diameter. Table 8 and Figure 51 outline the different electrospinning conditions investigated and the resulting fibre diameters, measured from SEM images (Figure 52). Fibre diameter steadily increased with increasing polymer flow rate, with significant differences between almost all groups of fibres fabricated using different flow rates ($P \leq 0.01$, Kruskal-Wallis with Dunn's multiple comparison test). The only exceptions were groups E and F which were not significantly different (6 vs 9 ml/hr flow rate, 15 wt% PCL) and group H (11 ml/hr, 15 wt%) which was not significantly different from G (9 ml/hr, 20 wt%) or I (15 ml/hr, 15 wt%).

Polymer concentration did not have a great effect on fibre diameter. Non-significant differences in fibre diameter were found all groups pairs with the same flow rate but different polymer concentration (A vs B, C vs D, F vs G and I vs J). However, for flow rates of 9 ml/hr and 15 ml/hr, a higher polymer concentration resulted in lower variability of fibre diameter, demonstrated by the smaller standard deviation in the fibres produced with the 20 wt% vs the 15 wt% PCL solution (G vs F and J vs I).

Table 8. The different parameter sets used in the electrospinning of PCL and the fibre diameters produced.

Parameter Set	Flow rate (ml/hr)	Polymer concentration (wt%)	Mean fibre diameter (μm)	Standard deviation (μm)
A	1	10	2.25	1.00
B	1	15	2.60	1.31
C	4	10	5.29	0.66
D	4	15	5.95	0.82
E	6	15	8.21	1.99
F	9	15	9.39	2.86
G	9	20	9.88	1.92
H	11	15	11.38	3.02
I	15	15	14.10	5.34
J	15	20	15.68	3.07

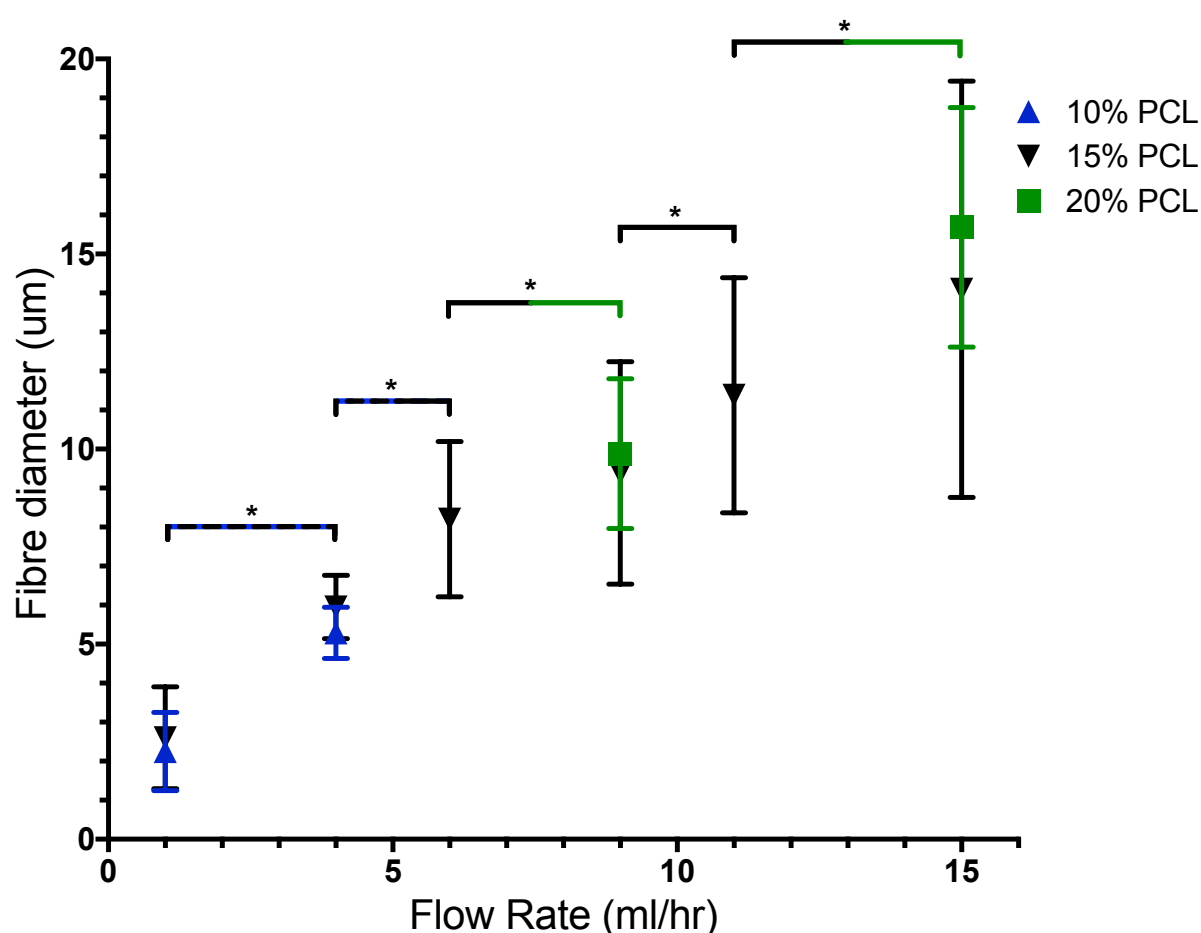


Figure 51. The effect of flow rate and polymer concentration on the diameter of electrospun PCL fibres. Values presented as mean \pm SD (N=3, n=50 average). Concentration of PCL displayed as wt% in DCM solution. * denotes significant difference between the groups indicated by the colour of the brackets ($P \leq 0.01$, Kruskal-Wallis with Dunn's multiple comparison test).

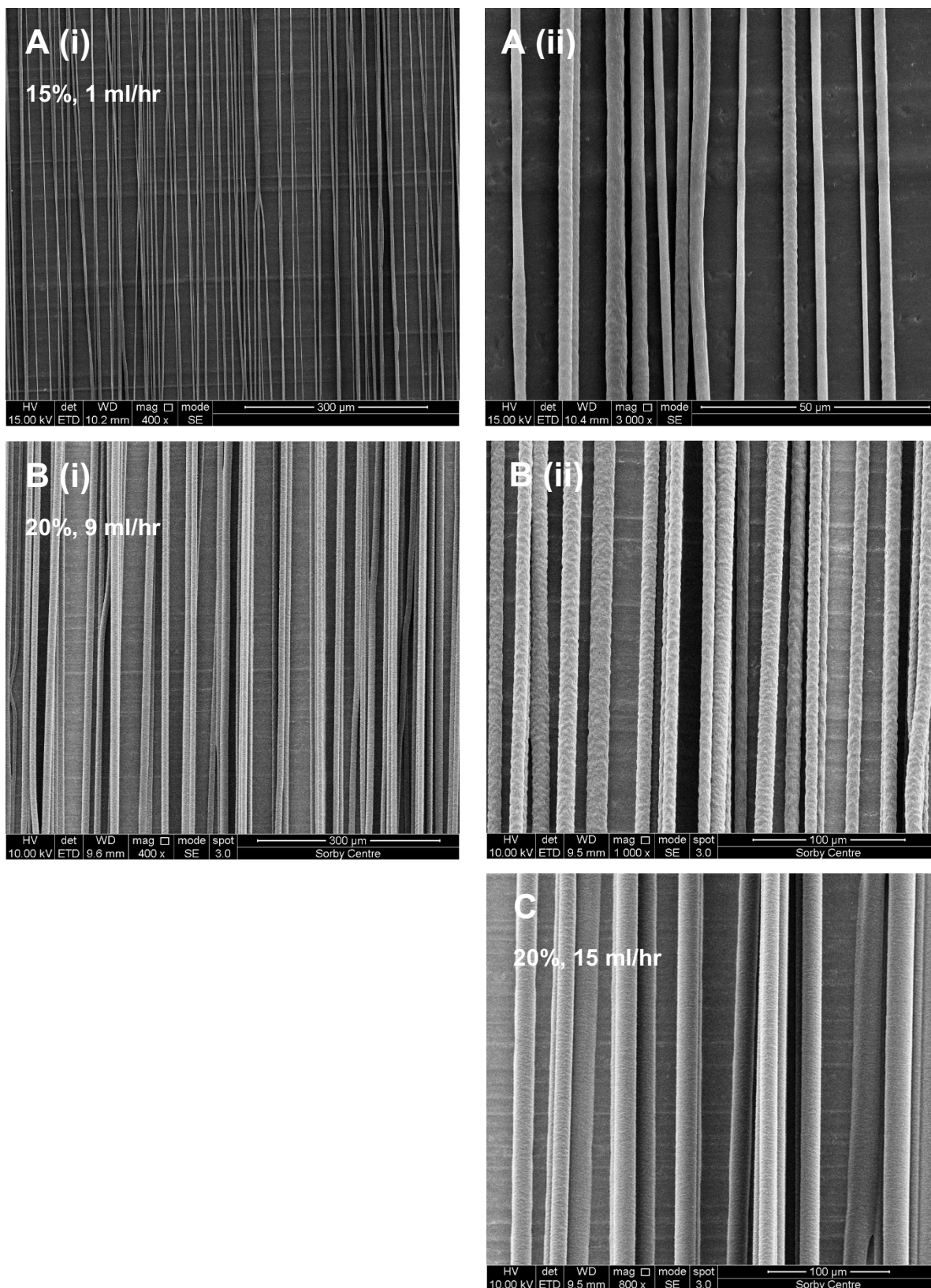


Figure 52. SEM images of aligned PCL microfibrils fabricating using different parameters. A: 15% PCL solution, 1 ml/hr. B: 20% PCL solution, 9 ml/hr. C: 20% PCL solution 15 ml/hr. Low magnification images (400x) displayed on the left and high magnification images (3000x, 1000x, 800x, respectively) displayed on the right.

3.5.4 Fibre-filled conduits – general observations via SEM and micro-CT imaging

3.5.4.1 Visualisation of internal fibres with micro-CT

Plain PCLMA tubes (section 3.5.1) were filled with PCL fibres as described in section 3.4.4.2 and imaged with micro-CT to visualise the packing of the fibres. Figure 53 shows a longitudinal cross-sectional image obtained from the micro-CT scan. The fibres were visible within the lumen of the conduit and retained a good level of alignment after the packing process. The fibres were also evenly spread throughout the conduit lumen.

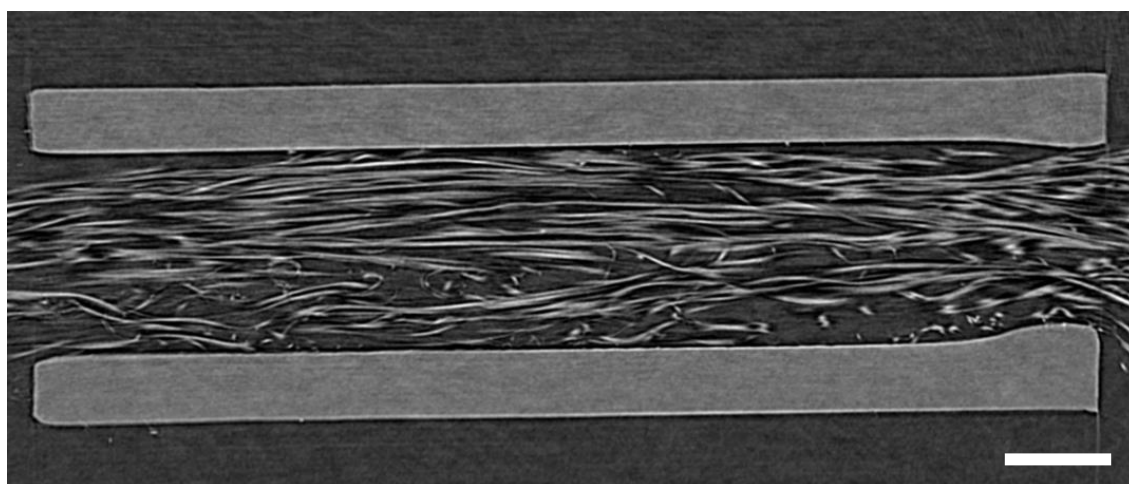


Figure 53. Longitudinal cross-sectional image of a fibre-filled tube with the aligned PCL microfibres visible within the lumen. Scan parameters - Source voltage: 50 kV, source current 200 μ A, rotational step: 0.7°, filter: none, pixel size: 4.0 μ m. Scale bar: 500 μ m.

3.5.4.2 Visualisation of conduit ends with SEM – comparison of different cutting techniques

Similar PCLMA tubes containing PCL fibres were cut using the cryostat (section 3.4.4.3) and imaged with SEM. The images in Figure 54 reveal a nice, clean cut from the cryostat with all the individual fibre ends distinctly visible. The conduit displayed here has an arbitrary ‘high’ packing density of PCL fibres.

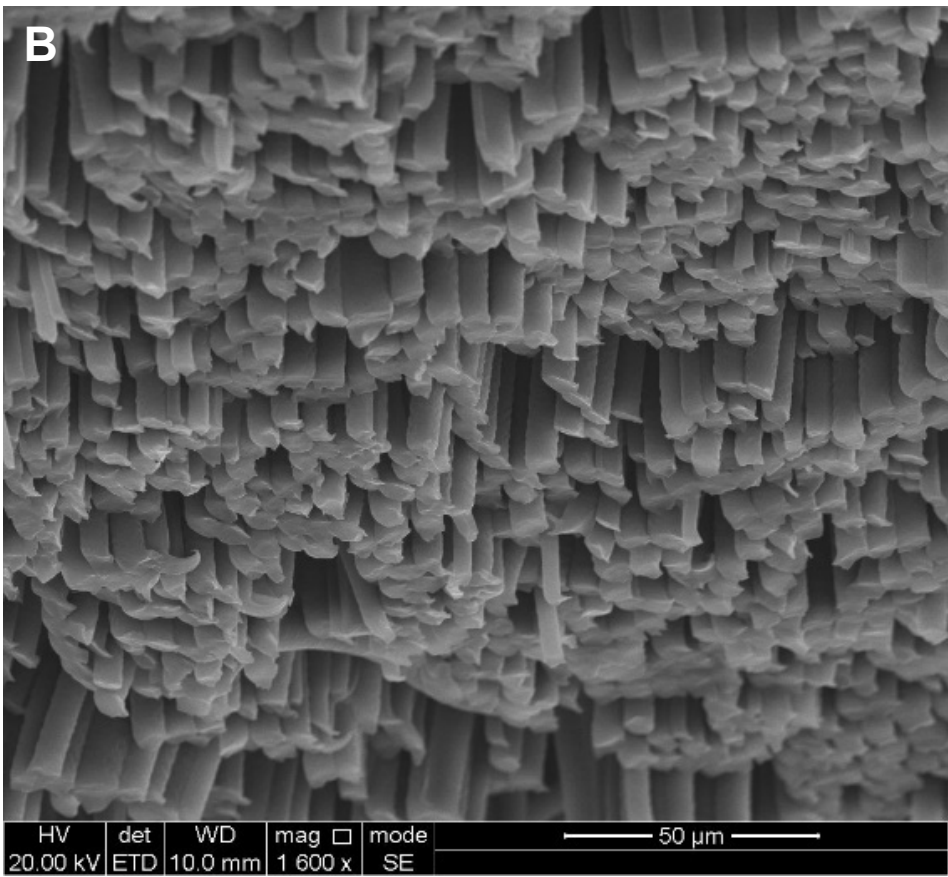
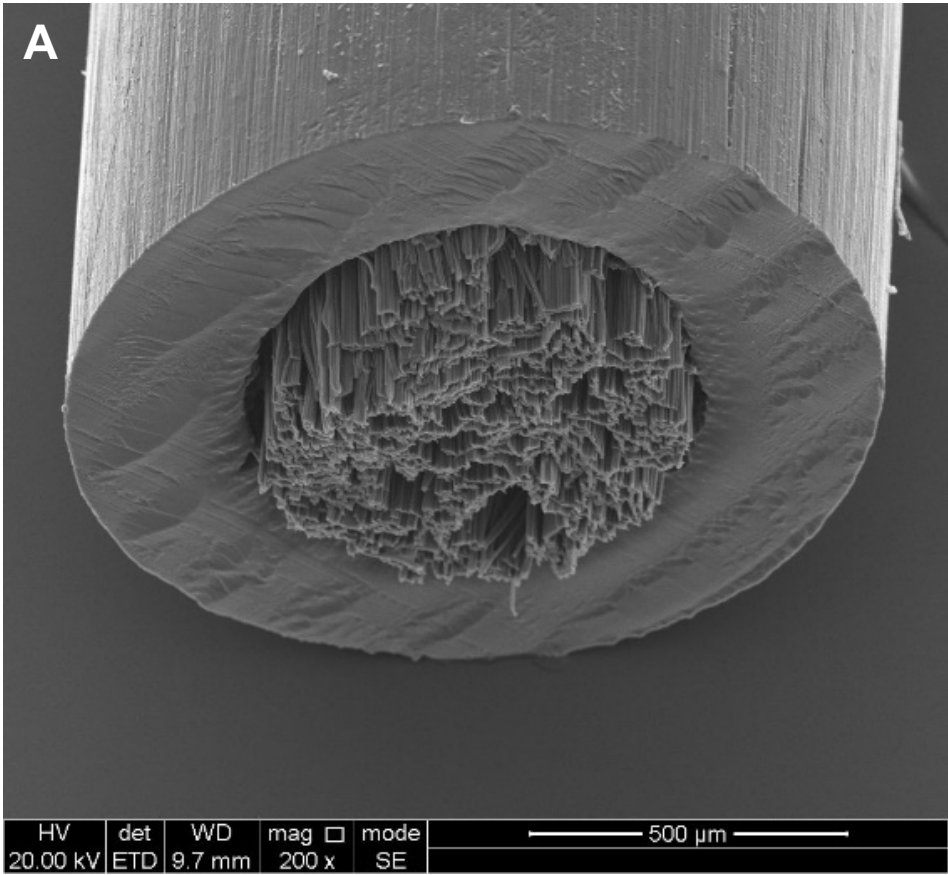


Figure 54. SEM images of PCL tubes containing aligned PCL microfibres, cut on the cryostat. A: Tube end with clean-cut fibres. B: Close up image of cut fibre ends.

Fibre-filled conduits were cut on the cryostat (as above) as cutting with a scalpel disrupted the ends of the fibres and often caused the fibres to clump together. Other cutting methods were trialed, however these were not successful in achieving a clean cut of the fibres at the ends of the tubes. For comparison, SEM images of fibre-filled conduits cut by these alternative methods can be found in Figure 55. Figure 55A shows a fibre-filled conduit cut with a scalpel (at room temperature). This compressed the fibres together so that the individual fibre ends were no longer distinguishable. Fibres were also bunched in the centre of the lumen. Freezing the conduit in liquid nitrogen prior to cutting with a scalpel achieved improved cuts (Figure 55B), preserving the individual fibre ends but there was still more disruption compared to cutting with the cryostat. The PCLMA tube also became brittle at the low temperature of the liquid nitrogen and often cracked on cutting (Figure 55C).

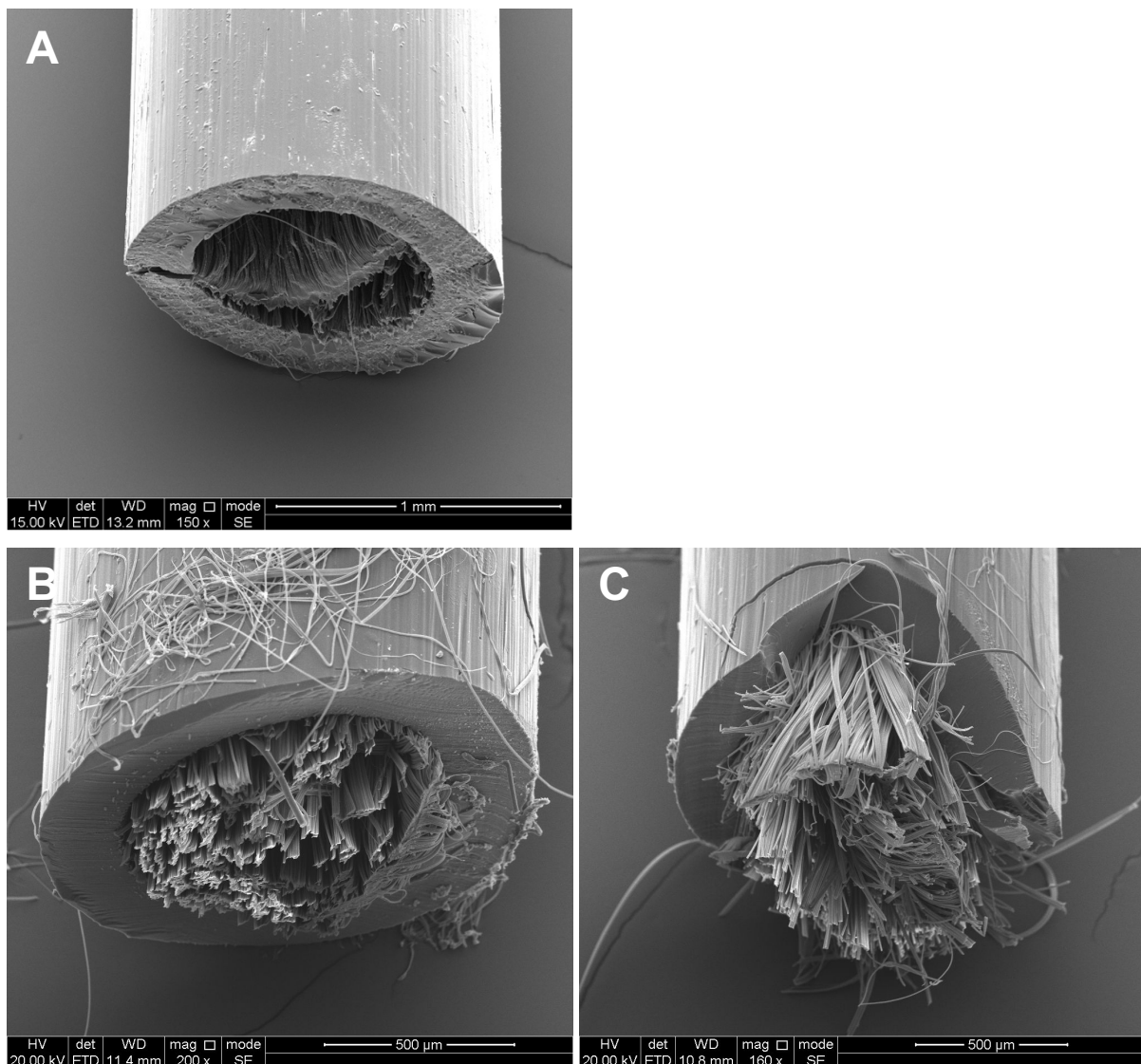


Figure 55. Fibre-filled conduits cut with a scalpel. A: Conduit cut with a scalpel at room temperature. B/C: Conduits frozen in liquid nitrogen and cut with a scalpel.

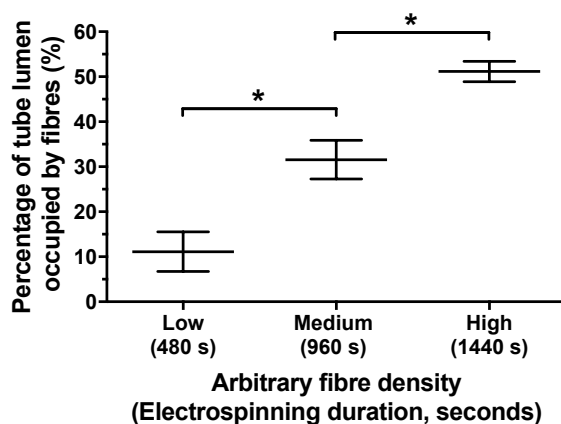
3.5.5 Analysis of fibre packing density with gas displacement pycnometry

Gas displacement pycnometry was used as a method for assessing the packing density of PCL fibres within the PCLMA tubes. 2 μm diameter PCL fibres were electrospun for varying durations and formed into bundles. The volume of these bundles was measured with gas displacement pycnometry. The bundles were then threaded into plain PCLMA tubes to produce conduits containing three different packing densities of fibres (Figure 56A). Longer electrospinning duration lead to a greater number of fibres deposited on collector therefore a larger fibre bundle which filled more of conduit lumen. 'Low' packing density conduits were produced with fibres electrospun for 8 minutes which filled around 10% of the conduit lumen. Increasing electrospinning duration to 16 minutes and 24 minutes produced 'medium' and 'high' packing density conduits with respectively around 30% and 50% fill of the conduit lumen. All three groups were significantly different ($P < 0.002$, one-way ANOVA with Tukey's multiple comparisons).

Using the same techniques, conduits were produced with different diameter fibres but filled to a similar 'low' packing density (Figure 56B). 2 μm , 9 μm and 16 μm fibres were respectively electrospun for 480 seconds, 22 seconds and 9 seconds to produce fibre bundles which were analysed with gas displacement pycnometry and threaded into tubes. This produced conduits with similar packing densities of around 12%. There were no significant differences between any of the three groups (Kruskal-Wallis test).

A

Conduits produced with
variable packing density
- all 2 μm fibres

**B**

Conduits produced with
variable fibre diameter
- all 'low' (~12%) packing density

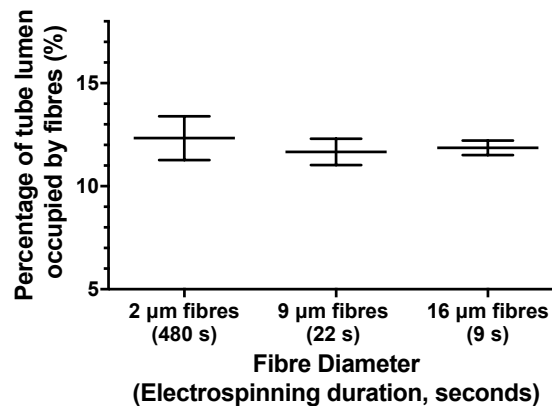


Figure 56. Graphs showing the packing density (percentage fill of the lumen) of PCLMA conduits filled with electrospun PCL fibres. Values displayed mean \pm SD (N=3, n=1).

A: Conduits filled with 2 μm fibres, to three different of packing densities. * denotes significant difference ($P < 0.01$, one-way ANOVA with Tukey's multiple comparison test).

B: Conduits filled with fibres of three different diameters, all to the same level of packing density. No significant differences between groups (Kruskal-Wallis test).

Referring to Table 8: the 2 μm fibres here were fabricated using parameter set A, 9 μm fibres were fabricated using parameter set F, 16 μm fibres were fabricated using parameter set J.

3.5.6 Analysis of fibre packing density with micro-computed tomography

Micro-CT imaging was trialled as a method of measuring the fibre packing density and compared to calculations obtained from the pycnometry measurements. A conduit was filled with 10 μm fibres (fabricated using parameter set G, Table 8) to match the 'low' packing density as described above. The 10 μm fibres were used due to their lower standard deviation compared to the 9 μm fibres (made using parameter set F) but it should also be noted that the mean fibre diameters of the two groups were not statistically different.

The fibre-filled conduit was imaged with micro-CT to obtain cross-sectional images (Figure 57A) which were thresholded (Figure 57B) and analysed to determine the percentage area occupied by the fibres. Images were analysed at 5 positions down the length of the tube and the mean packing density was calculated as $10.4 \pm 1.9\%$. This was non-significantly different from the 11.6% packing density calculated using pycnometry of the conduits filled with 9 μm fibres in Figure 56B (unpaired t-test).

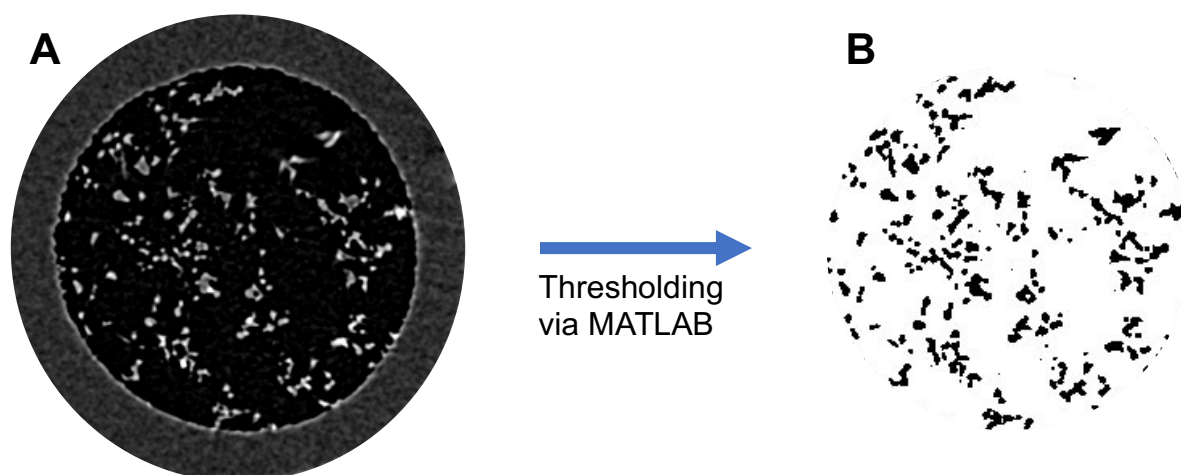


Figure 57. Method of calculating fibre packing density from micro-CT images. A: Example cross-sectional image of a fibre-filled conduit obtained by micro-computed tomography, showing the outer PCLMA tube and the inner PCL fibres (scan parameters - Source voltage: 40 kV, source current 250 μA , rotational step: 0.7°, filter: none, pixel size: 3.75 μm). B: The thresholded image produced in MATLAB displaying the fibres in black and the empty luminal space in white.

3.5.7 Fibre-filled conduits for *in vivo* use: modular conduit design

A three-part conduit was designed so that the inner tube could be filled with fibres and then capped with cuffs to produce empty regions at each end of the conduit. Figure 58 shows SEM images of a thin-wall tube and 3D cuff used to produce the fibre-filled conduits with this design. The thin-wall tubes had a well-defined structure with straight walls and an even wall thickness round the circumference of the lumen. The characteristic microgrooves from the μ SL process were also apparent. The stepped design of the 3D cuff can be seen, with the large internal diameter and thin wall of the upper section (sleeve), and the reduced internal diameter and increased wall thickness of the lower section. Figure 58E shows the assembled construct and Figure 58F shows a section of the assembled construct cut on a cryostat. The internal diameter was $883\pm 11\ \mu\text{m}$ (not significantly different to the plain conduits, section 3.5.1). The inner tube and outer cuff fit together well and were designed to have a combined wall thickness equal to the plain conduits ($284\ \mu\text{m}$). This was confirmed by cryosectioning to be around $280\ \mu\text{m}$.

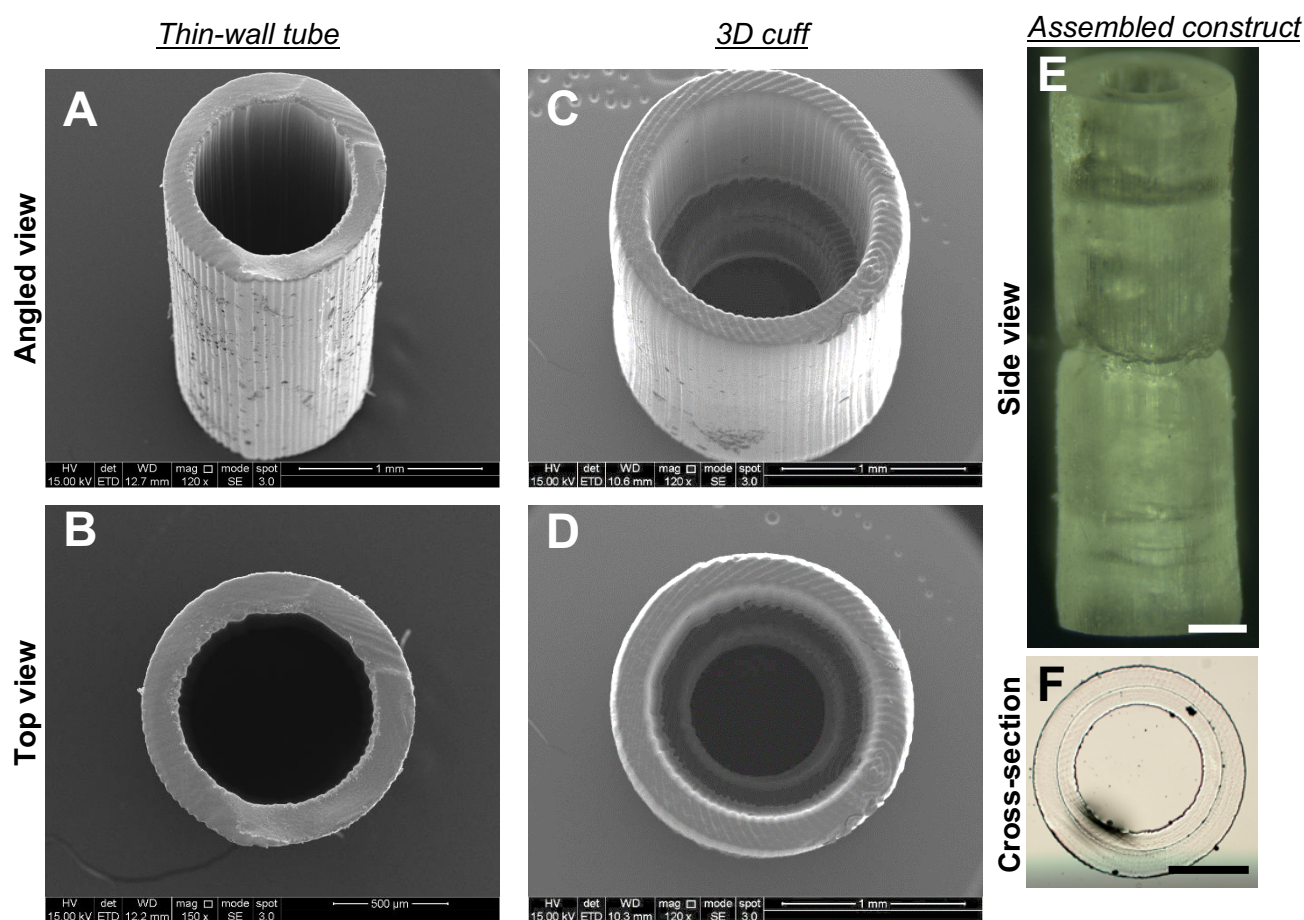


Figure 58. Modular design for the fibre-filled conduits. A-D: SEM images of a thin-wall tube (A, B) and a 3D cuff (C, D). E-F: Light microscopy images of the assembled construct (E) and a cryostat section of thin-wall tube with cuff (F), showing the tight fit of the cuff sleeve around the inner tube (scale bars: $500\ \mu\text{m}$).

Shown in Figure 59 are SEM images of fibre-filled conduits assembled with 3D cuffs. Thin-wall tubes were threaded with 2 μm (Figure 59A-B) or 10 μm (Figure 59C-D) fibres. These were assembled with 3D cuffs and laser-cut to 4.5 mm. The images show that fibres reach the end of the inner tube and the addition of the 3D cuff creates an empty region at the end of the conduit as desired. The magnified images show the fibres ends in greater detail and it can be seen that the 2 μm fibres were partially melted by the laser beam during laser-cutting. The melted regions formed more of a closed structure which may pose as a barrier to advancing cells. The 10 μm fibres, however, were undamaged and so should allow the migration of cells and regeneration of axons into the conduit.

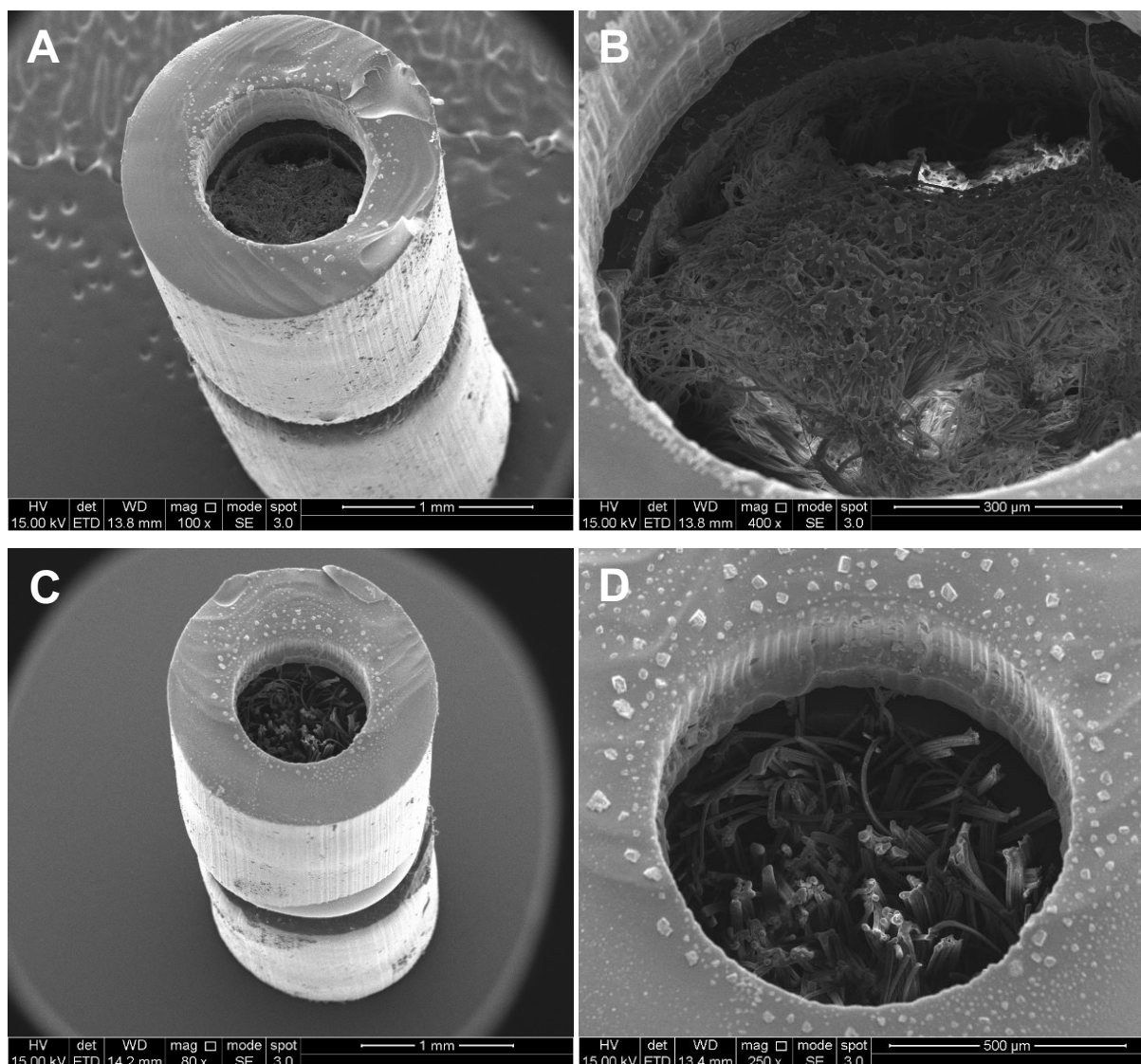


Figure 59. SEM images of assembled fibre-filled conduits with 2 μm fibres (A, B) and 10 μm fibres (C, D). Electrospun fibres were inserted into thin-wall tubes, cut using a cryostat and capped with a 3D cuff. The assembled product was then laser-cut to 4.5 mm. Magnified images (right) show more detail of the electrospun fibre ends.

3.5.8 Smooth conduits produced by injection moulding

Smooth PCLMA conduits were fabricated via an injection moulding technique to replicate the plain tubes produced by μ SL, but without the inherent microgrooves caused by the use of the DMD. Figure 60 shows SEM images of the resulting tubes with smooth inner and outer surfaces without any obvious features. The tubes had a good overall appearance, similar to the μ SL conduits, with a circular lumen and straight, parallel sides. Tube dimensions were measured from optical microscopy images to give an internal diameter of $962 \pm 10 \mu\text{m}$ and a wall thickness of $277 \pm 24 \mu\text{m}$ (not significantly different to the plain conduits). The internal diameter was slightly larger than the $900 \mu\text{m}$ expected from the size of the 20G needle used in the mould but was consistent across all samples, with a low standard deviation. The wall thickness was little more uneven round the circumference of the lumen. This was due to the needle in the mould not always being positioned perfectly in the centre of the outer silicone tube (see Figure 46).

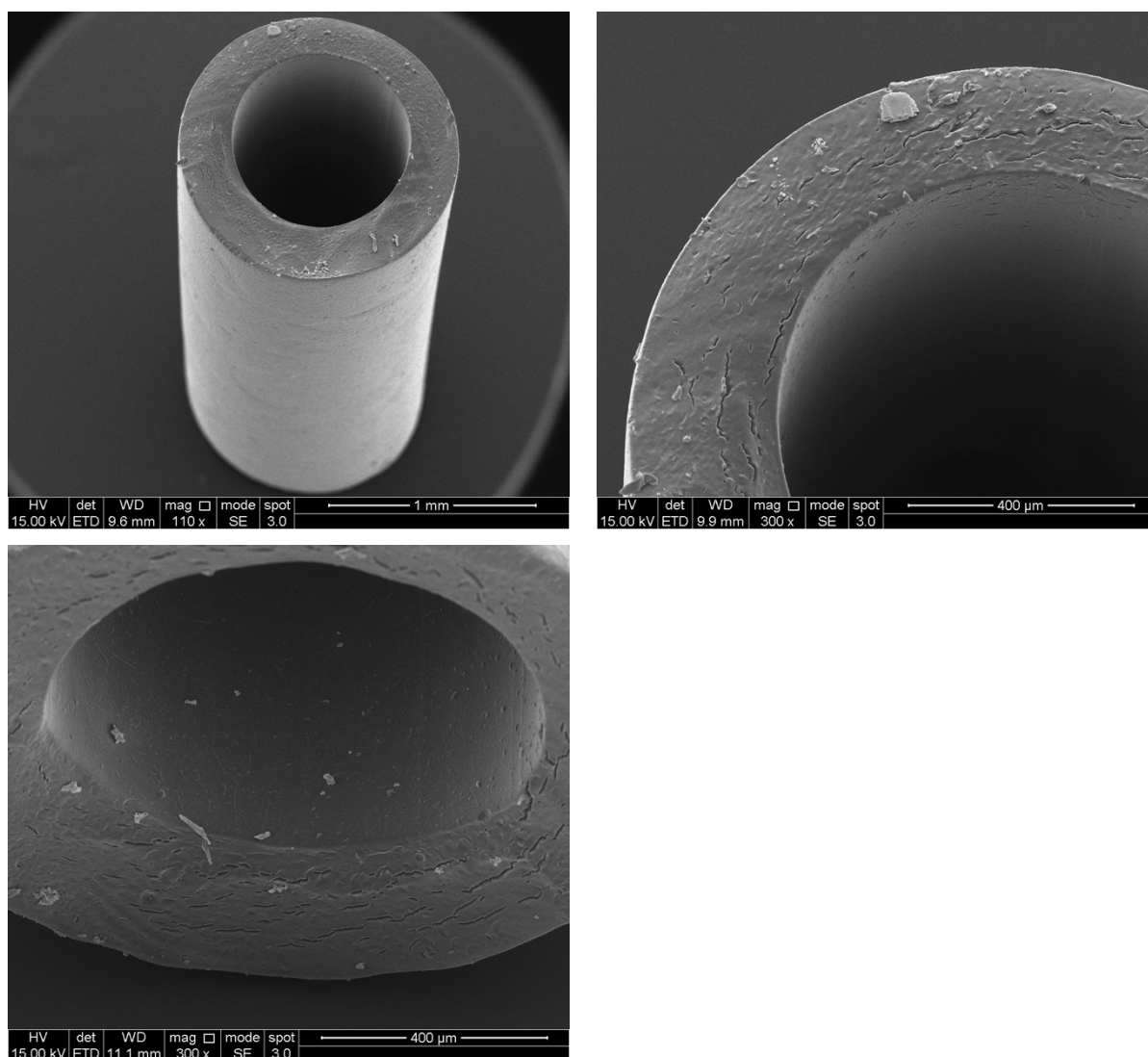


Figure 60. SEM images of smooth PCLMA conduits produced by injection moulding and curing with a UV lamp. The inner and outer surfaces lack the microgroove features present on conduits produced by μ SL.

3.5.9 Handling properties of PCLMA tubes

The PCLMA tubes showed a high degree of flexibility as would be expected from the Young's modulus values of the PCLMA measured in chapter 2. Shown in Figure 61 is a 20 mm PCLMA tube being bent between fingers. The tubes were able to flex to a high degree before kinking occurred. On release of pressure the tubes recovered without damage. The tube shown was produced using the injection moulding technique so that a long tube could be used to more easily demonstrate the bending properties. Short tubes made by μ SL exhibited similar properties and could be flexed without fracturing.

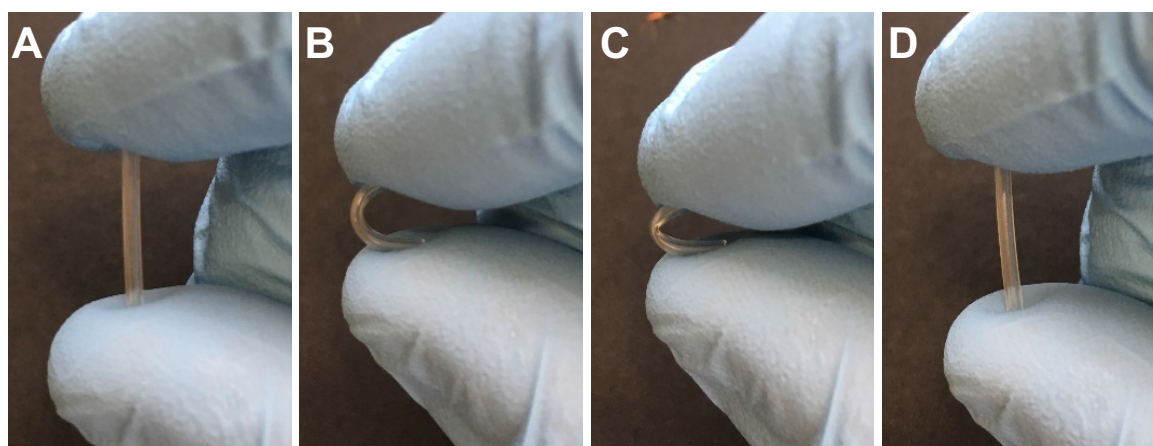


Figure 61. Bending of a PCLMA tube produced by injection moulding. 20 mm long tube held between fingers (A), bending without kinking (B), kinking upon extreme bending (C) and recovering from bending/kinking (D).

3.5.10 Autoclavability of PCLMA conduits

Plain PCLMA conduits (section 3.5.1) were autoclaved to demonstrate a clinically relevant method of sterilisation. The autoclaved conduits (Figure 62) maintained their physical appearance and suffered no visible damage from the autoclaving process.

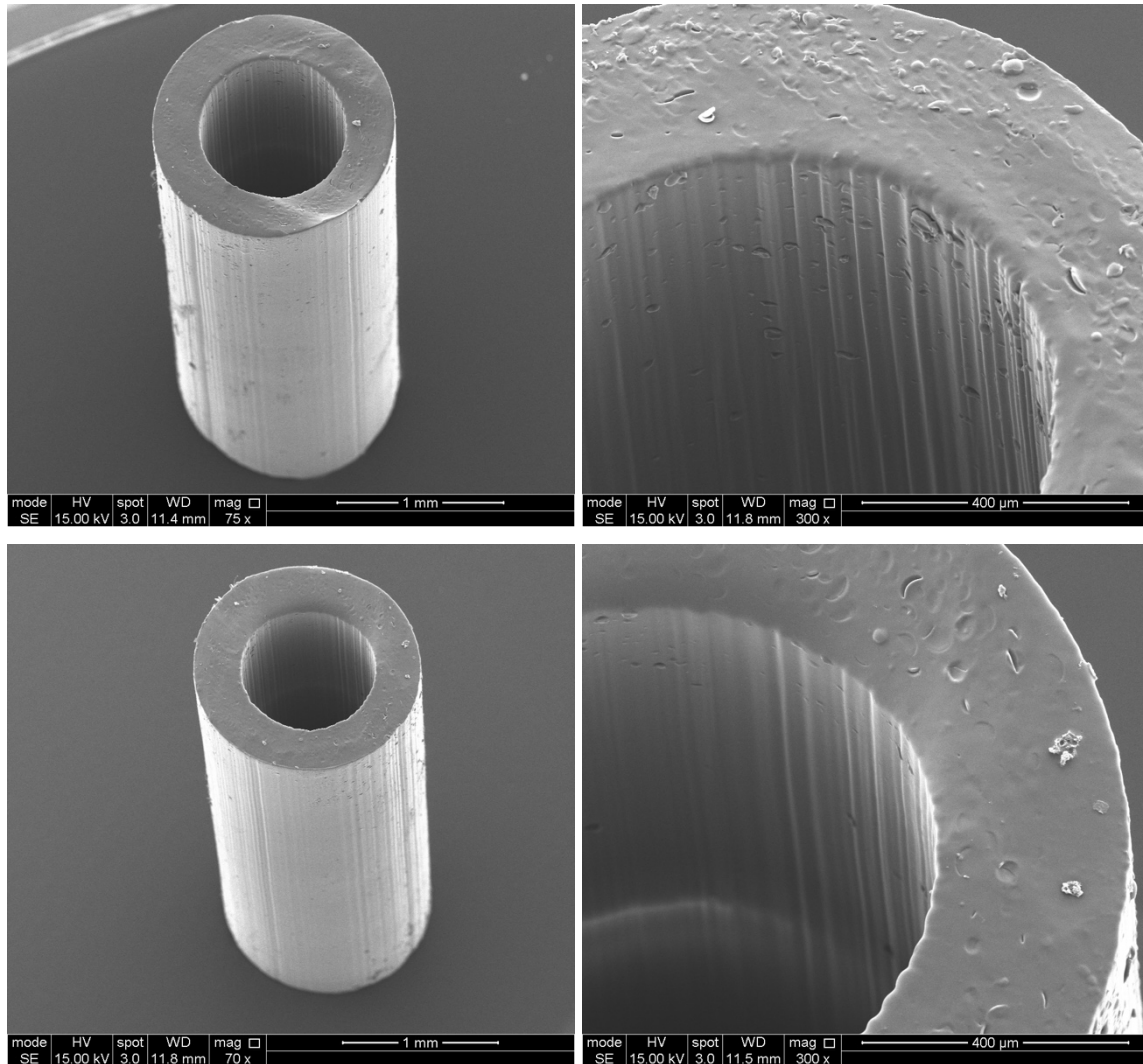


Figure 62. SEM images of autoclaved PCLMA conduits. No visible damage occurred from the autoclaving process.

3.6 Discussion

3.6.1 Grooved conduits

Grooved tubes were produced by μ SL using both plain PCLMA resin and PCLMA resin containing 0.075% beta-carotene. With the addition of beta-carotene the resolution of the grooved features was improved, making them more pronounced and continual down the length of the tube. The poor quality grooves produced when using the plain PCLMLA resin can be explained by the lack of photoabsorber; rather than just curing the polymer at the surface of the resin, the laser light is able to penetrate further down into the resin and continue to cure the structure as it is lowered by the descending z-stage. This effectively increases the exposure time for lower sections of the tube and causes the lower 'layers' to become over-cured and lose definition. The addition of beta-carotene as a photoabsorber reduces the depth penetration of the laser (as discussed in chapter 2) meaning that the polymer is only cured at the surface of the resin. Once the cured 'layer' descends beneath the surface of the polymer, the laser light no longer reaches it, leading to reduced exposure times of each 'layer' and less over-curing. The beta-carotene likely also reduces over-curing in the x-y plane by reducing the spread of light as the laser hits the polymer. This scattering has less of an effect on resolution in comparison to over-curing due to depth penetration, as the translucent PCLMA resin results in minimal light scattering. However, if using alternative resins where light scattering causes a significant limitation on resolution, this could be an important effect to consider and one where the use of beta-carotene as a photoabsorber may provide a solution.

The grooves on the luminal wall of the conduits were produced with a mean groove width of 48 μ m, strut width of 83 μ m and peak-to-peak width of 143 μ m. These are very similar dimensions to that of the conduits produced by Suo et al. using a dry-jet wet spinning method (discussed in section 1.6.5.1 [180]), as well as those produced by Johnson et al. [87]. Suo et al.'s conduits (with a peak-to-peak width of 183 μ m and a strut width of 73 μ m) effectively promoted the alignment of PC12 neurites *in vitro* so this shows promise for the beneficial effect of our grooved conduits in the *in vivo* model that will be explored in the final chapter.

3.6.2 Fibre-filled conduits

3.6.2.1 Electrospun fibre diameter

Highly aligned Electrospun fibres were produced to a range of diameters between 2-16 μm . The diameter range investigated was based on work by Daud et al. investigating the optimal fibre diameter for the guidance of neuronal and Schwann cells [153], discussed in section 1.6.2. In this work, 8 μm fibres were found to be the best for promoting growth and guidance of neurites. Larger diameters were not investigated so it is possible that the optimum fibre diameter for promoting neurite outgrowth may be larger than 8 μm . In our study, larger diameter fibres were also produced so this could be investigated. The smaller, 1 μm diameter fibres produced by Daud proved better for promoting Schwann cell adhesion and growth. For this reason, smaller diameter (in this case 2 μm) fibres were also considered as it is not obvious which cell type the fibres should be optimised for and how the dependence on fibre diameter may change as we move towards more complex *in vitro* models and *in vivo* studies. Work in the following chapter will explore the use of an *in vitro* DRG model to assess the effect of different fibre diameters on the growth of Schwann and neuronal cells in a more clinically relevant system.

3.6.2.2 Method of assessing packing density

The electrospun fibres were incorporated into tubes produced by μSL . When considering NGCs with luminal fillers (e.g. electrospun fibres), packing density is an important parameter to measure as there is plenty of data to suggest that a high volume of material in the conduit lumen can impede regeneration [126], [165], [166], [269]. Though this seems to be an important parameter, groups using electrospun fibres or filaments within a NGC have performed limited assessment of the packing density. Some groups do not assess this parameter at all and only use one type of scaffold without varying the fill percentage [36], [169]. With the few papers that do state a packing density, calculations are used to approximate the value based on the dimensions of the tube lumen and the size/number of the filaments inserted. Koh et al. roughly estimated a 10% packing density from the use of around 360 nanofibre yarns (each 25 μm diameter) inside a 1.5 mm diameter tube [168]. Ngo et al. similarly calculated packing densities based on the number of PLA microfilaments (40-100 μm diameter) inserted into silicone tubes to produce a range of packing density from 3.75-30% [172]. This technique of assessing packing density gives a rough estimate which may be accurate enough when using large diameter filaments or fibre bundles. However, when using a large number of small diameter electrospun fibres as in the present study, this method would not suffice. The difficulty in counting the number of electrospun fibres used would create too large an error in the end calculation.

Here we explored the use of gas displacement pycnometry to effectively assess the packing density of electrospun fibres in PCLMA tubes. It was possible to directly measure the volume of the fibre bundles used to fill the tubes and use this to calculate a packing density based on the measured luminal volume of the tubes. Micro-CT was also trialled as a method for assessing packing density and was seen to produce comparable results. Being able to quantifiably assess the packing density of the fibres as well as fibre diameter is critical as it will allow proper characterisation of conduits before use *in vitro* and *in vivo*. This makes it possible to change one parameter while keeping the other constant, allowing the isolation of each variable to independently assess how each parameter effects nerve regeneration. In the following chapter, as well as assessing the effect of fibre diameter with use of an *in vitro* DRG model, the effect of packing density will also be investigated.

3.6.2.3 Method of cutting conduit ends

Fibre-filled tubes were cut so that the ends of the electrospun fibres were flush with the ends of the tube. Cutting the conduits with a scalpel resulted in damage to the outer tube and clumping of fibres. It was thought that these dense areas of fibres could form a barrier to regenerating axons so evenly spread fibres were preferable. Embedding in OCT gel and cutting with a cryostat allowed the tube and fibres to be supported during the cutting process resulting in undamaged tubes and evenly distributed fibres across opening of conduit lumen.

3.6.2.4 Conduit design for *in vivo* use

The fibre-filled NGCs were designed so that there were empty cuffs present at the end of each tube. This was to allow for easier implantation of the conduits during the repair of a nerve injury as the empty cuffs provide a place for the proximal and distal nerve stumps to be inserted and secured. Evangelista et al. recognised this need for empty regions at the conduits ends and design their multi-lumen PEG conduits to have similar empty cuffs [126]. Most studies in literature which use conduits containing electrospun fibres do not consider including empty cuffs in the design but directly suture the nerve endings to the end of the conduits [154], [167], [168]. It is not clear how or if they are able to avoid disrupting the fibre distribution but this would be difficult in the case of our design with a low density of small-diameter fibres spread unsupported throughout the conduit lumen. This disruption of fibres on implantation may explain the low success rates and high variability in the results of the conduits implanted by Pateman and Harding [170]. The fibres in these conduits continued to the ends of the tubes and so insertion of the nerve stumps may have caused disruption of fibre alignment, preventing the successful guidance of the regenerating axons into and along the conduit.

Creation of conduits with filled lumens but empty cuffs is not widely explored, possibly due to the requirement for complex manufacturing methods. However, the use of μ SL enabled 3D structures to be produced which could be secured on the ends of fibre-filled conduits. This created the necessary empty cuffs which would allow for insertion of the nerve stumps without disrupting the fibres. Importantly, despite the modular structure of the fibre-filled conduits, they were fabricated to have the same overall wall thickness as plain conduit controls. The wall thickness of both the thin-wall inner tube and the 3D cuff were half that of the wall thickness of the plain tubes. Due to the difficulty in producing very thin structures, thicker walls were originally used in the tube and cuff but this produced an assembled construct with too great a wall thickness. By carefully balancing the laser power and stage speed during μ SL fabrication, tubes and 3D cuffs with very thin walls could be produced.

With the end goal of producing a product that could be used commercially, the handling and use of the conduits by the surgeon needs to be considered. The empty cuffs makes surgical implantation easier and surgeons would be more accepting of this design as it would be used in a similar fashion to current commercial NGCs.

3.6.3 Autoclavability of PCLMA conduits

Another important consideration for future commercial use is the ability to sterilise the conduits with a clinically relevant, FDA approved technique. This was demonstrated with the plain PCLMA conduits being able to survive sterilisation in the autoclave. The resistance to deformation at high temperatures is due to the presence of crosslinking in the photocured PCLMA. However, the tubes were only assessed for damage visually. Mechanical testing before and after autoclaving would be necessary to determine any detrimental impact on mechanical properties. Fibre-filled conduits however could not be autoclaved as the PCL used in electrospinning has a low melting point (around 60°C) and would melt during the autoclave cycle [270]. For this reason, ethanol sterilisation was used in the work in the following chapters. If the fibre-filled conduits were to be developed for clinical use, an alternative method of sterilisation such as gamma irradiation or ethylene oxide could be used, however these are also known to affect the properties of polymer samples. Gamma irradiation is used on electrospun samples but can lead to changes in hydrophilicity and Young's modulus, decreased tensile strength, decreased molecular weight and increased degradation rates [271], [272]. These effects could, however, be used as an advantage and Bosworth et al. demonstrated that these changes to electrospun PCL fibres did not have a detrimental effect on cell

response [271]. Ethylene oxide has also been shown to affect mechanical properties, material wettability and fibre morphology and orientation [273] and can cause PCL fibres to fuse and become brittle [270]. These effects would need to be considered if pursuing one of these methods.

Ethanol sterilisation has also been shown to affect the mechanical properties of polymer fibre scaffolds such as an increase in Young's modulus and/or decrease in tensile strength with PLGA scaffolds [274]–[276]. This effect is not always seen however, with Yoganarasimha et al. reporting no change of either tensile modulus or tensile strength after ethanol sterilisation of PCL fibre scaffolds [270].

3.7 Conclusions

Plain NGCs were produced as well as conduits with two types of physical guidance cue. Conduits containing aligned grooves were produced directly by μ SL. The incorporation of beta-carotene into the photocurable PCLMA resin improved the resolution of the structures, allowing the production of grooves with a size comparable to other NGCs described in literature. Secondly, by combining products from μ SL and electrospinning, conduits were produced containing aligned electrospun fibres running longitudinally and evenly spaced throughout the lumen. Gas displacement pycnometry was used to develop a simple method of assessing fibre packing density which is an important parameter to consider when using these fibre-filled conduits. The design of these conduits was optimised for surgical implantation by incorporating empty luminal spaces at each end of the conduit, allowing for insertion of the nerve stumps. Thirdly, using an injection moulding technique, smooth NGCs were produced which were devoid of any physical guidance cues. This was to determine if the inherent microgrooves produced from the use of μ SL have an effect on nerve regeneration.

4. Chapter 4: In Vitro analysis of conduit performance

4.1 Chapter Introduction

This chapter describes the *in vitro* work that was done prior to *in vivo* implantation of the conduits that were described in chapter 3. *In vitro* work is obviously necessary before progressing to the use of an *in vivo* model, however the main focus of this PhD was to assess the regeneration potential of the NGCs, using the specially developed *in vivo* model that will be discussed in Chapter 5.

The biocompatibility of the photocured PCLMA was tested as well as the biocompatibility of PCLMA containing beta-carotene. The biocompatibility of the PCL used in electrospinning was not investigated as this form of commercial PCL is widely known to be biocompatible. Biocompatibility of electrospun PCL microfibres for neural applications has been assessed previously in our lab with the growth of neuronal and Schwann cells [153], [277]. PCL fibre-filled conduits were used here *in vitro* to demonstrate the ability of Schwann cells to migrate along the fibres.

Air-plasma treatment was then investigated as a way of increasing the hydrophilicity of the polymer materials with the aim of promoting better cell attachment and growth. PCLMA and PCL samples were both treated with air-plasma and assessed for water contact angle.

Finally, fibre-filled conduits were tested in *ex vivo* cultures with chick dorsal root ganglia. This part of the chapter refers to work by M. Behbehani which was done concurrently with the work in this study and used to inform the work in this project. Here chick DRGs were cultured in fibre-filled conduits to assess:

1. The effect of air-plasma treatment on nerve outgrowth
2. The effect of fibre diameter on nerve outgrowth
3. The effect of fibre packing density on nerve outgrowth

The first two studies were performed solely by M. Behbehani and the third was done in collaboration. Selected outputs of this work will be briefly presented here as the results are necessary to justify the choice of NGCs used in the *in vivo* studies in the following chapter. The work is presented in full in the thesis of M. Behbehani [278]. This work focussed on the fibre-filled conduits, and the grooved conduits were not explored for this.

4.2 Background

4.2.1 Plasma Treatment

In this chapter, the use of plasma treatment is explored to improve the outgrowth of DRG explants in fibre-filled tubes. Plasma treatment is a technique that is used to alter the chemical properties of a material surface, most widely the material wettability. When polymers are exposed to plasma, the polymer surface reacts with the radicals generated by the plasma. This results in chemical modification of the surface (if simple gasses are used) or grafting of polymer fragments and functional groups onto the surface (if volatile monomers are used). When oxygen, air and nitrogen are used, this results in the oxidation of the polymer surface via reaction with oxygen and nitrogen radicals. This modifies the surface to produce surface functional groups containing oxygen or nitrogen and these polar groups act to increase the hydrophilicity of a surface [279]. Surface wettability is important for cell-material interactions as hydrophilic surfaces are generally preferential for cell attachment [280], [281]. The role of hydrophilicity/hydrophobicity in cell attachment is complex but it is thought that hydrophilic surfaces allow cell attachment proteins in serum-containing media to adhere and spread on the surface, which facilitates cell attachment; it has been shown that hydrophilic surfaces pre-adsorbed with serum support cell greater cell attachment and spreading compared to hydrophobic samples that have undergone the same treatment with serum [282].

Since the early 1970s air-plasma treatment has been widely used in the preparation of commercial TCP (polystyrene) cell culture plates. Early work demonstrated that though hydrophobic polystyrene did not support cell attachment, plasma treatment could be used to increase the hydrophilicity of polystyrene plates resulting in improved cell attachment and growth compared to non-treated plates [283], [284]. Since these early studies involving tissue culture plates, increased hydrophilicity after plasma treatment has been shown in a huge number of different polymers including PCL, PLA, PLGA, polycarbonate, polypropylene, polyethylene and poly(methyl methacrylate) [285]–[291]. Hydrophilic surfaces created by plasma treatment have been shown to improve the attachment, spreading, proliferation and metabolic activity of many cell types, including fibroblasts, osteoblasts, endothelial cells, smooth muscle cells and marrow stromal cells [282], [290], [292]–[294].

4.2.2 Assessment of nerve regeneration *in vitro* – the effect of different fibre diameter and the importance of 3D culture

As discussed in chapter 3, there are different parameters to consider when designing a fibre-filled conduit to support peripheral nerve regeneration, namely fibre diameter and fibre packing density.

Daud et al. investigated the effect of fibre diameter on the growth of neuronal and Schwann cells *in vitro*. It was found that 8 μm fibres were best for supporting growth and guidance of neurites, however 1 μm fibres promoted the best adherence of Schwann cells and supported increased Schwann cell extension [153]. Schwann cell 'extension', however, is not a very relevant factor as it is the migration of Schwann cells that plays an important role in peripheral nerve regeneration so migration needs to be compared on the different fibre diameters. As discussed in chapter 1, Schwann cell migration has been investigated *in vitro* on microgrooves, with 30 μm grooves supporting more directional migration compared to 60 μm grooves [179]. However, the migration of Schwann cells on electrospun fibres of different diameters fibres is less well studied (especially on fibres in the low micrometre range) so this will be investigated in this chapter.

Though 2D cell mono-culture is useful for gaining insight into how cells behave and interact with a material, the behaviour of cells in this type of culture is often not representative of behaviour *in vivo*; here cells are missing the physical and chemical cues from the 3D ECM and interactions from other cell types [295] (co-cultures are widely used but this is still not enough to represent the many cell types present *in vivo*). It is therefore desirable to use more complex methods to assess cell interaction in more physiologically relevant settings. Commonly used in peripheral nervous system research is the *ex vivo* culture of dorsal root ganglion explants. DRGs can be harvested from an animal (often rat or chick) and cultured *in vitro* with different biomaterials [143], [154], [159]. The DRG contains sensory, neuronal cell bodies as well as satellite glial cells, Schwann cells and fibroblasts together within a collagen ECM [296], [297]. This native, 3D structure of the DRG can be maintained *in vitro* which allows neurons and Schwann cells to be studied together in a physiologically relevant co-culture in a model representative of their arrangement *in vivo*.

DRGs are often grown *in vitro* on 2D mats of electrospun fibres (as discussed in section 1.6.2) and it is possible to measure Schwann cell migration and neurite outgrowth from the DRG as well as investigate the interactions between the two cell types. As well as introducing a 3D element to the culture by the use of DRG explants, 3D scaffolds can be used to provide a 3D platform for the outgrowth of cells from the DRG. Cell behaviour in 3D culture better resembles *in vivo* growth due to

the more accurate representation of cell microenvironment [298]. The combination of 3D DRG explants and 3D scaffolds will allow the creation of an *in vitro* model that more closely mimics the growth of a regenerating nerve through a NGC *in situ* and therefore be more predictive of NGC performance.

Work at the University of Sheffield by Behbehani et al. has been carried out, developing such a 3D *in vitro* model to assess DRG outgrowth through fibre-filled conduits [299]. Conduits were produced by μ SL and filled with fibres produced by electrospinning. Rat DRGs were then harvested and placed onto fibre-filled conduits, standing upright, in cell culture media. After 21 days, the fibres were removed and imaged to reveal that Schwann cells and axons had migrated out from the DRG, along the fibres. This *in vitro* model was developed as a platform for testing different intraluminal fibre scaffolds and since then, has been developed into a model using chick DRGs. This chick DRG model was used in the current study to assess different parameters of PCL fibres prior to *in vivo* implantation.

Other work has been carried out with DRGs cultured in fibre filled conduits. Wen et al, investigated the effect of fibre diameter on the outgrowth of rat DRG explants, through tubes filled with polypropylene filaments [300]. The work investigated a wide range of fibre diameters ranging from 5 μ m to 500 μ m. Neurite alignment increased with decreasing fibre diameter (assessed qualitatively) and the 5 μ m and 30 μ m fibres supported significantly greater outgrowth of Schwann cells and neurites compared to the 200 μ m and 500 μ m fibres. The results of this work suggest that smaller diameter fibres (in the order of 5-30 μ m) are beneficial but a range of small diameter fibres were not tested. It is necessary to determine how smaller changes in fibre diameter within this sub-30 μ m range affects outgrowth and this will be investigated in this chapter.

4.2.3 Effect of fibre packing density

In contrast to fibre diameter, the effect of fibre packing density is something that has not been widely studied. As far as the author is aware there have been no studies previously reported that explore *in vitro* nerve regeneration through conduits with various packing density of fibres.

There has been a small amount of *in vivo* work on the subject of packing density but this focuses on large diameter filaments. Ngo et al. produced NGCs containing PLA filaments; varying numbers of filaments (40-100 μ m in diameter) were inserted into silicone tubes to produce conduits with packing densities ranging from 3.75 % (16-24 filaments) to 30 % (128-160 filaments) [172]. These

conduits were used to repair 1 cm rat sciatic nerve gaps and histologically observed after a 10-week recovery. In conduits with 30% packing density there were the same number of myelinated axons present at the distal end compared to the empty conduit controls. With lower packing densities, the number of myelinated axons in the distal stump was seen to increase. Significantly more myelinated axons were present in repairs with conduits packed to 3.75% compared to the 30% conduit and the empty control. Conduits were tested in larger gaps (1.4-1.8 cm) with 7.5% packing density as these conduits had a more even distribution of filaments throughout the lumen and positive results were seen in comparison to the controls.

As discussed in the previous chapter, most other studies do not vary packing density, such as Koh et al. who inserted PLGA nanofiber yarns into conduits at roughly 10% packing density [168]. Benefits from the inclusion of the yarns were noted in terms of increased sensory recovery compared to empty conduits (see section 1.6.3). Matsumoto et al. also saw some positive results with conduits filled to a low packing density [36]. Here, conduits (4 mm internal diameter) containing 80 collagen filaments (50 μm diameter) supported common fibular nerve regeneration in beagle dogs (see section 1.6.4). By calculation from the device description, the conduit appears to have been filled to a 1.25% packing density.

From these studies, though no strong conclusions can be drawn, the common theme seems to be that low packing densities of $\geq 10\%$ are mostly used or accepted as beneficial. However, as these studies have been carried out with large diameter filaments or yarns, the packing density values may not be directly relatable to packing density with electrospun fibres. When large filaments are used, the gaps between the filaments are correspondingly large. This may not be analogous to the percentage fill using small diameter electrospun microfibrils inter-spaced with smaller gaps. It follows that a range of packing density of electrospun fibres should still be considered and will be explored in this chapter.

4.2.4 Conclusions from literature

- Plasma treatment can increase the hydrophilicity of polymer materials and improve cell attachment
- There is a need for physiologically relevant models to test the performance of fibre-filled NGCs
- Limited work had been carried out testing the effect of fibre diameter and fibre packing density so these need to be optimised before progression to an *in vivo* model.

4.3 Aims for this chapter

Determine the biocompatibility of the NGC material and the optimum parameters for fibre-filled scaffolds via *in vitro* testing. To achieve this, the following objectives were addressed:

- 1) Assess the biocompatibility of the materials used in NGC production (PCLMA and PCLMA containing beta-carotene)
- 2) Assess the ability of Schwann cells to migrate through fibre-filled conduits *in vitro*
- 3) Assess the effect of air-plasma treatment on the hydrophilicity of PCL and PCLMA
- 4) Assess the effect of plasma treatment, fibre diameter and fibre packing density on DRG outgrowth through fibre-filled conduits

4.4 Materials and Methods

4.4.1 General cell culture

All reagents used in cell culture were purchased from Sigma-Aldrich unless otherwise stated. TCP culture plates were purchased from Starlab and T75 flasks purchased from VWR. For all centrifugation steps, centrifuge rotor radius (r_{\max})=125 mm.

4.4.1.1 Media preparation and culture conditions

All cells were maintained and used in experiments with serum-containing cell culture media. This consisted of Dulbecco's Modified Eagle Medium (DMEM) supplemented with 10% foetal calf serum (FCS), 1% L-glutamine, 1% penicillin/streptomycin, and 0.25% amphotericin B. Cells were cultured in T75 flasks with 10-12 ml media at 37°C in a humidified atmosphere with 5% CO₂. On reaching 80-90% confluency, cells were passaged as described below and either reseeded at a lower density in T75 flasks or used in an experiment. Media was warmed in a 37°C water bath before use.

4.4.1.2 Freezing

Cells were frozen and stored in liquid nitrogen for long term storage. Cells in culture were trypsinised, centrifuged and resuspended in freezing solution: 10% dimethyl sulfoxide (DMSO, Alfa Aesar) in FCS. Cell suspension was aliquoted into 1 ml cryovials and placed in freezing containers (CoolCell®, Biocision) in a -80°C freezer. The containers ensure a standardised, controlled rate of temperature change of -1°C/minute. After 24 hours the cryovials were transferred to liquid nitrogen.

4.4.1.3 Defrosting

Required cells were removed from liquid nitrogen and defrosted by placing the cryovial in a 37°C water bath. To minimise cell death, as soon as the suspension was defrosted, the contents of the vial were transferred to a T75 flask with 12 ml of media. The flask was placed in an incubator and the media was changed after the first 24 hours to remove any residual DMSO.

4.4.1.4 RN22 cell culture and passage

RN22 cells (European Collection of Authenticated Cell Cultures) are a cancerous cell line derived from rat Schwann cells. RN22 cells were maintained in culture using the media described above and passaged as follows. Media was removed from the T75 flask and one wash with phosphate buffered saline solution (PBS) was performed. 5 ml trypsin-EDTA solution was added and the flask was incubated for up to 5 minutes. Cell detachment was confirmed by observation with light microscopy

and the trypsin was inhibited by adding 10 ml of media. The contents of the flask were centrifuged at 1000 rpm for 5 minutes. The supernatant was discarded and the cell pellet was resuspended in 3-6 ml of media. If using in an experiment, cell counting was performed using a haemocytometer and a suspension with the required number of cells was made up with fresh media.

4.4.1.5 Schwann cell culture and passage

Primary Schwann cells were obtained from rat sciatic nerve using methods described previously [301] and provided to the author by C.Taylor. Schwann cells were passaged as above for RN22 cells but using 2.5 ml trypsin in a T75 flask and an incubation time of 6-7 minutes. To avoid long times in trypsin, towards the end of the 6-7 minutes the bottom of the T75 flasks were tapped to ensure cell detachment. Upon detachment, 10 ml of media was added to the flask and contents were centrifuged at 1700 rpm for 6 minutes. The supernatant was removed and the cell pellet was resuspended in 1-3 ml of media. If using in an experiment, cell counting was performed using a haemocytometer and a suspension with the required number of cells was made up with fresh media. Schwann cells were used in experiments at a passage number of 6-8.

4.4.2 Biocompatibility testing of NGC materials

PCL is widely used in tissue engineering and regarded as a biocompatible polymer. Since the PCLMA used for the production of NGCs in this study is a chemically modified version of PCL, it was necessary to test this material to ensure its biocompatibility. The biocompatibility of beta-carotene-containing PCLMA was also tested to ensure the addition of beta-carotene into the resin did not have any adverse effects on cell growth. The PCLMA resins used in this chapter were made using 2M20 PCLMA with 2% photoinitiator and any beta-carotene content as described. Preparation of photocurable resins is described in section 2.4.2. All experiments were performed in triplicate (n=3) and repeated up to 3 times (N=3).

4.4.2.1 MTT assays

The MTT assay was used to measure the metabolic activity of cells grown on various polymer samples to give an indication of cell viability and material biocompatibility. MTT solution (0.5 mg/ml MTT powder in PBS) was made up and filter sterilised before use. Acidified isopropanol was made up with 125 μ l of 10 M hydrochloric acid in 100 ml IPA. Media was removed from the cell culture samples which were then washed once with PBS. 1-2.5 ml of MTT solution was added to each well (12-well plate) and samples incubated for 1-hour at 37°C. The MTT solution was removed and 350 μ l acidified isopropanol was added to each well to lyse the cells and elute the stain. 2x 100 μ l samples

of the IPA were then taken from each well and pipetted into wells of a 96-well plate. Plates were read on an absorbance plate reader (Bio-TEek ELx 800) with absorbance measured at 540 nm (reference 630 nm).

4.4.2.2 Biocompatibility testing of PCLMA

The biocompatibility of cured PCLMA was tested using flat PCLMA substrates produced by spin coating and compared to glass and TCP controls. Glass coverslips (22 mm diameter) were treated with Piranha solution (3:1 sulphuric acid:hydrogen peroxide, 60 minutes) followed by a treatment with 3-(Trimethoxysilyl)propyl methacrylate (MAPTMS) solution (10% MAPTMS in toluene, 24 hours). This treatment functionalises the glass surface and allows polymer films to bind to the glass during photocuring.

150 µl of PCLMA resin was dispensed onto the centre of a MAPTMS-functionalised glass coverslip which was placed on a spin coater (Laurell Technologies Corporation). The sample was spun at 3000 rpm for 30 seconds to evenly coat the coverslip and then cured under the UV lamp at 100% power for 100 seconds. The coated coverslips were then washed in IPA for 1 week prior to cell culture, changing the IPA at least twice in this time.

PCLMA-coated coverslips and plain glass coverslips were placed in 12-well plates, sterilised with 70% ethanol for two hours and washed 3 times with PBS. Confluent RN22 cells were trypsinised and seeded onto the coverslips as well as empty TCP wells. 25,000 cells in 3 ml media were added to each well and cultured at standard conditions. Cultures were maintained for either 24 or 72 hours (day 1 and day 3) when an MTT assay was performed as described above. 1 ml of MTT solution was added to the wells for a 1-hour incubation at 37°C.

This experiment was repeated with Schwann cells, also seeding 25,000 cells/well in 12-well plates but performing the two MTT assay timepoints at day 2 and day 5 to allow a greater time for the proliferation of the slower-growing Schwann cells.

4.4.2.3 Biocompatibility testing of beta-carotene-containing PCLMA

PCLMA resin containing beta-carotene was cured into discs and tested for biocompatibility against plain PCLMA discs containing no beta-carotene. PCLMA resins were prepared with 0% and 0.05% beta-carotene. Polymer discs (12 mm diameter, 2 mm thickness) were cured in PDMS wells. Resin was dispensed into the mould, a glass slide was placed on top to ensure a flat upper surface. The

polymer was then cured under a UV lamp at 30% power for 1 minute followed by 100% power for 4 minutes. The samples were flipped and cured for a further 5 minutes at 100% power. The polymer discs were washed for one week in IPA prior to cell culture, changing the IPA at least twice in this time.

The PCLMA discs were placed into 12-well plates, sterilised for two hours in 70% ethanol followed by 3 washes with PBS. Confluent RN22 cells were trypsinised and seeded into the wells at 48,000 cells per well in 3 ml media. At 24 hours, all discs were moved to new wells with fresh media so that only the cells attached to the discs were studied and cells attached to the TCP were left behind. Cultures were maintained for either 24 or 72 hours from the time of seeding (day 1 and day 3) when an MTT assay was performed as described above. 2.5 ml of MTT solution was added to the wells for a 1-hour incubation at 37°C.

4.4.3 Schwann cell migration study in fibre-filled conduits

Cells were seeded on fibres protruding from the end of fibre-filled conduits to investigate whether cells could migrate along the fibres into the tubes. After a period of culture it could be assessed whether cells proliferated and migrated along the fibres into the tubes or remained only on the end of the fibres at the location of seeding. A preliminary experiment was carried out with RN22 cells followed by an experiment with Schwann cells.

4.4.3.1 Scaffold preparation

Fibre-filled conduits were produced as described in section 3.4.4.2. PCL fibres were inserted into 5 mm long PCLMA tubes and cut with a scalpel to leave 3 mm of fibres sticking out one end and 1 mm of fibres sticking out the other – this was so each end could be easily identified. Conduits were sterilised in 70% ethanol for two hours and washed 3 times in PBS. Conduits were then placed in sterile media and put under vacuum. This removed the air from the scaffolds which caused them to sink (making them easier to use in cell culture) and ensured maximal contact of media with the conduit and internal fibres. Scaffolds were stored in media for 24 hours prior to cell seeding.

4.4.3.2 Cell seeding

To achieve isolated cell seeding on the ends of the fibres a protocol was developed as described in Figure 63. The scaffolds were individually placed into Eppendorf tubes with the 3 mm of fibres pointing towards the bottom of the tube. Cells were trypsinised, centrifuged and resuspended and 10 µl of cell suspension was aliquoted into each Eppendorf tube. This was the maximum volume that

could be added so that the cell suspension came only into contact with the protruding fibres and not the tube itself. The 10 μ l cell suspension contained approximately 16,000 cells for the experiment with RN22 cells and 4300 cells for the Schwann cell experiment. This difference was due to the smaller number of Schwann cells in a confluent flask compared to the RN22s. The Eppendorf tubes were sealed and incubated at 37°C for 1.5 hours to allow cell attachment to the fibres. After the 1.5-hour incubation, the conduits were washed in PBS to remove non-attached cells and transferred to wells in a 12-well plate, each with 2.5 ml fresh media. RN22 cultures were maintained for 4 days before fixing. Schwann cell cultures were maintained for either 3 or 21 days to give two timepoints: one early timepoint to demonstrate localised cell seeding and a late timepoint to investigate cell migration.

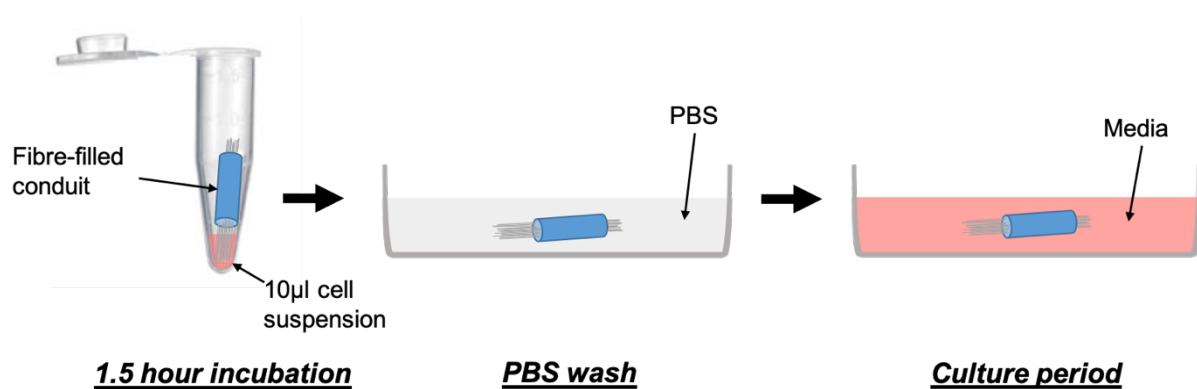


Figure 63. Cell seeding protocol for migration experiment in fibre-filled conduits.

4.4.3.3 Staining of cells on PCL fibres

At the endpoint of the experiment, samples were washed once with PBS wash and fixed with 3.7% paraformaldehyde for 10 minutes. Fibres were then removed from the tubes and, separately, the fibres/tubes were fixed for a further 10 minutes in 3.7% paraformaldehyde. This was followed with two PBS washes. Cells were permeabilised and unreactive binding sites blocked with 0.1% Triton X-100 (Fisher Scientific) and 1% bovine serum albumin (BSA) in PBS for 20 minutes. If required, samples were then incubated for 30 minutes with phalloidin-fluorescein isothiocyanate (phalloidin-FITC) (1:100 dilution in PBS) for staining of the actin cytoskeleton. Nuclei were stained by a 10 min incubation with 4',6-diamidino-2-phenylindole dihydrochloride (DAPI) (1:1000 dilution in PBS) then samples were stored in PBS until imaging.

4.4.3.4 Confocal imaging

For confocal imaging, PCL fibres with labelled cells were mounted with citifluor, AF1 mountant solution, on a histology slide under a glass coverslip. Samples were imaged using an upright Zeiss LSM 510 Meta confocal microscope with a 10× air objective, an argon ion laser (488 nm) for excitation of FITC and a Ti:sapphire laser (780 nm) for two photon excitation of DAPI. Z-stack images were taken through the depth of the fibre sample and combined into maximum intensity projection images.

4.4.3.5 Fluorescence microscopy imaging

To visualise the DAPI-stained nuclei of the Schwann cells on PCL fibres, samples were imaged using an epifluorescence microscope (Olympus IX73) equipped with an LED illumination unit (QImaging) and a monochrome camera (Retiga 6000, QImaging).

4.4.4 **Effect of plasma treatment**

Prior to work with the DRG model, air-plasma treatment was investigated as a way of increasing the hydrophilicity of the PCL and PCLMA with the aim of improving cell attachment and outgrowth.

4.4.4.1 Spin coating

Spin coated PCLMA coverslips were produced as described in section 4.4.2.2 in the preparation of PCLMA coverslips for biocompatibility testing. PCL films were produced in a similar fashion. PCL solution (15% PCL in DCM) was made up as used in electrospinning (section 3.4.3.1). 100 µl of PCL solution was dispensed onto a 13 mm coverslip placed on a spin coater and spun at 3000 rpm for 30 seconds. The solution evenly coated the coverslip and the DCM evaporated to produce a thin film of PCL that could be peeled off the coverslip.

4.4.4.2 Plasma treatment

To increase their hydrophilicity, PCLMA coverslips and PCL films were subjected to air-plasma treatment with a commercial plasma system (Zepto, Diener Electronic). Samples were placed on an aluminium foil-wrapped platform and loaded into the chamber. The chamber pressure was set to 0.4 mBar and the radio frequency power source was turned on at 50 W (40 kHz) for a treatment time of 60 seconds.

4.4.4.3 Water contact angle

Water contact angle of the plasma-treated samples was measured with a Drop Shape Analyser system (DSA100, Krüss) and compared to non-treated samples. Samples were placed on the stage and the needle of the syringe was lowered to the sample surface. 5 µl of ultrapure water (ELGA LabWater) was dosed to the sample and the needle tip was raised out of the droplet. The drop shape was immediately analysed (by sessile drop fitting) using the built-in camera and software to measure the contact angle. 5-7 samples of each type were analysed to obtain mean water contact angle values (n=5-7).

4.4.5 *Ex vivo* DRG culture in fibre-filled conduits

Chick embryo DRGs were extracted and cultured in fibre-filled conduits to assess the effect of different parameters on the outgrowth of Schwann cells and axons:

1. The effect of air-plasma treatment
2. The effect of fibre diameter
3. The effect of fibre packing density

Experiments 1 and 2 were performed solely by M. Behbehani and experiment 3 was done in collaboration with the author. All DRG extraction, culture and analysis was performed by M. Behbehani with methods reported in full in her thesis [278].

4.4.5.1 Production of fibre-filled conduits

PCL fibres were electrospun and threaded into conduits according to section 3.4.4.2. For the purpose of this *in vitro* study, empty cuffs at the ends of the conduits were not required so the three-part modular conduit design was not used. Plain tubes (5 mm in length) were filled with fibres and fibre ends were cut. These were used without the addition of the 3D cuffs.

For studies 1 and 2 (the effect of plasma treatment and fibre diameter), PEGDA tubes were produced by μ SL and filled with PCL fibres to a packing density of 20% (10 μ m fibres were used for study 1 and 1-13 μ m fibres were used for study 2). For study 3 (the effect of fibre packing density) conduits were produced by the author and provided to M. Behbehani for DRG culture. Here plain PCLMA conduits (section 3.5.1) were produced by μ SL and filled with 10 μ m PCL fibres of different densities, based on gas pycnometry results.

4.4.5.2 Plasma treatment of fibre-filled conduits

For the plasma-treated groups, fibre-filled conduits were treated with air-plasma with a commercial plasma system at 50 W for 60 seconds as described in section 4.4.4.2.

4.4.5.3 DRG culture, imaging and analysis

DRG explants were cultured in fibre-filled conduits as described here: [278]. Briefly, day 12 chick embryos (*Gallus gallus domesticus*, Henry Stewart Co. Ltd). were sacrificed and DRGs were removed, trimming the attached nerve roots. Fibre-filled conduits were individually held upright in the cut ends of 200 μ l pipette tips which were slotted into stainless steel grids. The grids containing the conduits were sterilised in 70% ethanol and placed in well plates for culture. The extracted DRGs were placed on top of the fibre-filled conduits and incubated for 30 minutes to allow attachment of the DRGs to the fibres. The culture plates were filled with media and returned to the incubator for a culture time of 7 days. Following culture, the fibres (with attached DRGs) were removed from the conduits, fixed and labelled for β III Tubulin, S100 β and DAPI for visualisation of axons, Schwann cells and nuclei respectively. Following this, the scaffolds were mounted in agarose and imaged with light sheet fluorescence microscopy (Lightsheet Z.1 microscope, Zeiss). Image analysis was conducted to measure the maximum outgrowth distance of axons and Schwann cells in each sample and these were compared between the different conduit types.

4.4.6 Statistical analysis

Statistical analysis was performed with GraphPad Prism. Data was tested for normality using Shapiro-Wilk normality test. To test for significant differences between groups, normally distributed data was then tested by ANOVA. For data affected by one factor, one-way ANOVA was used followed by Tukey's multiple comparisons tests. For data affected by two factors, two-way ANOVA was used followed by Tukey's multiple comparison tests. For non-normally distributed data, Kruskal-Wallis test was performed followed by Dunn's multiple comparison tests. $P < 0.05$ was used to determine a statistical difference. All data is presented mean \pm SD. Sample sizes are presented as N=experimental repeats, n=replicates per experiment i.e. N=1, n=3 signifies an experiment performed once in triplicate.

4.5 Results

4.5.1 PCLMA Biocompatibility

Biocompatibility of PCLMA was tested by culturing cells on PCLMA substrates as well as glass and TCP controls and performing an MTT assay to measure metabolic activity. This was performed with both RN22 and rat primary Schwann cells.

4.5.1.1 RN22s

Metabolic activity of RN22 cells was compared on PCLMA-coated coverslips, plain glass coverslips, and TCP wells (Figure 64A). For each of the three sample types, metabolic activity significantly increased from 24 hours to 72 hours, suggesting proliferation of cells between the two time points ($P > 0.001$, 2-way ANOVA with Tukey's multiple comparison). There was no significant difference between the three groups at either 24 hours or 72 hours, suggesting a comparable level of biocompatibility.

4.5.1.2 Schwann Cells

Metabolic activity of Schwann cells was compared on PCLMA-coated coverslips, plain glass coverslips, and TCP wells (Figure 64B). For all samples, metabolic activity significantly increased from day 2 to day 5 suggesting proliferation of cells between the two time points ($P > 0.0001$, $P < 0.05$ and $P < 0.001$ for PCLMA, glass and TCP respectively, 2-way ANOVA with Tukey's multiple comparison). No significant difference was found between any samples at day 2 but at day 5, the metabolic activity was significantly higher on PCLMA compared to both glass and TCP ($P < 0.001$ and $P < 0.01$ respectively). However, this experiment was only performed once in triplicate so would need to be repeated to verify the results.

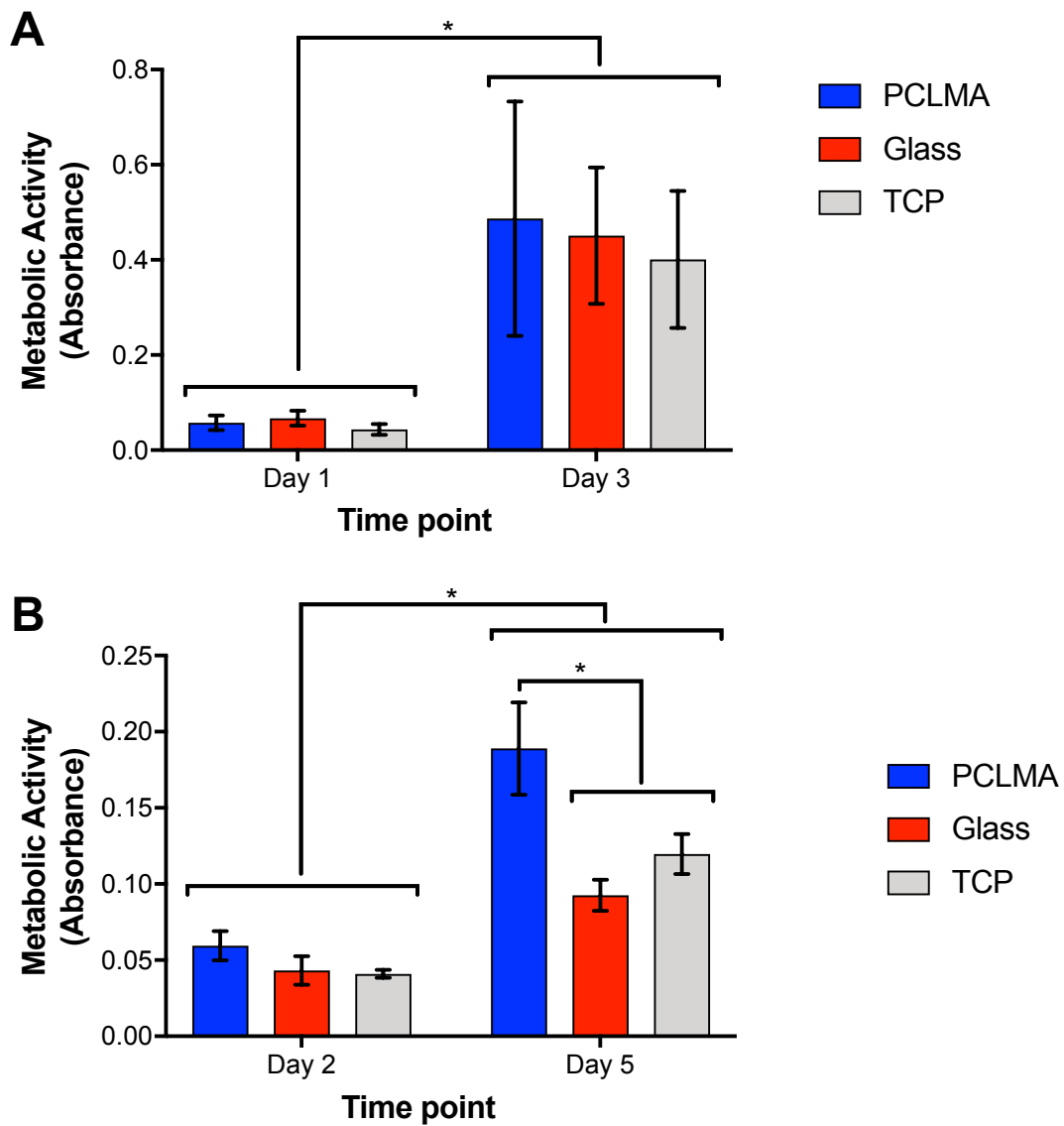


Figure 64. Biocompatibility testing of PCLMA, assessed by MTT assay. Values displayed mean±SD. A: Biocompatibility assessed with RN22 cells (N=2, n=3). B: Biocompatibility assessed with Schwann cells (N=1, n=3). * denotes a significant difference (2-way ANOVA with Tukey's multiple comparison).

4.5.2 Beta-carotene biocompatibility

4.5.2.1 PCLMA vs PCLMA + Beta-carotene

The biocompatibility of beta-carotene-containing PCLMA was tested by performing an MTT assay with RN22 cells (Figure 65). Cells were cultured on polymer discs of PCLMA and PCLMA with 0.05% beta-carotene. No significant difference was found between the PCLMA and PCLMA with beta-carotene at either time point. This suggests that the beta-carotene had no adverse effect on the viability of the RN22 cells. The increase in metabolic activity from day 1 to day 3 was significant for both materials ($P < 0.0001$, 2-way ANOVA with Tukey's multiple comparison) suggesting a large amount of proliferation on both samples and indicating their common biocompatibility.

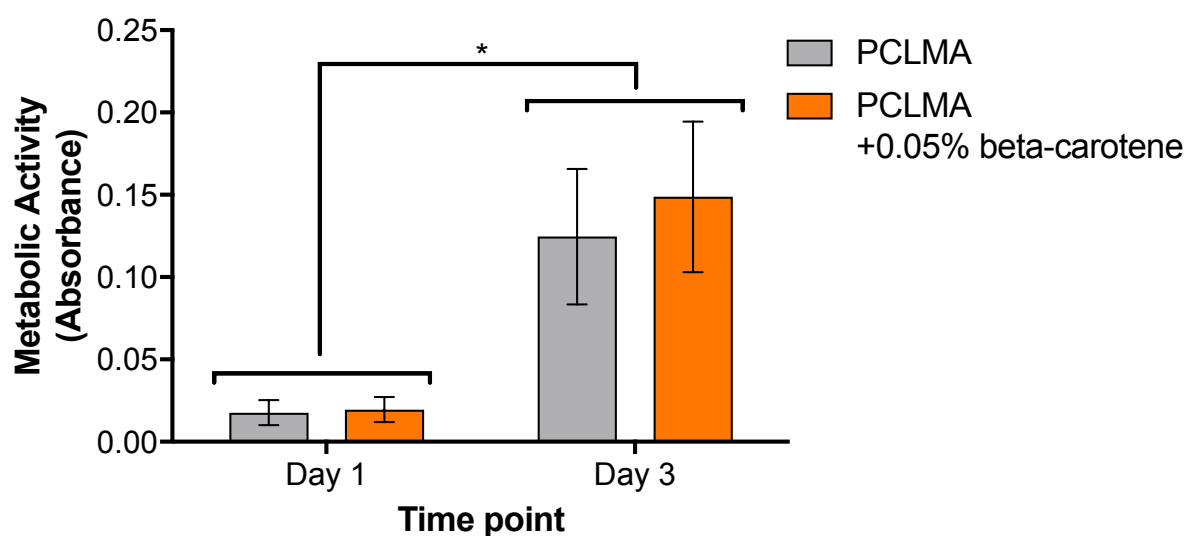


Figure 65. Biocompatibility testing of beta-carotene-containing PCLMA, assessed by MTT assay. Values displayed mean \pm SD ($N=3$, $n=3$). * denotes a significant difference (2-way ANOVA with Tukey's multiple comparison).

4.5.3 Cell migration through fibre-filled conduits *in vitro*

Experiments were carried out in which cells were seeded on the end of fibres in fibre-filled conduits to assess whether cells could proliferate and migrate along the fibres into the conduits.

4.5.3.1 5.4.1. RN22 cells cultured in fibre-filled conduits

RN22s were seeded at the end of fibre-containing conduits containing 2 μm PCL fibres. Samples were fixed on day 4 and imaged with confocal microscopy. A large number of cells adhered to the ends of the fibres, where the cells were seeded, however the cells clustered together in large clumps (Figure 66A, B) which is not representative of *in vivo* growth. Some cells were visible along the fibres, part the way into the tube (Figure 66C,D) and these were seen to align and extend along the fibres and sometimes join together to form bands.

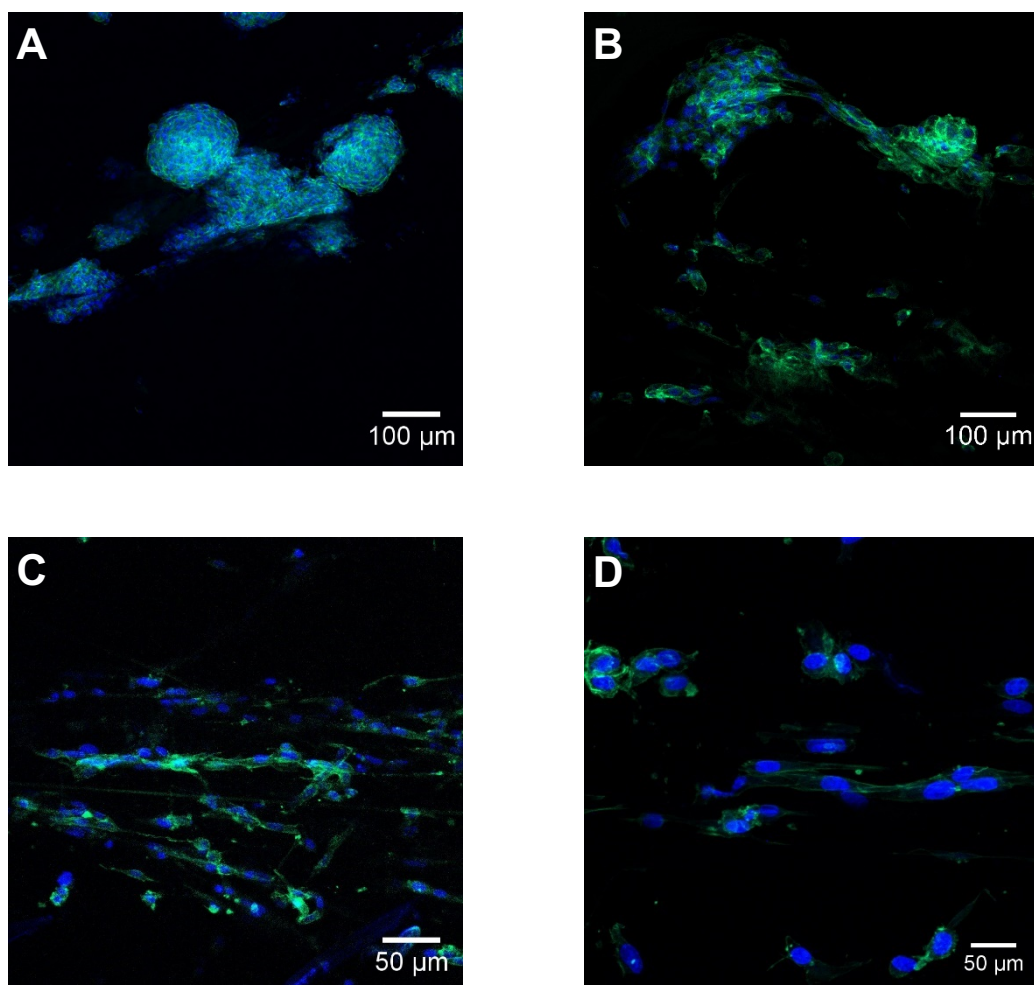
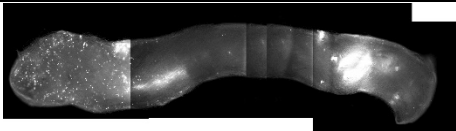
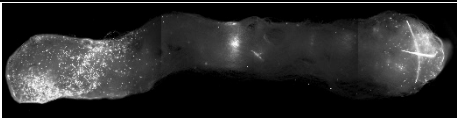
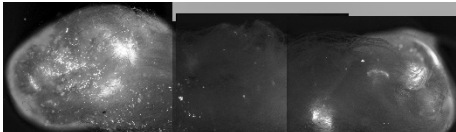
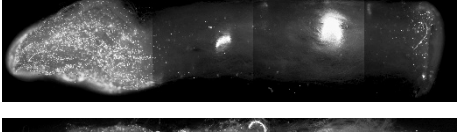
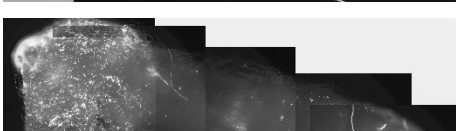
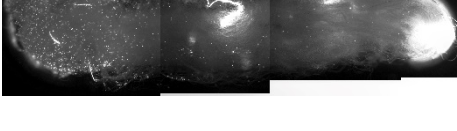
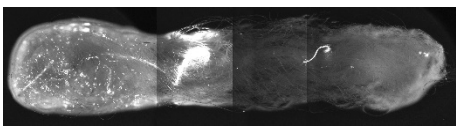
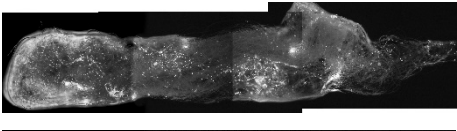
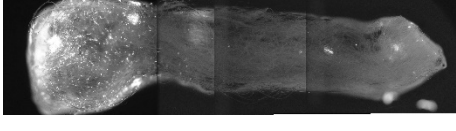
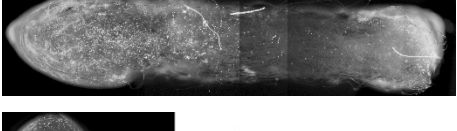
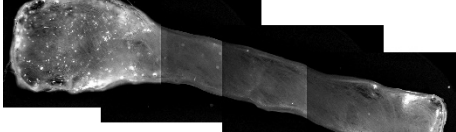
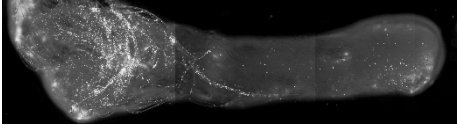


Figure 66. Confocal microscopy images of RN22 cells growing on electrospun fibres. A, B: Clusters of cells growing on fibres protruding from the tubes, at the position of cell seeding. C, D: Cells growing on fibres part the way into the tube. Green: Phalloidin-FITC, Blue: DAPI.

4.5.3.2 Schwann cells cultured in fibre-filled conduits

Schwann cells were seeded at the end of fibre-filled conduits and fixed on day 3 and day 21 before DAPI staining and imaging with fluorescence microscopy to assess cell migration. Table 9 displays the fibres that were imaged at each time point. Conduits containing both 2 μm and 10 μm PCL fibres at 10% packing density were tested. On day 3, on both 2 μm and 10 μm fibres, cells were confined to the ends of the fibres at the point of seeding. On day 21 on the 2 μm fibres, the cells seemed to have increased in number but were still confined to the ends of the fibres. At day 21 on the 10 μm fibres, in 2 out of the 3 samples, Schwann cells could be seen to have migrated along the fibres. The fibres in the 3rd sample seem somewhat disorganised which could have prevented migration along toward the centre of the tube.

Table 9. Schwann cell migration in fibre-filled tubes. DAPI stained nuclei of Schwann cells grown on 2 μm or 10 μm PCL fibres within PCLMA tubes. Cells were seeded at the ends of the fibres and fixed after 3 or 21 days.

	<u>Day 3</u>	<u>Day 21</u>	<u>Outgrowth?</u>
<u>2 μm Fibres</u>			X
			X
			X
<u>10 μm Fibres</u>			✓
			✓
			X

4.5.4 Effect of plasma treatment on water contact angle

Before progression to the DRG model, the effect of plasma treatment was investigated to determine the effect on the hydrophilicity of PCLMA and PCL samples. Flat polymer substrates were produced and water contact angle was tested on substrates with and without air-plasma treatment. The water contact angle of the non-treated PCLMA and PCL were not significantly different ($102.0 \pm 5.4^\circ$ and $89.8 \pm 7.7^\circ$ respectively). Plasma treatment significantly lowered the water contact angle of all three samples types, indicating increased hydrophilicity ($P < 0.0001$, one-way ANOVA with Tukey's multiple comparison). There was no significant difference between the water contact angle of plasma-treated PCLMA and plasma-treated PCL ($43.3 \pm 2.9^\circ$ and $47.0 \pm 10.9^\circ$ respectively).

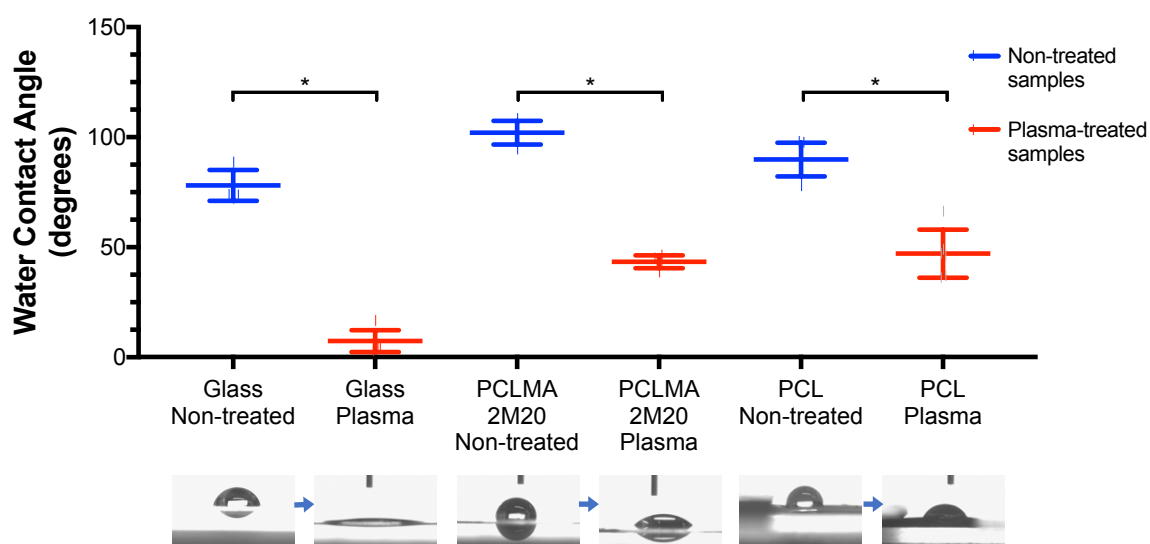


Figure 67. Water contact angle measurements for glass, PCLMA and PCL before and after air-plasma treatment. Values displayed mean \pm SD (N=1, n=5-7). * denotes significant difference (one-way ANOVA with Tukey's multiple comparison). The pictures below the x axis offer a visual representation of the water contact angle of each sample, showing the effect of treatment with air-plasma (blue arrow).

4.5.5 DRG outgrowth in fibre-filled conduits

The results in this section refer to work performed by M. Behbehani. Chick DRGs were cultured in different types of fibre-filled conduits to assess the effect of different parameters/treatments. The DRGs on fibres were imaged using light sheet microscopy to measure the outgrowth of both Schwann cells and axons.

In the first two experiments (investigating the effect of plasma treatment and the effect of fibre diameter) conduits were produced and DRG culture was performed by M. Behbehani. A brief summary of the results are shown here as the experiments were run concurrently with this work and used to inform the choices for the *in vivo* study in chapter 5. The third experiment (assessing the effect of packing density) was performed as a collaboration between J. Field and M. Behbehani; here, conduits with different packing density of fibres were produced by the author and provided to M. Behbehani for DRG culture and analysis. Full presentation and analysis of these results can be found in the thesis of M. Behbehani [278].

4.5.5.1 The effect of plasma treatment on DRGs cultured in fibre-filled conduits

Chick DRGs were cultured for 7 days in fibre-filled conduits containing 10 μm fibres at 20% packing density, both with and without plasma treatment. DRG outgrowth on the non-treated scaffolds was very limited, however a large degree of outgrowth was supported on the plasma-treated conduits. The probability of DRG outgrowth was significantly increased on plasma-treated vs non-treated conduits (from 56% to 85%). Additionally, the outgrowth distance of axons and Schwann cells was measured from the DRG body. A significant, five-fold increase in maximum outgrowth of both cell types was seen on the plasma-treated conduits compared to non-treated conduits. Average maximum outgrowth was measured to be 0.54 ± 0.29 mm and 0.50 ± 0.23 mm (axons and Schwann cells respectively) in non-treated conduits compared to 2.52 ± 0.36 mm and 2.46 ± 0.37 mm (axons and Schwann cells respectively) in plasma-treated conduits [278].

4.5.5.2 The effect of fibre diameter on DRGs cultured in fibre-filled conduits

Chick DRGs were cultured for 7 days in fibre-filled conduits containing fibres of different diameters (1, 5, 8, 10 and 13 μm) at 20% packing density. All conduit types were plasma-treated to promote outgrowth. The shortest maximum outgrowth of axons and Schwann cells was seen on 1 μm fibres, and the longest maximum outgrowth was seen on the 10 μm fibres. This trend of increasing outgrowth vs fibre diameter was evident and the 10 μm fibres were found to promote significantly greater maximum outgrowth compared to the 1 μm fibres (2.52 \pm 0.36 mm vs 1.25 \pm 0.06 mm for axons and 2.46 \pm 0.37 mm vs 1.34 \pm 0.29 mm for Schwann cells). The 13 μm fibres, promoted slightly lower outgrowth compared to the 10 μm fibres and though the difference was not significant, it suggests that 10 μm may be the optimal fibre diameter in this range for promoting outgrowth [278].

4.5.5.3 The effect of packing density on DRGs cultured in fibre-filled conduits

Chick DRGs were cultured for 7 days in fibre-filled conduits containing 10 μm fibres, filled to different packing densities (10, 20 and 40%). The maximum axon outgrowth was measured for each sample and the results are displayed in Figure 68. For non-treated conduits axonal outgrowth was slightly higher in the 10% packing density conduits compared to the 20% and 40% but the differences were not significant. No significant differences were found between the plasma-treated conduits of different packing densities (2.92 \pm 0.22 mm, 3.02 \pm 0.61 mm and 2.74 \pm 1.45 mm for 10%, 20% and 40% respectively).

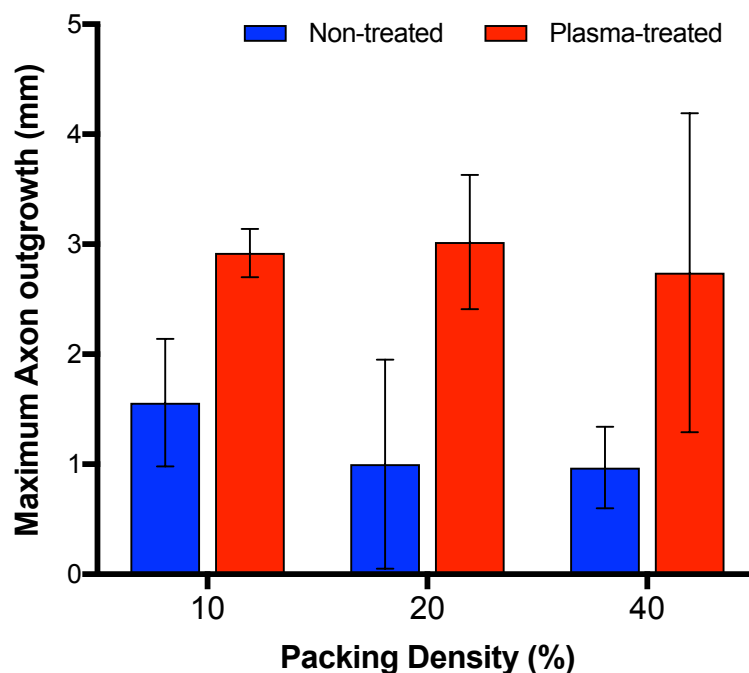


Figure 68. The effect of different fibre packing densities on the outgrowth of axons from DRGs cultured in fibre-filled conduits. Values displayed mean \pm SD (N=3, n=3). No significant differences were found between any of the groups (Two-way ANOVA with Tukey's multiple comparisons test for comparing different densities, Two-way ANOVA with Sidak's multiple comparisons test for comparing plasma-treated and non-treated samples).

4.6 Discussion

4.6.1 Biocompatibility testing of NGC materials

As discussed in chapter 1, PCL is widely known as a biocompatible material used in many applications including FDA approved medical devices. The PCLMA synthesised in this study was shown to be biocompatible, demonstrating its suitability for use in tissue engineering applications. The photocured PCLMA supported RN22 cell growth with a level of metabolic activity comparable to that on TCP. Schwann cells grown on PCLMA had a higher metabolic activity than TCP however this experiment was only performed once in triplicate, so it is necessary to repeat this to verify the results. The biocompatibility of this PCLMA resin could be an improvement on other photocurable forms of PCL i.e. the vinyl-terminated PCL by Ronca et al. which supported considerably lower metabolic activity of mesenchymal stem cells compared to TCP control [220]. Elomaa et al. used PCLMA similar to that in our study and demonstrated biocompatibility with fibroblasts assessing with MTS assay [219]. Again, slightly lower metabolic activity was seen in comparison to TCP so it may be that the PCLMA in our study demonstrates a greater biocompatibility. This biocompatibility may be a result of the long washing times (7 days) used for all PCLMA samples before cell culture, as it has been shown that prolonged washing of photocured polymers is necessary to improve their biocompatibility. Ortega et al. demonstrated that cured PEGDA supported significantly greater cell viability after washing for 7 days compared to 4 days or less [202].

It was also necessary to test the biocompatibility of beta-carotene. Since beta-carotene is a hydrophobic powder, its dissolution into culture media was not possible and so its biocompatibility could not be directly assessed in plain cell culture. Instead, the biocompatibility of beta-carotene-containing PCLMA was tested against plain PCLMA as this is the form it would be used *in vivo*. PCLMA discs were used here instead of spin-coated films as it was desired to use a bulk volume of material. This was to ensure that any low level dissolution of beta-carotene from μ SL structures *in vivo* would be replicated *in vitro* by the use of the bulk discs. The beta-carotene-containing PCLMA demonstrated an equal biocompatibility compared to the plain PCLMA. As expected, as a natural pigment present in food, beta-carotene showed no signs of toxicity to RN22 cells. This means it could offer a desirable alternative to commercially available photoabsorbers such as Tinuvin which has shown cardiotoxic effects in rats both *in vitro* and *in vivo* [254], [255]. Tinuvin has also been known to produce contact allergy [302]. Since RN22 cells are a cancerous cell line, it would be desirable to test biocompatibility with a more relevant cell type such as Schwann cells. Further

biocompatibility testing could be performed with a neuronal cell type such as NG108-15 cells [153] or primary neurons from dissociated DRG cultures.

4.6.2 Schwann cell migration study

The migration of Schwann cells within fibre-filled conduits was investigated due to the importance of Schwann cell migration during regeneration after a nerve injury. Preliminary experiments were carried out with RN22 cells however their behaviour is not completely representative of native Schwann cells. The RN22s were seen to form clumps on the fibres at the point of seeding which could have been a result of a high cell density due to the cells' rapid proliferation rate. Further along the fibres however, where cell density was lower, cell behaviour was more representative of Schwann cells, with RN22s being seen to extend and align along fibre direction, assuming a more Schwann-like phenotype. The formation of bands mimics native Schwann cell formation of Bands of Büngner during peripheral nerve regeneration and may suggest the scaffold's ability to promote desirable Schwann cell growth. It is unlikely however, that the cells were present along the fibres due only to migration. Since RN22s are a very proliferative cell type the large amount of proliferation will have contributed to the cells spreading along the fibres.

Further experiments were carried out with primary Schwann cells to investigate migration with a more relevant cell type. Schwann cells were seen to migrate more along 10 μm fibres compared to 2 μm fibres. These are of course qualitative observations only and the experiment was only performed once in triplicate so would need to be repeated to confirm observations. However, the preliminary data suggests that 10 μm fibres may be more effective at promoting and guiding the migration of Schwann cells within a conduit used to repair a nerve injury.

The migration of Schwann cells is an important behaviour to investigate as it is well understood that migrating Schwann cells guide the extension of regenerating axons within a nerve injury. Studies have shown in DRG cultures that the extension of axons is always preceded by Schwann cell outgrowth in that the axons always lag behind the advancing Schwann cells [153], [300] and that Schwann cells and axons are often found co-localised [143], [154], [300]. The presence of Schwann cells is known to enhance and align neurite outgrowth *in vitro* [177], [178] as well as *in vivo*. Numerous studies have reported on significantly improved nerve regeneration in implanted conduits filled with Schwann cells compared to acellular conduits as assessed by parameters such as axonal diameter, number of myelinated axons, nerve conduction velocity and post-operative time to achieve functional recovery [303] [304] [103].

These results all emphasise the importance of migrating Schwann cells and their ability to guide regenerating axons, implying that for a NGC to be successful, it needs to be designed to support Schwann cell growth and migration. If Schwann cells can be encouraged to rapidly migrate into the conduit, pre-seeding of Schwann cells would not be necessary, avoiding the need for immunosuppression that may be required with the use of allogenic Schwann cell transplantation. It has also been shown however, that on fibres coated with laminin or fibronectin, axons are able to extend beyond advancing Schwann cells [300]. This suggests that the beneficial effect of Schwann cells may be replicated by the inclusion of relevant ECM molecules and provides an alternative method for enhancing neurite growth.

4.6.3 Plasma treatment

Treatment with air plasma significantly increased the hydrophilicity of both PCL and PCLMA. The water contact angles of plasma-treated PCL and PCLMA ($\sim 45^\circ$) falls in the $40\text{-}70^\circ$ range that has been reported as optimum for cell attachment [281], [305], [306]. It is also interesting to note that the PCLMA synthesised in this study had the same water contact angle as the commercially available PCL (in both plasma-treated and non-plasma-treated states) showing that methacrylate functionalisation and photocuring does not cause a significant change in the material hydrophilicity.

Treatment with air-plasma acts to oxidise the material surface and incorporate hydroxyl, carbonyl and carboxyl groups onto the polymer backbone [284]. This is well known to increase the hydrophilicity of polymer materials and the effect of plasma treatment on PCL has been widely studied. Jacobs et al. showed that air-plasma treatment caused a 10% increase in oxygen content, with an increase in the presence of C-O and O-C=O bonds as assessed by X-ray photoelectron spectroscopy, as well as an appearance of C=O bonds. This was accompanied by a decrease of water contact angle from 74° to 52° [285]. This effect has also been studied with PCL microfibres produced by electrospinning. Can-Herrera et al. found similar results with air-plasma treatment resulting in increased oxygen content and decreased water contact angle with a more pronounced change being detected with increased power and longer treatment times [286].

This chemical change is usually accompanied by an increase in biocompatibility as reported by Yildirim et al. in the culture of mouse osteoblasts. Increasing plasma treatment time resulted in decreasing water contact angle (as reported by Can-Herrera et al.) and this was accompanied by increasing metabolic activity [292]. Valence et al. also reported benefits from air-plasma treatment

of electrospun PCL scaffolds. With *in vitro* culture of smooth muscle cells, plasma treatment resulted in slightly increased proliferation but also significantly increased cell spreading (cells appeared less rounded). Scaffolds were also implanted for 3 weeks *in vivo*, both subcutaneously and as vascular grafts. In both positions, a marked increase in cell infiltration was seen in plasma-treated PCL scaffolds, with cells penetrating deeper into the material [307]. This demonstrates the ability for plasma treatment to enhance cell migration and tissue ingrowth which is hugely important for the promotion of nerve regeneration through a conduit.

Plasma treatment of polymer materials is often performed with other gases such as oxygen, nitrogen, hydrogen, ammonia and argon (or combinations of these). These treatments have all been demonstrated to improve metabolic activity of cells grown on PCL scaffolds including human umbilical vein endothelial cells, mouse osteoblasts, fibroblasts and chondrocytes [294], [308], [309].

4.6.4 The effect of fibre parameters/properties on DRG outgrowth

In the study of DRG outgrowth within fibre-filled conduits, it was seen that: a) plasma treatment had a great effect in increasing Schwann cell and neuronal outgrowth, b) the greatest outgrowth was seen on 10 μm fibres and c) fibre packing density had little effect on DRG outgrowth.

The effect of plasma treatment on increasing DRG outgrowth is comparable to work by Valence et al., discussed above, that saw improved cell migration through plasma-treated PCL scaffolds. In a similar study, Cheng et al. treated PLA microfibre scaffolds with Ar and Ar-NH₃/H₂ plasmas. With *in vitro* culture of bovine aorta endothelial cells, greater cell infiltration was seen into both types of plasma-treated scaffolds. Scaffolds were then implanted subcutaneously in rats and cell infiltration was observed after 5 and 14 days. On day 5, the harvested samples showed greater infiltration in the plasma-treated samples compared to the controls but by day 14 this difference was less significant [293]. These results suggest that the plasma treatment can successfully speed up the rate of cell migration into the scaffold and is similar to the results here of increased DRG outgrowth in plasma-treated scaffolds.

Regarding fibre diameter, we saw that from 1 to 10 μm , there was a trend of increasing DRG outgrowth distance that correlated with increasing fibre diameter. This is the same trend as seen by Daud et al., growing neuronal cells on fibres of 1 to 8 μm diameter: the longest neurites were seen on 8 μm fibres however the authors did not test any fibres larger than this diameter [153]. In the present study it has been shown that 10 μm fibres supported greater outgrowth than 8 μm fibres

but outgrowth declined on the 13 μm fibres. Though this latter decrease is not significant, it seems that 10 μm may be the optimal fibre diameter for promoting axonal and Schwann cell outgrowth from DRG explants. Interestingly, this appears to be contradictory to the results from the DRG cultures by Daud et al. Though there were no significant differences, a decreasing trend of axonal and Schwann cell outgrowth was seen on increasing fibre diameters (1 to 8 μm) [153]. However, in this experiment DRGs were grown on mats of electrospun fibres compared to our experiment with DRGs in fibre-filled tubes. Containing the fibre bundles within tubes introduces a 3D element to the culture and highlights the importance of factors not considered in 2D culture. When filling tubes with a set packing density of fibres, it follows that using smaller diameter fibres results in smaller pores/smaller gaps between the fibres. It is thought that these small pores may present a barrier to impede the migration and outgrowth from the DRG explant. This highlights the indirect effects that need to be considered when varying parameters such as fibre diameter and emphasises the importance of using models that closer approximate the use of the device *in vivo*.

Other studies culturing DRGs on electrospun fibres mostly focus on fibres in the nanometre range [154], [155], [158], [159]. A limited number of studies have investigated the effect of fibre diameter on outgrowth from DRG explants and these have used fibres on the border of micro-nano range. Wang et al. electrospun aligned PLA microfibres with large, intermediate and small fibre diameters (1325 nm, 759 nm and 293 nm respectively) [310]. Chick DRGs were cultured on these fibre mats and it was found that the large and intermediate fibres promoted significantly longer neurite outgrowth compared to the small fibres. Schwann cell migration was also significantly increased on the large compared to the intermediate fibres and on the intermediate compared to the small fibres. As found by others, neurite extension lagged behind Schwann cell outgrowth on the large and small fibres. However, on intermediate fibres, the neurite outgrowth was significantly greater than Schwann cell outgrowth, suggesting that certain fibre morphologies are able to guide neurite growth in a similar fashion to Schwann cell Bands of Büngner. Gnani et al. also cultured DRGs on fibres in the range of 300-1300 nm and found similar results with significantly longer axonal outgrowth on the 600-1300 nm fibres vs 300 nm fibres [311]. These however, were randomly oriented fibres compared to the aligned fibres by Wang et al. Additional experiments with primary Schwann cells yielded some interesting results with Schwann cell migration being significantly faster on the larger fibres (assessed by time lapse imagery). The larger fibres also promoted increased formation of filopodia (structures important for cell migration) compared to the smaller diameter fibres. These two studies suggest that small diameter microfibres ($\sim 1.3 \mu\text{m}$) promote better outgrowth compared to smaller fibres in the nanometre range [310], [311]. Looking at larger fibres, the study mentioned

previously by Wen et al. (section 4.2.2) suggested that 5 μm microfibres performed better than 500 μm fibres [300]. Considering these results together, fibres in the small diameter micrometre range, either side of 5 μm , is of great interest to research in nerve regeneration. In the current study, we have investigated this range and shown that 10 μm fibres seem to be optimal for the promotion of axonal and Schwann cell outgrowth.

In terms of packing density it was shown that varying the packing density in the range of 10-40%, had little effect on DRG outgrowth. Previous studies have used packing densities of $\geq 10\%$ with positive results [36], [154], [168], [172] so 10% packing density seems to be a good starting point for use in preliminary *in vivo* studies.

4.7 Conclusions

PCLMA and PCLMA containing beta-carotene were shown to support the growth of Schwann and Schwann-like cells, demonstrating the material's biocompatibility and its suitability for use in the fabrication of NGCs. Schwann cells were also able to migrate along 10 μm fibres *in vitro*, indicating their potential use as scaffolds for nerve guidance. Treatment with air-plasma increased hydrophilicity of both PCL and PCLMA which significantly improved the outgrowth of DRG explants through fibre-filled conduits. Along with the other results from the DRG study it can be concluded that a plasma-treated, fibre filled conduit with 10 μm fibres, filled to 10% packing density is the best candidate to go forward with preliminary *in vivo* testing.

5. Chapter 5: In Vivo analysis of conduit performance

5.1 Chapter Introduction

This chapter investigates the *in vivo* performance of the different conduit types with the use of a 3 mm nerve injury model in thy-1-YFP mice. The presence of fluorescent axons in this transgenic mouse strain allows for the use of unique methods in the assessment of nerve regeneration.

Preliminary work which was performed during the early stages of the study will be discussed. This involved the use of conduits produced before the conduit designs were finalised for the full studies, with the results showing limited success.

In the main studies, the conduit designs presented in chapter 3 were assessed for their ability to support nerve regeneration in the above model. Conduits with aligned grooves and conduits containing aligned electrospun PCL fibres (both produced by microstereolithography) were tested against plain (empty) conduits and graft controls. Following the beneficial results from using plasma-treated conduits *in vitro* (chapter 4), the effect of plasma treatment was also investigated *in vivo*. Both plain and fibre-filled conduits were plasma-treated and tested alongside the non-treated conduits. Smooth conduits, without the inherent microfeatures from μ SL production, were also tested to investigate the effect of these features on nerve regeneration.

5.2 Background

5.2.1 Methods of assessing nerve regeneration *in vivo*

There are a variety of methods used to evaluate the regeneration of peripheral nerves and compare the success of different repair strategies. Observational techniques such as histology are widely used to gain an overall view of nerve regeneration in terms of the physical characteristics of the regenerated nerve. Fixed nerve tissue is usually paraffin wax-embedded and sectioned to allow for staining and imaging with light microscopy. Non-specific stains such as haematoxylin and eosin can be used to evaluate tissue ingrowth into conduits [134] and compounds such as toluidine blue or osmium tetroxide can be used to highlight myelinated axons [106], [312]. Transverse sections are usually taken and allow for measurements such as axon number or density and the diameter of nerve fibres. These measurements can be performed on sections at various locations along the repair, usually at the graft midpoint or in the distal nerve [313]. Immunohistochemical staining with antibodies can also be used to stain for specific cellular components such as S100 (present in Schwann cells) and neurofilament or beta-III tubulin (present in axons) [314]. The presence and distribution of Schwann cells and axons within the repair can then be measured and together with longitudinal sections, Schwann cell migration and axon growth distance can be quantified [154], [182].

Other than direct observational techniques, functional recovery during nerve regeneration can also be assessed to determine the level of sensory or motor function regained following nerve repair. Electrophysiological methods can be employed to quantitatively measure the functional performance of a regenerated nerve in terms of its ability to transmit signals in the form of compound action potentials (CAPs) [315]. With the use of electrodes placed either side of the injury site, the nerve is stimulated and the transmitted CAP waveform can be recorded. Motor nerve function can be specifically assessed by detecting the signal transmitted to the innervated muscle fibres (the compound muscle action potential) [184]. The amplitude of the CAP signal is used as a measure of function as it depends on the number and size of regenerated axons within the nerve tissue [315]. The amplitude can be compared between groups and to uninjured controls to compare the success of different repair types [36], [316]. Nerve conduction velocity can also be calculated [134], [316] and is another measure of functional recovery and nerve maturation due to the dependence on axon diameter and myelination [315]. Alternatively, end-point muscles can be harvested and weighed, and the level of atrophy in comparison to normal muscle weight can give an indication of the level of muscle reinnervation [168], [182].

Functional recovery can also be assessed by behavioural methods such as walking track analysis in rodent models. Here, paw prints are recorded and measurements made, including print length, toe spread and stride length - parameters which rely on activation of various muscles [313]. Since walking is dependent on the activation of different muscles in response to sensory input, walking track analysis can give an overall view of coordinated nerve function [317], [318]. In case of sciatic nerve injury, sciatic function index is widely used as a measure of functional recovery and is calculated from a number of parameters from walking track analysis, in comparison to normal values [13]. Other behavioural methods can be used to assess sensory recovery such as the response to thermal stimuli, including thermal withdrawal latency [134], [168]. These behavioural methods are non-invasive, so measurements can be taken at multiple time points, allowing the progression and rate of recovery to be monitored over the whole recovery period.

In the present study, nerve regeneration was assessed via observational techniques, using a particular strain of transgenic mice (thy-1-YFP-H). In these mice, axons express yellow fluorescent protein (YFP) and with fluorescence microscopy, axons are visible through the depth of the tissue. This allows nerves to be imaged, without the need for histological processing and destructive sectioning techniques which lead to loss of information. The lack of sectioning means that axons remain intact and high-resolution images of whole nerve samples can be obtained in which axons can be traced across the injury site and into the distal nerve. By observing at the individual axon level, detailed information can be obtained on the success of nerve regeneration and the effect of different treatment methods.

5.2.2 The thy-1-YFP mouse model

The thy-1-YFP mouse strains were generated by Feng et al. [319], along with variants expressing red, green and cyan fluorescent proteins (collectively termed XFP). The result was a number of strains of mice, possessing neurons, labelled in their entirety with these fluorescent proteins. The pattern of expression in each strain is comprised of different subsets of neurons in different combinations. The thy-1-YFP lines are by far the most widely used of the XFP variants with the thy-1-YFP-H and thy-1-YFP-16 lines being the most commonly used of these. The thy-1-YFP-H line express YFP in a smaller subset of axons in comparison to other strains, which is useful for certain applications as fluorescent axons are individually distinguishable when numbers are low enough.

There are a number of research groups who have utilised thy-1-YFP-H mouse strains for the study of peripheral nerve regeneration, with the greatest number of publications coming from the Arthur W. English lab in Atlanta, Georgia. In a 2005 paper from this lab by Groves et al. [320] common fibular nerves of YFP⁺ mice were injured and repaired using graft tissue from wild type (WT, YFP⁻) mice. As part of their study, work was done to characterise the labelled axons in the thy-1-YFP-H strain. Counting the number of YFP⁺ axons in the dorsal and ventral roots of the L4 spinal nerve it was found that 58% of the labelled axons were sensory and 42% were motor neurons (122.6 axons found in the dorsal root vs 87.2 in the ventral root). Comparing the 122.6 labelled sensory axons found to the 4625 that make up the dorsal root [321] allowed for their estimation that 2.6% of all sensory axons in the thy-1-YFP-H strain are YFP⁺. They further studied the common fibular nerve (which is a branch of the sciatic nerve) to find an average of 36.03 (± 2.35 SEM) YFP⁺ axons and using the above ratio of sensory:motor axons, we can assume that 21 are sensory axons from the dorsal root ganglion and 15 are motor neurons.

From this work we can see why the common fibular nerve is commonly used in the study of peripheral nerve regeneration in YFP mice. The relatively small number of YFP⁺ axons present in the common fibular nerve means that each axon is individually identifiable. This allows the visualisation and tracing of individual axons and the utilisation of the YFP strain to its full potential. The number of axons in the common fibular nerve is however still higher than the tibial branch of the sciatic so is preferred for these studies.

5.2.3 Methods of assessing regeneration with the thy-1-YFP mouse model

In the English lab, the thy-1-YFP-H model has also been used to investigate the effect of electrical stimulation [322] and the effect of exercise [323] on peripheral nerve regeneration. To quantify nerve regeneration, the groups counted the number of axons present in the graft tissue and presented this as a percentage of the number of axons in the nerve at a point proximal to the injury site. This gave a 'sprouting index' as an indicator of the amount of regenerative sprouting in the repair [320]. The group also traced the regenerated axons from the point of injury to the most distal point reached. The lengths of these axons were measured and presented as frequency distributions. A shift in the distribution of axons towards a longer length was seen as a marker for improved regeneration [320]. For example, in the study on electrical stimulation, graft repairs with WT tissue were performed with or without a single 1-hour application of electrical stimulation to the common fibular nerve immediately after repair. By averaging the frequency distributions of axon length in the WT repairs, it was found that electrical stimulation resulted in a shift in the distributions signifying a

significantly larger number of longer axons within the regenerating nerve. In terms of their method used to assess nerve regeneration, the measurements made give an overall view of axon length, which is obviously an important parameter, indicative of the level of recovery. However, the group do admit a disadvantage in this method in that it is not possible to tell if an increase in the number of long axons is due to more unique, long axons or due to an increase in axon branching. This is obviously an important factor to consider when the aim is to promote functional recovery as it is critical that as many unique proximal axons as possible are able to traverse the injury site and regrow down the distal stump. An alternative method to assess regeneration is therefore desirable, which takes into account axon branching.

In previous work in our lab by A. Harding et al. [128], [324], [325], a more complex method of assessing nerve regeneration in thy-1-YFP-H mice was and developed with the use of a 3 mm common fibular nerve injury model. A similar measure of sprouting index to that of Groves et al. was calculated, but axon counting was performed at 0.5 mm intervals from the proximal to the distal point of the nerve injury, giving more information of the sprouting profiles along the length of the nerve repairs. This measure of sprouting is a useful statistic as increased sprouting/branching can indicate increased disruption to the nerve growth [326]. Axons were also traced back from each 0.5 mm interval (starting with the most distal) until they either reached the proximal site or rejoined with a branch of a previously traced axon. This allowed the calculation of the number of unique axons at each interval, taking into account axons originating from the same proximal axon, something not considered by the previous studies or the sprouting index measurements. Thus, giving a truer measure of regeneration success. The proximal region of the nerve injury was further studied in more detail as this is where the most axonal disruption occurs (where regenerating axons enter the graft tissue/conduit). Axon lengths were measured and compared to the most direct path to give a percentage increase in axon length. This indicates the level of axonal disruption and the 'ease' of the axons' entry into the repair material (graft/conduit). These methods of assessment demonstrate a number of advantages compared to the previously discussed studies allowing more information to be drawn on how axon growth is affected by different repair types.

5.2.4 Method of nerve repair

The method of coaptation during nerve repair is another topic for debate with the gold standard being the use of microsurgical suturing. However, fibrin glue has become a more widely considered alternative, especially for use in rodent models, and is the method of choice used in the studies by the Arthur W. English lab, discussed above. Although there are a number of advantages to micro-

suturing (high precision and maintenance of tensile strength at the repair site), the disadvantages such as tissue damage which can lead to scarring, increased inflammation and foreign body reaction, may be overcome by the use of fibrin glue. Other benefits of fibrin glue coaptation include a decreased skill required by the surgeon [327]. For small diameter nerves such as the mouse common fibular nerve, suturing would likely be especially difficult, requiring a high level of expertise compared to fibrin glue repair. Kouloxouzis et al. performed a study to investigate the differences in regeneration between nerve repairs by suturing and fibrin glue coaptation [327]. The sciatic nerve in both legs of thy-1-YFP mice were transected and 1 cm segments of WT donor nerve were attached to the proximal stumps using fibrin glue on one side and two 11-0 sutures on the other. After a seven-day recovery period, the results showed an increased regeneration distance in the fibrin repairs, demonstrated by a significantly longer mean axon length (2.62 ± 0.10 mm vs 2.10 ± 0.08 mm, $P < 0.001$). Fibrin glue has also been shown to promote less inflammation than suture repairs and avoid disadvantages from suture placement and granuloma formation at suture sites which can hinder axonal growth [328]. Additionally, repair with fibrin glue is less time consuming than with sutures and surgical repair times can be cut by up to two thirds [327].

5.3 Aims for this chapter

Assess the *in vivo* nerve regeneration potential of the NGCs discussed in chapter 3 using the thy-1-YFP mouse model and determine the effect of aligned physical guidance cues on nerve regeneration. Conduits containing physical guidance cues were tested in comparison to plain conduits and the gold standard autograft treatment in order to:

- 1) Investigate the effect of aligned grooves along the surface of the conduit lumen
- 2) Investigate the effect of aligned PCL fibres within the conduit lumen
- 3) Investigate the effect of plasma treatment of the PCLMA conduits (both with and without internal PCL fibres)
- 4) Investigate the effect of the inherent microfeatures present on conduits produced by microstereolithography

5.4 Materials and Methods

Nerve repairs were carried out using a 3 mm nerve injury model in thy-1-YFP-H mice. Conduits of different designs (described in chapter 3) were produced to be surgically implanted in the nerve gap and compared in their capacity to support nerve regeneration. Nerve graft repairs were also performed to act as a control as the clinical, gold standard approach.

5.4.1 Conduit preparation

Conduits were produced as described in chapter 3, using microstereolithography, electrospinning and injection moulding. All conduits were 4.5 mm in length to leave 0.75 mm either side of the 3 mm nerve gap to insert the proximal and distal nerve stumps.

5.4.1.1 Plain conduits

Plain conduits were produced by μ SL as described in section 3.4.1, with an internal diameter of around 920 μ m and a wall thickness of around 280 μ m (see section 3.5.1).

5.4.1.2 Grooved conduits

Grooved conduits were produced to assess the effect of aligned grooves on nerve regeneration *in vivo*. These were produced by μ SL as described in section 3.4.2. Since these were produced using PCLMA resin containing beta-carotene (to improve groove resolution), plain tubes were also produced with beta-carotene-containing resin to be used as a control. The grooved conduits had an internal diameter of around 830 μ m and a wall thickness of around 300 μ m. The plain conduits had an internal diameter of around 900 μ m and a wall thickness of around 280 μ m (see section 3.5.2.3).

5.4.1.3 Fibre-filled conduits

Fibre-filled conduits were produced to assess the effect of aligned microfibres on nerve regeneration *in vivo*. These were produced as described in section 3.4.7, using the three-part, modular design and a combination of μ SL and electrospinning. These conduits contained 10 μ m fibres filled to 10% packing density had an internal diameter of around 880 μ m and a wall thickness of around 280 μ m (see section 3.5.7).

Preliminary *in vivo* trials were also carried out before this design was finalised using conduits filled with either 2 μ m and 9 μ m fibres to a 12% packing density. These conduits had an internal diameter of around 890 μ m and a wall thickness of around 400 μ m.

5.4.1.4 Smooth conduits

Smooth conduits were produced to test against plain conduits to determine if the inherent microfeatures present from the use of μ SL had an effect on nerve regeneration. These were produced by injection moulding as described in section 3.4.8. The internal diameter of the conduits was around 960 μ m and the wall thickness was around 280 μ m (see section 3.5.8). The inner luminal surface and outer surface lacked any obvious features.

5.4.1.5 Plasma treatment of conduits

In chapter 4, plasma treatment of fibre-filled conduits was shown to promote DRG outgrowth *in vitro*. For this reason, both plain and fibre-filled conduits were plasma-treated to investigate the effect of this surface treatment on nerve regeneration *in vivo*.

Plasma treatment was performed as described in section 4.4.4.2 with a Deiner electronics commercial plasma system (60 seconds at 50 W, 0.4 mBar). Plasma-treated conduits were used in surgery within 5 days after plasma treatment to avoid any problems due to instability of the surface modification.

5.4.1.6 Conduit preparation and sterilisation for implantation

Following production, conduits were washed in IPA and laser cut to 4.5 mm (section 3.4.9). IPA washing was carried out for at least 7 days, changing the IPA at least twice during this time. Plasma treatment (if required) was performed after this washing step. Prior to implantation, conduits were sterilised in 70% ethanol for 24 hours and then washed 5 times in sterile PBS. Conduits were then stored individually in sterile PBS until use.

5.4.2 In vivo surgery methods

Conduits and nerve grafts were used to repair 3 mm common fibular nerve injuries following a protocol developed by A. Harding, and reported in [128], [324], [325]. Surgeries were carried out by the author, after training from (and in some cases under supervision by) A. Harding.

5.4.2.1 Animals

All experimental protocols were carried out in accordance with the Animals (Scientific Procedures) Act 1986, under valid UK Home Office project licence (PPL 70/8194, Licence holder: F. Boissonade) and personal licence (PIL 39680, Licence holder: J. Field). Experiments were carried out with thy-1-YFP-H transgenic mice (described in section 5.2.2) in which a subset of axons express YFP along their length. This allows for whole nerve samples to be imaged without the need for sectioning and staining. This means that the whole tissue structure remains intact and individual axons can be visualised across the nerve injury/repair site.

Thy-1-YFP-H mice were obtained from a Home Office-approved UK supplier (JAX Mice, USA via Charles River UK Limited) and bred for experimental use. The breeding pairs used in this study were heterozygous for the thy-1-YFP gene. The offspring were therefore a mixture of mice possessing the modified thy-1 gene (YFP⁺ mice) and mice without the modified gene. The offspring without the modified thy-1 gene revert back to the WT genotype of the C57BL-6J strain, used in the production of the thy-1-YFP-H strain. YFP⁺ mice were used for both types of nerve repairs (conduit or graft) and WT mice were used as donors to provide non-fluorescent nerve tissue for use in graft repairs. Heterozygous breeding pairs were used to produce a greater number of YFP⁺ than WT mice to match the numbers required for experiments and minimise surplus mice numbers (a greater number of conduit repairs were performed compared to graft repairs as there were different conduit types to test). Experiments were carried out with mice aged between 17 and 23 weeks.

5.4.2.2 Surgery groups and animal numbers

A total of 99 mice were used in the following experiments (86 experimental mice and 13 graft donors). 63 of the experimental animals were used for the three main studies and were split between 8 different repair type groups (Table 10). It was desired to include 6-7 mice in each group (see section 5.4.5 for sample size calculations), with extra where possible, to account for any failures, but in some cases numbers were limited by the number of mice that were available at the time of each study. The remaining 23 experimental animals were used in preliminary experiments (see page 196).

Three main studies were carried out in line with the chapter aims:

- 1) Plain conduits vs grooved conduits (beta-carotene containing conduits)
 - a) To determine the effect of aligned grooves on peripheral nerve regeneration
- 2) Plain conduits vs fibre-filled conduits (plasma-treated and non-treated conduits of each type)
 - a) To determine the effect of plasma treatment in plain conduits
 - b) To determine the effect of plasma treatment in fibre-filled conduits
 - c) To determine the effect of aligned fibres (in both plasma-treated and non-treated conduits)
- 3) Plain conduits vs smooth conduits
 - a) To determine the effect of DMD microfeatures

As a positive control, graft repair surgeries were carried out alongside the repairs in the different studies and pooled into one group for analysis. This allowed the efficacy of each conduit type to be compared to the gold standard treatment for long gap injuries.

Table 10. Animal numbers for the three main studies

Repair type	No. of animals in group
Graft repairs	10 (plus 10 donors)
Plain conduits (containing beta-carotene)	7
Grooved conduits (containing beta-carotene)	8
Plain conduits	11
Plain conduits (plasma-treated)	9
Fibre-filled conduits	5
Fibre-filled conduits (plasma-treated)	5
Smooth conduits	8

The following preliminary experiments (see below) were performed before the conduit designs were finalised. The results will briefly be discussed in section 5.5.1. Nerve harvests from preliminary experiment 1 and 2 were imaged with fluorescence microscopy (yielding poorer quality images than with confocal microscopy) and analysed only qualitatively. Preliminary experiment 3 compared thick- and thin-wall plain conduits and confocal images were analysed quantitatively. The thin-wall conduits were chosen as the final design for the plain conduits and therefore included in the analysis of the main studies (Table 10), as were the graft repairs.

- Preliminary experiment 1:
 - 3x Plain conduit (thick-wall design)
 - 3x 2 μm fibre-filled conduit (thick-wall design)
 - 3x 9 μm fibre-filled conduit (thick-wall design)

- Preliminary experiment 2:
 - 3x Plain conduit (thick-wall design)
 - 3x 9 μm fibre-filled conduit (thick-wall design)
 - 3x Graft (plus 3 donors)

- Preliminary experiment 3:
 - 5x Thick-wall conduits
 - 5x Thin-wall conduits (included in Table 10 count for plain conduits)
 - 5x Graft (plus 5 donors) (included in Table 10 count)

5.4.2.3 Anaesthesia

For conduit or graft implantation, animals were anaesthetised using isoflurane (IsoFlo, Zoetis UK Limited) mixed with oxygen. Induction of anaesthesia was performed in an induction box connected to an anaesthetic machine (Harvard Apparatus Limited) with 4% isoflurane in 100% oxygen at a flow rate of 4 L/min. Once anaesthesia was confirmed by a fall in respiratory rate and by testing the toe-pinch reflex, the animal was transferred to the operating table. Animals were placed on top of a heated blanket, covered with a sterile surgical drape. Here anaesthesia was maintained using a nose-piece tube connected to the anaesthetic machine (2-4% isoflurane in 100% oxygen, 1 L/min).

For non-recovery animals (graft donor mice and tissue harvest at experiment end-point) were anaesthetised with a combination of Hypnorm (0.315 mg/ml fentanyl citrate, 10 mg/ml fluanisone; VetaPharma Limited) and Hypnovel (5 mg/ml midazolam; Roche Products Limited). An injectable solution of Hypnorm:Hypnovel:sterile water (2:2:3) was prepared and administered via intraperitoneal (IP) injection at 10 ml/kg.

5.4.2.4 Nerve repair with conduit implantation

YFP⁺ mice were anaesthetised using isoflurane in oxygen (as described in section 5.4.2.3). The rear left leg was shaved, disinfected with hibitane and an incision was made up the back of the leg. The muscles were parted to reveal the common fibular nerve which was freed from surrounding tissue using blunt dissection techniques where possible. The common fibular nerve was then cut and the ends were trimmed to produce the required gap. The conduit was positioned between the proximal and distal nerve stumps, which were inserted approximately 0.75 mm into each conduit end (Figure 69A). This resulted in a 3 mm gap between the sectioned nerve endings. The conduit was secured in place with fibrin glue: equal quantities of fibrinogen (10 mg/ml; Sigma Aldrich) and thrombin (40 IU/ml; Sigma Aldrich) both prepared in distilled water. 5-7 minutes was allowed for the glue to set before muscle and skin were respectively sutured (6-0, coated vicryl sutures; Ethicon) to close the wound. A single dose of analgesic was administered subcutaneously: 0.01 ml of Vetergesic (0.3 mg/ml buprenorphine hydrochloride; Ceva Animal Health Limited). The mouse was placed in an incubator to recover from anaesthesia before returning to cages. For the recovery period of 21 days, mice were individually housed in cages to minimise the chance of suture removal.

5.4.2.5 Nerve repair with graft

The donor mouse (a WT mouse, from the same litter as the experimental recipient mouse) was anaesthetised via IP injection of Hypnorm:Hypnovel:water (as described in section 5.4.2.3). The recipient mouse was anaesthetised using isoflurane (as described in section 5.4.2.3).

The left rear leg of the donor mouse was shaved, disinfected and an incision was made. The common fibular nerve was exposed and freed from connective tissue as described for conduit surgery (section 5.4.2.4). Once complete, the nerve was re-covered with the muscle and skin to prevent it from drying out. The common fibular nerve of the experimental mouse was then exposed in the same way. A silicone trough, 5 mm length, was placed under the nerve to provide support during repair and the nerve was sectioned to create a 3 mm gap. The common fibular nerve of the donor mouse was sectioned to produce a 3 mm graft and immediately positioned in the silicone trough between the proximal and distal ends of the nerve in the recipient mouse (Figure 69B). The nerve ends were secured with fibrin glue as described in section 5.4.2.4, the silicone trough was carefully removed and the muscle and skin were sutured. A single dose of analgesic was administered (0.01 ml of Vetergesic) and the mouse was placed in an incubator to recover from anaesthesia. The donor mouse was culled by cervical dislocation. For the recovery period of 21 days, experimental mice were individually housed to minimise the chance of suture removal.

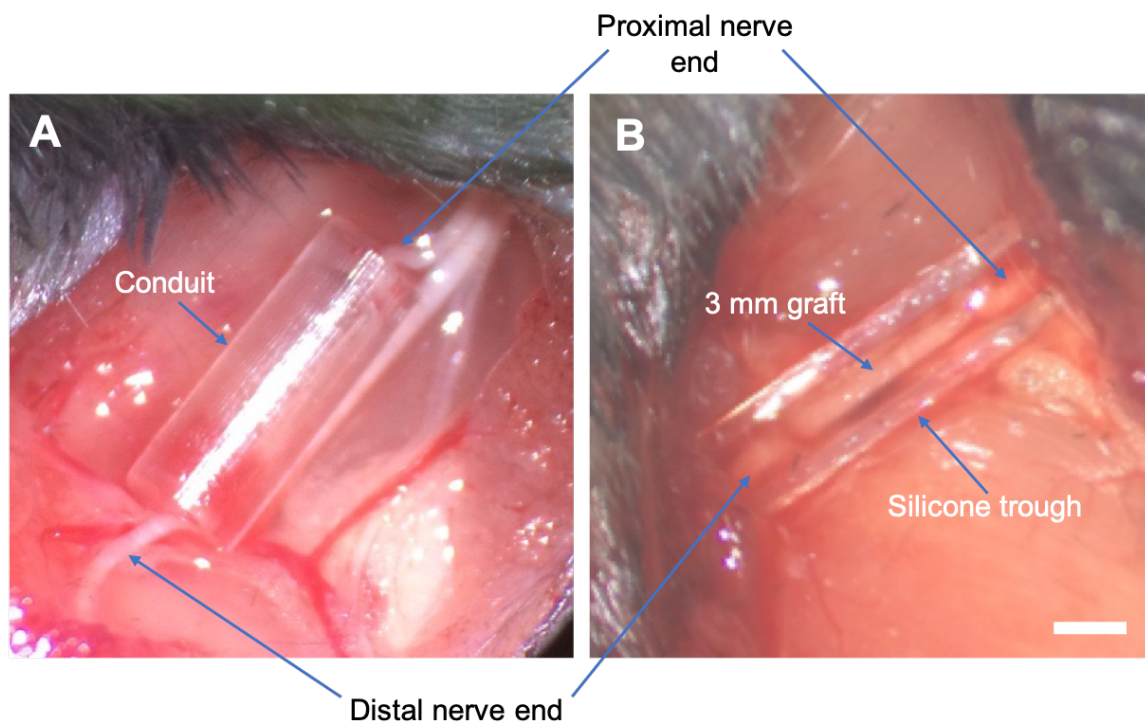


Figure 69. Photographs of common fibular repair surgery. A: Conduit repair, B: Graft repair. The position of the conduit between the proximal and distal nerve endings can be seen in A. The position of the silicone trough (removed after surgery) can be seen in B with the 3 mm nerve graft between the two nerve endings. Scale bar: 1 mm.

5.4.2.6 Conduit/Graft harvest

Mice were allowed to recover for a three-week period before nerve tissue was harvested for analysis. On day 21, mice were anaesthetised via IP injection of Hypnorm:Hypnovel:water (as described in section 5.4.2.3). The common fibular nerve was exposed and freed from surrounding tissues to reveal the conduit/graft repair. The skin was sutured to a raised ring, forming a pool which was filled with 4% formaldehyde for 30 minutes to fix the nerve *in situ*. The nerve was then harvested by sectioning at points proximal and distal to the repair site (as long a section as possible was taken). For conduit repairs, the conduits were always found surrounded in connective tissue (Figure 70Ai,Bi). This tissue was removed (Figure 70Aii,Bii) and the conduit was broken open to reveal the regenerated nerve cable (if the repair was successful, Figure 70Aiii,Biii). Excess tissue and large blood vessels around the nerve and neuroma sites were removed by microdissection. The nerve tissue was then fixed in 4% formaldehyde for a further 30 mins before mounting under a coverslip on a microscopy slide with Vectashield mounting medium (Vector Laboratories). The mouse was culled by cervical dislocation.

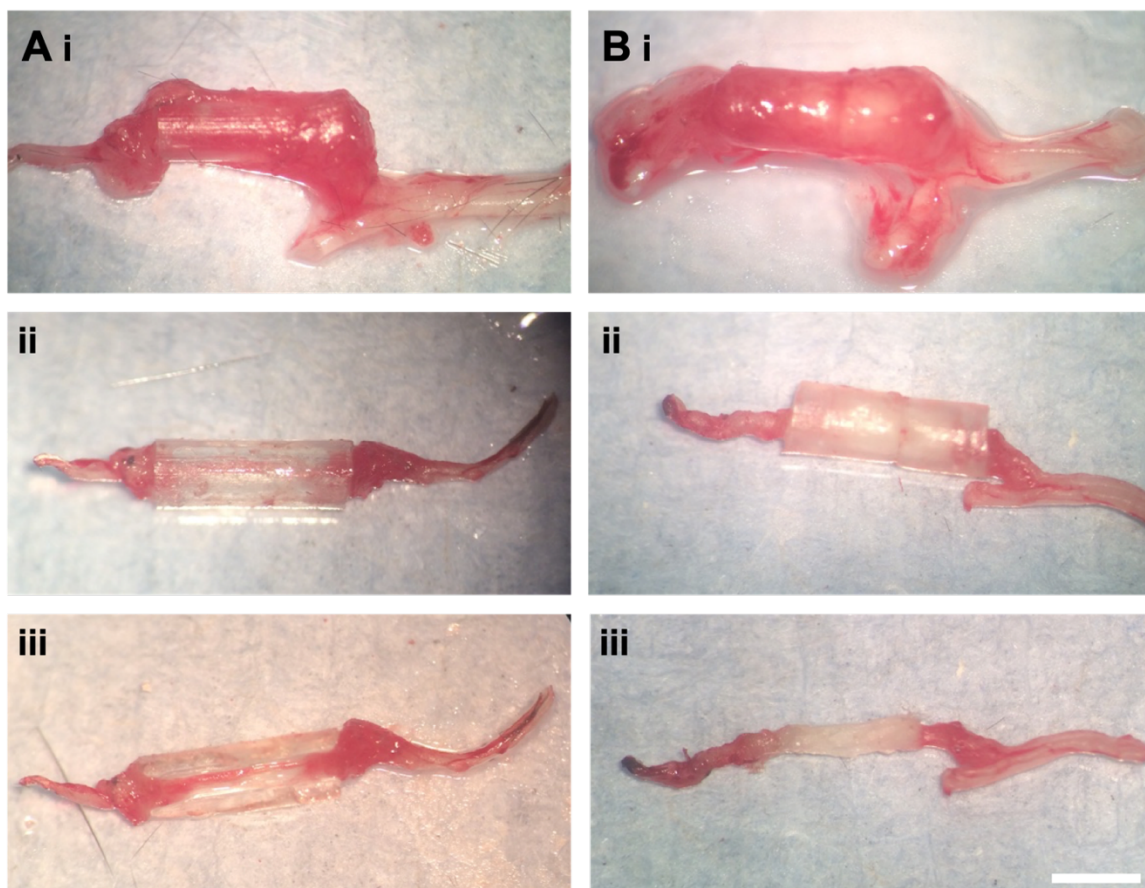


Figure 70. Photographs of the conduit harvest. A: Plain conduit, B: Fibre-filled conduit. Conduits (encased in connective tissue) were removed from repair site (i). Connective tissue was removed to reveal conduit (ii). The conduit was broken open to reveal nerve cable inside (iii). In A iii, the nerve cable connecting the proximal and distal nerve segments can be seen lying in half of the broken conduit. In B iii, the proximal and distal nerve ends are connected by a tissue cable containing the aligned PCL fibres. Scale bar: 2 mm.

5.4.3 Imaging of YFP nerve harvests

5.4.3.1 Imaging of YFP nerve samples with fluorescence microscopy

For preliminary experiment 1 and 2, harvested YFP nerve samples were imaged with a fluorescence microscope (Zeiss Axioplan2 equipped with a QImaging QI Click camera) using the FITC filter set (467-498 nm excitation). Image Pro-Plus software (Media Cybernetics) was used for image acquisition and processing. A 10× objective was used to obtain z-stack images with 10 μm slice intervals through the depth of the tissue. Z-stack images were taken at sequential positions along the nerve and each was processed into a single composite image (maximum intensity projection). Composite images were stitched using Adobe Photoshop to obtain composite images of the whole nerve segment.

5.4.3.2 Imaging of YFP nerve samples with confocal microscopy

For the main studies and preliminary study 3, YFP nerve samples were imaged using an upright confocal microscope (Zeiss LSM 510 Meta) with a 10× air objective and an argon ion laser for excitation of YFP (514 nm excitation, 535-590 nm detection). Z-stack images were taken at sequential overlapping positions along the nerve segment, starting at a position proximal to the injury site and finishing after the start of the distal nerve stump. The slice spacing in the z-stacks was set to 10 μm. Sequential z-stacks were stitched together using ImageJ (Grid/Collection Stitching plugin [329]) to produce a composite z-stack of the whole nerve segment. Minimal processing (adjustment of brightness and contrast) was applied to increase the visibility of individual axons.

5.4.4 Analysis of YFP nerve harvest images

5.4.4.1 Sprouting index (Axon counting)

Stitched confocal z-stacks of the whole nerve segments were processed using a maximum intensity projection to produce a single image for each nerve harvest. The start position of the regeneration was determined as the point where the nerve morphology and arrangement of axons became more irregular, just prior to the proximal neuroma site. A vertical line was drawn here (0.0 mm) and at 0.5 mm intervals along the whole nerve. An additional line was drawn at -0.5 mm before the start of axonal disruption where the nerve could be considered to be in its native, undamaged state. A nerve repair with 0.5 mm intervals can be seen in Figure 71A.

The number of axons present at each 0.5 mm interval along the nerve repair were counted to obtain a measure of the level of regeneration. The counts were performed twice, independently, to ensure validity. Where the two counts varied significantly, a third was performed to account for any erroneous counts and the numbers were averaged. The number of axons at each interval was normalised to by dividing by the number of axons at -0.5 mm. This gave the measure of sprouting index at each interval and allowed the counts to be compared between samples.

5.4.4.2 Unique axon tracing

Regenerated axons were traced to determine the number of unique axons present in the distal end of each repair. This method of analysis takes into account axon sprouting, which results in multiple axons from the same neuronal cell reaching the distal point.

Z-stack images of the whole nerve repairs were uploaded into Adobe Photoshop and individual axons were then traced to determine whether they reached the start point or joined with another axon which had already been traced. Starting at the distal end, an axon was chosen at random and followed back towards the proximal start point, by observing the axon path through the different slices of the z-stack images. Axons were traced in a single slice from the z-stack until the axon 'disappeared' from the current slice. Tracing was continued by switching the view to the adjacent slice into which the axon path continued. Tracing through the individual z-stack images (rather than maximum intensity projections), reduced the number of axons visible at one time, making the tracing process more reliable. Axons were traced (drawing a pseudo-colour line) until reaching the start point (0.0 mm interval) or until the axon joined a previously traced axon. This process was repeated until 50% of all the axons from the distal end were traced (or as many as possible due to image quality). The number of unique axons present at the distal stump was calculated and used to calculate the percentage of the start axons (at 0.0 mm) that are represented at the distal point. Figure 71B shows an example nerve repair with axons traced back from the distal end. A magnified view of a sprouting axon can be seen in Figure 72.

Due to a difference in the length of regenerated nerve in graft and conduit repairs, it was necessary to pick different distances to define the 'distal end'. In graft repairs, regenerating axons entered the distal stump at around 3-3.5 mm whereas in the conduit studies, the distal stump started at around 5-5.5 mm. It was chosen to trace axons in the graft repairs from a distal point of 5.0 mm and in the conduit repairs from 6.0 mm.

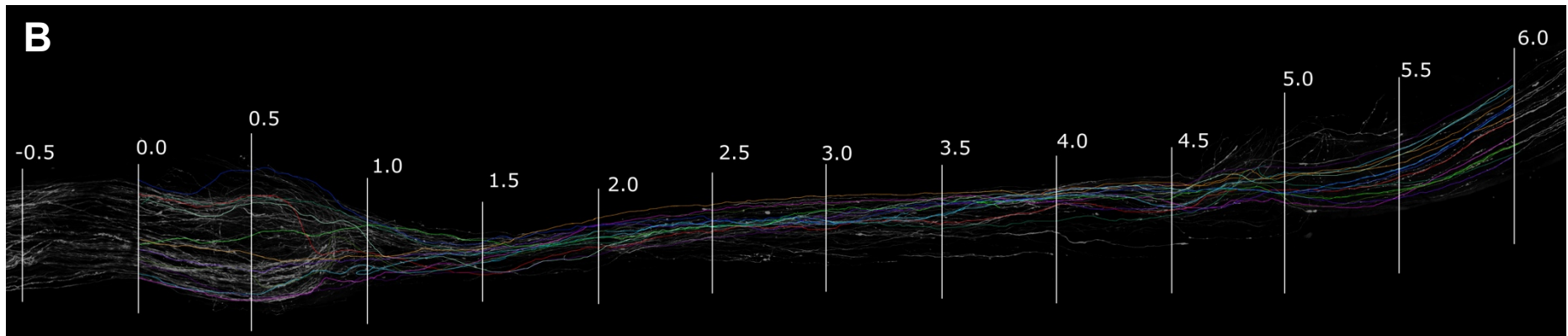
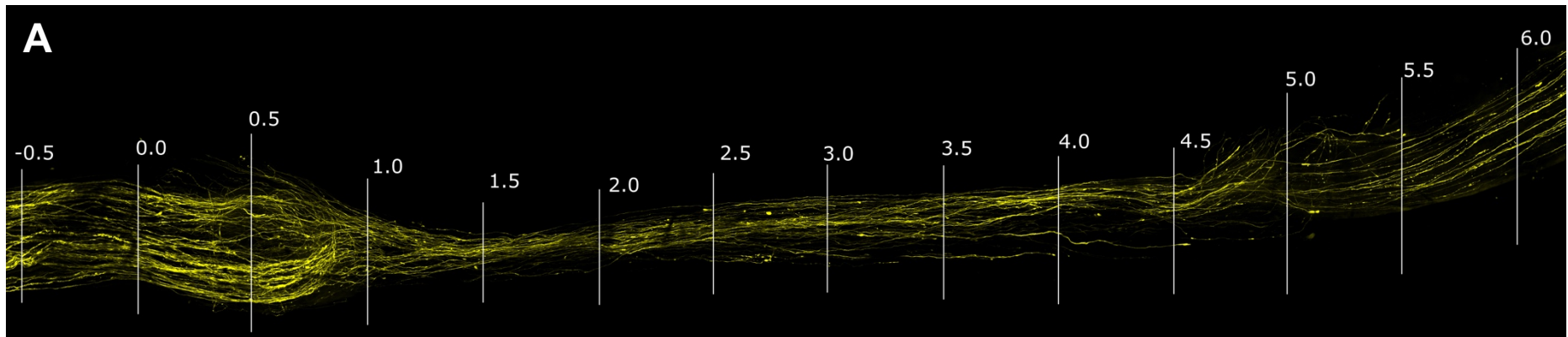


Figure 71. Unique axon tracing of YFP nerve repairs. A: Image of nerve repair with 0.5 mm intervals marked. B: The same image with pseudo-colour axons traced back from the distal end (YFP axons converted to black and white to improve visibility of traced axons).

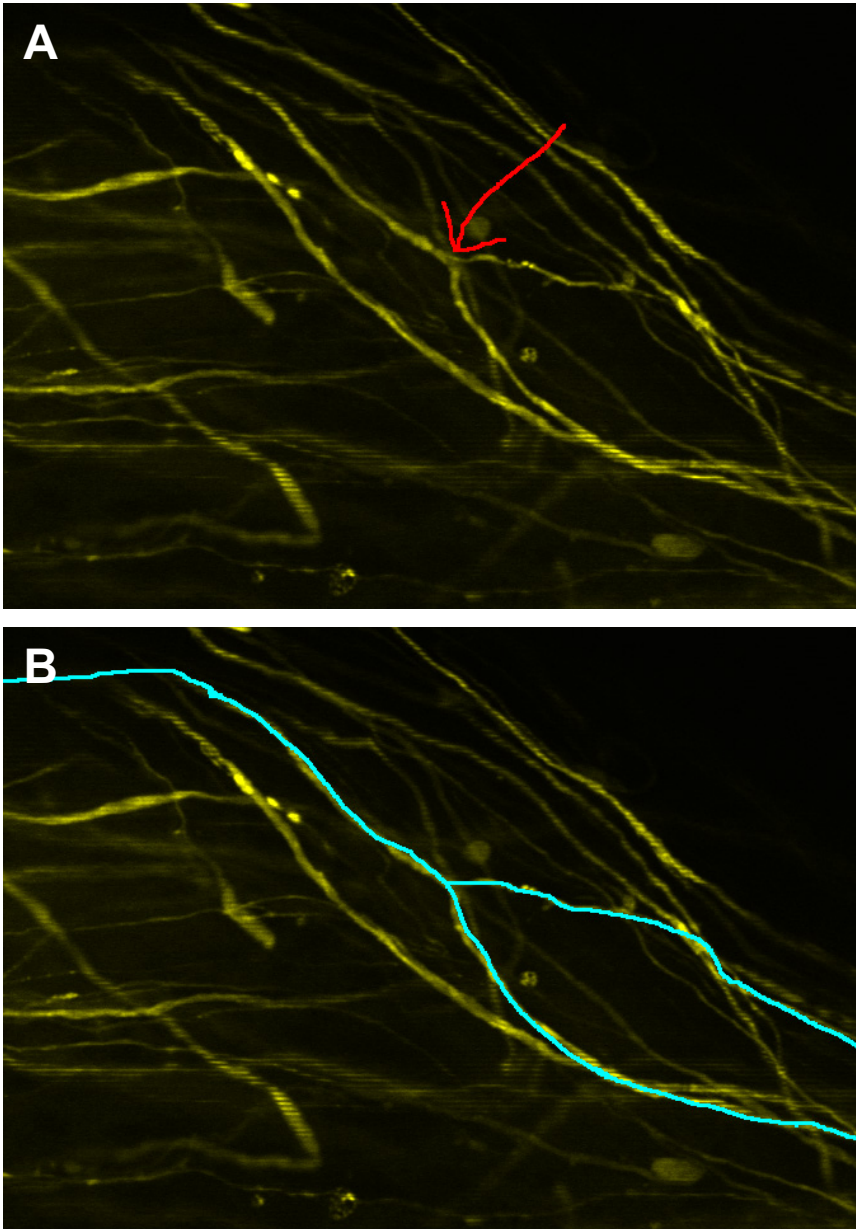


Figure 72. A magnified view of a sprouting axon from the nerve repair in Figure 71. The red arrow (A) indicates the point where sprouting occurs, and the axon path can be seen traced in B.

5.4.4.3 Measurement of initial axon disruption

Axon lengths were measured at the proximal segment of each repair to give a measure of axon disruption during entry into the conduit/graft. Extra axons present at 1.5 mm (not already traced) were traced back to the start point (0.0 mm) as described in section 5.4.4.2 and shown in Figure 73. Axon path lengths were measured between 0.0 mm and 1.5 mm (using ImageJ) and compared to the shortest possible path between the intervals to give a percentage increase in axon length. Average increase in axon length was calculated for each repair and used to compare between repair types.

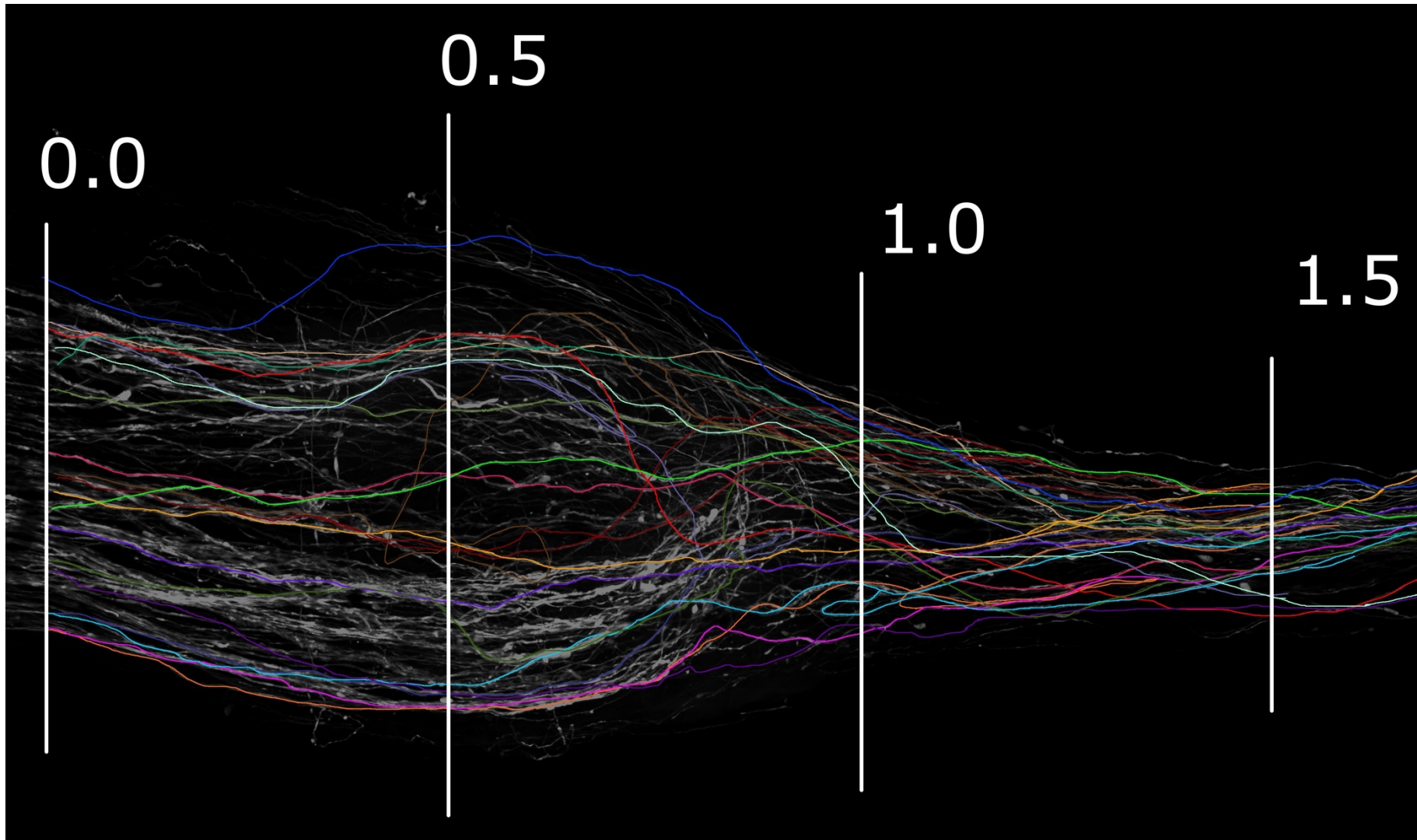


Figure 73. Axon disruption measurements. A magnified view of proximal portion of the nerve repair showing extra axons traced from 1.5 mm. The length of each axon was measured to calculate axon disruption. 0.5 mm intervals marked. YFP axons converted to black and white to improve visibility of traced axons.

5.4.5 Sample size calculations

Sample size calculations were carried out using PiFace software (obtained from <http://www.stat.uiowa.edu/~rlenth/Power>, v1.76 [330], see Appendix, Figure 93 and Figure 94) and using standard deviation values from a previous study in our group by Harding et al. [324]. Summary data from these calculations is displayed in Table 11.

For Study 1, comparing plain conduits, grooved conduits (both containing beta-carotene) and graft repairs, a sample size of N=7 was chosen. This would allow differences of 35.3%, 18.3% and 7.8% to be detected for sprouting index, unique axon tracing and axon disruption, respectively (Table 11). A difference of 35% in sprouting index was considered quite large, meaning that small differences could be difficult to detect. However, differences between repair types of up to 57% have been seen in previous studies [324]. Even if few significant differences are found, it should still be possible to identify trends within the data which could suggest the better performance of certain repair types. Differences of 18.3% and 7.8% in unique axon tracing and axon disruption should be able to be detected more easily and seemed reasonable based on the results of previous studies in our group [324], [331]. This sample size calculation also applied to Study 3 (comparing smooth conduits, plain conduits and graft repairs) as this contained the same number of groups as Study 1.

For Study 2, comparing plain and fibre-filled conduits (both plasma-treated and non-treated) and graft repairs, a sample size of N=6 would allow a difference of 31.9% to be detected for sprouting index measurements (Table 11). From pilot studies, it was expected that unique axon tracing would be difficult due to difficulties obtaining high enough quality images when imaging the fibre-containing constructs, so these measurements were not considered during the sample size calculations.

Where possible, extra animals were included to account for failures in some cases. Despite this, in some of the analysis groups, the final number of animals was not as high as desired due to either a higher failure rate than expected or an insufficiency in the number of mice available at the time of study. Difficulties associated with in-house breeding of the animals and the mixed genotypes present in offspring meant that animal numbers available for experiments were not always as expected.

Table 11. Summary data from sample size calculations showing the sample sizes for each study and the resulting power and detectable differences, based on the parameters of the statistical testing and standard deviation data from a previous study. Refer to Appendix (Figure 93, Figure 94) for calculations with PiFace software.

Study 1 & 3							
	Sample size	Analysis type	Number of groups (columns)	Number of intervals (rows)	Standard deviation (previous study data)	Power	Detectable difference (%)
Sprouting index	7	Two-way ANOVA	3	13	27.83	0.8	35.3
Unique axon tracing	7	One-way ANOVA	3	-	9.96	0.8	18.3
Axon Disruption	7	One-way ANOVA	3	-	4.24	0.8	7.8
Study 2							
	Sample size	Analysis type	Number of groups (columns)	Number of intervals (rows)	Standard deviation (previous study data)	Power	Detectable difference (%)
Sprouting index	6	Two-way ANOVA	5	13	27.83	0.8	31.9

5.4.6 Statistical analysis

Statistical analysis was performed with GraphPad Prism. To test for significant differences between groups, ANOVA was used, followed by the relevant multiple comparison tests. For sprouting index, two-way ANOVA was used with Bonferroni multiple comparison tests. For unique axon tracing and axonal disruption, one-way ANOVA was used, followed by Tukey's multiple comparison tests. $P < 0.05$ was used to determine a statistical difference. All data is presented mean \pm SD with N=number of animals in each group.

5.5 Results

5.5.1 Preliminary *in vivo* studies

In the early stages of *in vivo* work, before the full trials were conducted, a number of studies were performed to carry out preliminary testing with a number of different conduit designs. These conduits were tested in the same 3 mm common fibular nerve repair as the main studies and left for the full three-week recovery before harvesting the nerve segments and imaging with either fluorescence or confocal microscopy. The images were mainly analysed by observational analysis as the small sample numbers would make it difficult to draw any strong conclusions from quantitative analysis. The results were of varying success but helped to understand some underlying problems and informed conduit design for the full studies that followed.

5.5.1.1 Preliminary experiment 1: Plain conduits vs Fibre-filled conduits (both with thick-wall design)

Before the design of the fibre-filled conduits was optimised, preliminary *in vivo* trials were carried out with fibre-filled conduits with a thicker-walled design. This was due to difficulties in producing conduits with the three-part design with a total wall thickness of $\sim 280 \mu\text{m}$ to match the intended design of the plain conduits. The fibre-filled conduits used here were of the same three-part design as described in section 3.4.7 but with a total wall thickness of $400 \mu\text{m}$. These conduits were filled with either $2 \mu\text{m}$ and $9 \mu\text{m}$ fibres (12% packing density) and tested *in vivo* in common fibular nerve repairs. Thick-wall plain (empty) conduits with a comparable wall thickness were used as a control. Three animals per conduit group were used (nine mice in total) and the nerve tissue was harvested after three weeks and imaged with fluorescence microscopy (Figure 74).

As can be seen in Figure 74, the level of nerve regeneration in all conduits was very poor. In the plain conduits (Figure 74A) tissue cables formed in 2/3 cases as can be seen from the faint fluorescence between the proximal and distal ends. However only one or two axons regenerated through these tissue cables and no axons reached the distal ends. In the fibre-filled conduits (Figure 74B,C), axons were seen to regenerate up to or just past the start of the fibres. Here the fibres seemed to form a barrier to regenerating axons with only a small number of axons growing partly into the fibre-filled sections. These results were surprisingly poor, especially considering the failure of the plain conduits of which similar designs had been shown to work in previous studies by A. Harding [324]. It was hypothesised that the unsuccessful regeneration was a result of poor surgical techniques as these were the first surgeries performed by the author.

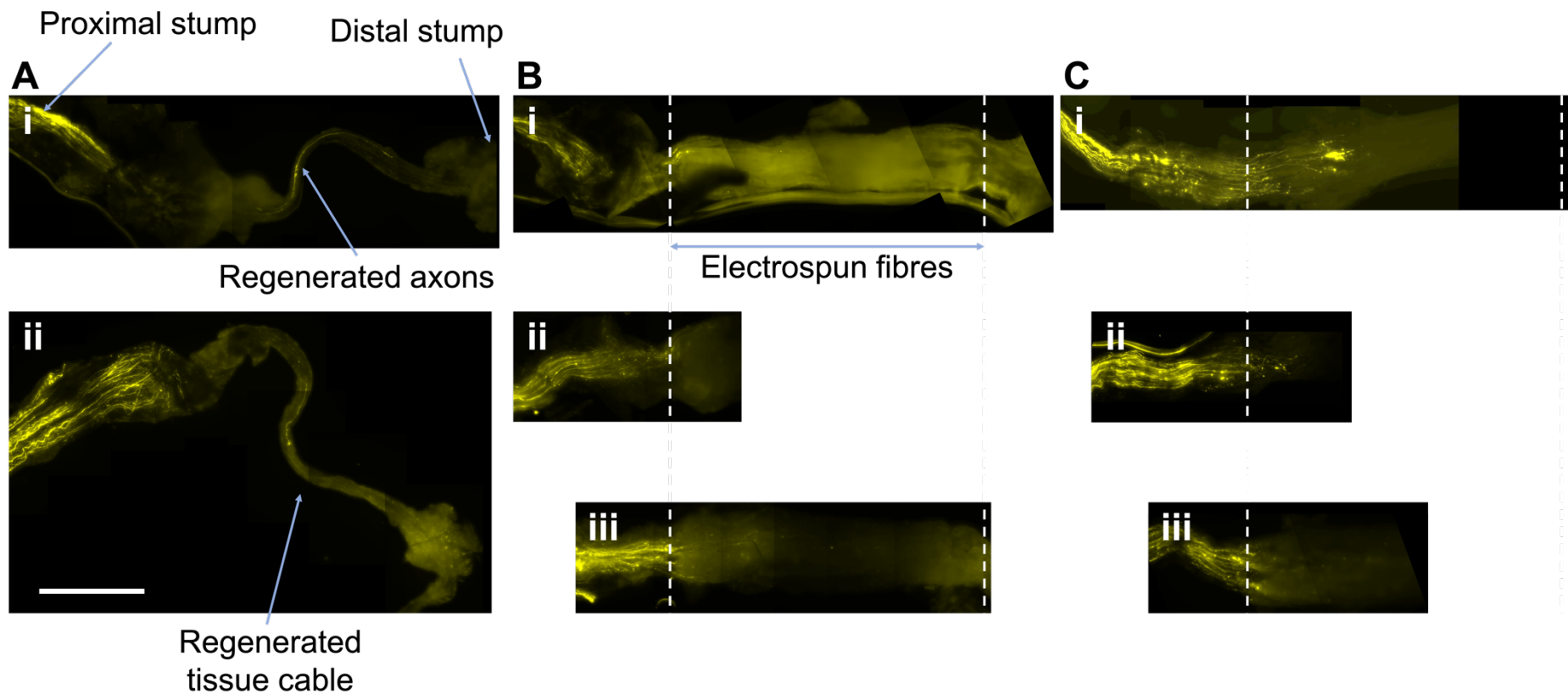


Figure 74. Fluorescence microscopy images of nerve harvests from preliminary experiment 1: Nerve repair with plain conduits (A) and fibre-filled conduits containing 2 μm fibres (B) and 9 μm fibres (C) (both conduit types were the thick-wall design). Axons are visible in yellow due to the expression of YFP. Scale Bar: 1 mm.

A: Plain conduits - tissue cables connecting proximal and distal ends can be seen but very limited axonal regeneration has occurred.

B: 2 μm fibre-filled conduits and C: 9 μm fibre-filled conduits - axons have regenerated until reaching the start of the fibres, which seem to act as a barrier to regenerating axons. The white dotted lines represent the start and end of the electrospun fibres inside the conduit.

5.5.1.2 Preliminary experiment 2: Grafts vs Plain conduits vs Fibre-filled conduits (thick-wall design)

A set of nine surgeries were then carried out with three plain conduits and three 9 μm fibre-filled conduits (of the same designs as preliminary experiment 1). Three graft surgeries were also carried out to act as a positive control to help deduce if any failures could be attributed to poor surgical technique or if they were related to the use of the conduits. Fluorescence microscopy images of nerve harvests showing the resulting regeneration are displayed in Figure 75. From observational analysis, 2/3 graft repairs possessed a good level of regeneration with a large number of axons crossing the gap and growing into the distal end (Figure 75A). All three plain conduits (one is not shown) completely failed to regenerate, with no tissue cable connecting the proximal and distal stump and no axons extending into the conduit lumen (Figure 75B). The three fibre-filled conduit repairs showed a varying level of success. In Figure 75Ci, a number of axons have regenerated across the gap and grown into the distal stump. In Figure 75Cii, axons have started to regenerate through the fibres but the longest axons only reached a little past the mid-way point of the conduit/fibres. In Figure 75Ciii, the regenerating axons have only made it a very short distance into the fibres, similar to the repairs in Figure 74C.

The positive results from the graft repairs suggested that the surgical technique was sufficient enough not to hinder nerve regeneration. The results from the fibre-filled conduits was more promising than the previous experiment (albeit still highly variable) and showed enough promise to continue to test fibre-filled conduits of a similar design. The continued failure of the plain conduits however was unexpected. As mentioned, the conduits in this study had a wall thickness of around 400 μm which is considerably thicker than the 250 μm wall thickness of conduits used in the successful conduit repairs by A. Harding [324]. It was thought that the increased wall thickness of the conduits may have had a detrimental effect on the nerve regeneration.

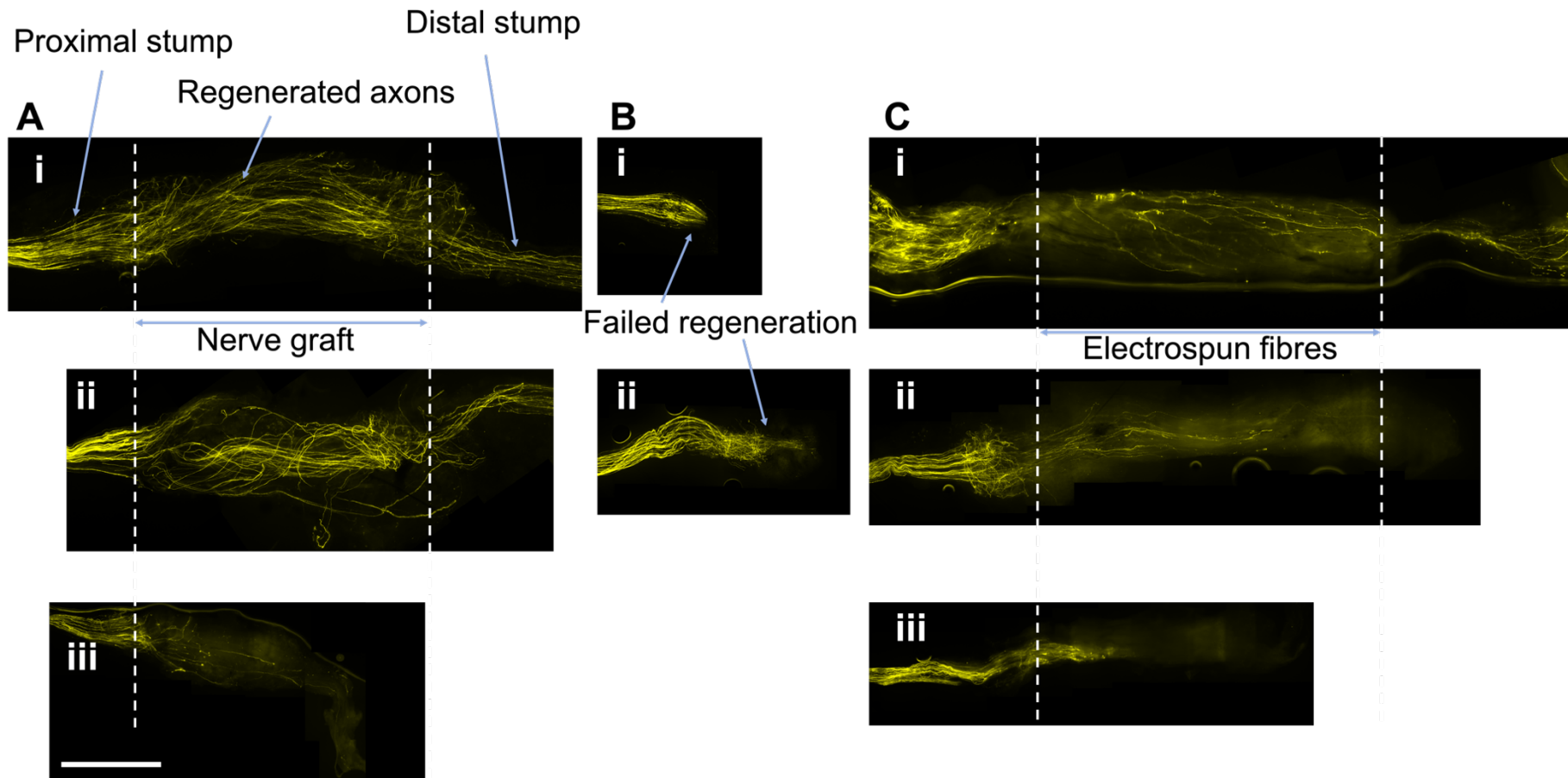


Figure 75. Fluorescence microscopy images of nerve harvests from preliminary experiment 2: Nerve repair with grafts (A), plain conduits (B) and 9 μm fibre-filled conduits (C) (both conduit types were the thick-wall design). Axons are visible in yellow due to the expression of YFP. Scale Bar: 1 mm.

A: Grafts – A good level of regeneration is seen in repairs Ai and Aii with a large number of axons reaching and growing down the distal nerve stump.

B: Plain conduits – No regeneration is seen with axons failing to regenerate into the conduits.

C: 9 μm fibre-filled conduits – Ci shows a good level of regeneration with a number of axons reaching and growing down the distal nerve stump. In Cii, some axons have regenerated part the way through the electrospun fibres but none reached the distal end. In Ciii axon regeneration stopped a short distance into the fibres. The white dotted lines represent the start and end of the graft tissue (B) and the electrospun fibres (C)

5.5.1.3 Preliminary experiment 3: Thick vs thin-wall conduits

A third preliminary experiment was performed to assess the effect of conduit wall thickness on nerve regeneration. Nerve repairs were carried out with five grafts, five thick-wall conduits (380 μm wall thickness) and five thin-wall conduits (270 μm wall thickness). Both conduit types were plain conduits containing no electrospun fibres. Regenerated nerves were imaged with confocal microscopy (Figure 76). 3/5 grafts became disconnected during the recovery period (due to a failure in the fibrin glue) leaving only two for analysis. These two grafts however, possessed a good level of regeneration (Figure 76A). Of the five thick-wall conduit repairs, four nerve harvests were imaged (one was lost due to an error in harvesting). One completely failed to regenerate (not shown) and the remaining three possessed varying level of success. Figure 76Bi shows an excellent regeneration with many axons reaching the distal stump, however in Bii far fewer axons traversed the repair site. Repair Biii was significantly worse, with no axons reaching the distal stump. For the thin-wall conduits, improved results were seen. 1 out of 5 repairs completely failed to regenerate (not shown) but of the four that did, all showed a high level of regeneration with many axons reaching the distal point (Figure 76C).

Axon counts were performed to calculate the sprouting index of the thick-wall and thin-wall conduit repairs (and the graft controls) and compare the number of axons present at each interval along the repair site (Figure 77). Quantifying the above observations, the sprouting index was lower in the thick-wall conduits at the majority of intervals compared to the thin-wall conduits. The difference was especially evident at the 5.5 mm interval in the distal end however the results were highly variable (as demonstrated by the large standard deviations) and no significant differences were found (two-way ANOVA with Bonferroni multiple comparison). Looking at the results, together with preliminary experiments 1 and 2, the higher failure rate of the thick conduits may also be indicative of poorer performance (compared to the 1/5 failure rate in the thin conduits).

Though it is difficult to draw a strong conclusion from the small sample size, the qualitative observations were enough to suggest that the thin-wall conduits may be preferable and were certainly not detrimental to nerve regeneration. For this reason, and to keep the studies comparable to previous work [128], [324] it was decided to perform the full *in vivo* studies with thin-wall conduits. Following this, the fabrication parameters of the μSL constructs were optimised and the design of the three-part, fibre-filled conduits was changed to the thin-wall design, outlined in section 3.5.7 (total wall thickness of 280 μm). The plain conduits and grooved conduits were fabricated to have a similar wall thickness (280 μm and 300 μm respectively).

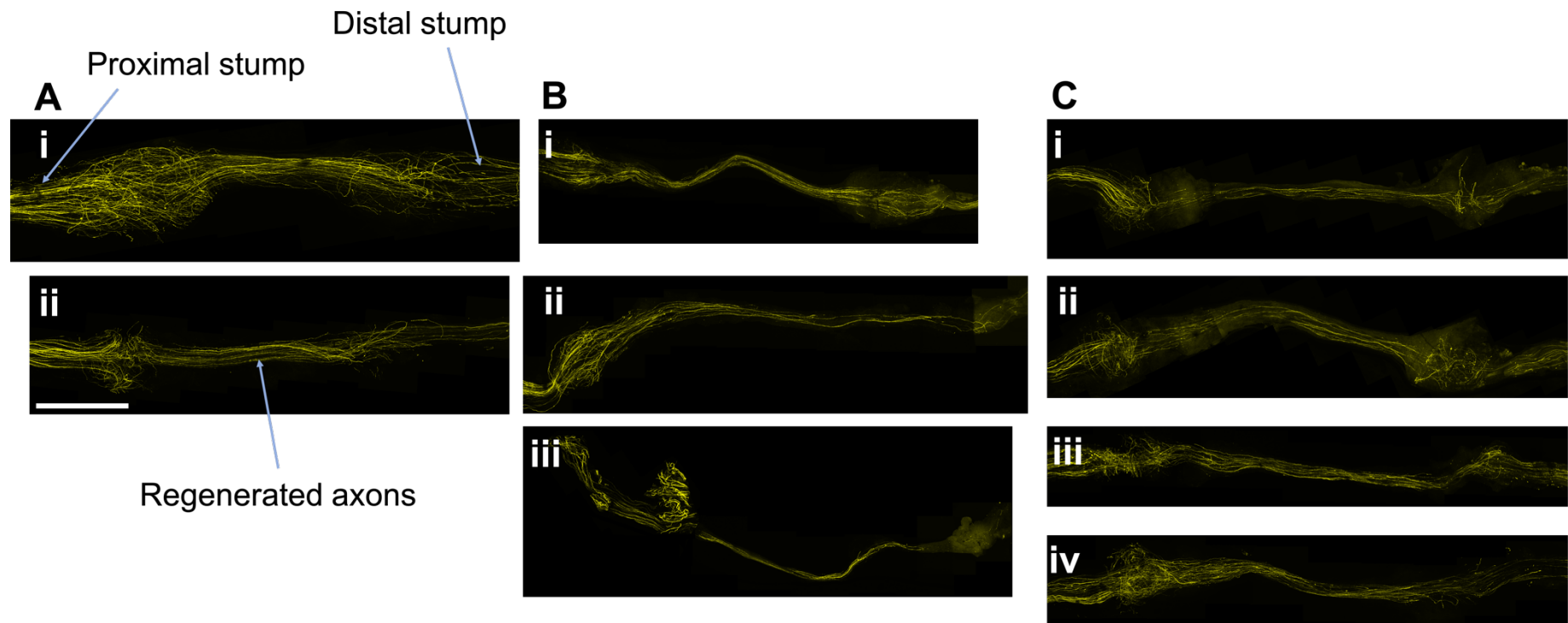


Figure 76. Confocal fluorescence microscopy images of nerve harvests from preliminary experiment 3: Nerve repair with graft (A), thick-wall plain conduits (B) and thin-wall plain conduits (C). Axons are visible in yellow due to the expression of YFP. Scale Bar: 1 mm.

A: Graft repairs show a good level of regeneration with many axons regenerating across the repair site and growing into the distal stump.

B: thick-wall conduits showed a varying level of success - good regeneration in i, and some regeneration in ii and iii with a few and no axons reaching the distal end, respectively (note that the nerve cable in Biii was accidentally transected during harvest). C: thin-wall showed good regeneration with many axons reaching the distal stump in all four cases.

Preliminary experiment 3: The effect of conduit wall thickness

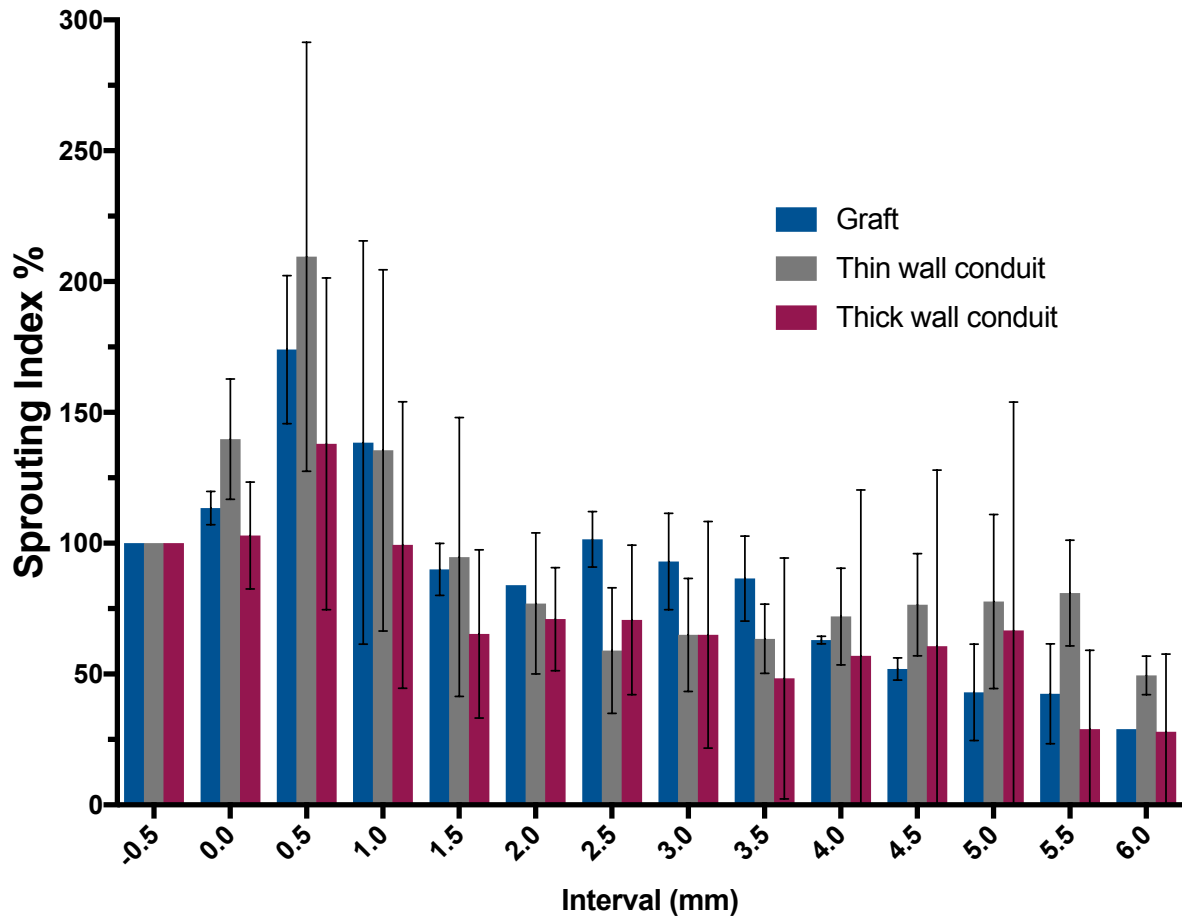


Figure 77. Sprouting index measurements from preliminary experiment 3 (thin-wall vs thick-wall conduits) Number of axons (expressed as a percentage of start axons) present at each 0.5 mm interval distal to the proximal injury point. Values presented mean \pm SD (N= 2, 3 and 4 for graft, thick-wall and thin-wall, respectively). No significant differences were found at any interval (two-way ANOVA with Bonferroni multiple comparison test).

5.5.1.4 Confocal vs fluorescence microscopy

What was evident when comparing the images of nerve harvests from the three preliminary experiments was a huge increase in image quality when using confocal microscopy (Figure 76) compared to fluorescence microscopy (Figure 74 and Figure 75). The graft repair in Figure 76Ai was imaged both with fluorescence (section 5.4.3.1) and confocal microscopy (section 5.4.3.2). Figure 78 shows a comparison of the maximum intensity projection images obtained with the two imaging modalities. The blurred portions of the fluorescence microscopy image (Figure 78A) obscure the smaller axons and much higher contrast can be seen in the confocal image (Figure 78B). Individual axons are more easily distinguishable which allowed more accurate analysis.

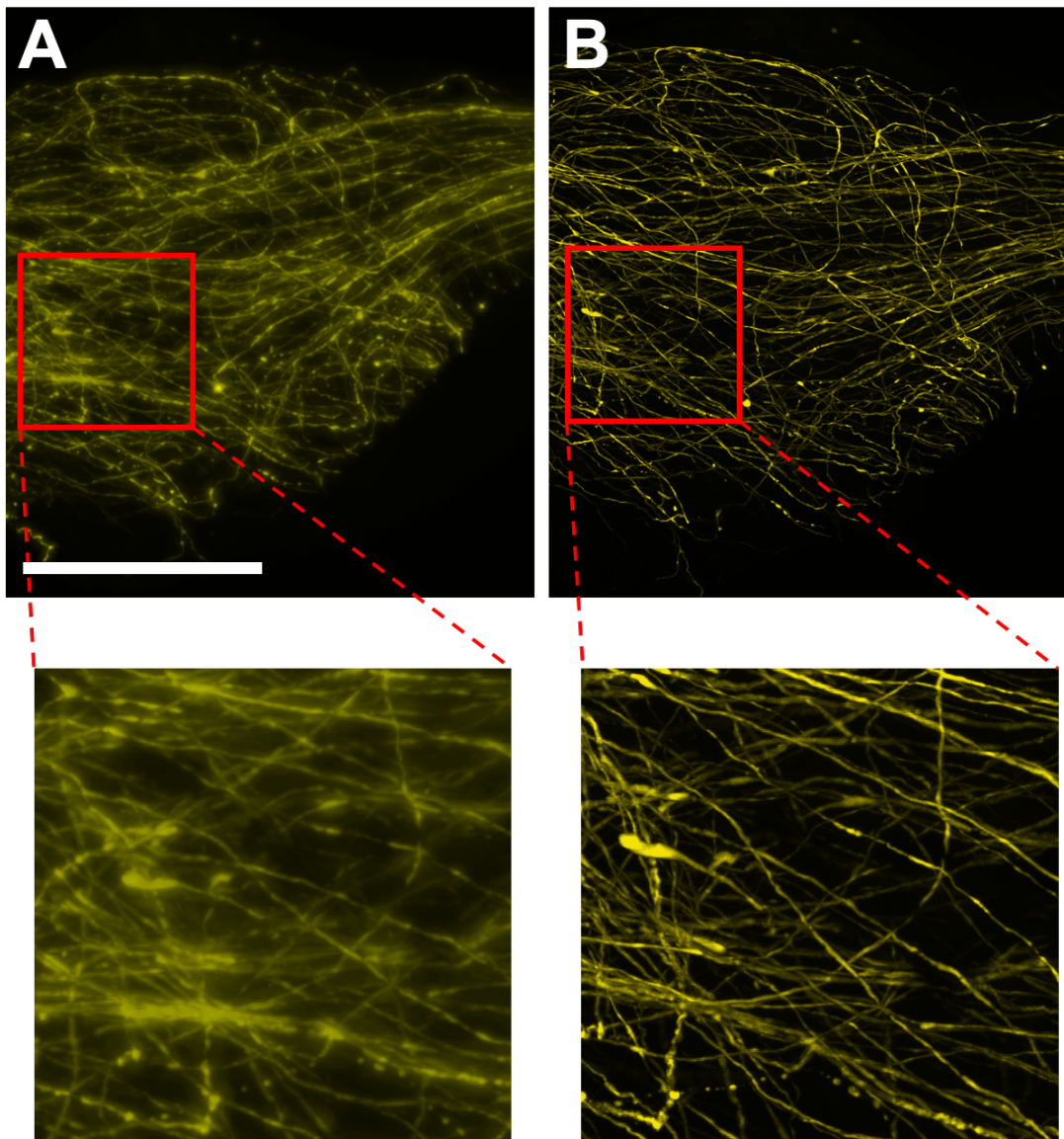


Figure 78. Increased image quality when imaging YFP harvests with confocal vs fluorescence microscopy.

A: Maximum intensity projection from fluorescence microscopy.

B: Maximum intensity projection from confocal microscopy.

Enlarged images of selected regions shown. Confocal images exhibit much higher contrast with less background fluorescence. This makes individual axons more easily distinguishable. Scale Bar: 0.5 mm.

5.5.2 General observations regarding failed regeneration

Before presenting the results of the *in vivo* studies with grooved and fibre-filled conduits, it is worth commenting on the failure rate of the repairs and how this affected the inclusion criteria of the analysis.

As discussed in (section 1.3.2), successful regeneration through a conduit must always be preceded with the formation of a fibrin cable between the proximal and distal nerve stumps. This acts as a scaffold to support the migration of Schwann cells and regeneration of axons. In the present study, if a connecting tissue cable was found within the conduit (during harvest), at least some axons would always be present within this tissue cable (visible with confocal microscopy), having regenerated fully, or at least partly, across the nerve injury site. In some (~15-30% of) cases, regeneration completely failed, and no tissue cable was found connecting the proximal and distal stumps. Examples of these failures are shown in Figure 79, where the regenerating axons have formed a neuroma and failed to regenerate into the conduit. For the graft repairs, if the graft tissue remained secured between the proximal and distal nerve endings, regenerated axons were always found within the graft tissue (as with the tissue cable in conduit repairs). In a few cases the graft tissue became disconnected from the proximal or distal nerve stump and regeneration failed in a similar fashion to the failed conduit repairs.

Conduit and graft repairs which completely failed like this (no nerve cable or graft disconnection) were excluded from the following analysis of sprouting index and axon tracing but were included when considering the overall success and failure of the different repair types (section 5.5.7).

Additionally, 1 out of the 9 plasma-treated plain conduits was excluded from analysis due to a technical failure of the distal nerve stump becoming detached from the conduit during the recovery period. This was the only case where a conduit became disconnected from the nerve stumps.

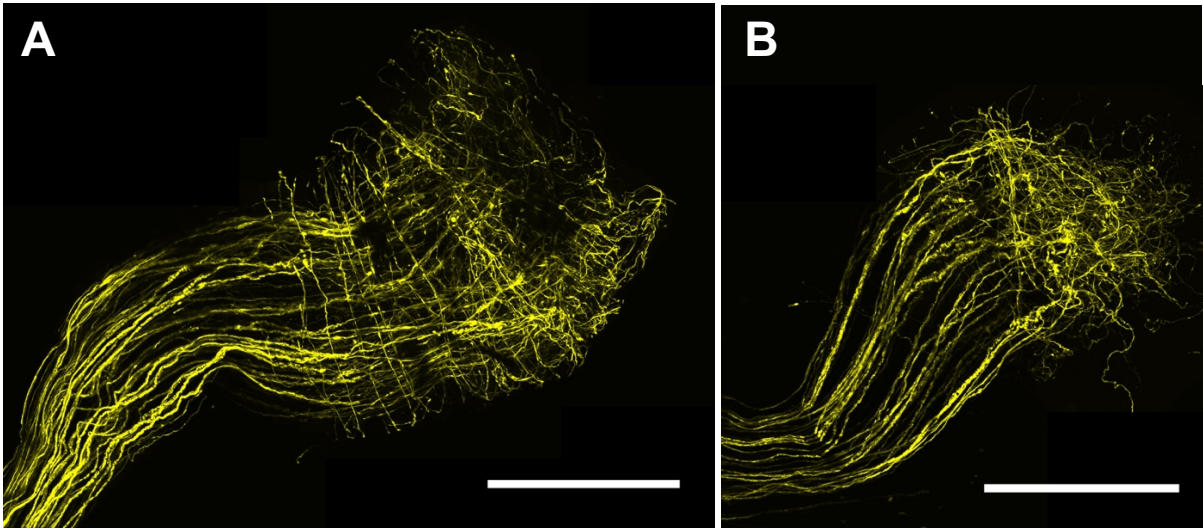


Figure 79. Examples of two failed conduit repairs where no nerve cable was found connecting the proximal and distal stumps. A: Grooved conduit repair. B: Plain conduit repair. Scale bars: 0.5 mm.

5.5.3 Study 1: The effect of aligned grooves on nerve regeneration

(Plain conduits vs Grooved conduits)

Grooved conduits were tested against plain conduits to determine the effect of aligned grooves on nerve regeneration. Grooved conduits were produced with PCLMA resin containing beta-carotene (to improve groove resolution) and so the plain conduits were produced using the same resin to serve as the appropriate control. Graft repairs were also used for comparison as the clinical gold standard.

5.5.3.1 General observations

Representative images of the three repair types can be seen Figure 80. All three groups showed a good level of regeneration with many axons regenerating through the graft tissue/conduit lumen and into the distal stump. Two obvious sites of disorganisation were observed in all repairs. At the proximal injury site (between 0.0 mm and 1.5 mm) axons became disorganised as they exited the proximal stump and entered the graft tissue or the conduit lumen but organisation was regained within the mid portion of the repair. The second site of axonal disorganisation was where axons entered the distal stump (Figure 80, white arrows).

The plain conduits (Figure 80B) and grooved conduits (Figure 80C) showed very similar levels of regeneration with no obvious differences to each other or to the graft repairs (Figure 80A). One notable difference was that in the graft repairs, the distal stump was seen to start between the 3.0 mm and 3.5 mm interval. However, in the conduit repairs the distal stumps started between 5.0 mm and 5.5 mm.

The regenerated nerve cables within the conduits (between intervals 1.0 mm and 4.5 mm) showed axons with a good level of organisation, similar to those within the graft tissue. However, the nerve cable in the conduit repairs tended to be slightly thinner (with axons less spread out) compared to those in the graft repair. It is thought that this is due to an absence of any support structure within the conduit and reliance on the native fibrin cable produced to support regeneration.

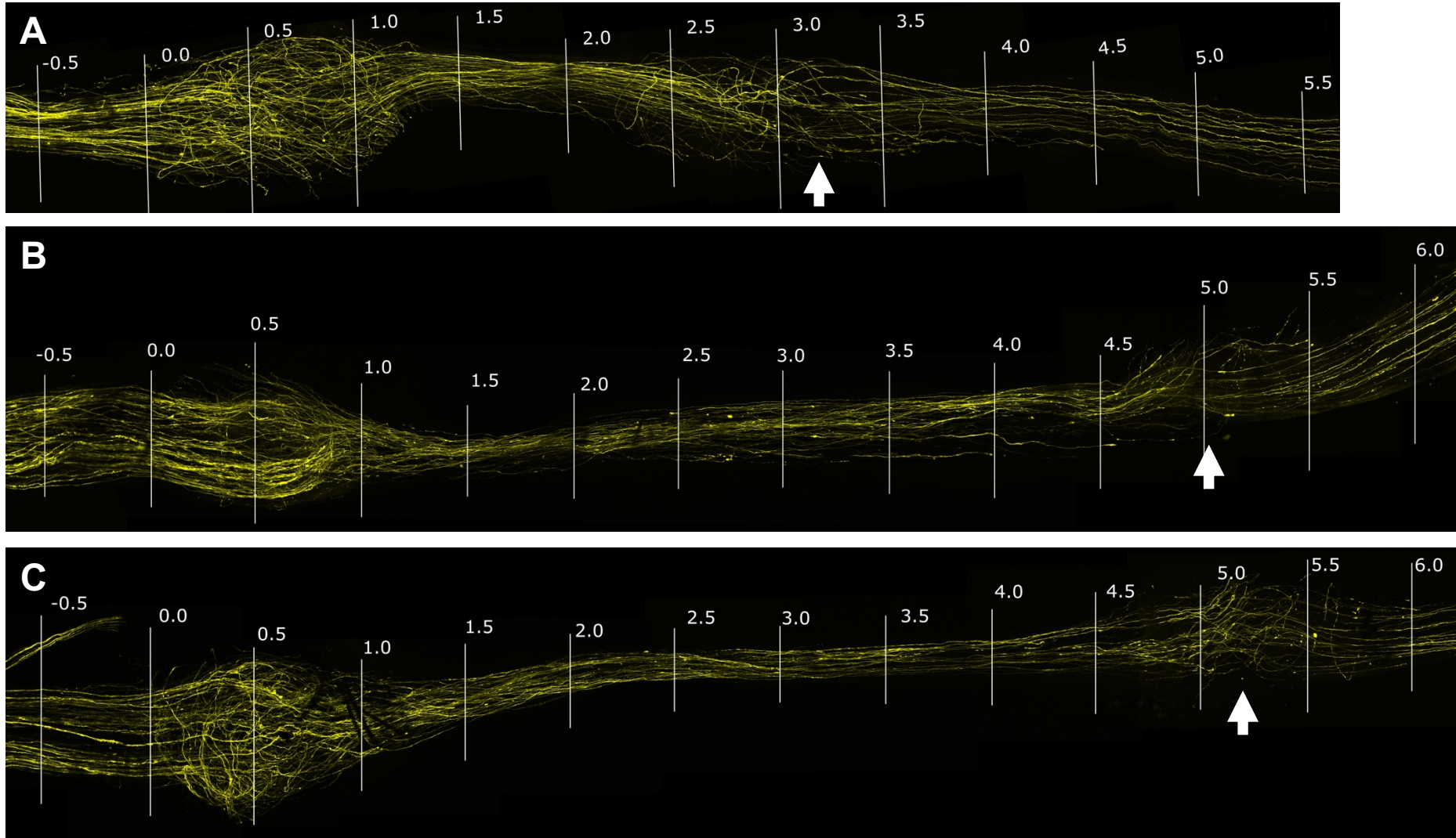


Figure 80. Typical images for common fibular nerve repairs with Graft (A), Plain conduit (B) and Grooved conduit (C), (Both conduits containing beta-carotene). 0.5 mm intervals marked from the proximal point of injury. The Proximal nerve ends are visible leading up to the 0.0 mm interval (proximal injury point). In all cases, regenerated axons can be seen growing across the repair site (through the graft tissue/conduit) and entering the distal stump (marked by white arrow).

5.5.3.2 Sprouting index

To quantify the above observations and the overall level of regeneration in each repair type, the number of axons at each 0.5 mm were counted and expressed as a percentage of number of start axons (at -0.5 mm). This gives the sprouting index (see sections 5.2.3 and 5.4.4.1) and the results are displayed in Figure 81.

The sprouting index in all three repair types peaked at 0.5 mm as the axons begin to regenerate out from the proximal stump and enter into the graft tissue/conduit. The sprouting index at 0.5 mm was slightly lower for the grooved conduits in comparison to the plain conduits, though not significantly different. Despite this lower initial sprouting index, the sprouting index between 1.0-5.5 mm was consistently slightly higher for grooved conduits, but comparing the conduit types, no significant differences were found at any interval (two-way ANOVA with Bonferroni multiple comparison).

A significantly higher sprouting index was seen at 1.0 mm for the grafts in comparison to the plain and grooved conduits ($P < 0.001$ and $P < 0.05$, respectively) corresponding to axons entering the graft tissue and encountering a level of resistance. In the middle of the graft tissue (1.5 and 2.0 mm), the sprouting index fell to a comparable (not significantly different) level to both the conduit types. As the axons in the graft tissue approach the distal nerve stump at 2.5 mm, the sprouting index increased and was significantly higher than in the plain conduits ($P < 0.05$). This increase continued at 3.0 mm where the graft sprouting index was significantly higher than both the plain and grooved conduits ($P < 0.01$ and $P < 0.05$, respectively). At 3.5 mm, the sprouting index of the grafts remained significantly higher than the plain conduits ($P < 0.05$). The sprouting index of the graft repairs then fell to a level comparable to the conduit repairs and the values between the three groups remained non-statistically different for the remainder of the intervals and at the distal end. This increase in sprouting index around 3 mm was not mirrored by the conduit repairs as the distal stump was not present until around the 5.0 mm interval.

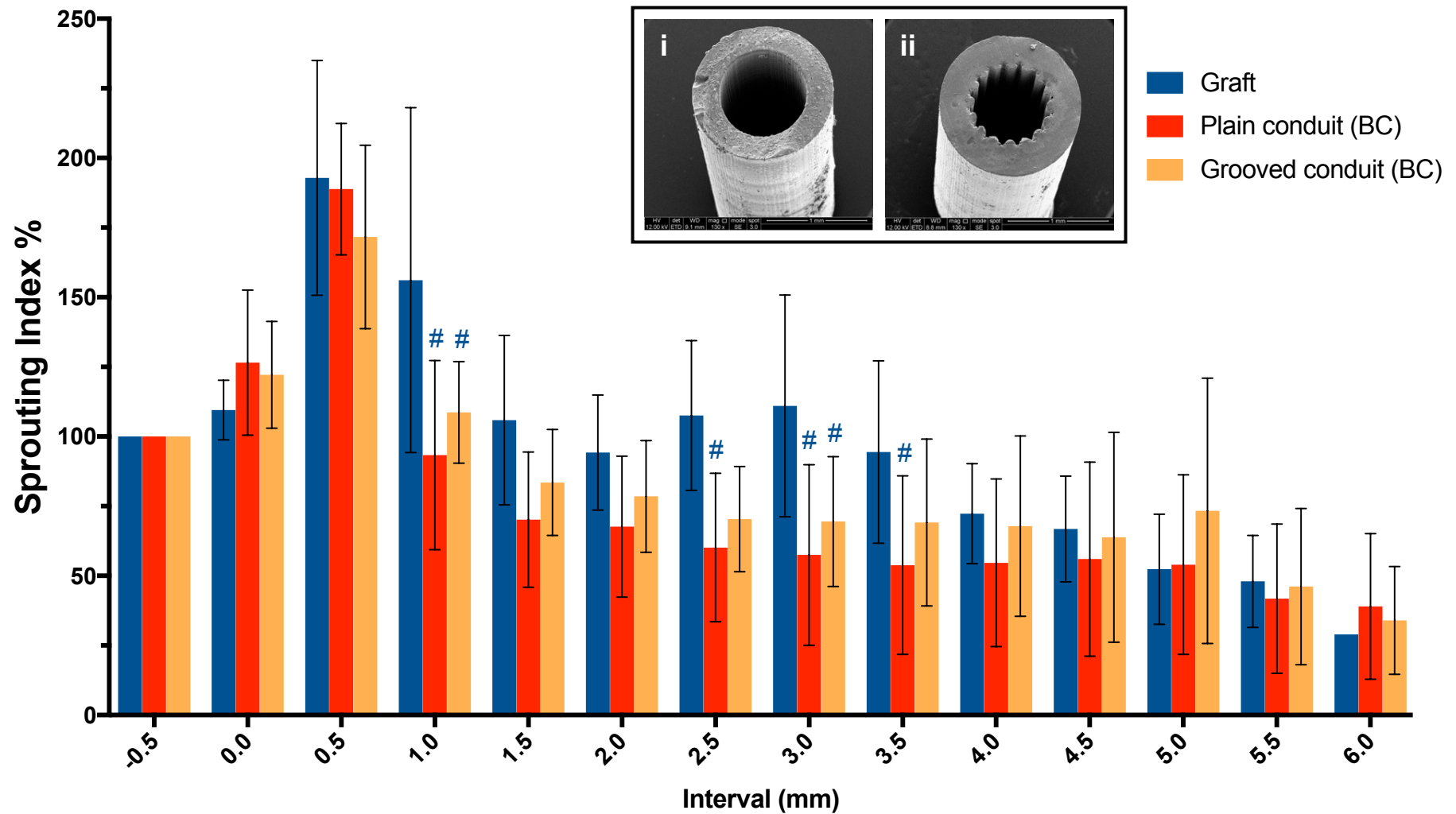


Figure 81. Sprouting index values at 0.5 mm intervals along the repair for Graft repairs (N=7), Plain and Grooved conduits (both containing beta-carotene (BC), N=6). Values presented mean±SD. # denotes significant difference from graft (two-way ANOVA with Bonferroni multiple comparison test). Inset: SEM images of Plain conduit (i) and Grooved conduit (ii).

5.5.3.3 Unique Axon Tracing

Unique axon tracing was performed to calculate number of unique start axons that are represented at the distal end of each nerve repair (Figure 82). This provides more detailed information about the success of regeneration than the sprouting index values, as it takes into account the sprouting of axons and avoiding the same axon being counted multiple times due to the occurrence of branching.

The number of unique axons present in the distal end of the plain and grooved conduits was very similar ($21.25 \pm 15.70\%$ and $21.75 \pm 12.96\%$, respectively). These values were lower than the number of unique axons in the distal end of the graft repairs ($39.62 \pm 18.98\%$) though the differences were not significant (one-way ANOVA with Tukey's multiple comparisons).

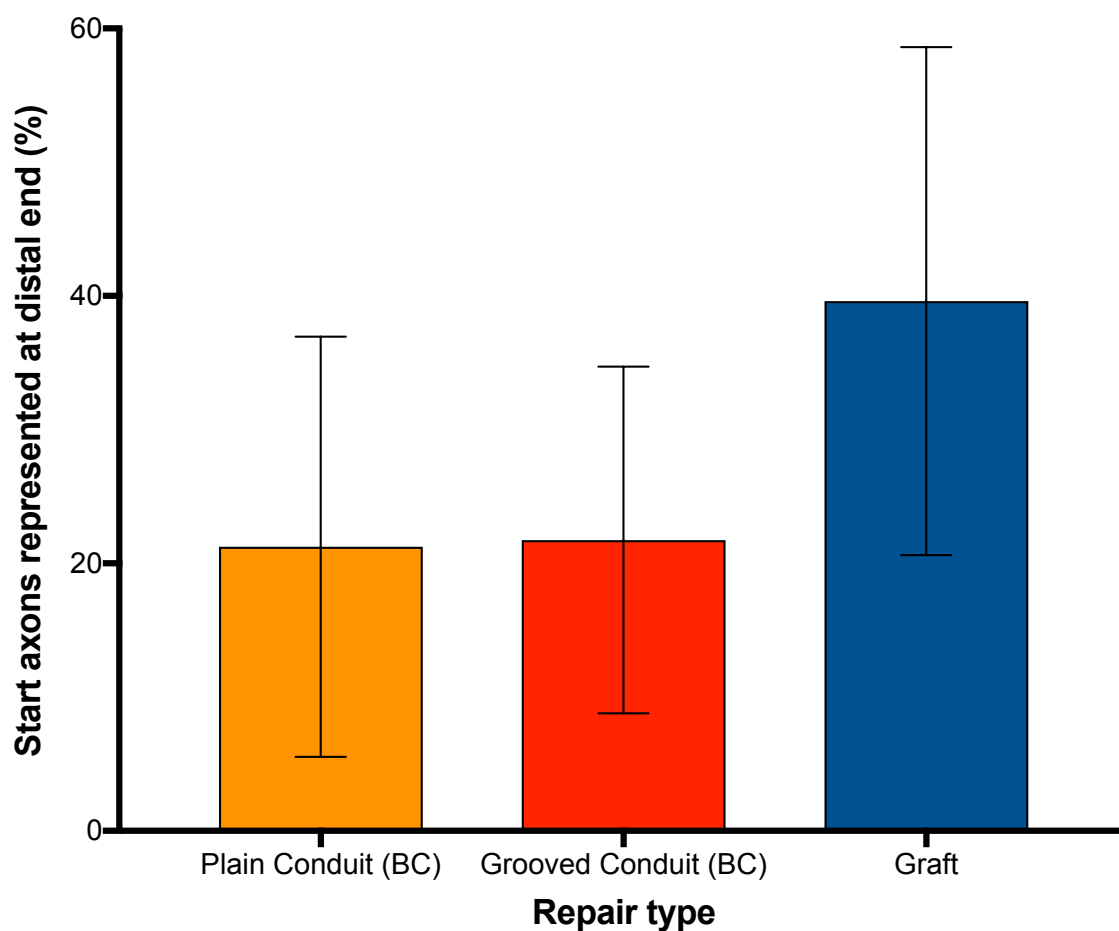


Figure 82. Unique axon tracing: The number of unique start axons present in the distal end of the Plain conduits, Grooved conduits and Graft repairs. (Both conduits containing beta-carotene.) Values presented mean \pm SD, (N=6). No significant differences were found (one-way ANOVA with Tukey's multiple comparison test).

5.5.3.4 Axonal disruption

The length of axons between the start of the repair (0.0 mm) and the 1.5 mm interval were measured and compared to the shortest possible path, to give the percentage increase in axon length (Figure 83). This gives a measure of axon disruption during the exit from the proximal stump and entry into the graft tissue/conduit lumen. The smallest increase in axon length was seen in the grooved conduits and highest in the graft repairs (15.26±5.60% and 29.22±8.12%, respectively). This was a significant difference ($P<0.05$) meaning that axon disruption was significantly lower in the grooved conduits. The plain conduits had an intermediate level of axon disruption (23.46±11.80%) which was not significantly different to either the grooved conduits or the graft repairs. As well as having a lower average increase in axon length, the variation in the axon disruption of the grooved conduits was also much lower than the plain conduits, demonstrating a more consistent result. Example traced axons from each group can be seen in Figure 84.

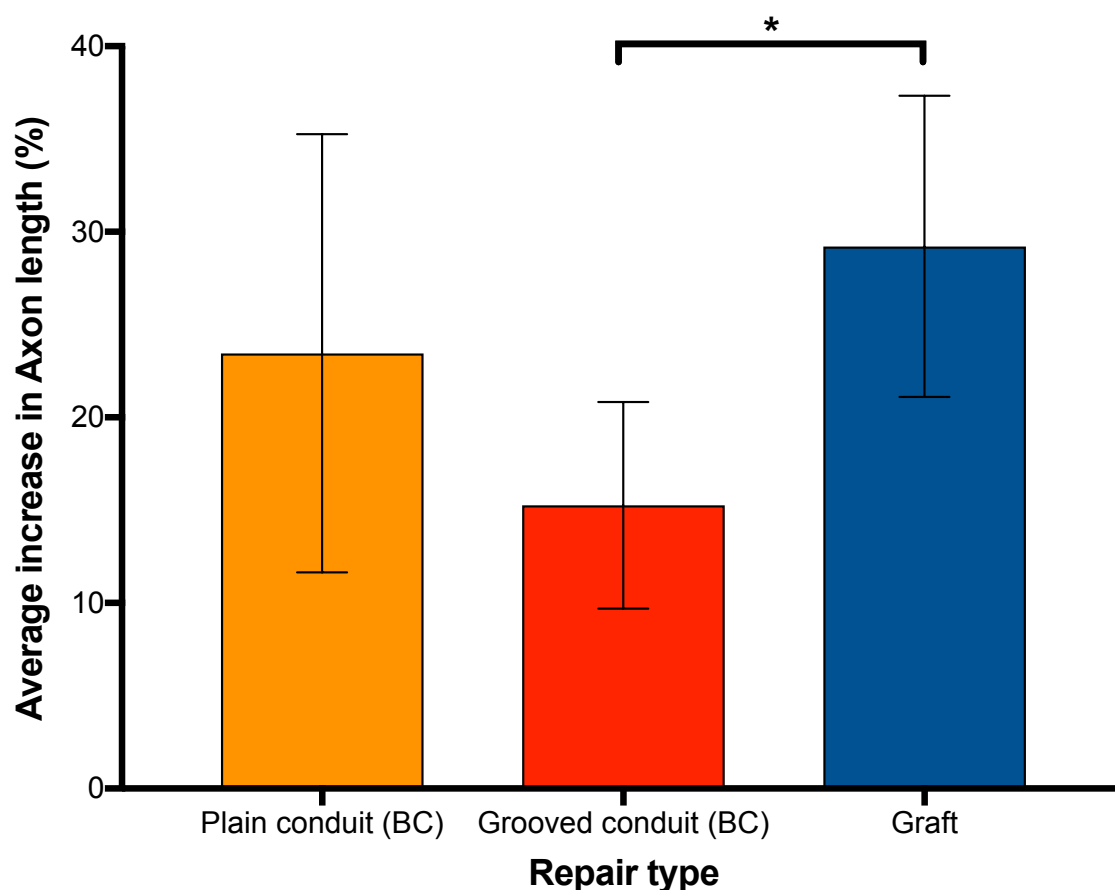


Figure 83. Axon disruption measurements: The % increase in axon length between 0.0 mm and 1.5 mm (compared to the most direct path). A comparison between Plain conduits, Grooved conduits and Graft repairs. (Both conduits containing beta-carotene (BC).) Values presented mean±SD, (N=6).

* Denotes significant difference (one-way ANOVA with Tukey's multiple comparisons)

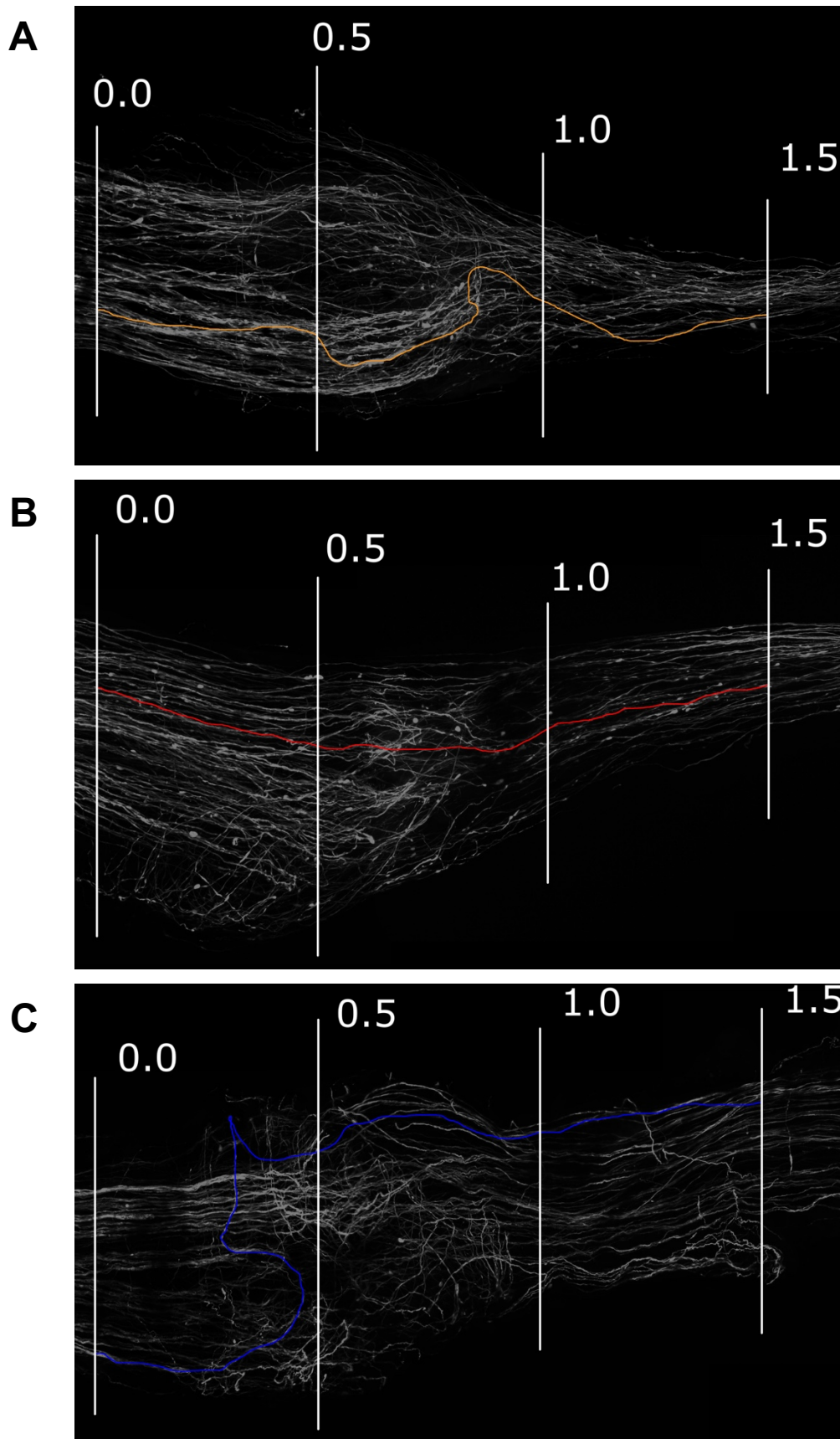


Figure 84. Example axons traced for axon disruption measurements. A: Plain conduit (intermediate disruption), B: Grooved conduit (low disruption), C: Graft repair (high disruption). (both conduits containing beta-carotene) 0.5 mm intervals.

5.5.4 Study 2: The effect of aligned fibres and plasma treatment on nerve regeneration

(Fibre-filled vs plain conduits, with and without plasma treatment)

Fibre-filled conduits were tested against plain (empty) conduits to determine the effect of aligned fibres on nerve regeneration. Since plasma treatment was shown to improve nerve regeneration through fibre-filled conduits *in vitro* (section 4.5.5.1) the effect was also tested here *in vivo*. Plasma-treated fibre-filled conduits and plasma-treated plain conduits were included in the study along with graft controls. All conduits were fabricated with PCLMA resin without beta-carotene.

5.5.4.1 General observations

Representative images of the nerve repairs can be seen in Figure 85 and Figure 86. Regeneration in the plain conduits (Figure 85) was very similar to the regeneration in the beta-carotene-containing plain and grooved conduits in the previous experiment (Figure 80B,C). There was no obvious difference between the non-treated plain conduits (Figure 85A) and the plasma-treated plain conduits (Figure 85B).

Looking at the fibre-filled conduits, there was an obvious difference between the non-treated and plasma-treated conduits. The non-treated conduits (Figure 86A) performed very poorly, with axons only regenerating a short way into the fibres. On the other hand, the plasma-treated conduits (Figure 86B) supported much improved regeneration. In some cases (e.g. Figure 86Bi) axons seemed more spread out within the regenerated cable compared to the plain conduits however in other cases (e.g. Figure 86Bii) axons were seen to grow round start of fibres and continue between fibres and conduit wall.

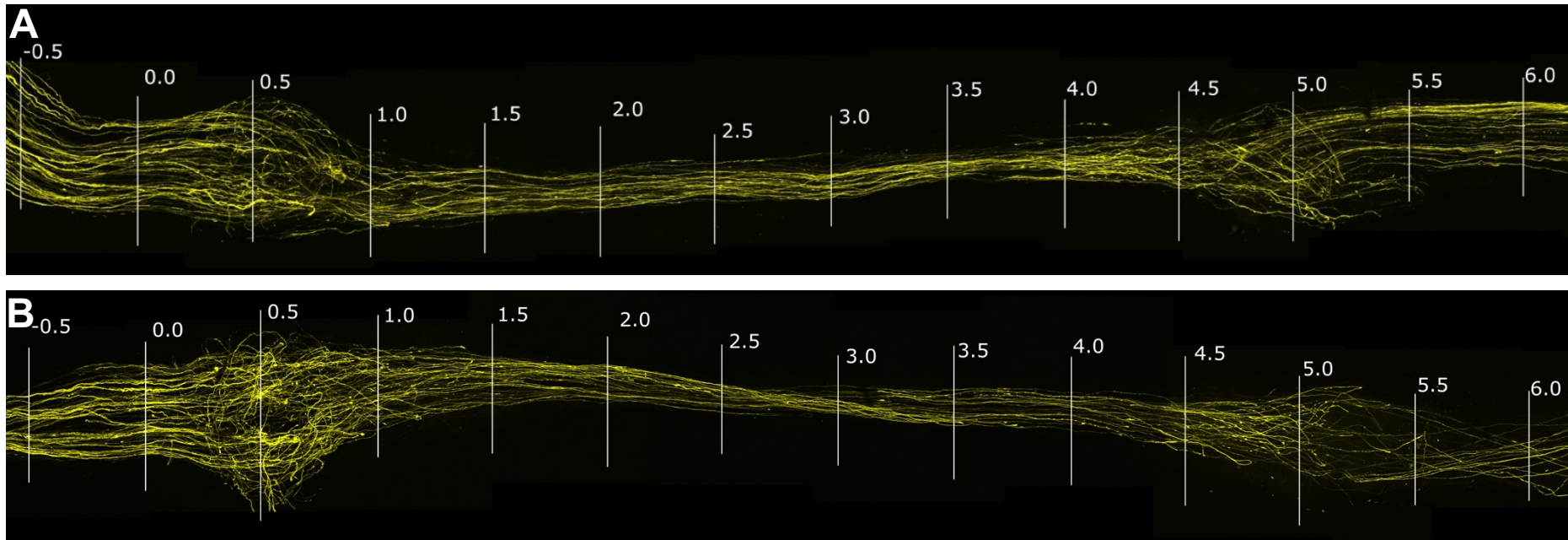
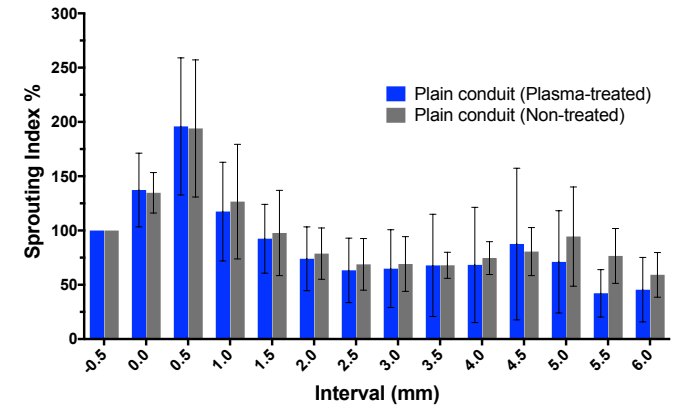


Figure 85. Typical images for common fibular nerve repairs with Plain conduits. A: Non-treated conduits. B: Plasma-treated conduits. 0.5 mm intervals marked from the proximal point of injury (0.0 mm). In both cases, many axons regenerated across the injury site and into the distal nerve endings (5.0 mm). Inset: Graph of sprouting index (values isolated from Figure 87).

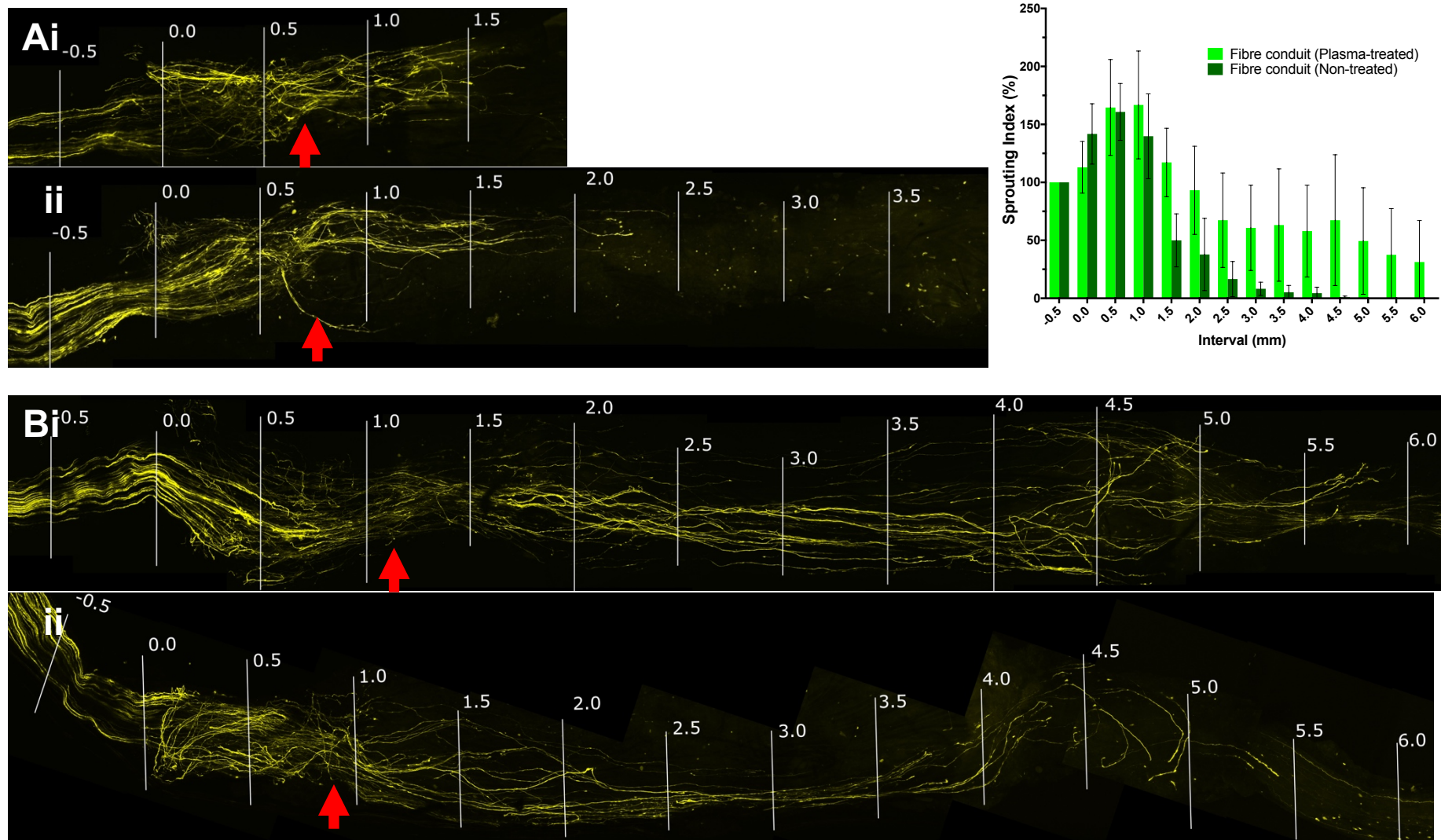


Figure 86. Typical images for common fibular nerve repairs with Fibre-filled conduits. Red arrow indicates the start of the fibres. A: Non-treated conduits (axons failed to regenerate far past the start of the fibres). B: Plasma-treated conduits (axons regenerated across the injury site and into the distal nerve endings (5.0 mm). 0.5 mm intervals marked from the proximal point of injury (0.0 mm). Inset: Graph of sprouting index (values isolated from Figure 87).

5.5.4.2 Sprouting index

Figure 87 shows the sprouting index measurements from all 5 repair types. Again, the sprouting index of all groups peaked at 0.5 mm, however (like the graft repairs) this stayed elevated for the plasma-treated fibre-filled conduits at 1.0 mm.

At all intervals, there were no significant differences in the sprouting index of any conduit type in comparison to the graft, except the non-treated fibre-filled conduit. These possessed significantly lower sprouting index compared to the graft at all intervals from 2.5-4.5 mm ($P < 0.0001$, $P < 0.0001$, $P < 0.001$, $P < 0.01$, $P < 0.05$). Comparing between the two non-treated conduit types, the sprouting index of the fibre-filled conduits was significantly lower than the plain conduits at every interval from 3.0-6.0 mm ($P < 0.05$, $P < 0.05$, $P < 0.01$, $P < 0.001$, $P < 0.0001$, $P < 0.01$, $P < 0.05$). As observed in Figure 86A axon numbers in the non-treated fibre-filled conduits declined rapidly after the start of the fibres (0.5-1.0 mm).

Plasma treatment had little effect on the plain conduits with no significant differences in sprouting index at any interval between the plasma-treated and non-treated plain conduits. On the other hand, in the fibre-filled conduits, sprouting index was higher in the plasma-treated group at all intervals from 0.5 mm onwards. Significant differences were seen in the fibre-filled conduits at 1.5 and 4.5 mm ($P < 0.05$) between the plasma-treated and the non-treated groups. The improved regeneration in plasma-treated fibre-filled conduits is reflected by the absence of any significant differences between plasma-treated fibre-filled conduits and plain conduits (either plasma-treated or non-treated).

Unique axon tracing was not performed on the images from this experiment as the presence of electrospun fibres in the harvested nerve tissue resulted in poorer quality images where axons could not be as reliably traced.

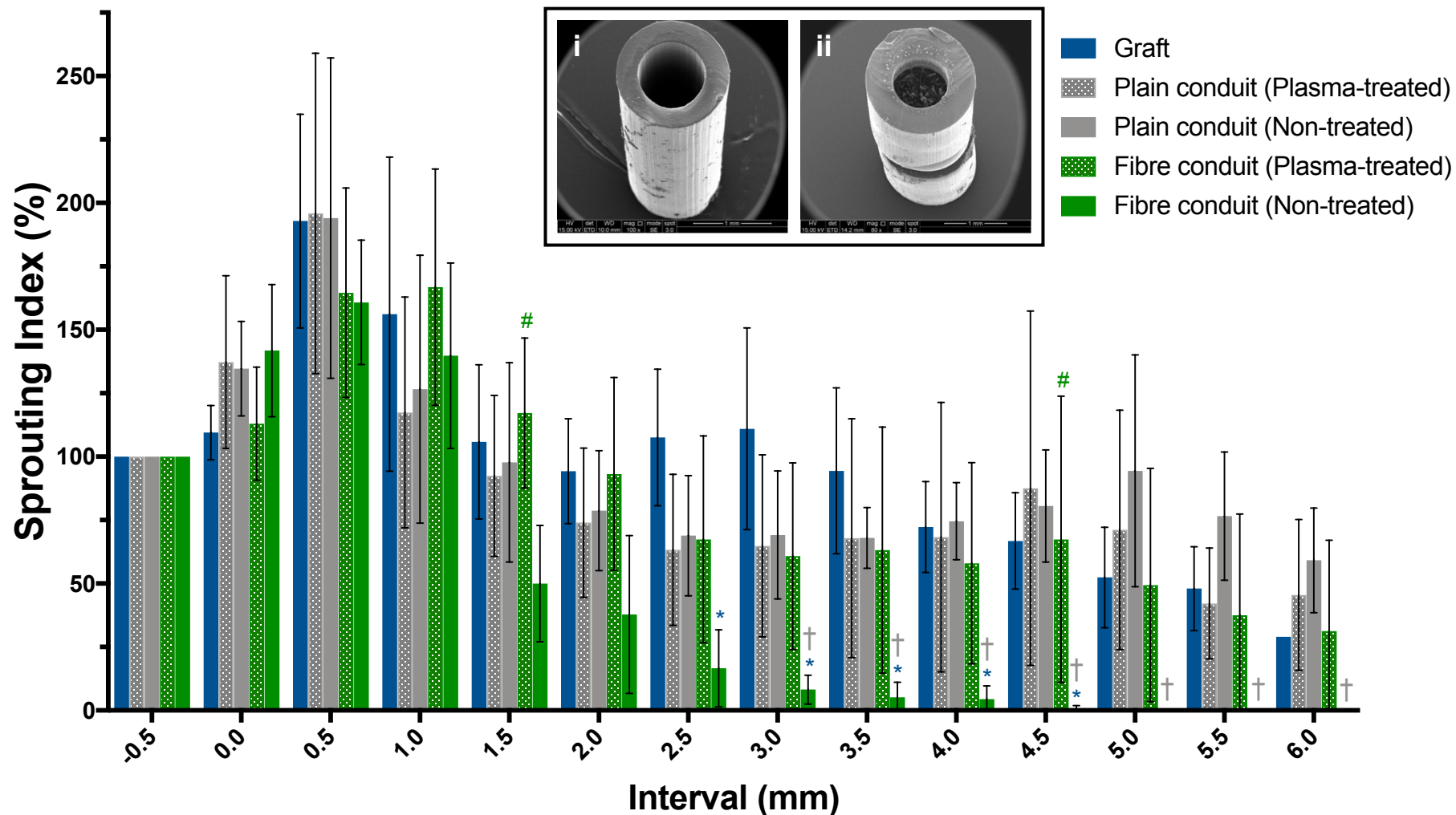


Figure 87. Sprouting index values at 0.5 mm intervals along the repair for Graft repairs (N=7), Plain conduits (plasma-treated and non-treated, N=7) and Fibre-filled conduits (plasma-treated and non-treated, N=5). Values presented mean±SD. Conduits of the same physical design are displayed in a common colour and plasma treatment is represented by spotted bars. * denotes significant difference to Graft, † denotes significant difference to Plain conduit (non-treated), # denotes significant difference to Fibre conduit (non-treated) (two-way ANOVA with Bonferroni multiple comparisons). Inset: SEM images of Plain conduit (i) and Fibre-filled conduit (ii).

5.5.5 The effect of beta-carotene: Plain conduit vs Plain conduit containing beta-carotene

Looking at the sprouting index values from Study 1 and Study 2 (Figure 81 and Figure 87) we can compare the regeneration in the plain conduits (Figure 85A) and the plain conduits containing beta-carotene (Figure 80B). This allows us to determine if the inclusion of beta-carotene in the conduits had an effect on nerve regeneration. As seen in Figure 88, the increase in sprouting index at 0.5 mm was consistent between the two plain conduit types. The values then fell to a similar level in the within the conduit (from 2.0-4.0 mm). As the axons entered the distal nerve stump (around 5.0 mm) there was an increase in sprouting index in the non-beta-carotene conduits, which is not evident in the beta-carotene conduits. However, there were no significant differences between the two groups at any interval.

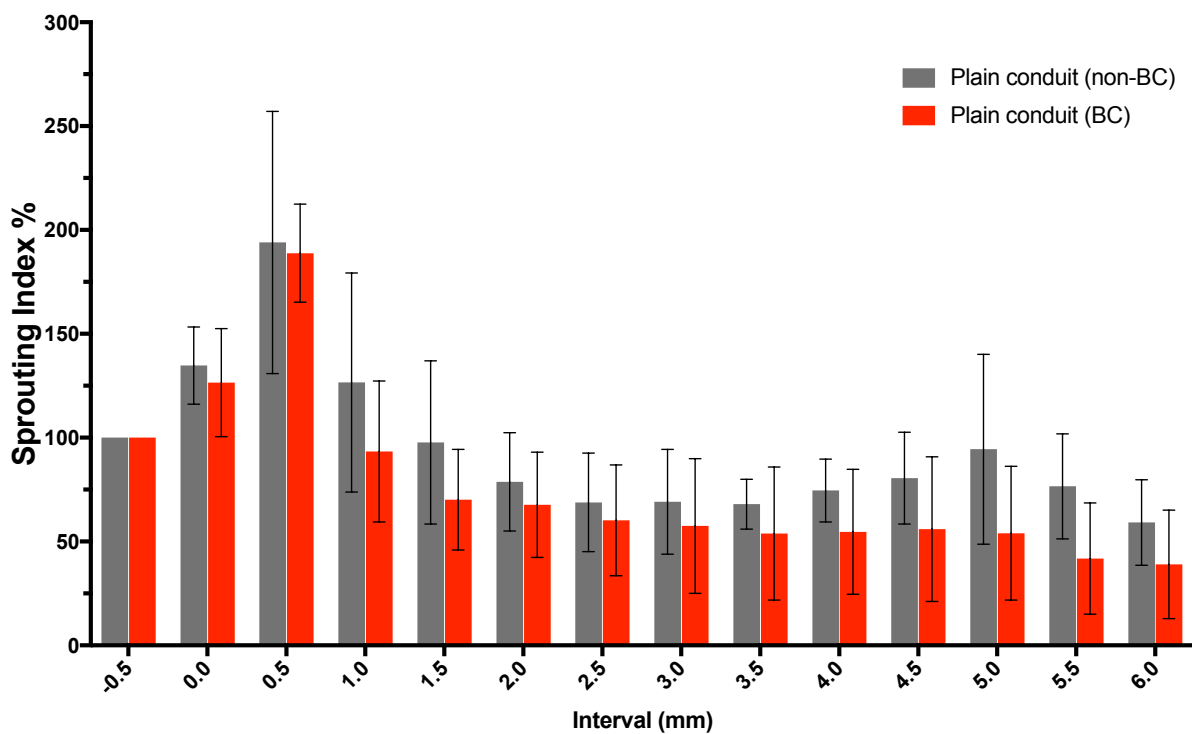


Figure 88. Sprouting index values at 0.5 mm intervals along the repair for Plain conduits (taken from Figure 87) and Plain conduits containing beta-carotene (BC) (taken from Figure 81) (N=7,6 respectively). Values presented mean \pm SD. No significant differences were found (two-way ANOVA with Bonferroni multiple comparison test).

5.5.6 Study 3: The effect of μ SL microfeatures on nerve regeneration

(Plain vs Smooth conduits)

As discussed in section 2.5.3.1, on the surface of the plain conduits were aligned microfeatures present as an artefact from the μ SL production using the DMD. To see whether these features had an effect on nerve regeneration, conduits with smooth luminal and outer surfaces were produced by injection moulding and tested *in vivo* to compare with plain conduits and graft repairs.

Eight surgeries with smooth conduits were performed however 2 mice developed problems with the sutures closing the wound and had to be culled. Additionally, 2 complete failures were seen (no tissue cable found connecting the proximal and the distal stump) and as a result the sample size for analysis was only N=4. Example images can be seen in Figure 89. Figure 89A shows a typical plain conduit from study 2 and Figure 89B shows two smooth conduits. 3 of the 4 smooth conduits possessed a good level of regeneration (e.g. Figure 89Bi), visually comparable to the plain conduits. 1 smooth conduit supported very poor regeneration (Figure 89Bii) with only one axon regenerating into the conduit. This variation resulted in large standard deviations in the sprouting index values of the smooth conduits which are displayed in Figure 90. No significant differences were found in the sprouting index between the plain conduit, smooth conduits and grafts at any interval.

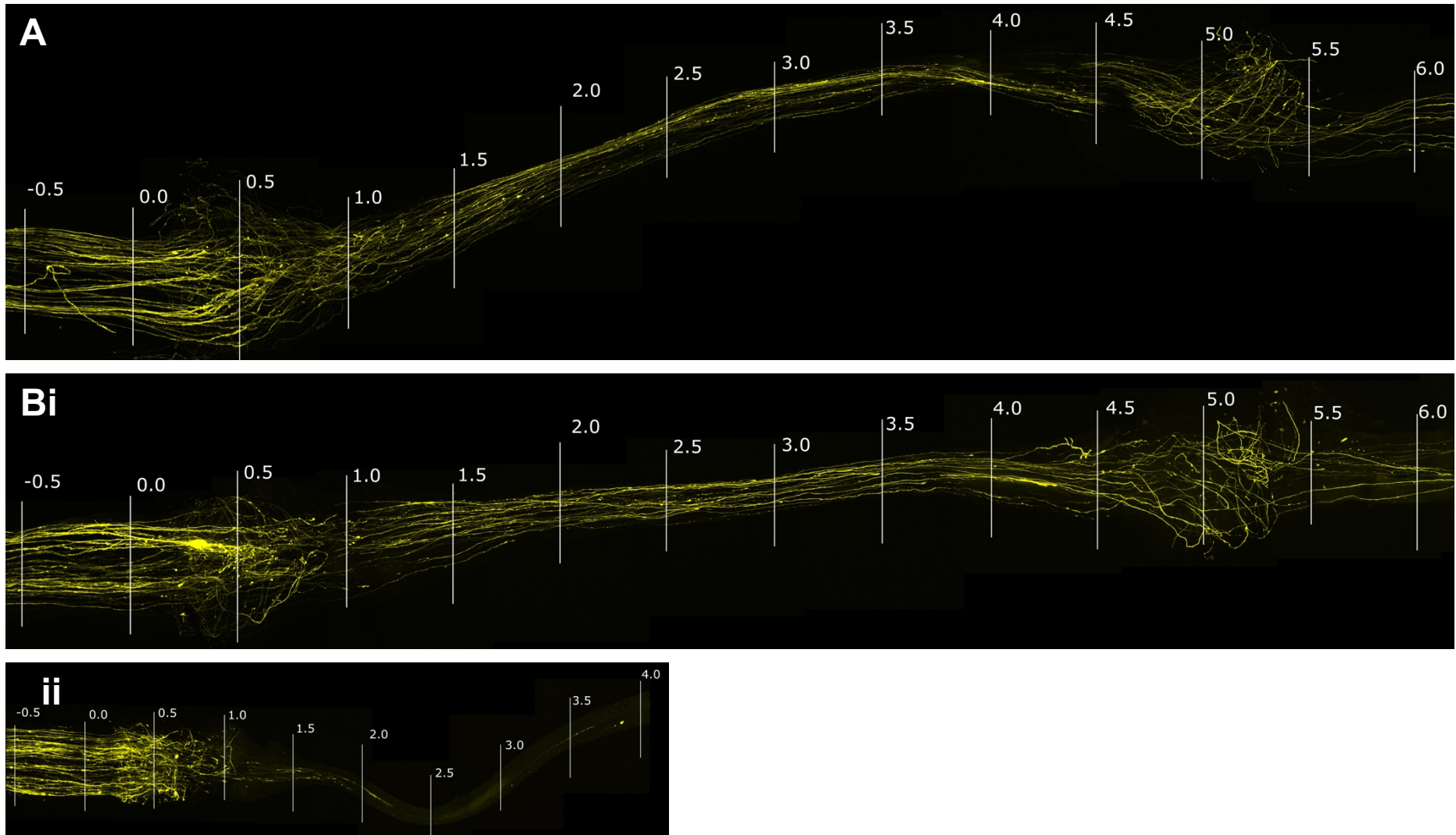


Figure 89. Typical images for common fibular nerve repairs with Plain conduits (A) and Smooth conduits (B).
 A: Plain conduit from study 2 showing good regeneration. B: Smooth conduits showing good (i) and poor (ii) regeneration. 0.5 mm intervals marked from the proximal point of injury.

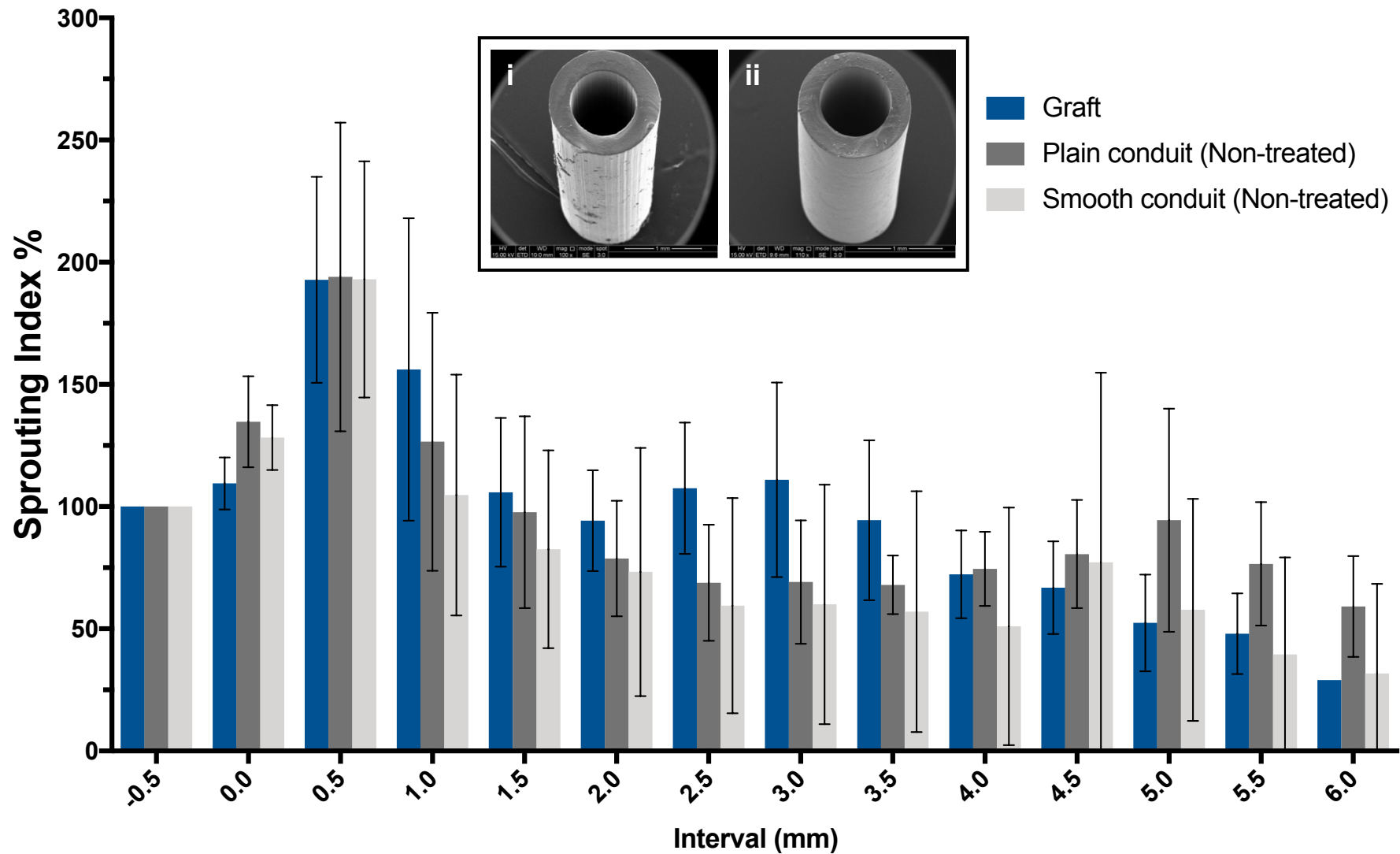


Figure 90. Sprouting index values at 0.5 mm intervals along the repair for Graft repairs, Plain conduits and Smooth conduits (N=7,7,4 respectively).

No significant differences were found (two-way ANOVA with Bonferroni multiple comparison test). Inset: SEM images of Plain conduit (i) and Smooth conduit (ii).

5.5.7 Overall success/failure: Comparison between all repair types

It was highlighted in 5.5.2 that in around 10-30% of conduit repairs, no tissue cable formed between the proximal and distal nerve stumps and no axons were able to regenerate past the proximal neuroma. If no tissue cable was present during harvest, the repair was considered a failure. This failure rate was quantified (Figure 91A), allowing us to compare the overall success of the different repair types. Most interestingly, in 100% of the fibre-filled conduits (both plasma-treated and non-treated), a tissue cable formed and at least some axon regeneration was present. All other groups had some instances where complete failure occurred (no tissue cable and no axon regeneration). The poorest performing groups were the plain (non-treated) and smooth conduits where complete failure occurred in around 35% of cases. Failure in the graft repairs was also around 30% but this was always due to the graft tissue becoming disconnected from either the proximal or distal nerve stump.

A second method of quantifying the overall success is to determine if any regenerating axons reached the point of the distal nerve stump (at around 3.5 mm for graft repairs and between 4.5-5.5 mm for conduit repairs). This result is shown in Figure 91B and indicates whether the repairs were successful in supporting axons to fully traverse the injury site. The two graphs in Figure 91A and B are largely the same for most of the repair groups. This was due to the fact that if a nerve cable formed, in almost all cases, at least one axon would reach the distal stump. Exceptions include one smooth conduit (Figure 89Bi) and one plasma-treated plain conduit where cable formed but axons regenerated only partly into the conduit. The most striking difference between Figure 89A and B is in the non-treated fibre-filled conduits. Here, even though a tissue cable formed and axonal regeneration began in all cases, there was only one repair in which a single axon reached distal end. This 80% failure rate (despite successful tissue cable formation) further highlights the poor performance of the non-treated fibre-filled conduits. On the contrary, the plasma-treated fibre-filled conduits were the only conduit type with no complete failures. In 100% of plasma-treated fibre-filled conduits, at least one axon successfully reached the distal end.

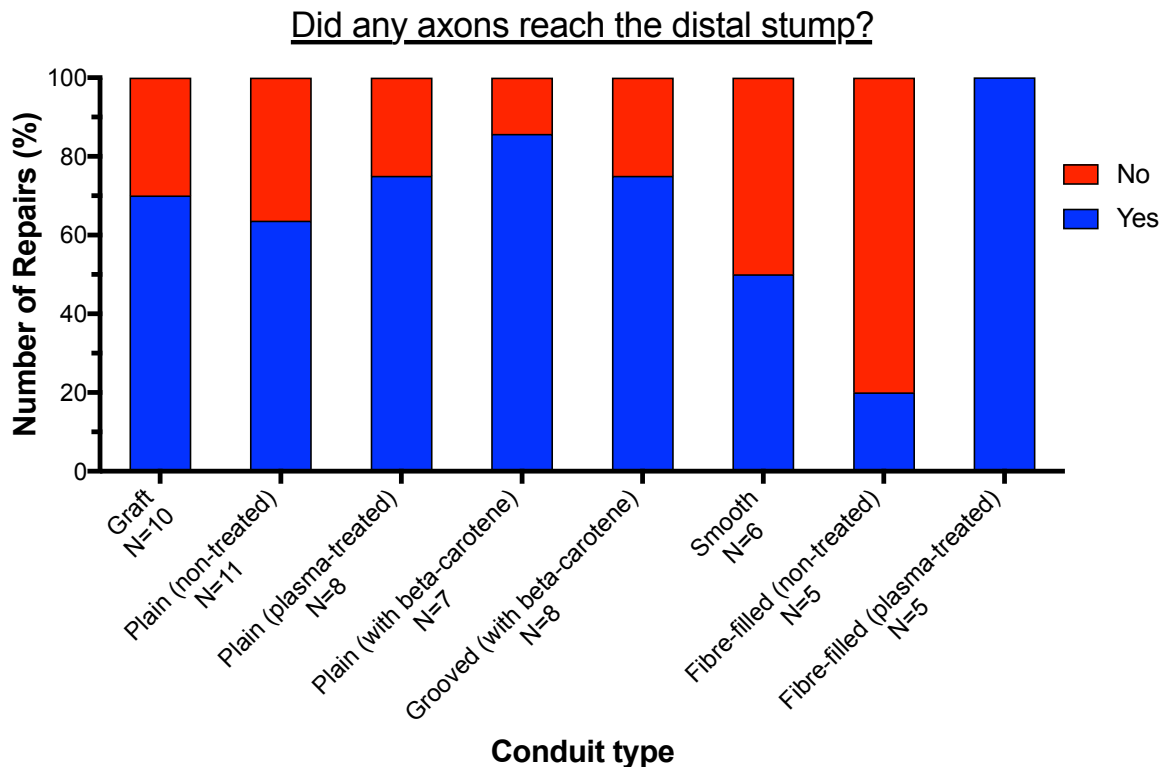
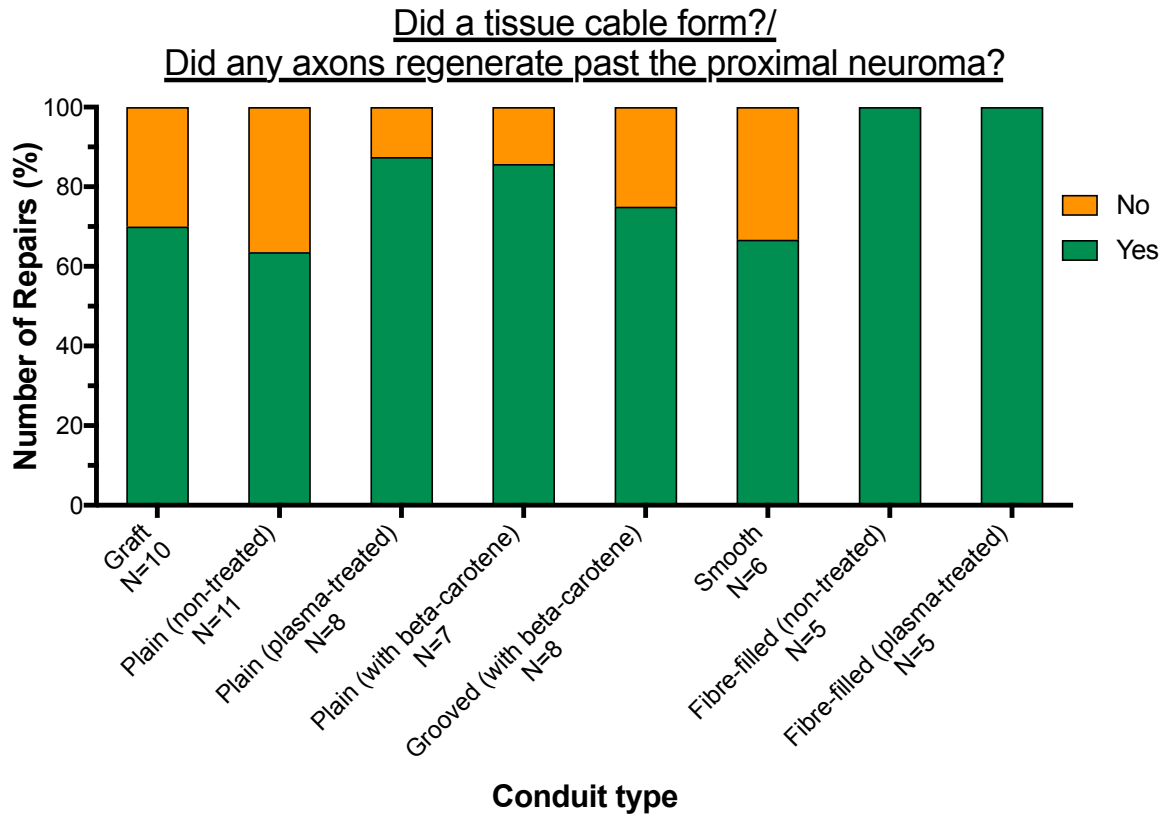


Figure 91. The overall success/failure of each conduit type, quantified using 2 criteria:
 A: 'Did a tissue cable form between the proximal and distal nerve stumps?' If 'yes', in all cases, this supported the regeneration of at least some axons into the injury site.
 B: 'Did any axons reach the distal nerve stump?' This measured whether the repair was successful in supporting any axons to fully traverse the injury site and grow into the distal nerve stump.

Discussion

5.6.1 Preliminary experiments

Before the conduit designs were finalised and the three main studies were conducted, preliminary experiments were carried out using alternative conduit designs (plain and fibre-filled conduits with a greater wall thickness). Failure rates were higher than expected, especially in the plain conduits, but this was partly attributed to poor surgical technique. It was thought that the thick-wall designs of the conduits may also have been affecting the efficacy of the plain conduits as thinner-wall plain PCLMA conduits had been successful in previous studies in our lab [324]. The fibre-filled conduits, although highly variable, out-performed the plain conduits, showing promise for their use. In the third preliminary experiment, conduits with a thin-wall design were shown to perform slightly better than the thick-wall conduits, though small sample sizes made it difficult to draw any firm conclusions. Previous studies have shown that increased wall thickness can lead to limited nerve regeneration and the effect may be due to decreased conduit permeability for the exchange of nutrients or oxygen [184]. Our PCLMA conduits do not have a microporous structure so nutrient diffusion through the wall is unlikely but gas permeability studies could be performed in the future to determine whether oxygen diffusion is a limiting factor. With improvements in the manufacturing technique making the thin-wall conduits possible and the suggestion of better performance, this conduit design was chosen for the main studies to keep the conduits comparable to those in previous studies from our group [128], [129], [324], [331].

5.6.2 The advantages of confocal over fluorescence microscopy: allowing an improved axon tracing method

Previous studies in our lab performed axon counting and axon tracing using maximum intensity projection images from fluorescence microscopy z-stacks. As mentioned in section 5.5.1.4, the use of confocal imaging in this study allowed a greater quality of image acquisition and the maximum intensity projection images obtained were of a higher quality than those obtained by fluorescence microscopy (Figure 78). This meant individual axons were more easily distinguishable and axon counting analysis could be performed more accurately. The increase in image quality is due to the fact that in fluorescence microscopy images, out of focus axons remain visible, contributing to background fluorescence and a low contrast image. On the other hand, in confocal microscopy, a pinhole is used in the optical set-up to remove out-of-focus light from the image and so the images have a much higher contrast (Figure 78B).

The second difference between the analysis in this study and the analysis in previous studies, was that tracing of axons was performed using single slices from the z-stack images rather than using maximum intensity projections. This reduced the number of axons visible at one time, allowing for more accurate determination of axon path. The reduction of visible axons can be seen by comparing images in Figure 92A and Figure 92B which show maximum intensity projections and single slices respectively. Axons in Figure 92B can be much more easily traced. The difference in image quality between fluorescence and confocal images was even more evident when looking at the individual slices from the z-stacks. Figure 92C shows a single z-stack slice from a fluorescence microscopy image of the same position, where out of focus axons contribute to a blurred looking image, making tracing through individual slices not possible.

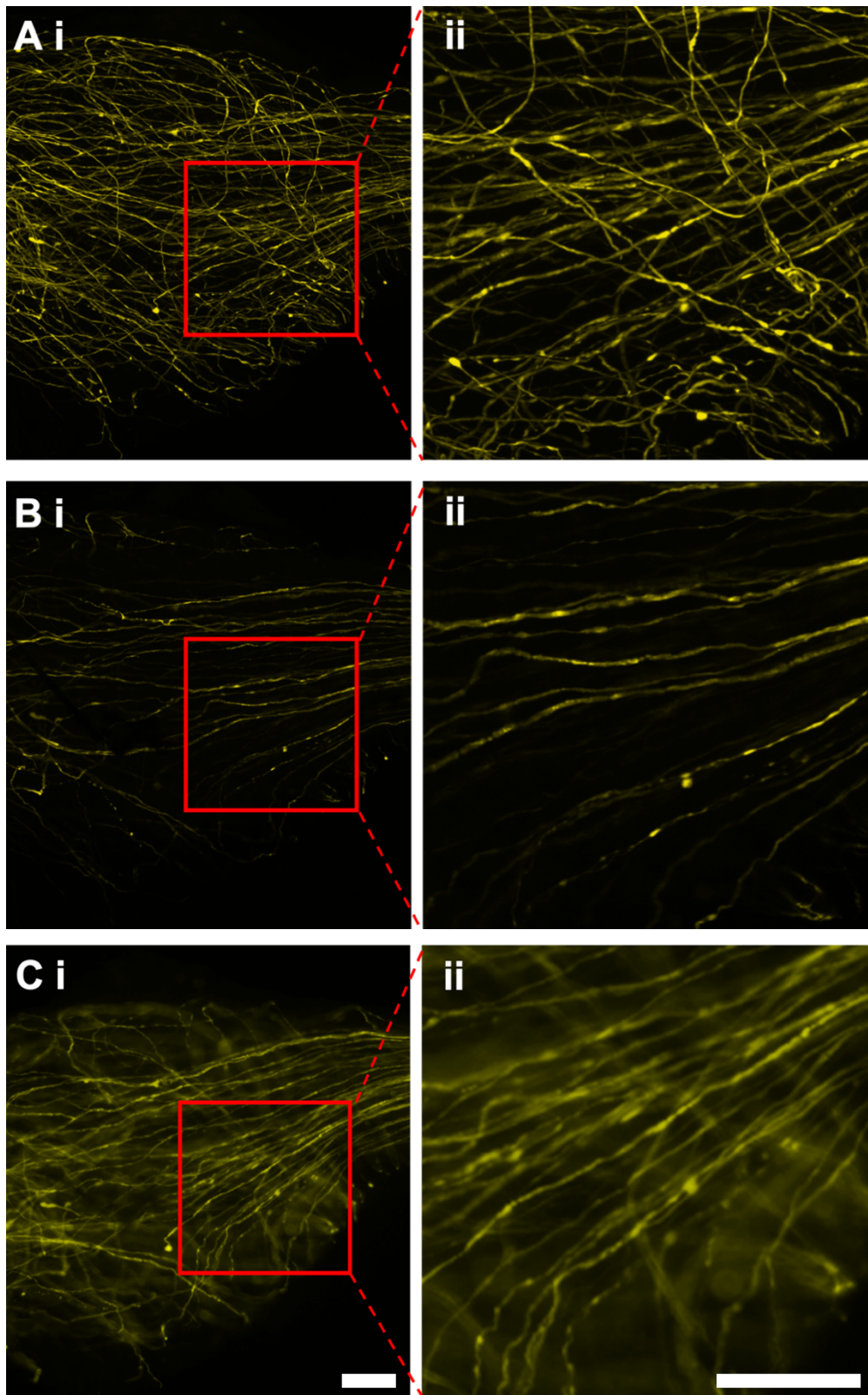


Figure 92. Image quality of YFP nerve harvests imaged by fluorescence vs confocal microscopy. The same position of a nerve segment was imaged with confocal (A,B) and fluorescence (C) microscopy. Enlarged images of selected regions shown for clarity (ii). Scale bars: 100 μm .

A: Confocal microscopy, maximum intensity projection image. (Many axons visible.)

B: Confocal microscopy, single z-stack slice. (Fewer axons visible so individual axon paths are more clear.)

C: Fluorescence microscopy, single z-stack slice. (Presence of blurry axons decreases image clarity.)

5.6.3 Study 1: The effect of aligned grooves on nerve regeneration

Plain conduits and grooved conduits (both containing beta-carotene) were tested in the 3 mm common fibular nerve injury model and regenerated nerves were analysed to give measurements of sprouting index, unique axon number and axon disruption.

5.6.3.1 Sprouting Index

Axons were counted at 0.5 mm intervals along the repair site to give an overall view of axonal regeneration and the level of sprouting occurring at various points along the repair. This allows us to obtain similar information to that which can be obtained via histological methods. Using histological methods, sections of nerve tissue can be taken and axons counted, however most studies which use this form of analysis only count the number of axons at one or two points along the repair (i.e. the mid graft or distal end) [171], [181], [184]. Our method allows us to gain information across the whole length of the repair giving a sprouting index profile for each repair type. This makes it possible to look in more detail at the effect of each repair type.

From the images of the conduit and graft repairs (Figure 80), it was clear that the locations with the greatest amount of axonal disorganisation were the proximal injury site and the beginning of distal nerve stump. The quantitative analysis of axon number revealed that the sprouting index in all repair types peaked at 0.5 mm, confirming that this visible disorganisation was due to the regenerative sprouting of axons as they regenerated out from the proximal stump, into the injury site. There was a second (lower) peak in sprouting index as axons entered the distal stump which was most evident in graft repairs (around the 3.0 mm interval). At these proximal and distal points, there is a discontinuity in axonal guidance cues as axons leave the aligned structures of the proximal tissue and enter the graft tissue/conduit or leave the graft tissue/conduit and enter the distal stump. It is thought that this lack of appropriate physical guidance is a strong contributing factor which leads to increased sprouting.

Axon sprouting in areas of disorganisation has been reported as early as 1934 by Weiss in experiments observing axons growing through clotted fibrin [140]. He observed that axon branching was limited in fibrin with parallel organisation, but in areas where fibrin was less organised, axons branched much more readily. It was hypothesised that this increased branching was due to axons being presented with mechanical obstruction in the form of disorganised guidance cues and this can explain the increased sprouting at the proximal/distal points in our study.

Looking at the proximal portion of the sprouting index profiles, the sprouting index in all repairs was similarly elevated at 0.5 mm but at 1.0 mm, the sprouting index of the graft repairs remained high and was significantly greater than the plain and grooved conduits. This prolonged, elevated sprouting index in the graft repairs is thought to be caused by the greater discontinuity in guidance cues as axons exit the endoneurial tubes of the proximal nerve tissue and attempt to find new guidance cues in the form of the endoneurial tubes of the graft tissue. Conversely, in the conduit repairs, axons extend into the lumen, guided instead by the fibrin matrix which forms during in the first few days of the nerve repair. This aligned fibrin matrix acts to guide migrating cells (including Schwann cells and fibroblasts) into the injury site, resulting in a cellularised matrix which supports axonal regeneration [35] (see section 1.3.2 for more info). Based on the lower degree of sprouting in the conduit repairs, it would seem that the supportive fibrin matrix within the conduits offers less mechanical obstruction to regenerating axons compared to the pre-formed arrangement of endoneurial tubes in the graft tissue. Once in mid portion of the repair (1.5-2.5 mm in the grafts and 1.5-4.5 mm in the conduits), axonal organisation resumed, seen by a stable sprouting index and visibly aligned axons. This reinforces the idea that organised axon growth depends on organised, continuous guidance cues as here, structural guidance is provided by the extracellular matrix of the graft tissue or the fibrin matrix of the conduit repairs.

Comparing the sprouting index of the plain and grooved conduits, no significant differences were found. It was hypothesised that the grooves would improve regeneration by providing guidance to Schwann cells and axons, resulting in quicker, more directional axonal growth with less sprouting and more axons reaching the distal stump. However, to see a significant difference in sprouting index, the effect would need to have been quite large (see section 5.4.5). Previous studies showed that grooved conduits can result in a larger number of regenerated axons [106], [181] or a larger area of axonal regeneration [106], [184] however differences were often absent at longer time points. It is possible that our three-week recovery time was too long to see differences between the two conduit types (this will be discussed in more detail in the following section).

5.6.3.2 Unique axon tracing

As discussed, the counting of axons (sprouting index) gives a good indication of the number of axons that have regenerated across the repair site. However, it is not possible to tell the number of unique axons; even if there is a large number of axons present in the distal stump, many of these could have originated from a small number of proximal axons which have undergone a high degree of sprouting. As a result of this, a number of studies have reported differences in functional recovery where differences in axon number were not present [183], [332].

Using the thy-1-YFP mouse model, whole nerve samples were imaged without sectioning and it was therefore possible to trace individual axons across the repair site. By doing this, we can determine where axons have sprouted and calculate the number of unique axons present in the distal end of each nerve repair. This may highlight differences that were not seen in sprouting index values and give a good indication of functional recovery.

As discussed in section 5.2.1, one of the most common ways of assessing functional recovery is via electrophysiological assessment of the regenerated nerve. One method is to record CAP signals from two stimulation electrodes placed either side of the repair site [332]. The ratio of these CAP signals (distal/proximal) gives a measure of the percentage efficiency of signal transmission through the repair site. In a study in our lab by Albadawi, it was shown that the CAP ratio was very closely related to the number of unique axons present distally from unique axon tracing (25.3% and 27.1%, respectively) [331]. It then follows that by performing unique axon tracing and calculating the number of unique axons present at the distal end, we can obtain a pseudo-measure of functional recovery which can be considered an alternative to electrophysiology measurements.

In the current study, no significant differences were found in the number of unique distal axons between any repair type. Both conduit types had slightly lower values compared to the graft but this was not significant. This slight difference in unique axon number could be attributed to the fact that unique axons were counted after tracing back from 5.0 mm in the graft repairs and 6.0 mm in the conduit repairs. These distal points were chosen so that they were well clear of the proximal neuroma site. Due to the shorter length of the graft repairs, 6.0 mm could not be chosen as harvested tissue usually ended around the 5 mm mark. The longer length of the conduit repairs has been noted previously [331] and was thought to be caused by the retraction of the proximal and distal stumps causing them to slip to the ends of the conduit, overcoming the relatively weak hold of the fibrin glue. Looking at the sprouting index results (Figure 81), the axon number in the grafts

started to decline after entering the distal stump so if it was possible to trace axons from the 6.0 mm interval, the number of unique axons would likely be lower and closer to that of the conduits.

Comparing the grooved and plain conduits, the number of unique distal axons was almost identical (21.25% and 21.75%, respectively). From previous studies (discussed in section 1.6.5.2), it was expected that the grooved conduits would promote an improved level of regeneration but unique axon tracing did not reveal any difference. A possible explanation is that the presence of grooves alone was not sufficient to promote improved regeneration and that additional factors are needed to facilitate their beneficial effect. Rutkowski et al. repaired 10 mm rat sciatic gaps with grooved and non-grooved PLA conduits, with and without the pre-seeding of Schwann cells, prior to implantation. Neither the presence of grooves or Schwann cells alone were found to be beneficial but when combined (grooved conduits pre-seeded with Schwann cells) significantly greater functional recovery was seen compared to the control conduits (assessed by sciatic function index) [183]. Another study found that when using grooved PLGA conduits, improvements were only seen in comparison to non-grooved conduits when the conduits were coated to make the surface more hydrophilic [182]. We have previously discussed how cell attachment and spreading can be improved on hydrophilic surfaces (sections 4.2.1 and 4.6.3) and this could promote enhanced cell-material interaction, allowing the cells to detect and respond to the underlying physical features. This result suggests that it would be interesting to study the use of plasma-treated, grooved conduits (something that was not included in the present study).

Revisiting the idea of the fibrin matrix which supports nerve regeneration, we arrive at an alternative explanation for the similar level of recovery between the two conduit types. This is that the axons regenerate through the fibrin matrix (and the resulting tissue cable), rather than along the conduit wall. It has been noted in a number of studies that the connecting cable between the proximal and distal stump is always suspended in the centre of the conduit lumen, separated by fluid from the conduit wall [35], [333]. This was also evident during the harvest of regenerated tissue in the present study - in Figure 70Aiii the tissue cable can be seen lying in the centre of the conduit lumen. If this is the case, and axons and Schwann cells regenerate only through the fibrin cable, they may not come into contact with the grooves and therefore not experience any guidance effects.

It may also be possible that with our 3 mm injury model, the three-week recovery time was too long to detect differences in the number of unique distal axons. Studies have shown that differences in functional recovery at earlier time points do not always remain as recovery continues (similar to the

disappearance in differences of axon number at later time points discussed in section 5.6.3.1). Kim et al. found that grooved conduits resulted in improved sciatic function index at 2 weeks but the difference was absent at 4 weeks [182]. If the grooved conduits in our study promoted a similar increased rate of functional recovery and unique axon number, this difference may have disappeared by the three-week time point as the majority of regenerating axons in all repairs had extended past the distal point (6.0 mm). A shorter time point would be necessary to determine if there are any differences in initial regeneration between the plain and grooved conduits.

The use of a longer gap model would highlight differences in the repairs more easily, especially at longer time points. Since the plain conduits in our study did not perform significantly worse than the grafts, there was no room for improvement with the use of a different conduit design and it would only have been possible to detect a detrimental effect. To see a potential beneficial effect, a longer gap model could be chosen in which axonal regeneration in plain conduits is severely limited compared to grafts (seen in 6 mm mouse sciatic conduit repairs [334]) or where the fibrin cable formation is disrupted (around 10-15 mm in a rat model [92]). To detect differences in functional recovery in our 3 mm model with a three-week recovery time, different parameters could be assessed such as compound muscle action potential which indicates the number of functional axons which have regenerated the full distance to the distal target muscle [184].

5.6.3.3 Axonal disruption

For measurement of axon disruption, axon path lengths were measured from 0.0-1.5 mm and compared to shortest, most direct path. Extra axons were traced back from 1.5 mm and measured in addition to ones traced from the distal end. This was so that all axons were considered rather than just the ones that reached the distal end (and therefore likely to be less disrupted). This measurement provides information about axon growth in the transitional region between the proximal nerve stump and the graft tissue/conduit indicating how easily axons were able to regenerate into the graft/conduit. This may highlight if the presence of grooves has an effect on axon growth that is not reflected by the number of axons (either sprouting index or unique axon tracing).

Both conduit types presented lower axon disruption compared to the grafts. This relates to the lower sprouting index at 1.0 mm and the hypothesis that fibrin cable offers less resistance compared to the graft tissue so it is easier for axons to regenerate into and find an appropriate path.

Interestingly axon disruption in the grooved conduits was significantly lower than the grafts but the

plain conduits had intermediate level and was much more variable, meaning it was not significantly different to either the grooved conduits or grafts. The consistently low axon disruption in the grooved conduits resulted in a significant difference to the grafts. In the grooved conduits, axons grew in a more directional and aligned fashion, parallel to groove direction, therefore exhibiting a shorter path length. This implies that the grooves are providing some guidance to regenerating axons in this proximal region.

The ability of grooved substrates in guiding axonal and Schwann cell growth has been widely demonstrated *in vitro* (discussed in section 1.6.5.1). Beneficial effects have been seen with a wide variety of groove sizes ranging from 5 to 180 μm . In studies with neuronal and Schwann cell culture, aligned grooves have been shown to promote the alignment of neurites [174], [176], [180], [182], [335], [336] and Schwann cells [174], [175], [335], [336], increase neurite outgrowth distance [182], [335] and enhance Schwann cell migration [174], [182], [335]. Similar effects have also been seen with the culture of DRG explants with longer neurite outgrowth [337] and improved Schwann cell alignment [177] on grooved substrates. The mechanism by which grooves promote axonal alignment *in vitro* has also been hypothesised by previous groups. It is thought that the filopodia in the growth cone of advancing axons which are sent out to explore the area (see section 1.2.3) come into contact with grooves and, on contraction, experience directional traction forces which direct movement [43], [338]. Additionally the microtubules which make up the cytoskeleton of axons are thought to be inflexible and so cannot deform over grooves [338]. This means that once in contact with a groove, axons have a limited angle in which they are able to advance, resulting in growth along the groove direction.

Though grooved conduits have been tested by a number of studies *in vivo*, beneficial effects are usually assessed by conventional parameters such as axon number [106], [181]–[183], axon area [181], [183], [184], percentage success rates [106] or functional recovery (electrophysiology [182] and sciatic function index [182], [183]). These methods do not determine how axons and Schwann cells respond to grooved topographies *in vivo*, as this information is difficult to obtain from conventional histological methods. This highlights the advantages of our thy-1-YFP mouse model as the tracing of individual axons allows the measurement of axonal disruption, which is similar to measurements of axon alignment *in vitro*. The response of axons to grooves *in vivo* can then be studied and compared to *in vitro* observations. In our study, the smaller axonal disruption in the grooved conduits showed that some axonal guidance was provided by the grooves, similar to what is seen *in vitro*.

However, the mechanisms by which axonal regeneration is improved by the grooved conduits is unclear. Hsu et al. [106] and Mobasserri et al. [184] hypothesised that the grooved surface of conduits directly influences cell growth by promoting enhanced Schwann cell migration and resulting axonal outgrowth. However it is thought that the axons regenerate through the supportive fibrin matrix, not in contact with the conduit wall (see section 5.6.3.2). Interestingly, however, it has been shown that properties of conduit wall can influence the formation and structure of the fibrin matrix. In a study by Aebischer et al. repairing a 4 mm mouse sciatic gap, smooth-walled conduits promoted the formation of an oriented fibrin matrix and successful regeneration, whereas rough-walled conduits caused a disorganised matrix and resulted in poor regeneration [333]. Building on this, some studies have hypothesised that the grooved topography of conduits can promote the organisation of this fibrin matrix and influence the remodelling of this ECM bridge, resulting in a more regular aligned structure to support enhanced Schwann cell migration and axon extension [181].

From our results it is unclear whether the grooves directly promoted directional Schwann cell migration, and by extension, axon alignment or if there was an indirect effect on axonal guidance from the promotion of an organised fibrin matrix. The fact that the regenerated tissue within the conduit did not appear to be in contact with the conduit wall suggests that cells were not migrating directly along the wall and the latter, indirect effect, may be the case. In future studies, histological examination of the harvested tissue could be included to determine if any effects on ECM structure can be observed.

Regardless of the mechanism, the grooved conduits resulted in a lower axon disruption meaning that axon growth was more directed towards the distal stump. The shorter distance travelled by axons may indicate faster initial recovery in the grooved conduits. This gives further reason to investigate the same conduits with a shorter recovery time to see if differences can be detected in sprouting index or unique axon number.

5.6.4 Study 2: The effect of aligned fibres and plasma treatment on nerve regeneration

Plain conduits and fibre-filled conduits (both non-treated and plasma-treated) were tested in the 3 mm common fibular nerve injury model and regenerated nerves were analysed to give measurements of sprouting index. This allowed the effect of plasma treatment and aligned fibres to be investigated independently as well as in combination.

5.6.4.1 The effect of plasma treatment in plain conduits

In terms of sprouting index, plasma treatment had no effect on the regeneration through plain conduits. Despite the fact that plasma treatment was seen to reduce water contact angle of PCLMA in a similar way to PCL (section 4.5.4), the improvement seen on plasma-treated vs non-treated fibres was not mirrored on plasma-treated vs non-treated plain conduits. This gives further evidence to support the hypothesis that Schwann cells and axons do not migrate and regenerate along the conduit wall, but instead through the fibrin cable in the centre of the conduit lumen.

5.6.4.2 The effect of fibres and plasma treatment

As with the plain and grooved conduits in section 5.6.3.1, the sprouting index of all repairs peaked at 0.5 mm, however in the plasma-treated fibre-filled conduits, the sprouting index at 1.0 mm was still at the maximal level and higher than the other repair types (though not significantly different). This is similar to the observation made in section 5.6.3.1 about an elevated sprouting index in the graft repairs at 1.0 mm. This suggests that, like in the grafts, the regenerating axons are being presented with a level of resistance as they meet the edge of the fibres adjust their growth according to the new guidance cues. This has been noted previously by Kim et al. who observed increased sprouting in the proximal portion of repairs with fibre-filled conduits in comparison to autografts [154].

In terms of sprouting index, all conduit types performed comparably to the graft except for the non-treated fibre-filled conduits. There were no significant differences between any group except the non-treated fibre-filled conduits which possessed significantly lower sprouting index at multiple intervals compared to the grafts and plain conduits. This result indicates that the non-treated fibres impede nerve regeneration. The drastic failure of non-treated fibre-filled conduits was surprising considering the results seen in literature on the beneficial effects of fibres within conduits. These studies have used many different approaches such as the use of larger diameter fibres/filaments compared to that produced by electrospinning [171], [172], the use of electrospun fibres with

alternative methods of incorporating them into conduits [154], [168] or the addition of ECM proteins and growth factors to improve regeneration [134], [168].

Successful studies using plain polymer fibres/filaments (no treatment or additional components) include that by Cai et al. [171] Ngo et al. [172] who used PLA microfilaments of 60-80 μm and 40-100 μm diameter, respectively. Conduits containing these microfilaments were used to repair 18 mm rat sciatic nerve gaps and compared to empty conduit controls. Cai et al saw a greater number of axons present in the distal end of the repairs containing filaments as well as enhanced Schwann cell migration and improved axon myelination [171]. Ngo et al. saw similar results with significantly more myelinated axons in the filament conduits at regular intervals along the repairs [172]. Kim et al. also saw beneficial results with conduits containing stacked sheets of aligned electrospun fibres (poly(acrylonitrile-co-methacrylate), ~ 500 nm diameter). In a 17 mm rat tibial nerve gap, these conduits performed comparably to autograft in terms of distal axon number and muscle reinnervation, whereas empty conduits did not support axonal regeneration [154].

The difference between these three studies and the present study is the use of larger diameter filaments or the use of electrospun fibre sheets. Despite the similar packing densities to this study (around 10%) the larger filaments or sheets of fibres mean that there are larger voids between the areas occupied by material, which may allow tissue to regenerate more easily. This suggests that our arrangement of evenly spread fibres throughout the conduit lumen may be detrimental, presenting a barrier to the regenerating tissue. In some cases in our results (e.g. Figure 86Aii, Bii) axons were seen growing largely around the start of the fibres rather than through the centre of the conduit, indicating the resistance presented by the fibres. Impedence to regenerating axons from luminal fillers has been seen previously in the form of laminin gels and collagen sponges [165], [166] as well as conduits containing dense electrospun fibres [164]. In these studies, the presence of fewer regenerating axons or shorter axonal outgrowth in the filled conduits compared to empty conduits is thought to be due to the filler presenting a mechanical barrier. This can prevent the diffusion of molecules, Schwann cell migration and axon growth as well limiting the formation of the fibrin cable. In such studies, axons were also often seen growing in areas not occupied by the gels/fibres i.e. round the lumen periphery or between fibre layers [164], [165] suggesting the empty space provided less resistance than the gels/fibres. ECM gel-filled conduits have been successful in a number of studies but a dependence on gel concentration has been shown. Gels with higher concentrations of collagen/laminin were more dense and therefore presented an obstruction to regenerating cells [339]. Lower concentration gels supported successful regeneration, further

showing the importance of the density and composition of luminal fillers and the need for sufficient space for cell migration and axon regeneration.

With the use of plasma treatment, regeneration through the fibre-filled conduits was significantly improved to make the growth comparable to the graft and plain conduit repairs. This beneficial effect of plasma treatment was expected based on results from the DRG study (section 4.5.5.1), which showed a 5-fold increase in Schwann cell migration and axon outgrowth in plasma-treated fibre-filled conduits compared to non-treated controls. Plasma treatment is well known to improve cell attachment/migration on polymer substrates (see sections 4.2.1 and 4.6.3). For example, increased rate of cell infiltration has been observed on plasma-treated PCL and PLA electrospun fibres scaffolds by Valence et al. [307] and Cheng et al. [293], respectively. This increased migration rate on plasma-treated surfaces could explain the improvement of the plasma-treated PCL fibres in the present study. As discussed in chapter 1, Schwann cell migration is essential to nerve regeneration and always precedes axonal regeneration. If Schwann cells are able to attach and migrate more readily along the plasma-treated fibres during the early stages of the nerve repair, they would be able to support improved axonal outgrowth through the conduit. This relates to observations by Kim, Cai and Ngo who saw improved Schwann cell migration in fibre-filled conduits [154], [171], [172]. Kim et al. hypothesised that the electrospun fibre sheets supported migration of Schwann cells which were able to form of Bands of Büngner and lay down laminin to guide axonal regeneration. Since the results from our DRG study showed improved migration on plasma-treated fibres, it suggests that this process was also supported *in vivo* by our plasma-treated fibres but not by the non-treated fibres.

Despite improvements in plasma-treated vs non-treated conduits, the plasma-treated fibre-filled conduits still offered no improvement compared to the empty plain conduits. A number of studies have shown that beneficial effects of fibres within conduits can be amplified by incorporating some ECM components such as laminin. Laminin, which is produced by Schwann cells during nerve regeneration is important for the guidance of axonal regeneration [340] and has been shown to enhance Schwann cell migration *in vivo* [341]. Neal et al. fabricated similar conduits to those of Kim et al. by inserting electrospun fibre sheets into outer tubes and used them to repair a 10 mm rat tibial nerve gap. Conduits containing aligned PCL fibres promoted improved thermal withdrawal latencies and recovery of toe spread (measures of sensory and motor recovery, respectively) but improvement in both parameters was increased when a PCL/laminin blend was used. A similar result was also seen with nerve conduction velocities in conduits containing fibres of PCL and PCL/laminin

[134]. Koh et al. also investigated the effect of laminin inclusion in PLA conduits containing bundles/yarns of PLGA fibres. In measurements of both axon density within the midgraft and muscle weight, no difference was seen between the fibre-filled conduits and the empty conduits, but with the inclusion of laminin, regeneration was significantly increased [168]. Neal et al. hypothesised that laminin supported improved Schwann cell attachment along with greater basal lamina secretion and neurotrophic factor production, all factors which would be expected to improve axon outgrowth. These results suggest that the inclusion of laminin may facilitate the beneficial effect of intraluminal fibres and would be an area of interest for future studies.

Aside from fibre properties, the apparent lack of improvement from the plasma-treated fibre-filled conduits, compared to plain conduits could be due to the 3 mm nerve gap length in the model utilised in this study. This is for the same reasons as discussed in sections 5.5.3.2 and 5.5.3.3 on the grooved conduit performance; since the plain conduits performed comparably to the gold-standard grafts, there is not much room for improvement with the inclusion of fibres. If the fibres improve axonal regeneration in the initial stages due to increased migration and attachment of Schwann cells, these differences may be absent by the three-week timepoint as regeneration in the plain conduits catch up. A shorter time point or longer gap length may more easily highlight differences in the performance of different conduit designs. The beneficial effects of filament-containing conduits from Cai et al. and Ngo et al., discussed earlier, were only apparent in gap lengths of 18 mm. In both studies, 14 mm nerve repairs were also carried out but no significant differences were found in distal axon number between empty and filament-containing conduits [171], [172]. Differences in the 18 mm gaps were more evident due to a higher failure rate of the empty conduits. Many of the studies mentioned above which highlight the benefit of intraluminal fibres were also carried out in gap lengths where empty conduits performed very poorly with high instances of complete failure and no axonal regeneration [154], [168], [171], [172]. For example, Neal et al. used a 10 mm rat tibial nerve gap where empty conduits performed significantly worse than all other repair types, exhibiting no recovery of motor function or nerve conduction velocity [134].

The failure of empty conduits in longer gaps and the improvement with the use of fibres, relates to another potential mechanism by which intraluminal fibres can support improved regeneration. Specifically, that the intraluminal fibres help the formation and stabilisation of the fibrin cable during the early stages of the nerve repair and allow the cable to form over distances where it would fail in an empty conduit. We can see evidence of this effect when looking at the failure rates of the different conduit types in this study.

5.6.4.3 Differences in overall success rates and the importance of fibrin cable formation

Comparing all conduit types in terms of overall success/failure, we can see some big differences between fibre-filled and plain conduits. In terms of tissue cable formation (Figure 91A) 100% of both fibre-filled conduit groups successfully formed a connecting cable between the proximal and distal nerve stumps compared to 64% in plain conduits. Secondly, in terms of successful axonal regeneration (Figure 91B), 100% of the plasma-treated fibre-filled conduit had axons present in the distal nerve ending compared to 64% and 75% in non-treated and plasma-treated plain conduits, respectively. The plasma-treated fibre-filled conduits was the only repair group where no complete failures occurred.

These results of increased cable formation and presence of distal axons has been shown by a number of the studies mentioned previously. Cai et al. saw 100% nerve cable formation in fibre-filled conduits repairing an 18 mm nerve gap compared to 56% in empty conduits. This was accompanied by 90% of fibre conduits having distal axons present compared to 56% in the empty controls [171]. Ngo et al saw 70% and 75% cable formation in empty conduits repairing 10 mm and 14 mm nerve gaps which was increased to 100% with fibre-filled conduits. With this, came an increased number of repairs with distal axons in the fibre-filled vs empty conduits (95% vs 53% in 10 mm and 75% vs 25% in 14 mm) [172]. Similar results were also seen in Kim et al.'s electrospun fibre-containing conduits with 100% successful regeneration compared to only 15% cable formation in empty conduits [154].

The increased cable formation in fibre-filled conduits (and subsequent improved axonal regeneration) has led to the hypothesis that the fibres provide mechanical support to stabilise and aid the formation of the fibrin cable [171], [172], [342]. Lundborg et al., who also saw more successful cable formation with fibre-filled conduits, suggested that in longer gaps within empty conduits, the fibrin matrix dissolves before it can become cellularised and remodelled by migrating cells from the two nerve endings. However with the presence of fibres, the matrix is stable over longer time periods, allowing greater cell infiltration [342].

Ngo et al. and Koh et al. separately observed that Schwann cells and axons were not found in contact with fibres suggesting that the fibres were not directly guiding Schwann cell migration/axon growth, giving more evidence that the beneficial effect was due to the support of the fibrin matrix which in turn acts to guide the cells. This relates to observations made by Weiss in early studies on contact guidance (see section 1.5.1). It was shown that very large fibres (500 µm diameter) could still direct axonal growth from tissue explants despite them being thousands of times larger than the axonal processes and too large for axons to 'see' a discernible fibre with a distinct direction. He

hypothesised that fibres caused the fluid exudate from the explants to advance directionally (by capillary action) laying down an aligned fibrous matrix, which coated the structures and in turn guided the cell migration and growth [138]. It could be by a similar method that the fibres within a conduit are able to support the formation of the fibrin matrix which then supports Schwann cell migration and subsequent axonal regeneration.

It is an interesting result from our study that despite successful cable formation in the non-treated fibre-filled conduits, there was an 80% failure rate in axons reaching the distal stump. Even in the one case which was 'successful' only a single axon regenerated to the end of the conduit. The failure mode in these conduits was different to the plain conduits, which when failure occurred, no tissue cable was found and the proximal axons formed a neuroma-like knot of axons (see Figure 79). In all failed repairs with non-treated fibres, axons always regenerated a short distance into the fibres, but axon number declined rapidly with each interval (see Figure 86A). This suggests that the fibres must be providing some guidance (either directly or indirectly) but the properties of the material are not optimised (for example, the increased hydrophobicity in comparison to the plasma-treated fibres). It may be that the fluid exudate secreted from the nerve endings (from which the fibrin matrix forms) cannot flow properly through the conduit or that the hydrophobic fibres support reduced protein binding from this fluid. If the fibrin cable fails to form properly (such as the disorganised ECM cable seen in rough-walled conduits by Aebischer et al. [333]), a tissue cable may form but axonal regeneration would still be limited. It would be interesting to perform histology on the tissue cable from the treated and non-treated fibre-filled conduits to investigate any differences in structure. This would also allow investigation of the proximity of Schwann cells and axons to the electrospun fibres, to see whether guidance is being provided directly or indirectly, and determine if the plasma-treated fibres can provide guidance where the non-treated fibres cannot.

Direct guidance to regenerating cells from NGC luminal fillers has been hypothesised with the use of gels containing collagen and laminin. Since these proteins are able to guide Schwann cell migration and axonal growth, such gels may be able to provide support in place of the failed fibrin cable by providing these exogenous ECM components into the injury site [343]. Conduits filled with collagen and laminin-containing gels have allowed regeneration in mouse sciatic nerves over longer distances compared to control conduits [339]. The guidance provided by these gels is evident when comparing gels with differing orientations. Aligned collagen/laminin gels can be produced in a variety of ways, such as the with the use of magnetic fields. Verdú et al. demonstrated that magnetically aligned gels supported faster functional recovery compared to non-aligned gels in mouse sciatic nerve repairs [343]. Conduits containing self-aligning collagen gel have been produced by Phillips et al. who filled

conduits with Schwann cell and fibroblast-containing gels. The gel was tethered at either end of the conduits, resulting in the generation of uniaxial tension and alignment of collagen fibrils as the cells contracted. These conduits outperformed empty tubes in the repair of 5 mm rat sciatic nerve gaps [344]. The guidance provided by gels containing ECM components complements the studies discussed earlier which demonstrated the beneficial effect of laminin-containing fibres [134], [168]. These results suggest that the incorporation of collagen/laminin into the PCL fibres of the present study, would be an alternative method which may help the fibres provide an element of direct guidance in addition to the stabilisation of the fibrin cable.

Of the conduit designs investigated in the present study, looking together at the results of sprouting index and the overall success rates, the plasma-treated fibre-filled conduits promoted the most successful regeneration. Even though no improvements were seen in axon number compared to the plain conduits, the 0% failure rate is obviously an important factor. In this way, the plasma-treated fibre-filled conduits performed similarly to the graft repairs - Ignoring the 3 cases where graft became detached, all graft repairs promoted successful regeneration. If these conduits were tested in longer gaps, it would be expected that the incidence of failure in the plain conduits would increase as the fibrin matrix fails more frequently. However, based on the results of this study, and results seen in literature, the plasma-treated fibres should stabilise the fibrin matrix and provide guidance to regenerating cells (either directly or indirectly) leading to improved regeneration. This suggests there is promise for the use of fibre-filled NGCs in the clinical setting as they may overcome disadvantages of plain conduits which can only support regeneration in short distance nerve gaps.

5.6.5 Study 3: The effect of μ SL microfeatures on nerve regeneration

Smooth conduits (produced by injection moulding) were tested in the 3 mm common fibular nerve injury model to compare with plain conduits produced by microstereolithography. This study was carried out due to unpublished work from our lab which suggested the inherent microfeatures in conduits produced by microstereolithography were important for the regenerative capacity of these conduits. The small groove height and width of the micropatterns are similar to some of the smaller dimension microgrooves reported in literature [174], [183], [184] (see section 1.6.5). It was thought that they might replicate the beneficial effects seen in studies with grooved conduits via the mechanisms discussed in section 5.6.3.

This assumption was not entirely in line with our observations. In terms of sprouting index, the smooth conduits seemed to promote comparable regeneration compared to the plain (μ SL) conduits, however the lower sample size made it difficult to draw any strong conclusions. The occurrence of a repair with only a few regenerating axons caused high variability in the smooth conduit results, making it necessary to perform more surgeries to confirm these findings.

Looking at the overall success rate of the smooth conduits, in 50% of cases, no axons regenerated into the distal stump. This was the highest failure rate of all conduit types except the non-treated fibre-filled conduits. Despite the similar sprouting index to plain conduits (when successful repairs are counted) the high failure rate suggests that the smooth conduits could be detrimental to regeneration and that the microgrooves of the plain conduits may help initiate recovery and improve success rates. In the clinical setting, the reliability of a procedure is of great importance and so the plain conduits (which promoted less variable, more successful regeneration) would be preferable over the smooth conduits.

5.7 Conclusions

Both grooved and fibre-filled conduits supported a comparable level of regeneration to graft repairs and empty conduits. Plasma treatment was found to be essential for the fibre-filled conduits to support nerve regeneration as regeneration was significantly impaired by the presence of non-treated fibres.

Regeneration through empty conduits was characterised with lower axon disruption compared to graft repairs, especially in the grooved conduits in which axons took a more direct path in the proximal region. This suggests that the grooves supported axon guidance, either by directing Schwann cell migration or influencing the fibrin cable, justifying the further investigation of grooved conduits in longer distance nerve injuries.

Plasma-treated fibre-filled conduits achieved higher success rates compared to any other repair type by stabilising the formation of the fibrin matrix and providing guidance to migrating and regenerating cells. This demonstrates the potential for the use of fibre-filled conduits in longer distance nerve gaps where empty conduits typically fail due to the failure of the fibrin matrix.

The higher failure rate of the smooth conduits in comparison to the plain conduits suggests that the inherent microfeatures from μ SL may play a role in promoting successful regeneration but a larger sample size is necessary to confirm these findings.

6. General Discussion and Future work

6.1 Materials

6.1.1 Suitability of PCLMA as a NGC material

Photocurable PCLMA resin was developed for use in μ SL and used for the production of the NGCs in this study. Since the mechanical properties of NGCs are of importance, the Young's Modulus of the PCLMA material was measured and shown to be tuneable by varying the DM of the prepolymer (chapter 2). The flexion of PCLMA NGCs was also demonstrated (chapter 3) with the ability of the conduits to bend to a high degree without kinking. Future work could entail further characterisation of the mechanical properties of the PCLMA tubes. Three-point bending tests could be performed to quantify the results seen in section 3.5.9 and level of kink-resistance. Uniaxial (longitudinal) compression of conduits can also be performed to calculate maximum stress at failure [128] however this method does not adequately represent the forces the conduit would experience *in vivo*. More physiologically relevant testing would be to apply compression perpendicular to the long axis to the conduit. This transverse compression allows quantification of the conduits' resistance to luminal collapse from external forces (which would lead to nerve compression and limited recovery). Previous studies have recorded the load required to cause different levels of compressive deformation (between 10-60%) [78], [345]–[347] and calculated compressive strength from the force required to cause complete luminal collapse [348]. These tests could be performed with PCLMA conduits to compare with previous studies and determine the effect of DM on these values.

As well as mechanical properties, the degradability of NGC materials is of importance. Appropriate degradation rates for NGCs are a topic of discussion with FDA approved conduits having a range of degradation times between 3 months and 3-4 years [61] (see Table 1). Conduit degradation within the first 6 months (i.e. with PGA conduits and some collagen conduits) is thought to be too fast to allow full regeneration to occur [61] [349]. Long-term degradation is also problematic due to long-term placement of conduits leading to pain or local discomfort caused by compression of the regenerated nerve [94], [350]. For this reason, Dahlin found that non-degradable silicone conduits often had to be removed after 12-44 months [351], [352].

In chapter 2, PCLMA was produced with a range of degradation rates (determined by DM) all of which were faster than the degradation of commercial, linear PCL which is known for its slow

degradation. In a long-term *in vivo* study, PCL implants were shown to retain their structure for around 2 years with PCL fragments still remaining after 3 years [353]. Since our PCLMA degraded faster than the commercial PCL, it would be expected that the *in vivo* degradation of PCLMA would be faster than the 3+ years in the aforementioned study, meaning it would likely fall in an acceptable range for use in NGCs. Future work is necessary to confirm the *in vivo* degradation of the PCLMA material and the degradation timescale for PCLMA with differing DM. Degradation can be carried out *in vitro* under simulated physiological conditions in PBS or with the addition of enzymes such as lipase [129] or cholesterol esterase [233]. For true determination of degradation rates, *in vivo* implantation would be necessary, harvesting the material at various time-points to determine mass loss.

The 2M20 PCLMA was chosen for initial testing of conduit designs as this showed mid-level stiffness and degradation rate. The short gap nerve injury model and short recovery time used in the present study meant that the mechanical and degradation properties of the conduits were not of huge importance. Moving forward to longer gap lengths would mean that the mechanical properties may have more of an influence on recovery due to a greater chance of the conduit being subjected to external bending forces. Longer recovery times would also mean that degradation rate would need to be considered. For future studies, conduits could be used with PCLMA of different DM, depending on the requirements and the results of future degradation studies and mechanical testing.

Another problem not highlighted with short gap was the suturability of the PCLMA conduits. Unfortunately, the PCLMA material is unable to hold sutures, which is not a problem with short distance nerve gaps in mice as the use of fibrin glue was suitable. Suturable conduits are more likely to be accepted into the clinic as they would fit better with current methods used by surgeons. If suturability is a required feature, conduits could be designed with holes in the cuffs to act as anchor points for sutures. These could be directly printed into the structure during μ SL production, making use of the ability to create more complex geometries. Alternatively, other materials could be investigated. In the Claeysens lab, PGS has been methacrylated in a similar way to the PCL in the present study and the resulting PGS-M has shown the ability to hold sutures [129]. Since the PGS-M is biodegradable, has tuneable mechanical properties [233] (with Young's modulus in a similar range to PCLMA) and is structurable by μ SL [129], the work in this thesis could easily be applied to the use of this material.

6.1.2 Porous materials

The PCLMA conduits in this study successfully supported nerve regeneration however the bulk form of PCLMA may not be ideal due to a lack of porosity. Though non-porous conduits can allow the build-up of beneficial neurotrophic factors, essential nutrient diffusion may also be prevented [354]. Porous materials allow for the inward diffusion of nutrients and the outward diffusion of waste products. As a result, many studies have shown more successful regeneration through porous conduits compared to non-porous alternatives [171], [355]–[358]. Materials with too large a pore size, however, may be detrimental as a result of fibroblast invasion and production of excess connective tissue [355] so tight control of porosity (percentage porosity and pore size) is essential.

One way of including porosity in a polymer material is the use of polymerised high internal phase emulsions (polyHIPEs) which have been produced in the Claeysens lab from a variety of polymers. Here a hydrophobic prepolymer (oil phase) is mixed with water and surfactants to create a water-in-oil emulsion, with water droplets dispersed through a continuous phase of prepolymer. The prepolymer phase is then cured and with the removal of the water phase, voids are created in the polymer, resulting in a highly interconnected porous structure [359], [360]. Porosity and pore size can be controlled by varying the parameters used in the preparation of the emulsion. Additionally, the ability to produce polyHIPE structures via μ SL has been demonstrated with production of simple tubes [361]. Recent work has resulted in the production of a PCLMA polyHIPE produced using a PCLMA prepolymer similar to that in the present study [362]. Future work would include the adaptation of this method to produce porous PCLMA conduits with emulsion preparation and structuring with μ SL. This would allow for the *in vivo* assessment of porous PCLMA conduits to compare with the non-porous conduits in the present study.

6.2 The *in vivo* model

6.2.1 Use of thy-1-YFP mice – Analysis methods

The thy-1-YFP mouse nerve injury model was successfully used to assess nerve regeneration through different conduit designs in comparison to autograft controls. The advantages of this model were highlighted in the study of plain vs grooved conduits where a significant difference was found in the measurement of axon disruption, when there were no differences in sprouting index or unique axon number. The ability to trace fluorescent axons allows much more detailed information to be obtained about axon behaviour in different conduit designs (i.e. axon disruption). This allows differences to be found which would be missed by conventional histological methods or functional testing. This was also seen also by Pateman et al. [128] with the use of PEGDA conduits, where axon disruption was lower in the conduits compared to the grafts despite no differences in sprouting index or unique axon number.

Imaging nerve harvests with confocal microscopy rather than fluorescence microscopy led to higher quality images and more reliable axon tracing. However, axon tracing was still a very time-consuming process. Automated tracing methods were investigated as it was thought that this could remove human error and speed up analysis but the resolution of the images was still too low for this to be possible. Alternative imaging systems were trialed such as the Zeiss LSM 880 Airyscan which can produce even higher resolution images than the confocal. The resulting images showed promise for automated tracing but image file sizes were too large to be easily processed. Future work could involve optimising these imaging methods for automated tracing to allow for a much higher throughput of results.

Additionally, it was not possible to obtain high enough quality images of the fibre-filled nerve harvests to carry out axon tracing. This was due to the presence of PCL fibres blocking the light from the confocal microscope. Future work is necessary to determine a post-processing method for the harvested tissue to allow full visualisation of the regenerated axons. Previous studies have treated nerve tissue in DCM to dissolve PLA fibres [171] so this could be explored but the effect on tissue morphology and preservation of YFP fluorescence would need to be considered.

6.2.2 The importance of nerve gap length and recovery time

As discussed in chapter 5, the 3 mm mouse common fibular nerve gap model did not highlight many differences in axon number between conduits containing physical guidance cues (fibre-filled or grooved) and plain conduit controls. The high regenerative capacity of mouse nerves coupled with the short gap and the long three-week recovery time meant that the plain conduits performed equally well compared to the autograft, and so did the grooved and plasma-treated fibre-filled conduits. This meant that it was difficult to use this model to highlight any differences in performance between these conduit designs.

The short gap model however, was useful for preliminary, proof of concept testing and for screening a large number of potential devices. By testing a number of different conduit designs we were able to identify those which would be worth perusing in future work, i.e. a longer gap study. Both the grooved conduits and plasma-treated fibre-filled conduits showed promise compared to plain conduits by respectively decreasing axon disruption and increasing overall success rates.

The decreased axon disruption in the grooved conduits suggested that axons regenerated in a more directional fashion and it would therefore be interesting to carry out the same 3 mm nerve repairs but terminate the recovery at shorter time points (i.e. 1 week and 2 weeks). This would reveal whether regeneration can occur at a faster rate in the grooved conduits due to guidance effects from the grooves, even if differences are absent at a later time point.

Both grooved and fibre-filled conduits should then be tested in longer distance nerve gaps. A critical gap length should be chosen in which poor regeneration occurs in plain conduits. This has been demonstrated in a 6 mm mouse sciatic nerve gap by Gómez et al. where conduits resulted in severely limited axonal regeneration compared to autografts. This was contrast to 4 mm repairs in which conduits and grafts performed comparably [334]. Testing the conduits in longer gap lengths should more easily reveal beneficial effects from the guidance cues in terms of influencing or stabilising the fibrin cable. For nerve gaps of >3 mm, the mouse common fibular nerve could not be used due to its short length but recent work has developed the imaging and axon tracing methods to work with the sciatic nerve in thy-1-YFP mice [331]. For even longer gaps, it may be necessary to move to a larger animal model. The next step would be the use of a rat sciatic or tibial nerve gap. Here gap lengths of around 10-18 mm are commonly used in which poor regeneration often occurs in empty conduits, likely due to the failure of the fibrin cable [92], [134], [154], [171], [172].

6.2.3 Ideas for conduit improvements

Aside from testing the current conduit designs in longer nerve gaps, alternative designs should also be considered to improve the performance seen in the current studies. In chapter 5 it was highlighted that the small spaces between the 10 μm fibres in the fibre-filled conduits may be detrimental to regeneration and that a number of studies use conduit designs with larger inter-fibre spaces [154], [171], [172]. Larger diameter fibres would help with this issue and in chapter 3, fibres were electrospun up to a diameter of 16 μm and inserted into conduits to the same packing density as the 10 μm fibres. Future work could include the testing of these conduits filled with larger fibres but electrospinning parameters could also be altered to further increase fibre diameter. Although the *in vitro* results from chapter 4 suggested that 10 μm diameter fibres were optimal for Schwann cell and neuronal outgrowth, *in vitro* models do not adequately mimic the *in vivo* environment and so optimisation of parameters *in vitro* may not always be possible.

Surface treatment of the conduits was discussed in chapter 5 to improve the biological response from migrating Schwann cells and regenerating axons. Plasma treatment was shown to increase the hydrophilicity of both PCL and PCLMA and improve the regeneration through fibre-filled conduits. Previous studies have also shown that surface treatment to improve the hydrophilicity of grooved conduits can facilitate the beneficial effect of grooves [182]. It would therefore be interesting to test plasma-treated grooved conduits in the current *in vivo* model to determine any beneficial effects.

Alternatively, biological response from regenerating cells can be influenced by incorporation of ECM proteins such as laminin and collagen which can promote the attachment and migration of regenerating cells. A number of studies have successfully utilised collagen/laminin containing fibres for peripheral nerve repair [36], [173], [312]. Specific benefits have also been seen with incorporation of these proteins into polymer fibres which supported improved nerve regeneration compared to plain polymer fibres both *in vitro* and *in vivo* [134], [159], [168]. The PCL fibres produced in the present study could simply be coated with laminin by immersion in a laminin solution [156], which would allow the current scaffold designs to be used with minimal alteration. More complex methods could be explored such as creating PCL-collagen/laminin blends for use in electrospinning [134], [159] or filling the fibre-filled conduits with collagen/laminin-containing gels [339], [343].

Finally, a cellular component may be added to the conduit to facilitate improved regeneration. Since Schwann cells play a vital role in nerve regeneration following injury, they are the main cell type of choice for cell-based therapy. A Schwann cell suspension may be injected directly into the conduit during device implantation or pre-seeded and cultured in the conduit prior to use [133], [363]. Using these techniques, many studies have shown the ability of conduits containing Schwann cells to promote enhanced peripheral nerve regeneration compared to cell-free conduits [103], [303], [304], [363]. Future work could include implanting both grooved and fibre-filled conduits containing or pre-seeded with Schwann cells. The actions of Schwann cells, such as growth factor production and basal lamina secretion would hopefully facilitate the beneficial effects of the physical guidance cues as seen in the study by Rutkowski et al. (where improved regeneration was seen in grooved conduits pre-seeded with Schwann cells, but not in cell-free grooved conduits) [183].

6.2.4 More complex nerve injury models and other applications

In chapter 2, the ability to produce complex 3D PCLMA structures was demonstrated with the use of μ SL. Bifurcated conduits were produced, which would be much more difficult to manufacture using conventional methods such as extrusion or the rolling of films. These bifurcated conduits could be used in more complex *in vivo* models such as the repair of the sciatic nerve where it branches into the common fibular and tibial nerve. Such repair of bifurcated nerves has been demonstrated by Johnson et al [87] and could be replicated with bifurcated conduits produced in this study. Bifurcated conduits could also be produced with a grooved luminal structure. If successful, this would open the door for the use of conduits in the repair of more complex nerve injuries.

Finally, the PCLMA material is not just limited to use in the production of NGCs. The ability to produce any structure 3D with use of μ SL means that scaffolds could be produced in a variety of shapes for different tissue engineering applications. The tuneable mechanical and degradation properties mean that the material could be adapted for use in a wide range of tissues.

7. Final Conclusions

The work in this thesis has explored the manufacture, characterisation and assessment of NGCs containing physical guidance cues. The aim was to produce conduits with the capability to support improved regeneration compared to simple conduit designs. A tuneable, photocurable resin was produced for use in μ SL with a range of possible mechanical and degradation properties. This was used to produce conduits containing physical guidance cues in the form of grooves and, in combination with electrospinning, aligned polymer microfibres. Conduit characterisation allowed control over important parameters thought to influence nerve regeneration, such as fibre diameter and packing density. The effect of plasma treatment was also studied and found to improve the hydrophilicity of the conduit materials. In the repair of 3 mm nerve injuries, both grooved conduits and plasma-treated fibre-filled conduits supported comparable nerve regeneration in comparison to gold standard autograft controls. Grooved conduits showed lower axon disruption compared to autografts (where plain conduits did not) and plasma-treated fibre-filled conduits resulted in higher success rates compared to empty conduits. The results justify the use of these conduits in future work to determine their potential in larger distance nerve gaps.

From the results of this study and comparisons to observations in literature, it seems evident that level of guidance provided to Schwann cells and axons within a NGC is a clear determinant of successful *in vivo* regeneration. The lack of guidance cues within plain/empty conduits is likely a large contributing factor to their low success rates. Guidance may be provided by luminal grooves within a NGC, which may influence the formation of the fibrin cable or directly guide regenerating cells. Additional factors such as surface treatment or Schwann cell pre-seeding may help to facilitate the full beneficial effect of the grooves. The most critical factor for guidance of regenerating cells is the formation of the fibrin cable in the early stages of repair. In cases where the fibrin cable would normally fail, if it can be stabilised or mimicked by internal guidance cues (i.e. fibres), successful regeneration will usually follow. The reliance on the fibrin cable highlights the disadvantages of *in vitro* models, (which cannot adequately simulate fibrin cable formation) and emphasises the importance of appropriate *in vivo* models in which control conduits fail to regenerate successfully.

8. Appendix



Figure 93. Sample size calculation results (from PiFace software) for Study 1 and Study 3, showing the detectable differences in Sprouting index (A), Unique axon tracing (B) and Axon disruption (C). levels[row]=number of intervals (A), levels[col] (A)/levels[treatment] (B, C)=number of repair groups (graft, plain conduit grooved/smooth conduit), n[Within]=sample size, SD[Within]=standard deviation from previous study, # tests=the number of tests performed during Bonferroni multiple comparisons.

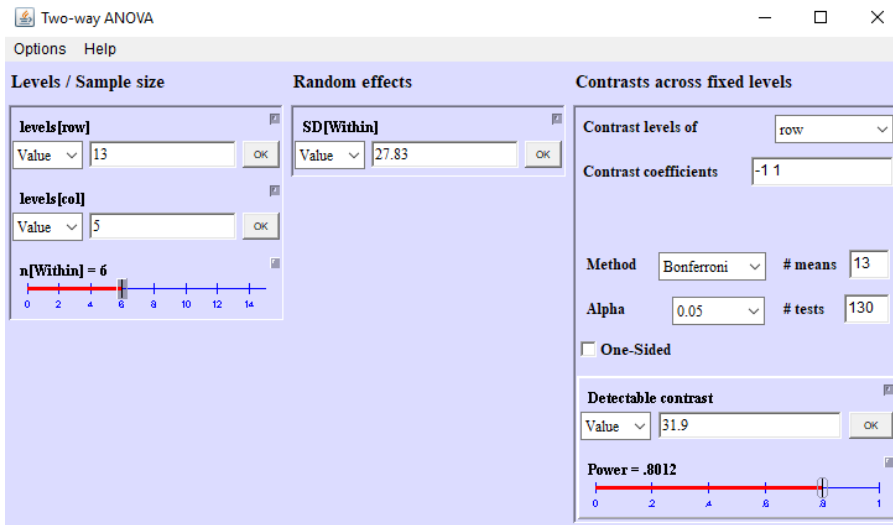


Figure 94. Sample size calculation results (from PiFace software) for Study 2, showing the detectable difference in Sprouting index.

levels[row]=number of intervals, *levels[col]*=number of repair groups (non-treated plain conduit, plasma-treated plain conduit, non-treated fibre-filled conduit, plasma-treated fibre-filled conduit and graft), *n[Within]*=sample size, *SD[Within]*=standard deviation from previous study, # tests=the number of tests performed during Bonferroni multiple comparisons.

9. References

-
- [1] C. A. Heath and G. E. Rutkowski, "The development of bioartificial nerve grafts for peripheral nerve regeneration," *Trends Biotechnol.*, vol. 16, no. 4, pp. 163–168, 1998.
 - [2] D. SHIER, J. BUTLER, and R. LEWIS, *Hole's Human Anatomy & Physiology, Twelfth Edition*. McGraw-Hill, 2010.
 - [3] J. Kiernan and N. Rajakumar, *Barr's The Human Nervous System: An Anatomical Viewpoint*. 2014.
 - [4] G. R. D. Evans, "Peripheral nerve injury: A review and approach to tissue engineered constructs," *Anatomical Record*. 2001.
 - [5] K. Bhatheja and J. Field, "Schwann cells: origins and role in axonal maintenance and regeneration.," *Int. J. Biochem. Cell Biol.*, vol. 38, no. 12, pp. 1995–9, Jan. 2006.
 - [6] S. K. Lee and S. W. Wolfe, "Peripheral nerve injury and repair," *J. Am. Acad. Orthop. Surg.*, vol. 8, no. 4, pp. 243–252, 2000.
 - [7] J. D. Stewart, "Peripheral nerve fascicles: Anatomy and clinical relevance," *Muscle and Nerve*. 2003.
 - [8] D. Grinsell and C. P. Keating, "Peripheral Nerve Reconstruction after Injury: A Review of Clinical and Experimental Therapies," *Biomed Res. Int.*, 2014.
 - [9] M. Asplund, M. Nilsson, A. Jacobsson, and H. Von Holst, "Incidence of traumatic peripheral nerve injuries and amputations in Sweden between 1998 and 2006," *Neuroepidemiology*, vol. 32, no. 3, pp. 217–228, 2009.
 - [10] C. A. Taylor, D. Braza, J. B. Rice, and T. Dillingham, "The incidence of peripheral nerve injury in extremity trauma.," *Am. J. Phys. Med. Rehabil.*, vol. 87, no. 5, pp. 381–385, 2008.
 - [11] G. Ciardelli and V. Chiono, "Materials for peripheral nerve regeneration," *Macromolecular Bioscience*, vol. 6, no. 1. pp. 13–26, 2006.
 - [12] J. A. Kouyoumdjian, "Peripheral nerve injuries: A retrospective survey of 456 cases," *Muscle and Nerve*, vol. 34, no. 6, pp. 785–788, 2006.
 - [13] L. R. Robinson, "Traumatic injury to peripheral nerves," *Muscle Nerve*, vol. 23, no. 6, pp. 863–873, 2000.
 - [14] A. B. Tay, J. B. Lai, K. W. Lye, W. Y. Wong, N. V. Nadkarni, W. Li, and D. Bautista, "Inferior Alveolar Nerve Injury in Trauma-Induced Mandible Fractures," *J Oral Maxillofac Surg*, vol. 73, no. 7, pp. 1328–1340, 2015.
 - [15] B. J. Pfister, T. Gordon, J. R. Loverde, A. S. Kochar, S. E. Mackinnon, and D. K. Cullen, "Biomedical Engineering Strategies for Peripheral Nerve Repair: Surgical Applications, State of the Art, and Future Challenges," *Crit. Rev. Biomed. Eng.*, vol. 39, no. 2, pp. 81–124, 2011.
 - [16] R. J. Sawyer, M. N. Richmond, J. D. Hickey, and J. A. Jarratt, "Peripheral nerve injuries associated with anaesthesia," *Anaesthesia*, vol. 55, no. 10. pp. 980–991, 2000.
 - [17] H. J. Kim and S. H. Park, "Sciatic nerve injection injury," *J. Int. Med. Res.*, vol. 42, no. 4, pp. 887–897, 2014.
 - [18] Q. H. Hogan, "Pathophysiology of peripheral nerve injury during regional anesthesia," *Reg Anesth Pain Med*, vol. 33, no. 5, pp. 435–441, 2008.
 - [19] S. B. Graff-Radford and R. W. Evans, "Lingual nerve injury," *Headache*, vol. 43, no. 9, pp. 975–983, 2003.
 - [20] H. J. Seddon, "A Classification of Nerve Injuries," *Br. Med. J.*, vol. 2, no. 4260, pp. 237–239, 1942.
 - [21] R. Birch, *Surgical Disorders of the Peripheral Nerves*. Springer Science & Business Media, 2011.
 - [22] F. Biglioli, F. Allevi, and A. Lozza, "Surgical treatment of painful lesions of the inferior alveolar nerve," *J Craniomaxillofac Surg*, vol. 43, no. 8, pp. 1541–1545, 2015.
 - [23] A. A. Alhassani and A. S. T. AlGhamdi, "Inferior alveolar nerve injury in implant dentistry: diagnosis, causes, prevention, and management.," *J. Oral Implantol.*, vol. 36, no. 5, pp. 401–7,

- Jan. 2010.
- [24] A. B. G. Tay and J. R. Zuniga, "Clinical characteristics of trigeminal nerve injury referrals to a university centre.," *Int. J. Oral Maxillofac. Surg.*, vol. 36, no. 10, pp. 922–7, Oct. 2007.
- [25] G. Juodzbaly, H. L. Wang, G. Sabalys, A. Sidlauskas, and P. Galindo-Moreno, "Inferior alveolar nerve injury associated with implant surgery," *Clin Oral Implant. Res*, vol. 24, no. 2, pp. 183–190, 2013.
- [26] M. Abarca, D. van Steenberghe, C. Malevez, J. De Ridder, and R. Jacobs, "Neurosensory disturbances after immediate loading of implants in the anterior mandible: An initial questionnaire approach followed by a psychophysical assessment," *Clin. Oral Investig.*, vol. 10, no. 4, pp. 269–277, 2006.
- [27] E. Valmaseda-Castellon, L. Berini-Aytes, and C. Gay-Escoda, "Inferior alveolar nerve damage after lower third molar surgical extraction: a prospective study of 1117 surgical extractions," *Oral Surg Oral Med Oral Pathol Oral Radiol Endod*, vol. 92, no. 4, pp. 377–383, 2001.
- [28] a B. Bataineh, "Sensory nerve impairment following mandibular third molar surgery.," *J. Oral Maxillofac. Surg.*, vol. 59, no. 9, p. 1012–1017; discussion 1017, 2001.
- [29] W. Jerjes, B. Swinson, D. R. Moles, M. El-Maaytah, B. Banu, T. Upile, M. Kumar, M. Al Khawalde, M. Vourvachis, H. Hadi, S. Kumar, and C. Hopper, "Permanent sensory nerve impairment following third molar surgery: a prospective study.," *Oral Surg. Oral Med. Oral Pathol. Oral Radiol. Endod.*, vol. 102, no. 4, pp. e1–e7, 2006.
- [30] D. Gülicher and K. L. Gerlach, "Sensory impairment of the lingual and inferior alveolar nerves following removal of impacted mandibular third molars.," *Int. J. Oral Maxillofac. Surg.*, vol. 30, no. 4, pp. 306–312, 2001.
- [31] V. Lopes, R. Mumanya, C. Feinmann, and M. Harris, "Third molar surgery: an audit of the indications for surgery, post-operative complaints and patient satisfaction," *Br. J. Oral Maxillofac. Surg.*, vol. 33, no. 1, pp. 33–35, Feb. 1995.
- [32] R. B. Donoff, "Raising lingual flaps increases the risk of nerve damage," *Evid. Based. Dent.*, vol. 1, no. 1, pp. 14–14, Nov. 1998.
- [33] "Clinically important ramifications of the 3rd division of trigeminal nerve." [Online]. Available: https://www2.aofoundation.org/wps/portal/!ut/p/a1/04_Sj9CPykssy0xPLMnMz0vMAfGjzOKN_A0M3D2DDbz9_UMMDRyDXQ3dw9wMDAx8jYEKlvEocDQnTr8BDuBoQEh_QW5oKABbd3c9/dI5/d5/L2dJQSEvUUt3QS80SmfL1o2XzJPMDbHSVMws09PVDEwQVNFmUdWRjAwME0z/?ActiveNumber=1&StepPos=41&contentUr. [Accessed: 20-Sep-2008].
- [34] B. Alberts, A. Johnson, J. Lewis, M. Raff, K. Roberts, and P. Walter, *Molecular Biology of the Cell*. 2002.
- [35] L. R. Williams, F. M. Longo, H. C. Powell, G. Lundborg, and S. Varon, "Spatial-temporal progress of peripheral nerve regeneration within a silicone chamber: parameters for a bioassay.," *J. Comp. Neurol.*, vol. 218, no. 4, pp. 460–470, 1983.
- [36] K. Matsumoto, K. Ohnishi, T. Kiyotani, T. Sekine, H. Ueda, T. Nakamura, K. Endo, and Y. Shimizu, "Peripheral nerve regeneration across an 80-mm gap bridged by a polyglycolic acid (PGA)-collagen tube filled with laminin-coated collagen fibers: a histological and electrophysiological evaluation of regenerated nerves," *Brain Res.*, vol. 868, no. 2, pp. 315–328, 2000.
- [37] H. Taskinen and M. Roytta, "The dynamics of macrophage recruitment after nerve transection," *ACTA Neuropathol.*, vol. 93, no. 3, pp. 252–259, Mar. 1997.
- [38] P. S. Spencer, H. J. Weinberg, V. Krygier-Brévar, and V. Zabrenetzky, "An in vivo method to prepare normal Schwann cells free of axons and myelin," *Brain Res.*, vol. 165, no. 1, pp. 119–126, Apr. 1979.
- [39] S. Ichihara, Y. Inada, and T. Nakamura, "Artificial nerve tubes and their application for repair of peripheral nerve injury: an update of current concepts," *Inj. Int. J. Care Inj.*, vol. 39, no. 4, pp. 29–39, 2008.
- [40] W. C. Ngeow, "Scar less: a review of methods of scar reduction at sites of peripheral nerve

- repair," *Oral Surg. Oral Med. Oral Pathol. Oral Radiol. Endodontology*, vol. 109, no. 3, pp. 357–366, 2010.
- [41] K. Torigoe, H. F. Tanaka, A. Takahashi, A. Awaya, and K. Hashimoto, "Basic behavior of migratory Schwann cells in peripheral nerve regeneration," *Exp. Neurol.*, vol. 137, no. 2, pp. 301–308, 1996.
- [42] V. T. Ribeiro-Resende, B. Koenig, S. Nichterwitz, S. Oberhoffner, and B. Schlosshauer, "Strategies for inducing the formation of bands of Bungner in peripheral nerve regeneration," *Biomaterials*, vol. 30, no. 29, pp. 5251–5259, 2009.
- [43] W. Wood and P. Martin, "Structures in focus - Filopodia," *International Journal of Biochemistry and Cell Biology*. 2002.
- [44] R. Deumens, A. Bozkurt, M. F. Meek, M. A. E. Marcus, E. A. J. Joosten, J. Weis, and G. A. Brook, "Repairing injured peripheral nerves: Bridging the gap," *Prog. Neurobiol.*, vol. 92, no. 3, pp. 245–276, 2010.
- [45] M. Meyer, I. Matsuoka, C. Wetmore, L. Olson, and H. Thoenen, "Enhanced synthesis of brain-derived neurotrophic factor in the lesioned peripheral nerve: Different mechanisms are responsible for the regulation of BDNF and NGF mRNA," *J. Cell Biol.*, vol. 119, no. 1, pp. 45–54, 1992.
- [46] H. Hammarberg, F. Piehl, S. Cullheim, J. Fjell, T. Hökfelt, and K. Fried, "GDNF mRNA in Schwann cells and DRG satellite cells after chronic sciatic nerve injury," *Neuroreport*, vol. 7, no. 4, pp. 857–860, Mar. 1996.
- [47] C. Henderson, H. Phillips, R. Pollock, A. Davies, C. Lemeulle, M. Armanini, L. Simmons, B. Moffet, R. Vandlen, L. Simpson LC [corrected to Simmons, and al. et, "GDNF: a potent survival factor for motoneurons present in peripheral nerve and muscle," *Science (80-.)*, vol. 266, no. 5187, pp. 1062–1064, Nov. 1994.
- [48] C. R. Matheson, J. Carnahan, J. L. Urich, D. Bocangel, T. J. Zhang, and Q. Yan, "Glial cell line-derived neurotrophic factor (GDNF) is a neurotrophic factor for sensory neurons: Comparison with the effects of the neurotrophins," *J. Neurobiol.*, vol. 32, no. 1, pp. 22–32, Jan. 1997.
- [49] J.-Y. Zhang, X.-G. Luo, C. J. Xian, Z.-H. Liu, and X.-F. Zhou, "Endogenous BDNF is required for myelination and regeneration of injured sciatic nerve in rodents," *Eur. J. Neurosci.*, vol. 12, no. 12, pp. 4171–4180, Dec. 2000.
- [50] P. J. Kingham and G. Terenghi, "Bioengineered nerve regeneration and muscle reinnervation," *J. Anat.*, vol. 209, no. 4, pp. 511–526, 2006.
- [51] T. Iwase, C. G. Jung, H. Bae, M. Zhang, and B. Soliven, "Glial cell line-derived neurotrophic factor-induced signaling in Schwann cells," *J. Neurochem.*, vol. 94, no. 6, pp. 1488–1499, Sep. 2005.
- [52] S. Atkins, K. G. Smith, A. R. Loescher, F. M. Boissonade, S. O’Kane, M. W. J. Ferguson, and P. P. Robinson, "Scarring impedes regeneration at sites of peripheral nerve repair.," *Neuroreport*, vol. 17, no. 12, pp. 1245–9, Aug. 2006.
- [53] W. C. Ngeow, S. Atkins, C. R. Morgan, A. D. Metcalfe, F. M. Boissonade, A. R. Loescher, and P. P. Robinson, "A Comparison between the Effects of Three Potential Scar-Reducing Agents Applied at a Site of Sciatic Nerve Repair," *Neuroscience*, vol. 181, pp. 271–277, 2011.
- [54] A. Pabari, S. Y. Yang, A. M. Seifalian, and A. Mosahebi, "Modern surgical management of peripheral nerve gap," *J. Plast. Reconstr. Aesthetic Surg.*, vol. 63, no. 12, pp. 1941–1948, 2010.
- [55] M. Artico, L. Cervoni, F. Nucci, and R. Giuffrè, "Birthday of peripheral nervous system surgery: The contribution of Gabriele Ferrara (1543-1627)," *Neurosurgery*, vol. 39, no. 2, pp. 380–382, 1996.
- [56] H. Millesi, "Microsurgery of peripheral nerves.," *Hand*, vol. 5, no. 2, pp. 157–160, 1973.
- [57] G. Lundborg, "A 25-year perspective of peripheral nerve surgery: Evolving neuroscientific concepts and clinical significance," *Journal of Hand Surgery*, vol. 25, no. 3. pp. 391–414, 2000.
- [58] E. O. Johnson and P. N. Soucacos, "Nerve repair: Experimental and clinical evaluation of

- biodegradable artificial nerve guides," *Inj. J. Care Inj.*, vol. 39, pp. S30–S36, 2008.
- [59] R. A. Weber, W. C. Breidenbach, R. E. Brown, M. E. Jabaley, and D. P. Mass, "A randomized prospective study of polyglycolic acid conduits for digital nerve reconstruction in humans," *Plast Reconstr Surg*, vol. 106, no. 5, pp. 1036–1038, 2000.
- [60] G. Ciardelli and V. Chiono, "Materials for peripheral nerve regeneration," *Macromol. Biosci.*, vol. 6, no. 1, pp. 13–26, 2006.
- [61] S. Kehoe, X. F. Zhang, and D. Boyd, "FDA approved guidance conduits and wraps for peripheral nerve injury: A review of materials and efficacy," *Inj. J. Care Inj.*, vol. 43, no. 5, pp. 553–572, 2012.
- [62] V. Matejčík, "Peripheral nerve reconstruction by autograft," *Injury*, vol. 33, no. 7, pp. 627–631, 2002.
- [63] W. Z. Ray and S. E. Mackinnon, "Management of nerve gaps: Autografts, allografts, nerve transfers, and end-to-side neurotomy," *Exp. Neurol.*, vol. 223, no. 1, pp. 77–85, 2010.
- [64] K. G. Smith and P. P. Robinson, "The effect of delayed nerve repair on the properties of regenerated fibres in the chorda tympani," *Brain Res.*, 1995.
- [65] P. P. Robinson and K. G. Smith, "A study on the efficacy of late lingual nerve repair," *Br. J. Oral Maxillofac. Surg.*, 1996.
- [66] S. E. Mackinnon, "Nerve allotransplantation following severe tibial nerve injury. Case report," *J. Neurosurg.*, vol. 84, no. 4, pp. 671–6, Apr. 1996.
- [67] S. E. Mackinnon, V. B. Doolabh, C. B. Novak, and E. P. Trulock, "Clinical Outcome following Nerve Allograft Transplantation," *Plast. Reconstr. Surg.*, vol. 107, no. 6, pp. 1419–1429, May 2001.
- [68] D. N. Brooks, R. V. Weber, J. D. Chao, B. D. Rinker, J. Zoldos, M. R. Robichaux, S. B. Ruggeri, K. A. Anderson, E. E. Bonatz, S. M. Wisotsky, M. S. Cho, C. Wilson, E. O. Cooper, J. V. Ingari, B. Safa, B. M. Parrett, and G. M. Buncke, "Processed nerve allografts for peripheral nerve reconstruction: A multicenter study of utilization and outcomes in sensory, mixed, and motor nerve reconstructions," *Microsurgery*, vol. 32, no. 1, pp. 1–14, Jan. 2012.
- [69] A. M. Moore, M. MacEwan, K. B. Santosa, K. E. Chenard, W. Z. Ray, D. A. Hunter, S. E. Mackinnon, and P. J. Johnson, "Acellular nerve allografts in peripheral nerve regeneration: A comparative study," *Muscle and Nerve*, 2011.
- [70] M. A. Pogrel and A. Maghen, "The use of autogenous vein grafts for inferior alveolar and lingual nerve reconstruction," *J. Oral Maxillofac. Surg.*, vol. 59, no. 9, pp. 985–8; discussion 988–93, Sep. 2001.
- [71] R. H. B. Jones, "Repair of the trigeminal nerve: A review," *Aust. Dent. J.*, vol. 55, no. 2, pp. 112–119, 2010.
- [72] A. C. J. Ruijs, J.-B. Jaquet, S. Kalmijn, H. Giele, and S. E. R. Hovius, "Median and ulnar nerve injuries: a meta-analysis of predictors of motor and sensory recovery after modern microsurgical nerve repair," *Plast. Reconstr. Surg.*, vol. 116, pp. 484–494; discussion 495–496, 2005.
- [73] F. J. Paprottka, P. Wolf, Y. Harder, Y. Kern, P. M. Paprottka, H.-G. Machens, and J. a Lohmeyer, "Sensory recovery outcome after digital nerve repair in relation to different reconstructive techniques: meta-analysis and systematic review," *Plast. Surg. Int.*, vol. 2013, p. 704589, 2013.
- [74] M. A. Woodruff and D. W. Hutmacher, "The return of a forgotten polymer - Polycaprolactone in the 21st century," *Prog. Polym. Sci.*, vol. 35, no. 10, pp. 1217–1256, 2010.
- [75] J. M. Anderson, "BIOLOGICAL RESPONSES TO MATERIALS," *Annu. Rev. Mater. Res.*, vol. 31, no. 1, pp. 81–110, Aug. 2001.
- [76] M. J. O. E. Bertleff, M. F. Meek, and J.-P. A. Nicolai, "A prospective clinical evaluation of biodegradable neurolac nerve guides for sensory nerve repair in the hand," *J. Hand Surg. Am.*, vol. 30, no. 3, pp. 513–8, May 2005.
- [77] M. S. Taylor, A. U. Daniels, K. P. Andriano, and J. Heller, "Six bioabsorbable polymers: In vitro

- acute toxicity of accumulated degradation products," *J. Appl. Biomater.*, 1994.
- [78] N. Bhattarai, Z. Li, J. Gunn, M. Leung, A. Cooper, D. Edmondson, O. Veiseh, M.-H. Chen, Y. Zhang, R. G. Ellenbogen, and M. Zhang, "Natural-Synthetic Polyblend Nanofibers for Biomedical Applications," *Adv. Mater.*, vol. 21, no. 27, pp. 2792–2797, Jul. 2009.
- [79] M. R. Ahmed, U. Venkateshwarlu, and R. Jayakumar, "Multilayered peptide incorporated collagen tubules for peripheral nerve repair," *Biomaterials*, 2004.
- [80] M. S. Widmer, P. K. Gupta, L. Lu, R. K. Meszlenyi, G. R. D. Evans, K. Brandt, T. Savel, A. Gurlek, C. W. Patrick, A. G. Mikos, and W. P. J. Charles, "Manufacture of porous biodegradable polymer conduits by an extrusion process for guided tissue regeneration," *Biomaterials*, vol. 19, no. 21, pp. 1945–1955, 1998.
- [81] D. Shahriari, M. Shibayama, D. A. Lynam, K. J. Wolf, G. Kubota, J. Y. Koffler, M. H. Tuszynski, W. M. Campana, and J. S. Sakamoto, "Peripheral nerve growth within a hydrogel microchannel scaffold supported by a kink-resistant conduit," *J. Biomed. Mater. Res. - Part A*, 2017.
- [82] M. P. Prabhakaran, J. R. Venugopal, T. Ter Chyan, L. B. Hai, C. K. Chan, A. Y. Lim, and S. Ramakrishna, "Electrospun biocomposite nanofibrous scaffolds for neural tissue engineering," *Tissue Eng Part A*, vol. 14, no. 11, pp. 1787–1797, 2008.
- [83] G. H. Borschel, K. F. Kia, W. M. Kuzon, and R. G. Dennis, "Mechanical properties of acellular peripheral nerve," *J. Surg. Res.*, 2003.
- [84] L. Zilic, S. P. Wilshaw, and J. W. Haycock, "Decellularisation and histological characterisation of porcine peripheral nerves," *Biotechnol. Bioeng.*, 2016.
- [85] L. E. Kokai, Y.-C. Lin, N. M. Oyster, and K. G. Marra, "Diffusion of soluble factors through degradable polymer nerve guides: Controlling manufacturing parameters," *Acta Biomater.*, vol. 5, no. 7, pp. 2540–2550, 2009.
- [86] P. Aebischer, V. Guénard, and S. Brace, "Peripheral nerve regeneration through blind-ended semipermeable guidance channels: effect of the molecular weight cutoff," *J. Neurosci.*, vol. 9, no. 10, pp. 3590–3595, 1989.
- [87] B. N. Johnson, K. Z. Lancaster, G. Zhen, J. He, M. K. Gupta, Y. L. Kong, E. A. Engel, K. D. Krick, A. Ju, F. Meng, L. W. Enquist, X. Jia, and M. C. McAlpine, "3D Printed Anatomical Nerve Regeneration Pathways," *Adv. Funct. Mater.*, vol. 25, no. 39, p. n/a-n/a, Sep. 2015.
- [88] A. Mosahebi, P. Fuller, M. Wiberg, and G. Terenghi, "Effect of allogeneic Schwann cell transplantation on peripheral nerve regeneration," *Exp. Neurol.*, vol. 173, no. 2, pp. 213–223, 2002.
- [89] F. M. Longo, S. D. Skaper, M. Manthorpe, L. R. Williams, G. Lundborg, and S. Varon, "Temporal changes of neuronotrophic activities accumulating in vivo within nerve regeneration chambers," *Exp. Neurol.*, vol. 81, no. 3, pp. 756–69, 1983.
- [90] F. M. Longo, M. Manthorpe, S. D. Skaper, G. Lundborg, and S. Varon, "Neuronotrophic activities accumulate in vivo within silicone nerve regeneration chambers," *Brain Res.*, vol. 261, no. 1, pp. 109–16, 1983.
- [91] B. A. Yankner and E. M. Shooter, "The biology and mechanism of action of nerve growth factor," *Annu. Rev. Biochem.*, vol. 51, pp. 845–68, Jan. 1982.
- [92] G. Lundborg, L. B. Dahlin, N. Danielsen, R. H. Gelberman, F. M. Longo, H. C. Powell, and S. Varon, "Nerve regeneration in silicone chambers: Influence of gap length and of distal stump components," *Exp. Neurol.*, 1982.
- [93] W. Daly, L. Yao, D. Zeugolis, A. Windebank, and A. Pandit, "A biomaterials approach to peripheral nerve regeneration: bridging the peripheral nerve gap and enhancing functional recovery," *J R Soc Interface*, vol. 9, no. 67, pp. 202–221, 2012.
- [94] B. Schloschauer, L. Dreesmann, H. E. Schaller, and N. Sinis, "Synthetic nerve guide implants in humans: A comprehensive survey," *Neurosurgery*, vol. 59, no. 4, pp. 740–747, 2006.
- [95] J. S. Taras, S. M. Jacoby, and C. J. Lincoski, "Reconstruction of Digital Nerves With Collagen Conduits," *YJHSU*, vol. 36, no. 9, pp. 1441–1446, 2011.

- [96] K. J. Wangenstein and L. K. Kalliainen, "Collagen tube conduits in peripheral nerve repair: a retrospective analysis.," *Hand (N. Y.)*, vol. 5, no. 3, pp. 273–7, 2009.
- [97] G. S. Munding, R. B. Prucz, S. M. Rozen, and A. P. Tufaro, "Reconstruction of the inferior alveolar nerve with bioabsorbable polyglycolic acid nerve conduits.," *Plast. Reconstr. Surg.*, vol. 129, no. 1, p. 110e–117e, Jan. 2012.
- [98] N. Donoghoe, G. D. Rosson, and A. L. Dellon, "Reconstruction of the human median nerve in the forearm with the Neurotube.," *Microsurgery*, vol. 27, no. 7, pp. 595–600, Jan. 2007.
- [99] M. Navissano, F. Malan, R. Carnino, and B. Battiston, "Neurotube for facial nerve repair.," *Microsurgery*, vol. 25, no. 4, pp. 268–71, Jan. 2005.
- [100] G. D. Rosson, E. H. Williams, and A. L. Dellon, "Motor Nerve Regeneration across a Conduit," *Microsurgery*, vol. 29, no. 2, pp. 107–114, 2009.
- [101] B. D. Bushnell, A. D. McWilliams, G. B. Whitener, and T. M. Messer, "Early clinical experience with collagen nerve tubes in digital nerve repair.," *J. Hand Surg. Am.*, vol. 33, no. 7, pp. 1081–7, 2008.
- [102] V. Chiono, G. Vozzi, F. Vozzi, C. Salvadori, F. Dini, F. Carlucci, M. Arispici, S. Burchielli, F. Di Scipio, S. Geuna, M. Fornaro, P. Tos, S. Nicolino, C. Audisio, I. Perroteau, A. Chiaravalloti, C. Domenici, P. Giusti, and G. Ciardelli, "Melt-extruded guides for peripheral nerve regeneration. Part I: Poly(ϵ -caprolactone)," *Biomed. Microdevices*, vol. 11, no. 5, pp. 1037–1050, 2009.
- [103] Q. Ao, C. K. Fung, A. Yat-Ping Tsui, S. Cai, H. C. Zuo, Y. S. Chan, and D. Kwok-Yan Shum, "The regeneration of transected sciatic nerves of adult rats using chitosan nerve conduits seeded with bone marrow stromal cell-derived Schwann cells," *Biomaterials*, 2011.
- [104] C. Sundback, T. Hadlock, M. Cheney, and J. Vacanti, "Manufacture of porous polymer nerve conduits by a novel low-pressure injection molding process," *Biomaterials*, vol. 24, no. 5, pp. 819–830, 2003.
- [105] S. Y. Chew, R. F. Mi, A. Hoke, and K. W. Leong, "Aligned protein-polymer composite fibers enhance nerve regeneration: A potential tissue-engineering platform," *Adv. Funct. Mater.*, vol. 17, no. 8, pp. 1288–1296, 2007.
- [106] S.-H. Hsu, P. S. Lu, H.-C. Ni, and C.-H. Su, "Fabrication and evaluation of microgrooved polymers as peripheral nerve conduits," *Biomed. Microdevices*, vol. 9, no. 5, pp. 665–674, 2007.
- [107] S. Ichihara, Y. Inada, A. Nakada, K. Endo, T. Azuma, R. Nakai, S. Tsutsumi, H. Kurosawa, and T. Nakamura, "Development of new nerve guide tube for repair of long nerve defects.," *Tissue Eng. Part C. Methods*, 2009.
- [108] A. Wang, Q. Ao, W. Cao, C. Zhao, Y. Gong, N. Zhao, and X. Zhang, "Fiber-based chitosan tubular scaffolds for soft tissue engineering: Fabrication and in vitro evaluation," *Tsinghua Sci. Technol.*, 2005.
- [109] Synovis, "Neurotube - The Proven Choice in Nerve Conduits," 2010. [Online]. Available: http://www.synovismicro.com/pdfs/NeuroTube_sellsheet_40014B_09-10.pdf.
- [110] J. Giannatsis and V. Dedoussis, "Additive fabrication technologies applied to medicine and health care: a review," *Int. J. Adv. Manuf. Technol.*, vol. 40, no. 1–2, pp. 116–127, Dec. 2007.
- [111] Y. Pan, C. Zhou, and Y. Chen, "A Fast Mask Projection Stereolithography Process for Fabricating Digital Models in Minutes," *J. Manuf. Sci. Eng. Asme*, vol. 134, no. 5, 2012.
- [112] S. Singare, L. Dichen, L. Bingheng, L. Yanpu, G. Zhenyu, and L. Yaxiong, "Design and fabrication of custom mandible titanium tray based on rapid prototyping," *Med. Eng. Phys.*, vol. 26, no. 8, pp. 671–676, 2004.
- [113] M. Truscott, D. de Beer, G. Vicatos, K. Hosking, L. Barnard, G. Booyesen, and R. I. Campbell, "Using RP to promote collaborative design of customised medical implants," *RAPID Prototyp. J.*, vol. 13, no. 2, pp. 107–114, 2007.
- [114] J. S. Bill, J. F. Reuther, W. Dittmann, N. Kübler, J. L. Meier, H. Pistner, and G. Wittenberg, "Stereolithography in oral and maxillofacial operation planning," *Int. J. Oral Maxillofac. Surg.*,

- vol. 24, no. 1, pp. 98–103, Feb. 1995.
- [115] “Apparatus for production of three-dimensional objects by stereolithography,” 11-Mar-1986.
- [116] “Methods and apparatus for production of three-dimensional objects by stereolithography,” 12-Mar-1991.
- [117] “Method of making a three dimensional object by stereolithography.” 14-Jul-1992.
- [118] K. Ikuta and K. Kirowatari, “Real three dimensional micro fabrication using stereo lithography and metal molding,” *Proceedings of 6th IEEE Workshop on Micro Electro Mechanical Systems (MEMS’93)*. New York, p. 42–47., 1993.
- [119] J.-W. Choi, R. Wicker, S.-H. Lee, K.-H. Choi, C.-S. Ha, and I. Chung, “Fabrication of 3D biocompatible/biodegradable micro-scaffolds using dynamic mask projection microstereolithography,” *J. Mater. Process. Technol.*, vol. 209, no. 15–16, pp. 5494–5503, 2009.
- [120] A. Bertsch, J. Y. Yezequel, and J. C. Andre, “Study of the spatial resolution of a new 3D microfabrication process: the microstereophotolithography using a dynamic mask-generator technique,” *J. Photochem. Photobiol. a-Chemistry*, vol. 107, no. 1–3, pp. 275–281, 1997.
- [121] J. W. Choi, Y. M. Ha, S. H. Lee, and K. H. Choi, “Design of microstereolithography system based on dynamic image projection for fabrication of three-dimensional microstructures,” *J. Mech. Sci. Technol.*, vol. 20, no. 12, pp. 2094–2104, 2006.
- [122] Texas-Instruments, “DMD 101: Introduction to Digital Micromirror Device (DMD) Technology,” 2013. [Online]. Available: <http://www.ti.com/lit/an/dlpa008a/dlpa008a.pdf>. [Accessed: 21-Dec-2015].
- [123] Texas-Instruments, “DLP® 0.7 XGA 2xLVDS Type A DMD.” 2013.
- [124] K. Arcaute, B. K. Mann, and R. B. Wicker, “Fabrication of Off-the-Shelf Multilumen Poly(Ethylene Glycol) Nerve Guidance Conduits Using Stereolithography,” *Tissue Eng. Part C- Methods*, vol. 17, no. 1, pp. 27–38, 2011.
- [125] K. Arcaute, L. Ochoa, B. K. Mann, and R. B. Wicker, “Stereolithography of PEG hydrogel multi-lumen nerve regeneration conduits,” *Manuf. Eng. Mater. Handl. 2005 Pts A B*, vol. 16, pp. 161–167, 2005.
- [126] M. S. Evangelista, M. Perez, A. A. Salibian, J. M. Hassan, S. Darcy, K. Z. Paydar, R. B. Wicker, K. Arcaute, B. K. Mann, and G. R. D. Evans, “Single-lumen and multi-lumen poly(ethylene glycol) nerve conduits fabricated by stereolithography for peripheral nerve regeneration in vivo,” *J. Reconstr. Microsurg.*, vol. 31, no. 5, pp. 327–335, 2015.
- [127] C. Sun, N. Fang, D. M. Wu, and X. Zhang, “Projection micro-stereolithography using digital micro-mirror dynamic mask,” *Sensors and Actuators a-Physical*, vol. 121, no. 1, pp. 113–120, 2005.
- [128] C. J. Pateman, A. J. Harding, A. Glen, C. S. Taylor, C. R. Christmas, P. P. Robinson, S. Rimmer, F. M. Boissonade, F. Claeysens, and J. W. Haycock, “Nerve guides manufactured from photocurable polymers to aid peripheral nerve repair,” *Biomaterials*, vol. 49, pp. 77–89, 2015.
- [129] D. Singh, A. J. Harding, E. Albadawi, F. M. Boissonade, J. W. Haycock, and F. Claeysens, “Additive manufactured biodegradable poly(glycerol sebacate methacrylate) nerve guidance conduits,” *Acta Biomater.*, 2018.
- [130] A. C. Lee, V. M. Yu, J. B. Lowe, M. J. Brenner, D. A. Hunter, S. E. Mackinnon, and S. E. Sakiyama-Elbert, “Controlled release of nerve growth factor enhances sciatic nerve regeneration,” *Exp. Neurol.*, vol. 184, no. 1, pp. 295–303, Nov. 2003.
- [131] H. Liu, W. Wen, M. Hu, W. Bi, L. Chen, S. Liu, P. Chen, and X. Tan, “Chitosan conduits combined with nerve growth factor microspheres repair facial nerve defects,” *Neural Regen. Res.*, vol. 8, no. 33, pp. 3139–47, Nov. 2013.
- [132] H. S. Koh, T. Yong, C. K. Chan, and S. Ramakrishna, “Enhancement of neurite outgrowth using nano-structured scaffolds coupled with laminin,” *Biomaterials*, 2008.
- [133] T. Hadlock, C. Sundback, D. Hunter, M. Cheney, and J. P. Vacanti, “A Polymer Foam Conduit

- Seeded with Schwann Cells Promotes Guided Peripheral Nerve Regeneration," *Tissue Eng.*, vol. 6, no. 2, pp. 119–127, Apr. 2000.
- [134] R. A. Neal, S. S. Tholpady, P. L. Foley, N. Swami, R. C. Ogle, and E. A. Botchwey, "Alignment and composition of laminin-polycaprolactone nanofiber blends enhance peripheral nerve regeneration," *J. Biomed. Mater. Res. - Part A*, 2012.
- [135] Z. Ahmed, S. Underwood, and R. A. Brown, "Nerve Guide Material Made from Fibronectin: Assessment of *in Vitro* Properties," *Tissue Eng.*, vol. 9, no. 2, pp. 219–231, Apr. 2003.
- [136] Z. Zhang, M. Rouabhia, Z. Wang, C. Roberge, G. Shi, P. Roche, J. Li, and L. H. Dao, "Electrically conductive biodegradable polymer composite for nerve regeneration: Electricity-stimulated neurite outgrowth and axon regeneration," *Artif. Organs*, 2007.
- [137] X. Liu, A. L. Miller, S. Park, B. E. Waletzki, Z. Zhou, A. Terzic, and L. Lu, "Functionalized Carbon Nanotube and Graphene Oxide Embedded Electrically Conductive Hydrogel Synergistically Stimulates Nerve Cell Differentiation," *ACS Appl. Mater. Interfaces*, 2017.
- [138] P. Weiss, "Experiments on cell and axon orientation *in vitro*: The role of colloidal exudates in tissue organization," *J. Exp. Zool.*, vol. 100, no. 3, pp. 353–386, 1945.
- [139] R. G. Harrison, "The reaction of embryonic cells to solid structures," *J. Exp. Zool.*, vol. 17, no. 4, pp. 521–544, 1914.
- [140] P. Weiss, "In vitro experiments on the factors determining the course of the outgrowing nerve fiber," *J. Exp. Zool.*, vol. 68, no. 3, pp. 393–448, 1934.
- [141] S. Liu, X. Sun, T. Wang, S. Chen, C. Zeng, G. Xie, Q. Zhu, X. Liu, and D. Quan, "Nano-fibrous and ladder-like multi-channel nerve conduits: Degradation and modification by gelatin," *Mater. Sci. Eng. C*, vol. 83, pp. 130–142, Feb. 2018.
- [142] L. Yao, G. C. W. de Ruiter, H. Wang, A. M. Knight, R. J. Spinner, M. J. Yaszemski, A. J. Windebank, and A. Pandit, "Controlling dispersion of axonal regeneration using a multichannel collagen nerve conduit," *Biomaterials*, 2010.
- [143] A. Bozkurt, G. a Brook, S. Moellers, F. Lassner, B. Sellhaus, J. Weis, M. Woeltje, J. Tank, C. Beckmann, P. Fuchs, L. O. Damink, F. Schügner, I. Heschel, and N. Pallua, "In vitro assessment of axonal growth using dorsal root ganglia explants in a novel three-dimensional collagen matrix," *Tissue Eng.*, 2007.
- [144] A. Bozkurt, F. Lassner, D. O'Dey, R. Deumens, A. Böcker, T. Schwendt, C. Janzen, C. V. Suschek, R. Tolba, E. Kobayashi, B. Sellhaus, S. Tholl, L. Eummelen, F. Schügner, L. Olde Damink, J. Weis, G. A. Brook, and N. Pallua, "The role of microstructured and interconnected pore channels in a collagen-based nerve guide on axonal regeneration in peripheral nerves," *Biomaterials*, 2012.
- [145] L. Huang, L. Zhu, X. Shi, B. Xia, Z. Liu, S. Zhu, Y. Yang, T. Ma, P. Cheng, K. Luo, J. Huang, and Z. Luo, "A compound scaffold with uniform longitudinally oriented guidance cues and a porous sheath promotes peripheral nerve regeneration *in vivo*," *Acta Biomaterialia*, 2017.
- [146] W. Liu, S. Thomopoulos, and Y. Xia, "Electrospun nanofibers for regenerative medicine.," *Adv. Healthc. Mater.*, vol. 1, no. 1, pp. 10–25, Jan. 2012.
- [147] J. Cooley, "Improved methods of and apparatus for electrically separating the relatively volatile liquid component from the component of relatively fixed substances of composite," *Pat. GB*, 1900.
- [148] D. H. Reneker and I. Chun, "Nanometre diameter fibres of polymer, produced by electrospinning," *Nanotechnology*, vol. 7, no. 3, pp. 216–223, 1996.
- [149] Q. P. Pham, U. Sharma, and A. G. Mikos, "Electrospinning of polymeric nanofibers for tissue engineering applications: a review.," *Tissue Eng.*, vol. 12, no. 5, pp. 1197–211, 2006.
- [150] H. B. Wang, M. E. Mullins, J. M. Cregg, A. Hurtado, M. Oudega, M. T. Trombley, and R. J. Gilbert, "Creation of highly aligned electrospun poly-L-lactic acid fibers for nerve regeneration applications," *J. Neural Eng.*, vol. 6, no. 1, p. 15, 2009.
- [151] T. Subbiah, G. S. Bhat, R. W. Tock, S. Parameswaran, and S. S. Ramkumar, "Electrospinning of nanofibers," *J. Appl. Polym. Sci.*, vol. 96, no. 2, pp. 557–569, 2005.

- [152] N. Bhardwaj and S. C. Kundu, "Electrospinning: A fascinating fiber fabrication technique," *Biotechnology Advances*, vol. 28, no. 3, pp. 325–347, 2010.
- [153] M. F. B. Daud, K. C. Pawar, F. Claeysens, A. J. Ryan, and J. W. Haycock, "An aligned 3D neuronal-glia co-culture model for peripheral nerve studies," *Biomaterials*, vol. 33, no. 25, pp. 5901–5913, 2012.
- [154] Y. T. Kim, V. K. Haftel, S. Kumar, and R. V. Bellamkonda, "The role of aligned polymer fiber-based constructs in the bridging of long peripheral nerve gaps," *Biomaterials*, vol. 29, no. 21, pp. 3117–3127, 2008.
- [155] J. M. Corey, D. Y. Lin, K. B. Mycek, Q. Chen, S. Samuel, E. L. Feldman, and D. C. Martin, "Aligned electrospun nanofibers specify the direction of dorsal root ganglia neurite growth," *J. Biomed. Mater. Res. Part A*, vol. 83A, no. 3, pp. 636–645, 2007.
- [156] J. Xie, M. R. MacEwan, X. Li, S. E. Sakiyama-Elbert, and Y. Xia, "Neurite outgrowth on nanofiber scaffolds with different orders, structures, and surface properties," *ACS Nano*, vol. 3, no. 5, pp. 1151–1159, 2009.
- [157] J. Xie, S. M. Willerth, X. Li, M. R. MacEwan, A. Rader, S. E. Sakiyama-Elbert, and Y. Xia, "The differentiation of embryonic stem cells seeded on electrospun nanofibers into neural lineages," *Biomaterials*, vol. 30, no. 3, pp. 354–362, 2009.
- [158] J. W. Xie, W. Y. Liu, M. R. MacEwan, P. C. Bridgman, and Y. N. Xia, "Neurite Outgrowth on Electrospun Nanofibers with Uniaxial Alignment: The Effects of Fiber Density, Surface Coating, and Supporting Substrate," *ACS Nano*, vol. 8, no. 2, pp. 1878–1885, 2014.
- [159] E. Schnell, K. Klinkhammer, S. Balzer, G. Brook, D. Klee, P. Dalton, and J. Mey, "Guidance of glial cell migration and axonal growth on electrospun nanofibers of poly-epsilon-caprolactone and a collagen/poly-epsilon-caprolactone blend," *Biomaterials*, vol. 28, no. 19, pp. 3012–3025, 2007.
- [160] L. Yao, N. O'Brien, A. Windebank, and A. Pandit, "Orienting Neurite Growth in Electrospun Fibrous Neural Conduits," *J. Biomed. Mater. Res. Part B-Applied Biomater.*, vol. 90B, no. 2, pp. 483–491, 2009.
- [161] E. M. Jeffries and Y. Wang, "Biomimetic micropatterned multi-channel nerve guides by templated electrospinning," *Biotechnol. Bioeng.*, vol. 109, no. 6, pp. 1571–82, Jun. 2012.
- [162] T. M. Dinis, R. Elia, G. Vidal, Q. Dermigny, C. Denoëud, D. L. Kaplan, C. Egles, and F. Marin, "3D multi-channel bi-functionalized silk electrospun conduits for peripheral nerve regeneration," *J. Mech. Behav. Biomed. Mater.*, vol. 41, pp. 43–55, Jan. 2015.
- [163] J. Xue, H. Li, and Y. Xia, "Nanofiber-Based Multi-Tubular Conduits with a Honeycomb Structure for Potential Application in Peripheral Nerve Repair," *Macromol. Biosci.*, 2018.
- [164] H. K. Frost, T. Andersson, S. Johansson, U. Englund-Johansson, P. Ekström, L. B. Dahlin, and F. Johansson, "Electrospun nerve guide conduits have the potential to bridge peripheral nerve injuries in vivo," *Sci. Rep.*, vol. 8, no. 1, p. 16716, Dec. 2018.
- [165] R. F. Valentini, P. Aebischer, S. R. Winn, and P. M. Galletti, "Collagen-containing and laminin-containing gels impede peripheral-nerve regeneration through semipermeable nerve guidance channels," *Exp. Neurol.*, vol. 98, no. 2, pp. 350–356, 1987.
- [166] F. Stang, H. Fansa, G. Wolf, M. Reppin, and G. Keilhoff, "Structural parameters of collagen nerve grafts influence peripheral nerve regeneration," *Biomaterials*, vol. 26, no. 16, pp. 3083–3091, Jun. 2005.
- [167] W. Chang, M. B. Shah, P. Lee, and X. Yu, "Tissue-engineered spiral nerve guidance conduit for peripheral nerve regeneration," *Acta Biomater.*, 2018.
- [168] H. S. Koh, T. Yong, W. E. Teo, C. K. Chan, M. E. Puhaindran, T. C. Tan, A. Lim, B. H. Lim, and S. Ramakrishna, "In vivo study of novel nanofibrous intra-luminal guidance channels to promote nerve regeneration," *J. Neural Eng.*, vol. 7, no. 4, 2010.
- [169] D. Li, X. Pan, B. Sun, T. Wu, W. Chen, C. Huang, Q. Ke, H. A. El-Hamshary, S. S. Al-Deyab, and X. Mo, "Nerve conduits constructed by electrospun P(LLA-CL) nanofibers and PLLA nanofiber yarns," *J. Mater. Chem. B*, vol. 3, no. 45, pp. 8823–8831, 2015.

- [170] C. J. Pateman, "Development of microstereolithography and photopolymerisable polymers for peripheral nerve repair," The University of Sheffield, UK, 2014.
- [171] J. Cai, X. Peng, K. D. Nelson, R. Eberhart, and G. M. Smith, "Permeable guidance channels containing microfilament scaffolds enhance axon growth and maturation," *J Biomed Mater Res A*, vol. 75, no. 2, pp. 374–386, 2005.
- [172] T. T. B. Ngo, P. J. Waggoner, A. A. Romero, K. D. Nelson, R. C. Eberhart, and G. M. Smith, "Poly(L-lactide) microfilaments enhance peripheral nerve regeneration across extended nerve lesions," *J. Neurosci. Res.*, vol. 72, no. 2, pp. 227–238, 2003.
- [173] W. T. Daly, L. Yao, M. T. Abu-rub, C. O'Connell, D. I. Zeugolis, A. J. Windebank, and A. S. Pandit, "The effect of intraluminal contact mediated guidance signals on axonal mismatch during peripheral nerve repair," *Biomaterials*, 2012.
- [174] L. Cai, L. Zhang, J. Dong, and S. Wang, "Photocured Biodegradable Polymer Substrates of Varying Stiffness and Microgroove Dimensions for Promoting Nerve Cell Guidance and Differentiation," *Langmuir*, vol. 28, no. 34, pp. 12557–12568, 2012.
- [175] S. H. Hsu, C. Y. Chen, P. S. Lu, C. S. Lai, and C. J. Chen, "Oriented Schwann cell growth on microgrooved surfaces," *Biotechnol. Bioeng.*, vol. 92, no. 5, pp. 579–588, 2005.
- [176] C. Miller, H. Shanks, A. Witt, G. Rutkowski, and S. Mallapragada, "Oriented Schwann cell growth on micropatterned biodegradable polymer substrates," *Biomaterials*, vol. 22, no. 11, pp. 1263–1269, 2001.
- [177] C. Miller, S. Jeftinija, and S. Mallapragada, "Micropatterned Schwann cell-seeded biodegradable polymer substrates significantly enhance neurite alignment and outgrowth," *Tissue Eng.*, vol. 7, no. 6, pp. 705–715, 2001.
- [178] D. M. Thompson and H. M. Buettner, "Neurite outgrowth is directed by Schwann cell alignment in the absence of other guidance cues," *Ann. Biomed. Eng.*, vol. 34, no. 1, pp. 161–168, 2006.
- [179] J. A. Mitchel and D. Hoffman-Kim, "Cellular Scale Anisotropic Topography Guides Schwann Cell Motility," *PLoS One*, vol. 6, no. 9, 2011.
- [180] H. Suo, Z. Wang, G. Dai, J. Fu, J. Yin, and L. Chang, "Polyacrylonitrile nerve conduits with inner longitudinal grooved textures to enhance neuron directional outgrowth," *J. Microelectromechanical Syst.*, 2018.
- [181] S. Hsu and H.-C. Ni, "Fabrication of the Microgrooved/Microporous Polylactide Substrates as Peripheral Nerve Conduits and In Vivo Evaluation," *Tissue Eng. Part A*, vol. 15, no. 6, pp. 1381–1390, 2009.
- [182] S. M. Kim, M. S. Lee, J. Jeon, D. H. Lee, K. Yang, S. W. Cho, I. Han, and H. S. Yang, "Biodegradable Nerve Guidance Conduit with Microporous and Micropatterned Poly(lactico-glycolic acid)-Accelerated Sciatic Nerve Regeneration," *Macromol. Biosci.*, 2018.
- [183] G. E. Rutkowski, C. A. Miller, S. Jeftinija, and S. K. Mallapragada, "Synergistic effects of micropatterned biodegradable conduits and Schwann cells on sciatic nerve regeneration," *J. Neural Eng.*, vol. 1, no. 3, pp. 151–157, 2004.
- [184] A. Mobasser, A. Faroni, B. M. Minogue, S. Downes, G. Terenghi, and A. J. Reid, "Polymer Scaffolds with Preferential Parallel Grooves Enhance Nerve Regeneration," *Tissue Eng. Part A*, vol. 21, no. 5–6, pp. 1152–1162, 2015.
- [185] Integra, "NeuraGen® Nerve Guide." [Online]. Available: http://www.integralife.com/products%2Fpdfs%2Fneuragen_instructions_for_use.pdf.
- [186] A. Wang, Q. Ao, W. Cao, M. Yu, Q. He, L. Kong, L. Zhang, Y. Gong, and X. Zhang, "Porous chitosan tubular scaffolds with knitted outer wall and controllable inner structure for nerve tissue engineering," *J. Biomed. Mater. Res. - Part A*, 2006.
- [187] H. Matsumine, R. Sasaki, M. Yamato, T. Okano, and H. Sakurai, "A polylactic acid non-woven nerve conduit for facial nerve regeneration in rats," *J. Tissue Eng. Regen. Med.*, 2014.
- [188] F. P. W. Melchels, J. Feijen, and D. W. Grijpma, "A review on stereolithography and its applications in biomedical engineering," *Biomaterials*, vol. 31, no. 24, pp. 6121–6130, 2010.

- [189] B. M. Monroe and G. C. Weed, "PHOTOINITIATORS FOR FREE-RADICAL-INITIATED PHOTOIMAGING SYSTEMS," *Chem. Rev.*, vol. 93, no. 1, pp. 435–448, 1993.
- [190] Y. Yagci, S. Jockusch, and N. J. Turro, "Photoinitiated polymerization: Advances, challenges, and opportunities," *Macromolecules*, vol. 43, no. 15, pp. 6245–6260, 2010.
- [191] L.-H. Han, G. Mapili, S. Chen, and K. Roy, "Projection Microfabrication of Three-Dimensional Scaffolds for Tissue Engineering," *J. Manuf. Sci. Eng.*, vol. 130, no. 2, p. 021005, 2008.
- [192] A. Ovsianikov, M. Malinauskas, S. Schlie, B. Chichkov, S. Gittard, R. Narayan, M. Lobler, K. Sternberg, K. P. Schmitz, and A. Haverich, "Three-dimensional laser micro- and nano-structuring of acrylated poly(ethylene glycol) materials and evaluation of their cytotoxicity for tissue engineering applications," *Acta Biomater.*, vol. 7, no. 3, pp. 967–974, 2011.
- [193] K. Arcaute, B. Mann, and R. Wicker, "Stereolithography of spatially controlled multi-material bioactive poly(ethylene glycol) scaffolds," *Acta Biomater.*, vol. 6, no. 3, pp. 1047–1054, 2010.
- [194] G. Mapili, Y. Lu, S. Chen, and K. Roy, "Laser-layered microfabrication of spatially patterned functionalized tissue-engineering scaffolds," *J. Biomed. Mater. Res. - Part B Appl. Biomater.*, vol. 75, no. 2, pp. 414–424, 2005.
- [195] H. Lin, D. Zhang, P. G. Alexander, G. Yang, J. Tan, A. W. M. Cheng, and R. S. Tuan, "Application of visible light-based projection stereolithography for live cell-scaffold fabrication with designed architecture," *Biomaterials*, vol. 34, no. 2, pp. 331–339, 2013.
- [196] K. Arcaute, B. K. Mann, and R. B. Wicker, "Stereolithography of three-dimensional bioactive poly(ethylene glycol) constructs with encapsulated cells," *Ann. Biomed. Eng.*, vol. 34, no. 9, pp. 1429–1441, 2006.
- [197] V. Chan, P. Zorlutuna, J. H. Jeong, H. Kong, and R. Bashir, "Three-dimensional photopatterning of hydrogels using stereolithography for long-term cell encapsulation.," *Lab Chip*, vol. 10, no. 16, pp. 2062–2070, 2010.
- [198] F. Klein, B. Richter, T. Striebel, C. M. Franz, G. von Freymann, M. Wegener, and M. Bastmeyer, "Two-Component Polymer Scaffolds for Controlled Three-Dimensional Cell Culture," *Adv. Mater.*, vol. 23, no. 11, pp. 1341–1345, 2011.
- [199] M. C. Lensen and V. A. Schulte, "Cell Adhesion and Spreading on an Intrinsically AntiAdhesive PEG Biomaterial," in *Biomaterials - Physics and Chemistry*, R. Pignatello, Ed. InTech, 2011.
- [200] H.-C. Moeller, M. K. Mian, S. Shrivastava, B. G. Chung, and A. Khademhosseini, "A microwell array system for stem cell culture," *Biomaterials*, vol. 29, no. 6, pp. 752–763, 2008.
- [201] P. T. Charles, V. R. Stubbs, C. M. Soto, B. D. Martin, B. J. White, and C. R. Taitt, "Reduction of non-specific protein adsorption using poly(ethylene) glycol (PEG) modified polyacrylate hydrogels in immunoassays for staphylococcal enterotoxin B detection," *Sensors*, vol. 9, no. 1, pp. 645–655, 2009.
- [202] I. Ortega, P. Deshpande, A. A. Gill, S. MacNeil, and F. Claeysens, "Development of a microfabricated artificial limbus with micropockets for cell delivery to the cornea," *Biofabrication*, vol. 5, no. 2, 2013.
- [203] S. A. M. Ali, S.-P. Zhong, P. J. Doherty, and D. F. Williams, "Mechanisms of polymer degradation in implantable devices," *Biomaterials*, vol. 14, no. 9, pp. 648–656, Jul. 1993.
- [204] G. Pitt, M. Gratzl, G. Kimmel, J. Surlles, and A. Sohindler, "Aliphatic polyesters II. The degradation of poly (DL-lactide), poly (ϵ -caprolactone), and their copolymers in vivo," *Biomaterials*, vol. 2, no. 4, pp. 215–220, Oct. 1981.
- [205] D. Darwis, H. Mitomo, T. Enjoji, F. Yoshii, and K. Makuuchi, "Enzymatic degradation of radiation crosslinked poly(ϵ -caprolactone)," *Polym. Degrad. Stab.*, vol. 62, no. 2, pp. 259–265, 1998.
- [206] Z. Gan, Q. Liang, J. Zhang, and X. Jing, "Enzymatic degradation of poly(ϵ -caprolactone) film in phosphate buffer solution containing lipases," *Polym. Degrad. Stab.*, 1997.
- [207] R. S. Bezwada, D. D. Jamiolkowski, I. Y. Lee, V. Agarwal, J. Persivale, S. Trenka-Benthin, M. Erneta, J. Suryadevara, A. Yang, and S. Liu, "Monocryl® suture, a new ultra-pliable absorbable monofilament suture," *Biomaterials*, 1995.

- [208] P. D. Darney, S. E. Monroe, C. M. Klaisle, and A. Alvarado, "Clinical evaluation of the Capronor contraceptive implant: Preliminary report," *Am. J. Obstet. Gynecol.*, 1989.
- [209] A. Kumari, S. K. Yadav, and S. C. Yadav, "Biodegradable polymeric nanoparticles based drug delivery systems," *Colloids and Surfaces B: Biointerfaces*, vol. 75, no. 1. pp. 1–18, 2010.
- [210] M. Van Lieshout, G. Peters, M. Rutten, and F. Baaijens, "A Knitted, Fibrin-Covered Polycaprolactone Scaffold for Tissue Engineering of the Aortic Valve," *Tissue Eng.*, 2006.
- [211] H. Yoshimoto, Y. M. Shin, H. Terai, and J. P. Vacanti, "A biodegradable nanofiber scaffold by electrospinning and its potential for bone tissue engineering," *Biomaterials*, vol. 24, no. 12, pp. 2077–2082, 2003.
- [212] W.-J. W.-J. Li, R. Tuli, C. Okafor, A. Derfoul, K. G. K. G. Danielson, D. J. D. J. Hall, and R. S. R. S. Tuan, "A three-dimensional nanofibrous scaffold for cartilage tissue engineering using human mesenchymal stem cells.," *Biomaterials*, 2005.
- [213] S. Y. Chew, R. Mi, A. Hoke, and K. W. Leong, "The effect of the alignment of electrospun fibrous scaffolds on Schwann cell maturation," *Biomaterials*, vol. 29, no. 6, pp. 653–661, 2008.
- [214] D. W. Huttmacher, T. Schantz, I. Zein, K. W. Ng, S. H. Teoh, and K. C. Tan, "Mechanical properties and cell cultural response of polycaprolactone scaffolds designed and fabricated via fused deposition modeling," *J. Biomed. Mater. Res.*, vol. 55, no. 2, pp. 203–216, 2001.
- [215] W. Y. Yeong, N. Sudarmadji, H. Y. Yu, C. K. Chua, K. F. Leong, S. S. Venkatraman, Y. C. F. Boey, and L. P. Tan, "Porous polycaprolactone scaffold for cardiac tissue engineering fabricated by selective laser sintering.," *Acta Biomater.*, vol. 6, no. 6, pp. 2028–34, Jun. 2010.
- [216] J. M. Williams, A. Adewunmi, R. M. Schek, C. L. Flanagan, P. H. Krebsbach, S. E. Feinberg, S. J. Hollister, and S. Das, "Bone tissue engineering using polycaprolactone scaffolds fabricated via selective laser sintering," *Biomaterials*, vol. 26, no. 23, pp. 4817–4827, 2005.
- [217] S. Eshraghi and S. Das, "Mechanical and microstructural properties of polycaprolactone scaffolds with one-dimensional, two-dimensional, and three-dimensional orthogonally oriented porous architectures produced by selective laser sintering.," *Acta Biomater.*, vol. 6, no. 7, pp. 2467–76, Jul. 2010.
- [218] R. F. Storey, S. C. Warren, C. J. Allison, J. S. Wiggins, and A. D. Puckett, "Synthesis of bioabsorbable networks from methacrylate-endcapped polyesters," *Polymer (Guildf).*, vol. 34, no. 20, pp. 4365–4372, 1993.
- [219] L. Elomaa, S. Teixeira, R. Hakala, H. Korhonen, D. W. Grijpma, and J. V Seppala, "Preparation of poly(epsilon-caprolactone)-based tissue engineering scaffolds by stereolithography," *Acta Biomater.*, vol. 7, no. 11, pp. 3850–3856, 2011.
- [220] A. Ronca, S. Ronca, G. Forte, S. Zeppetelli, A. Gloria, R. De Santis, and L. Ambrosio, "Synthesis and characterization of divinyl-fumarate poly-epsilon-caprolactone for scaffolds with controlled architectures," *J. Tissue Eng. Regen. Med.*, vol. 12, no. 1, pp. e523–e531, Jan. 2018.
- [221] T. Matsuda, M. Mizutani, and S. C. Arnold, "Molecular design of photocurable liquid biodegradable copolymers. 1. Synthesis and photocuring characteristics," *Macromolecules*, vol. 33, no. 3, pp. 795–800, 2000.
- [222] M. Mizutani and T. Matsuda, "Liquid acrylate-endcapped biodegradable poly(epsilon-caprolactone-co-trimethylene carbonate). I. Preparation and visible light-induced photocuring characteristics," *J. Biomed. Mater. Res.*, 2002.
- [223] T. Matsuda and M. Mizutani, "Liquid acrylate-endcapped biodegradable poly(epsilon-caprolactone-co-trimethylene carbonate). II. Computer-aided stereolithographic microarchitectural surface photoconstructs," *J. Biomed. Mater. Res.*, 2002.
- [224] S. He, M. . Timmer, M. . Yaszemski, A. . Yasko, P. . Engel, and A. . Mikos, "Synthesis of biodegradable poly(propylene fumarate) networks with poly(propylene fumarate)-diacrylate macromers as crosslinking agents and characterization of their degradation products," *Polymer (Guildf).*, vol. 42, no. 3, pp. 1251–1260, 2001.
- [225] K. W. Lee, S. Wang, B. C. Fox, E. L. Ritman, M. J. Yaszemski, and L. Lu, "Poly(propylene

- fumarate) bone tissue engineering scaffold fabrication using stereolithography: Effects of resin formulations and laser parameters," *Biomacromolecules*, vol. 8, no. 4, pp. 1077–1084, 2007.
- [226] F. P. W. Melchels, J. Feijen, and D. W. Grijpma, "A poly(d,l-lactide) resin for the preparation of tissue engineering scaffolds by stereolithography," *Biomaterials*, vol. 30, no. 23–24, pp. 3801–3809, 2009.
- [227] F. P. W. Melchels, K. Bertoldi, R. Gabbriellini, A. H. Velders, J. Feijen, and D. W. Grijpma, "Mathematically defined tissue engineering scaffold architectures prepared by stereolithography," *Biomaterials*, vol. 31, no. 27, pp. 6909–6916, 2010.
- [228] S. A. Bencherif, A. Srinivasan, F. Horkay, J. O. Hollinger, K. Matyjaszewski, and N. R. Washburn, "Influence of the degree of methacrylation on hyaluronic acid hydrogels properties," *Biomaterials*, vol. 29, no. 12, pp. 1739–1749, 2008.
- [229] E. Hoch, T. Hirth, G. E. M. Tovar, and K. Borchers, "Chemical tailoring of gelatin to adjust its chemical and physical properties for functional bioprinting," *J. Mater. Chem. B*, vol. 1, no. 41, p. 5675, 2013.
- [230] E. Hoch, C. Schuh, T. Hirth, G. E. M. Tovar, and K. Borchers, "Stiff gelatin hydrogels can be photo-chemically synthesized from low viscous gelatin solutions using molecularly functionalized gelatin with a high degree of methacrylation," *J. Mater. Sci. Mater. Med.*, vol. 23, no. 11, pp. 2607–2617, 2012.
- [231] A. Abbadessa, M. M. Blokzijl, V. H. M. Mouser, P. Marica, J. Malda, W. E. Hennink, and T. Vermonden, "A thermo-responsive and photo-polymerizable chondroitin sulfate-based hydrogel for 3D printing applications," *Carbohydr. Polym.*, vol. 149, pp. 163–174, 2016.
- [232] O. Jeon, K. H. Bouhadir, J. M. Mansour, and E. Alsberg, "Photocrosslinked alginate hydrogels with tunable biodegradation rates and mechanical properties," *Biomaterials*, vol. 30, no. 14, pp. 2724–2734, 2009.
- [233] S. Pashneh-Tala, R. Owen, H. Bahmaee, S. Rekštytė, M. Malinauskas, and F. Claeysens, "Synthesis, Characterization and 3D Micro-Structuring via 2-Photon Polymerization of Poly(glycerol sebacate)-Methacrylate—An Elastomeric Degradable Polymer," *Front. Phys.*, 2018.
- [234] P. F. Jacobs, "Fundamentals of Stereolithography," in *Solid Freeform Fabrication Proceedings*, The University of Texas at Austin, 1992, pp. 196–211.
- [235] J. Choi, R. B. Wicker, S. Cho, C. Ha, and S. Lee, "Cure depth control for complex 3D microstructure fabrication in dynamic mask projection microstereolithography," *Rapid Prototyp. J.*, vol. 15, no. 1, pp. 59–70, 2009.
- [236] I. A. Barker, M. P. Ablett, H. T. J. Gilbert, S. J. Leigh, J. A. Covington, J. A. Hoyland, S. M. Richardson, and A. P. Dove, "A microstereolithography resin based on thiol-ene chemistry: towards biocompatible 3D extracellular constructs for tissue engineering," *Biomater. Sci.*, vol. 2, no. 4, p. 472, 2014.
- [237] E. Hachet, H. Van Den Berghe, E. Bayma, M. R. Block, and R. Auzély-Velty, "Design of Biomimetic Cell-Interactive Substrates Using Hyaluronic Acid Hydrogels with Tunable Mechanical Properties," *Biomacromolecules*, vol. 13, no. 6, pp. 1818–1827, Jun. 2012.
- [238] J. Jansen, F. P. W. Melchels, D. W. Grijpma, and J. Feijen, "Fumaric Acid Monoethyl Ester-Functionalized Poly(d, l-lactide)/N-vinyl-2-pyrrolidone Resins for the Preparation of Tissue Engineering Scaffolds by Stereolithography," *Biomacromolecules*, vol. 10, no. 2, pp. 214–220, Feb. 2009.
- [239] B. J. Green, K. S. Worthington, J. R. Thompson, S. J. Bunn, M. Rethwisch, E. E. Kaalberg, C. Jiao, L. A. Wiley, R. F. Mullins, E. M. Stone, E. H. Sohn, B. A. Tucker, and C. A. Guymon, "Effect of Molecular Weight and Functionality on Acrylated Poly(caprolactone) for Stereolithography and Biomedical Applications," *Biomacromolecules*, 2018.
- [240] I. Chung, D. Xie, A. D. Puckett, and J. W. Mays, "Syntheses and evaluation of biodegradable multifunctional polymer networks," *Eur. Polym. J.*, 2003.

- [241] A. Göpferich, "Mechanisms of polymer degradation and erosion1," in *The Biomaterials: Silver Jubilee Compendium*, 2006.
- [242] A. Heimowska, M. Morawska, and A. Bocho-Janiszewska, "Biodegradation of poly(ϵ -caprolactone) in natural water environments," *Polish J. Chem. Technol.*, 2017.
- [243] D. Cam, S. hyu Hyon, and Y. Ikada, "Degradation of high molecular weight poly(l-lactide) in alkaline medium," *Biomaterials*, 1995.
- [244] J. L. Ifkovits and J. A. Burdick, "Review: Photopolymerizable and Degradable Biomaterials for Tissue Engineering Applications," *Tissue Eng.*, 2007.
- [245] C. R. Nuttelman, S. M. Henry, and K. S. Anseth, "Synthesis and characterization of photocrosslinkable, degradable poly(vinyl alcohol)-based tissue engineering scaffolds," *Biomaterials*, 2002.
- [246] A. T. Metters, K. S. Anseth, and C. N. Bowman, "Fundamental studies of a novel, biodegradable PEG-b-PLA hydrogel," *Polymer (Guildf.)*, 2000.
- [247] C. X. F. F. Lam, D. W. Hutmacher, J.-T. T. Schantz, M. A. Woodruff, and S. H. Teoh, "Evaluation of polycaprolactone scaffold degradation for 6 months in vitro and in vivo.," *J. Biomed. Mater. Res. A*, vol. 90, no. 3, pp. 906–919, 2009.
- [248] S. H. Lee, J. H. Lee, and Y. S. Cho, "Analysis of degradation rate for dimensionless surface area of well-interconnected PCL scaffold via in-vitro accelerated degradation experiment," *Tissue Eng. Regen. Med.*, 2014.
- [249] C. X. F. Lam, M. M. Savalani, S. H. Teoh, and D. W. Hutmacher, "Dynamics of in vitro polymer degradation of polycaprolactone-based scaffolds: Accelerated versus simulated physiological conditions," *Biomed. Mater.*, 2008.
- [250] A. Bertsch, P. Bernhard, C. Vogt, and P. Renaud, "Rapid prototyping of small size objects," *Rapid Prototyp. J.*, vol. 6, no. 4, pp. 259–266, 2000.
- [251] C. Zhou, Y. Chen, Z. Yang, and B. Khoshnevis, "Digital material fabrication using mask-image-projection-based stereolithography," *Rapid Prototyp. J.*, vol. 19, no. 3, pp. 153–165, 2013.
- [252] J. R. Tumbleston, D. Shirvanyants, N. Ermoshkin, R. Januszewicz, A. R. Johnson, D. Kelly, K. Chen, R. Pinschmidt, J. P. Rolland, A. Ermoshkin, E. T. Samulski, and J. M. DeSimone, "Continuous liquid interface production of 3D objects," *Science (80-.)*, vol. 347, no. 6228, pp. 1349–1352, 2015.
- [253] B. Steyrer, B. Busetti, G. Harakály, R. Liska, and J. Stampfl, "Hot Lithography vs. room temperature DLP 3D-printing of a dimethacrylate," *Addit. Manuf.*, vol. 21, pp. 209–214, 2018.
- [254] P. Sótonyi, B. Merkely, M. Hubay, J. J. Járay, E. Zima, P. Soós, A. Kovács, and I. Szentmáriay, "Comparative study on cardiotoxic effect of tinuvin 770: A light stabilizer of medical plastics in rat model," *Toxicol. Sci.*, vol. 77, no. 2, pp. 368–374, Jan. 2004.
- [255] P. Sótonyi, É. Keller, J. Járay, B. Nemes, T. Benkő, A. Kovács, A. Tolokán, and I. Rajs, "A light stabilizer Tinuvin 770-induced toxic injury of adult rat cardiac myocytes," *Forensic Sci. Int.*, vol. 119, no. 3, pp. 322–327, Jul. 2001.
- [256] P. Newbold and S. D. Brain, "An investigation into the mechanism of capsaicin-induced oedema in rabbit skin.," *Br. J. Pharmacol.*, vol. 114, no. 3, pp. 570–577, 1995.
- [257] K. Ren, G. M. Williams, M. A. Ruda, and R. Dubner, "Inflammation and hyperalgesia in rats neonatally treated with capsaicin: effects on two classes of nociceptive neurons in the superficial dorsal horn," *Pain*, vol. 59, no. 2, pp. 287–300, 1994.
- [258] T. Tanvetyanon and G. Bepler, "Beta-carotene in multivitamins and the possible risk of lung cancer among smokers versus former smokers: A meta-analysis and evaluation of national brands," *Cancer*, vol. 113, no. 1, pp. 150–157, 2008.
- [259] M. A. Cotter, A. Love, M. J. Watt, N. E. Cameron, and K. C. Dines, "Effects of natural free radical scavengers on peripheral nerve and neurovascular function in diabetic rats," *Diabetologia*, vol. 38, no. 11, pp. 1285–1294, 1995.
- [260] G. Horváth, Á. Kemény, L. Barthó, P. Molnár, J. Deli, L. Szente, T. Bozó, S. Pál, K. Sándor, É. Szőke, J. Szolcsányi, and Z. Helyes, "Effects of Some Natural Carotenoids on TRPA1- and

- TRPV1-Induced Neurogenic Inflammatory Processes In Vivo in the Mouse Skin," *J. Mol. Neurosci.*, vol. 56, no. 1, pp. 113–121, 2015.
- [261] J. Yin, Z. Wang, W. Chai, G. Dai, H. Suo, N. Zhang, X. Wen, and Y. Huang, "Fabrication of Inner Grooved Hollow Fiber Membranes Using Microstructured Spinneret for Nerve Regeneration," *J. Manuf. Sci. Eng.*, 2017.
- [262] C.-C. Chen, J. Yu, H.-Y. Ng, A. Lee, C.-C. Chen, Y.-S. Chen, M.-Y. Shie, C.-C. Chen, J. Yu, H.-Y. Ng, A. K.-X. Lee, C.-C. Chen, Y.-S. Chen, and M.-Y. Shie, "The Physicochemical Properties of Decellularized Extracellular Matrix-Coated 3D Printed Poly(ϵ -caprolactone) Nerve Conduits for Promoting Schwann Cells Proliferation and Differentiation," *Materials (Basel)*, vol. 11, no. 9, p. 1665, Sep. 2018.
- [263] D. Radulescu, S. Dhar, C. M. Young, D. W. Taylor, H. J. Trost, D. J. Hayes, and G. R. Evans, "Tissue engineering scaffolds for nerve regeneration manufactured by ink-jet technology," *Mater. Sci. Eng. C*, 2007.
- [264] Y. Hu, Y. Wu, Z. Gou, J. Tao, J. Zhang, Q. Liu, T. Kang, S. Jiang, S. Huang, J. He, S. Chen, Y. Du, and M. Gou, "3D-engineering of cellularized conduits for peripheral nerve regeneration," *Sci. Rep.*, 2016.
- [265] A. E. Jakus, E. B. Secor, A. L. Rutz, S. W. Jordan, M. C. Hersam, and R. N. Shah, "Three-dimensional printing of high-content graphene scaffolds for electronic and biomedical applications," *ACS Nano*, 2015.
- [266] S. Suri, L. H. Han, W. Zhang, A. Singh, S. Chen, and C. E. Schmidt, "Solid freeform fabrication of designer scaffolds of hyaluronic acid for nerve tissue engineering," *Biomed. Microdevices*, 2011.
- [267] Í. Ortega, A. J. Ryan, P. Deshpande, S. MacNeil, and F. Claeysens, "Combined microfabrication and electrospinning to produce 3-D architectures for corneal repair," *Acta Biomater.*, 2013.
- [268] S.-J. Lee, M. Nowicki, B. Harris, and L. G. Zhang, "Fabrication of a Highly Aligned Neural Scaffold via a Table Top Stereolithography 3D Printing and Electrospinning," *Tissue Eng. Part A*, vol. 23, no. 11–12, pp. 491–502, Jun. 2017.
- [269] H. Y. Chiang, H. F. Chien, H. H. Shen, J. D. Yang, Y. H. Chen, J. H. Chen, and S. T. Hsieh, "Reinnervation of muscular targets by nerve regeneration through guidance conduits," *J. Neuropathol. Exp. Neurol.*, 2005.
- [270] S. Yoganarasimha, W. R. Trahan, A. M. Best, G. L. Bowlin, T. O. Kitten, P. C. Moon, and P. A. Madurantakam, "Peracetic acid: A practical agent for sterilizing heat-labile polymeric tissue-engineering scaffolds," *Tissue Eng. - Part C Methods*, 2014.
- [271] L. A. Bosworth, A. Gibb, and S. Downes, "Gamma irradiation of electrospun poly(ϵ -caprolactone) fibers affects material properties but not cell response," *J. Polym. Sci. Part B Polym. Phys.*, 2012.
- [272] Y.-C. Nho, J.-P. Jeun, and Y.-M. Lim, "Electrospinning of polycaprolactone and its degradation effect by radiation," in *Controlling of Degradation Effects in Radiation Processing of Polymers*, Vienna: IAEA, 2009, pp. 107–115.
- [273] T. A. M. Valente, D. M. Silva, P. S. Gomes, M. H. Fernandes, J. D. Santos, and V. Sencadas, "Effect of sterilization methods on electrospun poly(lactic acid) (PLA) fiber alignment for biomedical applications," *ACS Appl. Mater. Interfaces*, 2016.
- [274] M. Selim, A. J. Bullock, K. A. Blackwood, C. R. Chapple, and S. MacNeil, "Developing biodegradable scaffolds for tissue engineering of the urethra," *BJU Int.*, 2011.
- [275] F. J. Bye, L. Wang, A. J. Bullock, K. A. Blackwood, A. J. Ryan, and S. Macneil, "Postproduction processing of electrospun fibres for tissue engineering," *J. Vis. Exp.*, 2012.
- [276] H. Shearer, M. J. Ellis, S. P. Perera, and J. B. Chaudhuri, "Effects of common sterilization methods on the structure and properties of poly(D,L lactic-co-glycolic acid) scaffolds," *Tissue Eng.*, 2006.
- [277] M. F. B. Daud, "An organized 3D in vitro model for peripheral nerve studies," University of

- Sheffield, 2013.
- [278] M. Behbehani, "An ex vivo model of peripheral nerve regeneration," The University of Sheffield, 2019.
- [279] R. Morent, N. De Geyter, T. Desmet, P. Dubruel, and C. Leys, "Plasma surface modification of biodegradable polymers: A review," *Plasma Processes and Polymers*. 2011.
- [280] G. Altankov and T. Groth, "Reorganization of substratum-bound fibronectin on hydrophilic and hydrophobic materials is related to biocompatibility," *J. Mater. Sci. Mater. Med.*, 1994.
- [281] K. Nakazawa, Y. Izumi, and R. Mori, "Morphological and functional studies of rat hepatocytes on a hydrophobic or hydrophilic polydimethylsiloxane surface," *Acta Biomater.*, 2009.
- [282] K. Webb, V. Hlady, and P. A. Tresco, "Relative importance of surface wettability and charged functional groups on NIH 3T3 fibroblast attachment, spreading, and cytoskeletal organization," *J. Biomed. Mater. Res.*, 1998.
- [283] C. F. Amstein and P. A. Hartman, "Adaptation of plastic surfaces for tissue culture by glow discharge," *J. Clin. Microbiol.*, 1975.
- [284] W. S. Raey, W. Hertl, E. D. Nowlan, and N. J. Binkowski, "Surface treatments and cell attachment," *Vitr. J. Tissue Cult. Assoc.*, 1984.
- [285] T. Jacobs, N. De Geyter, R. Morent, T. Desmet, P. Dubruel, and C. Leys, "Plasma treatment of polycaprolactone at medium pressure," *Surf. Coatings Technol.*, 2011.
- [286] L. A. Can-Herrera, A. Ávila-Ortega, S. de la Rosa-García, A. I. Oliva, J. V. Cauich-Rodríguez, and J. M. Cervantes-Uc, "Surface modification of electrospun polycaprolactone microfibers by air plasma treatment: Effect of plasma power and treatment time," *Eur. Polym. J.*, 2016.
- [287] B. L. Johansson, A. Larsson, A. Ocklind, and Å. Öhrlund, "Characterization of air plasma-treated polymer surfaces by ESCA and contact angle measurements for optimization of surface stability and cell growth," *J. Appl. Polym. Sci.*, 2002.
- [288] J. Lai, B. Sunderland, J. Xue, S. Yan, W. Zhao, M. Folkard, B. D. Michael, and Y. Wang, "Study on hydrophilicity of polymer surfaces improved by plasma treatment," *Appl. Surf. Sci.*, vol. 252, no. 10, pp. 3375–3379, Mar. 2006.
- [289] S. Guruvenket, G. M. Rao, M. Komath, and A. M. Raichur, "Plasma surface modification of polystyrene and polyethylene," *Appl. Surf. Sci.*, vol. 236, no. 1–4, pp. 278–284, Sep. 2004.
- [290] I. Armentano, G. Ciapetti, M. Pennacchi, M. Dottori, V. Devescovi, D. Granchi, N. Baldini, B. Olalde, M. J. Jurado, J. I. M. Alava, and J. M. Kenny, "Role of PLLA plasma surface modification in the interaction with human marrow stromal cells," *J. Appl. Polym. Sci.*, 2009.
- [291] N. Hasirci, T. Endogan, E. Vardar, A. Kiziltay, and V. Hasirci, "Effect of oxygen plasma on surface properties and biocompatibility of PLGA films," *Surf. Interface Anal.*, vol. 42, no. 6–7, pp. 486–491, Mar. 2010.
- [292] E. D. Yildirim, H. Ayan, V. N. Vasilets, A. Fridman, S. Guceri, and W. Sun, "Effect of dielectric barrier discharge plasma on the attachment and proliferation of osteoblasts cultured over poly(ϵ -caprolactone) scaffolds," *Plasma Process. Polym.*, 2008.
- [293] Q. Cheng, B. L.-P. Lee, K. Komvopoulos, Z. Yan, and S. Li, "Plasma Surface Chemical Treatment of Electrospun Poly(L-Lactide) Microfibrous Scaffolds for Enhanced Cell Adhesion, Growth, and Infiltration," *Tissue Eng. Part A*, 2013.
- [294] N. Recek, M. Resnik, H. Motaln, T. Lah-Turnšek, R. Augustine, N. Kalarikkal, S. Thomas, and M. Mozetič, "Cell Adhesion on Polycaprolactone Modified by Plasma Treatment," *Int. J. Polym. Sci.*, 2016.
- [295] J. Lee, M. J. Cuddihy, and N. A. Kotov, "Three-Dimensional Cell Culture Matrices: State of the Art," *Tissue Eng. Part B Rev.*, 2008.
- [296] M. Hanani, "Satellite glial cells in sensory ganglia: from form to function," *Brain Res. Rev.*, vol. 48, no. 3, pp. 457–476, Jun. 2005.
- [297] W. Tongtako, A. Lehmbecker, Y. Wang, K. Hahn, W. Baumgärtner, and I. Gerhauser, "Canine dorsal root ganglia satellite glial cells represent an exceptional cell population with astrocytic and oligodendrocytic properties," *Sci. Rep.*, vol. 7, no. 1, p. 13915, Dec. 2017.

- [298] R. Edmondson, J. J. Broglie, A. F. Adcock, and L. Yang, "Three-Dimensional Cell Culture Systems and Their Applications in Drug Discovery and Cell-Based Biosensors," *Assay Drug Dev. Technol.*, 2014.
- [299] M. Behbehani, A. Glen, C. S. Taylor, A. Schuhmacher, F. Claeysens, and J. W. Haycock, "Pre-clinical evaluation of advanced nerve guide conduits using a novel 3D in vitro testing model," *Int. J. Bioprinting*, 2018.
- [300] X. J. Wen and P. A. Tresco, "Effect of filament diameter and extracellular matrix molecule precoating on neurite outgrowth and Schwann cell behavior on multifilament entubulation bridging device in vitro," *J. Biomed. Mater. Res. Part A*, vol. 76a, no. 3, pp. 626–637, 2006.
- [301] R. Kaewkhaw, A. M. Scutt, and J. W. Haycock, "Integrated culture and purification of rat Schwann cells from freshly isolated adult tissue," *Nat. Protoc.*, 2012.
- [302] V. B. Michelsen, H. Lygre, R. Skålevik, A. B. Tveit, and E. Solheim, "Identification of organic eluates from four polymer-based dental filling materials," *Eur. J. Oral Sci.*, 2003.
- [303] P. G. Di Summa, P. J. Kingham, W. Raffoul, M. Wiberg, G. Terenghi, and D. F. Kalbermatten, "Adipose-derived stem cells enhance peripheral nerve regeneration," *J. Plast. Reconstr. Aesthetic Surg.*, 2010.
- [304] A. D. Anselin, T. Fink, and D. F. Davey, "Peripheral nerve regeneration through nerve guides seeded with adult Schwann cells," *Neuropathol. Appl. Neurobiol.*, 1997.
- [305] Y. Arima and H. Iwata, "Effect of wettability and surface functional groups on protein adsorption and cell adhesion using well-defined mixed self-assembled monolayers," *Biomaterials*, 2007.
- [306] J. H. Lee, J. W. Lee, G. Khang, and H. B. Lee, "Interaction of cells on chargeable functional group gradient surfaces," *Biomaterials*, 1997.
- [307] S. De Valence, J. C. Tille, C. Chaabane, R. Gurny, M. L. Bochaton-Piallat, B. H. Walpoth, and M. Möller, "Plasma treatment for improving cell biocompatibility of a biodegradable polymer scaffold for vascular graft applications," *Eur. J. Pharm. Biopharm.*, 2013.
- [308] D. Yan, J. Jones, X. Y. Yuan, X. H. Xu, J. Sheng, J. C. M. Lee, G. Q. Ma, and Q. S. Yu, "Plasma treatment of electrospun PCL random nanofiber meshes (NFMs) for biological property improvement," *J. Biomed. Mater. Res. - Part A*, 2013.
- [309] A. Martins, E. D. Pinho, S. Faria, I. Pashkuleva, A. P. Marques, R. L. Reis, and N. M. Neves, "Surface modification of electrospun polycaprolactone nanofiber meshes by plasma treatment to enhance biological performance," *Small*, 2009.
- [310] H. B. Wang, M. E. Mullins, J. M. Cregg, C. W. McCarthy, and R. J. Gilbert, "Varying the diameter of aligned electrospun fibers alters neurite outgrowth and Schwann cell migration," *Acta Biomater.*, vol. 6, no. 8, pp. 2970–2978, Aug. 2010.
- [311] S. Gnavi, B. E. Fornasari, C. Tonda-Turo, G. Ciardelli, M. Zanetti, S. Geuna, and I. Perroteau, "The influence of electrospun fibre size on Schwann cell behaviour and axonal outgrowth," *Mater. Sci. Eng. C*, vol. 48, pp. 620–631, Mar. 2015.
- [312] S. Yoshii, M. Oka, M. Shima, A. Taniguchi, and M. Akagi, "Bridging a 30-mm nerve defect using collagen filaments," *J. Biomed. Mater. Res. - Part A*, 2003.
- [313] C. L. A. M. Vleggeert-Lankamp, "The role of evaluation methods in the assessment of peripheral nerve regeneration through synthetic conduits: a systematic review," *J. Neurosurg.*, 2007.
- [314] V. Carriel, I. Garzón, M. Alaminos, and M. Cornelissen, "Histological assessment in peripheral nerve tissue engineering," *Neural Regen. Res.*, 2014.
- [315] X. Navarro and E. Udina, "Chapter 6 Methods and Protocols in Peripheral Nerve Regeneration Experimental Research. Part III-Electrophysiological Evaluation," *International Review of Neurobiology*. 2009.
- [316] S. Das, M. Sharma, D. Saharia, K. K. Sarma, E. M. Muir, and U. Bora, "Electrospun silk-polyaniline conduits for functional nerve regeneration in rat sciatic nerve injury model," *Biomed. Mater.*, vol. 12, no. 4, p. 045025, Aug. 2017.

- [317] L. Sarikcioglu, B. M. Demirel, and A. Utuk, "Walking track analysis: An assessment method for functional recovery after sciatic nerve injury in the rat," *Folia Morphologica*. 2009.
- [318] A. S. P. Varejão, M. F. Meek, A. J. A. Ferreira, J. A. B. Patrício, and A. M. S. Cabrita, "Functional evaluation of peripheral nerve regeneration in the rat: Walking track analysis," *Journal of Neuroscience Methods*. 2001.
- [319] G. Feng, R. H. Mellor, M. Bernstein, C. Keller-Peck, Q. T. Nguyen, M. Wallace, J. M. Nerbonne, J. W. Lichtman, and J. R. Sanes, "Imaging Neuronal Subsets in Transgenic Mice Expressing Multiple Spectral Variants of GFP," *Neuron*, vol. 28, no. 1, pp. 41–51, 2000.
- [320] M. L. Groves, R. McKeon, E. Werner, M. Nagarsheth, W. Meador, and A. W. English, "Axon regeneration in peripheral nerves is enhanced by proteoglycan degradation," *Exp. Neurol.*, vol. 195, no. 2, pp. 278–292, 2005.
- [321] D. J. Liebl, L. Tessarollo, M. E. Palko, and L. F. Parada, "Absence of sensory neurons before target innervation in brain-derived neurotrophic factor-, neurotrophin 3-, and TrkC-deficient embryonic mice.," *J. Neurosci.*, vol. 17, no. 23, pp. 9113–9121, 1997.
- [322] A. W. English, G. Schwartz, W. Meador, M. J. Sabatier, and A. Mulligan, "Electrical stimulation promotes peripheral axon regeneration by enhanced neuronal neurotrophin signaling," *Dev. Neurobiol.*, vol. 67, no. 2, pp. 158–172, 2007.
- [323] M. J. Sabatier, N. Redmon, G. Schwartz, and A. W. English, "Treadmill training promotes axon regeneration in injured peripheral nerves," *Exp. Neurol.*, vol. 211, no. 2, pp. 489–493, 2008.
- [324] A. J. Harding, "The use of the thy-1-YFP-H transgenic mouse strain in studies of peripheral nerve injury," University of Sheffield, 2014.
- [325] A. J. Harding, C. R. Christmas, M. W. J. Ferguson, A. R. Loescher, P. P. Robinson, and F. M. Boissonade, "Mannose-6-phosphate facilitates early peripheral nerve regeneration in thy-1-YFP-H mice," *Neuroscience*, 2014.
- [326] Q. G. Xu, R. Midha, J. A. Martinez, G. F. Guo, and D. W. Zochodne, "Facilitated sprouting in a peripheral nerve injury," *Neuroscience*, vol. 152, no. 4, pp. 877–887, 2008.
- [327] G. Koulaxouzidis, G. Reim, and C. Witzel, "Fibrin glue repair leads to enhanced axonal elongation during early peripheral nerve regeneration in an in vivo mouse model," *Neural Regen. Res.*, vol. 10, no. 7, 2015.
- [328] A. Suri, V. S. Mehta, and C. Sarkar, "Microneural anastomosis with fibrin glue: An experimental study," *Neurol. India*, 2002.
- [329] S. Preibisch, S. Saalfeld, and P. Tomancak, "Globally optimal stitching of tiled 3D microscopic image acquisitions," *Bioinformatics*, 2009.
- [330] R. V. Lenth, "Java Applets for Power and Sample Size [Computer software]." .
- [331] E. Albadawi, "Neuroanatomical evaluation of the outcome of peripheral nerve repair using 3d printed biodegradable conduits," The University of Sheffield, 2018.
- [332] S. Atkins, A. R. Loescher, F. M. Boissonade, K. G. Smith, N. Ocleston, S. O’Kane, M. W. J. Ferguson, and P. P. Robinson, "Interleukin-10 reduces scarring and enhances regeneration at a site of sciatic nerve repair," *J. Peripher. Nerv. Syst.*, 2007.
- [333] P. Aebischer, V. Guénard, and R. F. Valentini, "The morphology of regenerating peripheral nerves is modulated by the surface microgeometry of polymeric guidance channels," *Brain Res.*, 1990.
- [334] N. Gómez, J. Cuadras, M. Butí, and X. Navarro, "Histologic assessment of sciatic nerve regeneration following resection and graft or tube repair in the mouse," *Restor. Neurol. Neurosci.*, 1996.
- [335] D. Zhang, S. Wu, J. Feng, Y. Duan, D. Xing, and C. Gao, "Micropatterned biodegradable polyesters clicked with CQAASIKVAV promote cell alignment, directional migration, and neurite outgrowth," *Acta Biomater.*, 2018.
- [336] M. Z. Sun, M. McGowan, P. J. Kingham, G. Terenghi, and S. Downes, "Novel thin-walled nerve conduit with microgrooved surface patterns for enhanced peripheral nerve repair," *J. Mater. Sci. Med.*, vol. 21, no. 10, pp. 2765–2774, 2010.

- [337] N. Zhang, C. Zhang, and X. Wen, "Fabrication of semipermeable hollow fiber membranes with highly aligned texture for nerve guidance," *J. Biomed. Mater. Res. - Part A*, 2005.
- [338] M. J. Mahoney, R. R. Chen, J. Tan, and W. Mark Saltzman, "The influence of microchannels on neurite growth and architecture," *Biomaterials*, 2005.
- [339] R. O. Labrador, M. Butí, and X. Navarro, "Influence of collagen and laminin gels concentration on nerve regeneration after resection and tube repair," *Exp. Neurol.*, 1998.
- [340] L. McKerracher, M. Chamoux, and C. O. Arregui, "Role of laminin and integrin interactions in growth cone guidance," *Mol. Neurobiol.*, 1996.
- [341] S. B. Bailey, M. E. Eichler, A. Villadiego, and K. M. Rich, "The influence of fibronectin and laminin during Schwann cell migration and peripheral nerve regeneration through silicon chambers," *J. Neurocytol.*, 1993.
- [342] G. Lundborg, L. Dahlin, D. Dohi, M. Kanje, and N. Terada, "A new type of 'bioartificial' nerve graft for bridging extended defects in nerves," *J. Hand Surg. J. Br. Soc. Surg. Hand*, vol. 22, no. 3, pp. 299–303, Jun. 1997.
- [343] E. Verdú, R. O. Labrador, F. J. Rodríguez, D. Ceballos, J. Forés, and X. Navarro, "Alignment of collagen and laminin-containing gels improve nerve regeneration within silicone tubes," *Restor. Neurol. Neurosci.*, 2002.
- [344] J. B. Phillips, S. C. J. Bunting, S. M. Hall, and R. A. Brown, "Neural tissue engineering: A self-organizing collagen guidance conduit," *Tissue Eng.*, 2005.
- [345] T. Cui, Y. Yan, R. Zhang, L. Liu, W. Xu, and X. Wang, "Rapid Prototyping of a Double-Layer Polyurethane–Collagen Conduit for Peripheral Nerve Regeneration," *Tissue Eng. Part C Methods*, vol. 15, no. 1, pp. 1–9, Mar. 2009.
- [346] F. Xie, Q. F. Li, B. Gu, K. Liu, and G. X. Shen, "In vitro and in vivo evaluation of a biodegradable chitosan-PLA composite peripheral nerve guide conduit material," *Microsurgery*, vol. 28, no. 6, pp. 471–479, 2008.
- [347] A. Wang, Q. Ao, Y. Wei, K. Gong, X. Liu, N. Zhao, Y. Gong, and X. Zhang, "Physical properties and biocompatibility of a porous chitosan-based fiber-reinforced conduit for nerve regeneration," *Biotechnol. Lett.*, vol. 29, no. 11, pp. 1697–1702, 2007.
- [348] Y. Yang, L. De Laporte, C. B. Rives, J.-H. Jang, W.-C. Lin, K. R. Shull, and L. D. Shea, "Neurotrophin releasing single and multiple lumen nerve conduits," *J. Control. Release*, vol. 104, no. 3, pp. 433–446, 2005.
- [349] E. Liodaki, I. Bos, J. A. Lohmeyer, O. Senyaman, K. L. Mauss, F. Siemers, P. Mailaender, and F. Stang, "Removal of collagen nerve conduits (NeuraGen) after unsuccessful implantation: Focus on histological findings," *J. Reconstr. Microsurg.*, 2013.
- [350] M. Merle, A. Lee Dellon, J. N. Campbell, and P. S. Chang, "Complications from silicon-polymer intubulation of nerves," *Microsurgery*, 1989.
- [351] G. Lundborg, B. Rosen, L. Dahlin, N. Danielsen, and J. Holmberg, "Tubular versus conventional repair of median and ulnar nerves in the human forearm: Early results from a prospective, randomized, clinical study," *J. Hand Surg. Am.*, 1997.
- [352] L. B. Dahlin, L. Anagnostaki, and G. Lundborg, "Tissue response to silicone tubes used to repair human median and ulnar nerves," *Scand. J. Plast. Reconstr. Surg. Hand Surg.*, 2001.
- [353] H. Sun, L. Mei, C. Song, X. Cui, and P. Wang, "The in vivo degradation, absorption and excretion of PCL-based implant.," *Biomaterials*, vol. 27, no. 9, pp. 1735–40, Mar. 2006.
- [354] G. E. Rutkowski and C. A. Heath, "Development of a bioartificial nerve graft. II. Nerve regeneration in vitro," *Biotechnol. Prog.*, 2002.
- [355] C. L. A. M. Vleggeert-Lankamp, G. C. W. De Ruiter, J. F. C. Wolfs, A. P. Pêgo, R. J. Van Den Berg, H. K. P. Feirabend, M. J. A. Malessy, and E. A. J. F. Lakke, "Pores in synthetic nerve conduits are beneficial to regeneration," *J. Biomed. Mater. Res. - Part A*, vol. 80, no. 4, pp. 965–982, 2007.
- [356] C. B. Jenq, L. L. Jenq, and R. E. Coggeshall, "Nerve regeneration changes with filters of different pore size," *Exp. Neurol.*, vol. 97, no. 3, pp. 662–671, 1987.

- [357] C. B. Jenq and R. E. Coggeshall, "Permeable tubes increase the length of the gap that regenerating axons can span," *Brain Res.*, 1987.
- [358] D. H. Kim, S. E. Connolly, S. Zhao, R. W. Beuerman, R. M. Voorhies, and D. G. Kline, "Comparison of macropore, semipermeable, and nonpermeable collagen conduits in nerve repair," *J. Reconstr. Microsurg.*, 1993.
- [359] C. Sherborne, R. Owen, G. C. Reilly, and F. Claeysens, "Light-based additive manufacturing of PolyHIPEs: Controlling the surface porosity for 3D cell culture applications," *Mater. Des.*, 2018.
- [360] R. Owen, C. Sherborne, T. Paterson, N. H. Green, G. C. Reilly, and F. Claeysens, "Emulsion templated scaffolds with tunable mechanical properties for bone tissue engineering," *J. Mech. Behav. Biomed. Mater.*, 2016.
- [361] D. W. Johnson, C. Sherborne, M. P. Didsbury, C. Pateman, N. R. Cameron, and F. Claeysens, "Macrostructuring of Emulsion-templated Porous Polymers by 3D Laser Patterning," *Adv. Mater.*, vol. 25, no. 23, pp. 3178–3181, 2013.
- [362] B. Aldemir Dikici, C. Sherborne, G. C. Reilly, and F. Claeysens, "Emulsion templated scaffolds manufactured from photocurable polycaprolactone," *Polymer (Guildf.)*, 2019.
- [363] A. Mosahebi, B. Woodward, M. Wiberg, R. Martin, and G. Terenghi, "Retroviral labeling of Schwann cells: In vitro characterization and in vivo transplantation to improve peripheral nerve regeneration," *Glia*, 2001.